STELLINGEN

behorende bij het proefschrift van R.A.W.M. Henkes

1. Het gebruik van de alom bekende warmteoverdrachtswet voor de turbulente natuurlijke convectie grenslaag langs een hete verticale plaat, waarbij het Nusselt getal aan de wand met een 1/3 macht van het Rayleigh getal afhangt, is af te raden voor Rayleigh getallen boven het beperkte gebied van Rayleigh getallen waar experimenten bekend zijn.
   Dit proefschrift.

2. De bronterm in de ϵ-vergelijking van het lage Reynolds $k-\epsilon$ turbulentie model van Jones & Launder wordt in de berekeningen van To & Humphrey voor de turbulente grenslaag langs een hete verticale plaat ten onrechte verwaarloosd.
   To, W.M. & Humphrey, J.A.C. 1986 Int. J. Heat Mass Transfer 29, 573-592.

3. Het is een nadeel van het gebruik van lage Reynolds $k-\epsilon$ modellen in natuurlijke convectie berekeningen dat de lage Reynolds termen, hoewel primair aan het $k-\epsilon$ model toegevoegd om de turbulentie dicht bij de wand te dempen, ook de laminaire-turbulente omslag op niet-eenduidige wijze uitstellen.
   Dit proefschrift.

4. Bij zijn afleiding van alle mogelijke gelijkvormige oplossingen van de grenslaagvergelijkingen voor de verticale natuurlijke convectie grenslaag heeft Semenov verzuimd zich af te vragen of al die oplossingen ook goed aansluiten op de fysische omgeving.
   Semenov, V.I. 1984 Heat Transfer - Sov. Res. 16, 69-85.

5. De grote waarden van de geschaalde verticale snelheid in de presentatie van de natuurlijke convectie rekenresultaten van onder meer De Vahl Davis en Markatos & Pericleous worden veroorzaakt door het gebruik van een onkarakteristieke snelheidsschaal. Orde 1 waarden zouden gevonden zijn indien niet de karakteristieke snelheidsschaal voor kleine Rayleigh getallen maar de karakteristieke snelheidsschaal voor grote Rayleigh getallen gekozen was.
   De Vahl Davis, G. 1983 Int. J. Num. Meth. Fluids 3, 249-264.
   Markatos, N.C. & Pericleous, K.A. 1984 Int. J. Heat Mass Transfer 27, 755-772.

6. De bechmark configuratie zoals geformuleerd in de GAMM workshop *Numerical Simulation of Oscillatory Convection in Low-Pr Fluids* (Marseille, 1988), ter berekening van de Hopf bifurcatie in de Navier-Stokes vergelijkingen, vormt een duidelijk voorbeeld waarbij het gebruik van een (eerste orde) upwind schema in de discretizatie van de convectie een veel onnauwkeuriger resultaat geeft dan het gebruik van een centraal schema.
Henkes, R.A.W.M. & Hoogendoorn, C.J. 1990 Proc. GAMM workshop, B. Roux (ed.), Notes on Numerical Fluid Mechanics, vol. 27, pp. 144-152. Vieweg.

7. De singulariteit die enige tijd na het plotseling in beweging brengen van een cylinder ontstaat in de stroming beschreven door de grenslaagvergelijkingen wordt uitgesteld door het toepassen van sterke visceuze-niet visceuze interactie.
Henkes, R.A.W.M. & Veldman, A.E.P. 1987 J. Fluid Mech. 179, 513-529.

8. Veel tekstverwerkers maken een slecht onderscheid tussen het italic symbool voor de v-snelheid (v) en het symbool dat doorgaans voor de kinematische viscositeit gebruikt wordt (ν), waardoor dergelijke tekstverwerkers minder geschikt zijn voor de beschrijving van problemen uit de stromingsleer.

9. Het zoeken naar een contactlens vergt veelal een bril.

10. Uit de overweldigende belangstelling die momenteel voor het werk van de schilder Van Gogh aan de dag wordt gelegd mag niet de conclusie worden getrokken dat men heden ten dage veelal genuanceerder over moderne kunst denkt dan honderd jaar geleden.

11. De ongeloofwaardige overacting die typerend is voor veel Nederlands toneel kan mogelijk verholpen worden door op de toneelscholen meer aandacht te besteden aan de methode van Stanislavski.

12. Mede doordat de meeste exemplaren van een proefschrift ongelezen blijven moet extra veel zorg besteed worden aan de omslag.

NATURAL-CONVECTION BOUNDARY LAYERS

NATURAL-CONVECTION BOUNDARY LAYERS

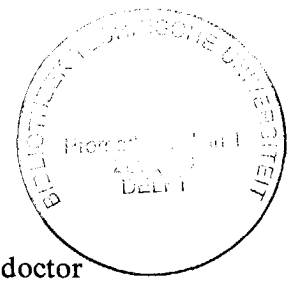

Proefschrift

ter verkrijging van de graad van doctor
aan de Technische Universiteit Delft,
op gezag van de Rector Magnificus,
Prof. drs P.A. Schenck,
in het openbaar te verdedigen
ten overstaan van
een commissie aangewezen door
het College van Dekanen
op dinsdag 5 juni 1990 te 16.00 uur

door

Rudolphus Aloysius Wijnandus Maria Henkes

geboren te Delft
vliegtuigbouwkundig ingenieur

Dit proefschrift is goedgekeurd door de promotor:
Prof. ir C.J. Hoogendoorn.

aan Martine

Hij zoog de borst vol adem en stapte in bed. 'Het is gezien,' mompelde hij, 'het is niet onopgemerkt gebleven.' Hij strekte zich uit en viel in een diepe slaap.

Uit *De Avonden*, Gerard Reve (1947).

CONTENTS

PRINCIPAL SYMBOLS

c_f	dimensionless wall-shear stress for cavity, $2\nu(\partial v/\partial x)_w/(g\beta\Delta TH)$
c_{fy}	dimensionless wall-shear stress for plate, $2\nu(\partial v/\partial x)_w/(g\beta\Delta Ty)$
f	frequency *also* transformed stream function *in chapter 3*
g	gravitational acceleration *also* transformed temperature *in chapter 3*
G_k	buoyant production of turbulent kinetic energy
H	height of cavity
k	turbulent kinetic energy
Nu	Nusselt number for cavity, $-(H/\Delta T)\ (\partial T/\partial x)_w$
Nu_y	Nusselt number for plate, $-(y/\Delta T)\ (\partial T/\partial x)_w$
$\overline{Nu}$	averaged Nusselt number in cavity, $\int_0^1 Nu\ d(y/H)$
p	pressure
p'	pressure correction in numerical iteration
P_k	shear production of turbulent kinetic energy
Pr	Prandtl number
Ra	Rayleigh number for cavity, $g\beta\Delta TH^3Pr/\nu^2$
Ra_y	Rayleigh number for plate, $g\beta\Delta Ty^3Pr/\nu^2$
S	gradient of thermal stratification in cavity center, $(H/\Delta T)\ (\partial T/\partial y)$
t	time
Δt	numerical time step
T	temperature
ΔT	characteristic temperature difference, $T_h - T_c$ for cavity, $T_h - T_\infty$ for plate
T_c	temperature of cold cavity wall
T_h	temperature of hot cavity wall or plate
u	horizontal velocity component
u_b	buoyant velocity scale for cavity, $\sqrt{g\beta\Delta TH}$
u_0	velocity scale for cavity, $(g\beta\Delta T\nu)^{1/3}$
v	vertical velocity component
v_b	buoyant velocity scale for plate, $\sqrt{g\beta\Delta Ty}$
v_0	velocity scale for plate, $(g\beta\Delta T\nu)^{1/3}$
w	velocity component perpendicular to u and v
x	horizontal coordinate
y	vertical coordinate

Greek symbols

β	coefficient of thermal expansion
δ	boundary-layer thickness *also* amplitude of oscillation *in chapter 5*
δ_{ij}	Kronecker delta, $=1$ for $i=j$, $=0$ for $i\neq j$

ϵ	dissipation rate of turbulent kinetic energy
ζ	dimensionless length for plate, xNu_y/y
ν	molecular kinematic viscosity
ν_t	turbulent kinematic viscosity
ρ	density
σ_T	turbulent Prandtl number for T
ψ	stream function, $u=-\partial\psi/\partial y$, $v=\partial\psi/\partial x$
ψ_c	stream function at center of cavity

Superscripts

k	iteration level
n	time level

Subscripts

cr	bifurcation in Navier-Stokes equations
i	grid point in x-direction
j	grid point in y-direction
max	maximum of a quantity
trans	laminar-turbulent transition in Reynolds equations
w	wall condition
∞	environment condition

1. INTRODUCTION

1.1. Essence of natural convection

The Greek scientist Archimedes (287-212 b.C.) seems to be the first who related the buoyant force to the influence of the earth's gravitational field on density differences. When Archimedes was getting into his bath-tub, maybe after a long day of deep thinking, he felt how the bath water gave an upward force on his body. The scientist became very enthusiastic and he cried out: eureka! (ηὑρηκα), I have found it. Archimedes formulated a law describing that a body immersed in a fluid reveals an upward buoyant force that is equal (but opposite in direction) to the gravity force on the fluid displaced by the body. Indeed Archimedes discovered the buoyant force, but this was only the beginning. He left many details to unravel by others, who were born after him.

An application of Archimedes' law that clearly demonstrates the essence of the physics that will be studied in this thesis is found in the rising of a hot-air balloon. The air inside the balloon is heated, which decreases the density of the air. Because now the density of the air inside the balloon becomes smaller than the density of the surrounding air, Archimedes' upward buoyant force will be larger than the downward gravity force on the balloon. The disbalance of forces sets the balloon into motion and causes it to rise. What happens to the large hot-air balloon is what in essence also happens to every small particle in a fluid with density differences. The density differences under influence of the gravity force give rise to the *natural-convection flow* of the fluid. Particles of fluid that are less dense are moved upward, and denser particles of fluid are moved downward. These natural-convection flows are investigated in this study.

The adjective *natural* indicates that a density difference drives the flow, in contrast to a *forced*-convection flow, where a pressure difference drives the flow. Instead of *natural convection* some studies use the synonym *free convection* if the external flow along a body in an open environment is concerned. Density differences can result from temperature differences, from differences in the concentrations of chemical species in the fluid, or from the presence of multiple phases of a fluid. In this study only natural-convection flows resulting from temperature differences will be considered. Two elementary classes of natural-convection flows with temperature differences are: heating (or cooling) from a horizontal wall (*heating-from-below*) and heating (or cooling) from a vertical wall (*heating-from-the-side*). The former class, for example, is characteristic for Rayleigh/Bénard convection and for the meteorology of the earth's atmospheric boundary layer. Both classes of natural-convection flows play a role in different technical applications, like solar collectors, climate conditioning of rooms, isolation by double glazing, heat removal in micro electronics and cooling of nuclear reactors.

This thesis gives a theoretical study of the natural-convection flow belonging to the heating-from-the-side class. We will solve the flow equations numerically. The emphasis is on those situations in which the flow occurs in a thin layer close to the wall, the so-called *natural-convection boundary layer*. Different flow

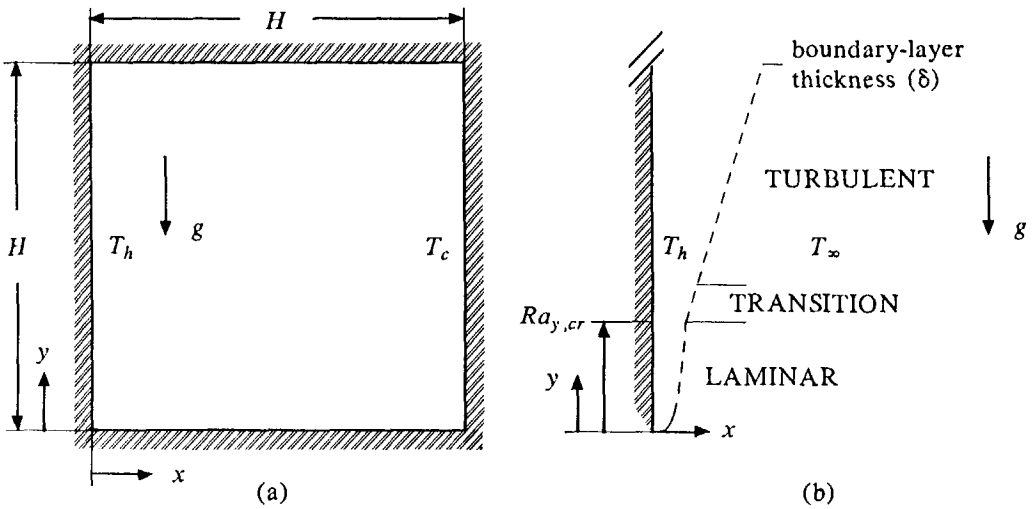

FIGURE 1.1. The two geometries to be studied; (a) square cavity heated from the side, (b) hot vertical plate.

phenomena related to the boundary layer will be investigated: laminar flow, bifurcation of the steady laminar flow to an unsteady flow, laminar-turbulent transition, fully turbulent flow, wall functions, flow reversal in the boundary layer and the thermal stratification in the environment of the boundary layer. The numerical results will be compared with existing experimental data as reported in the literature. The study is restricted to two-dimensional flows.

1.2. Two geometries to be studied

Figure 1.1 shows the two heating-from-the-side geometries that are investigated here: the square cavity and the vertical plate. In figure 1.1a we have the two-dimensional square cavity (enclosure) that is differentially heated over the vertical walls. The cavity has a hot left wall (with the temperature T_h) and a cold right wall (with the temperature T_c). The height of the cavity is H. x and y are the coordinates in the horizontal and vertical direction respectively. Inside the cavity is a fluid; both air and water will be considered. Figure 1.1b shows a further simplification of the hot vertical wall of the cavity, namely the semi-infinite hot vertical plate in an isothermal environment (in which T_∞ is the environment temperature). The temperature difference ΔT in both geometries ($\Delta T = T_h - T_c$ in the cavity and $\Delta T = T_h - T_\infty$ for the plate) gives density differences in the fluid. The density differences are proportional to ΔT and to the coefficient of thermal expansion of the fluid (β). The density differences under influence of the gravitation force (with the acceleration g) lead to buoyant forces, which set the fluid into motion. The moving fluid gets a resistance force due to the viscosity of the fluid (ν). Part of the buoyant force is needed to overcome this resistance force. The natural-convection flow depends on only two dimensionless parameters: the Rayleigh

number (Ra) and the Prandtl number (Pr). The Rayleigh number is defined by $Ra=g\beta\Delta TH^3Pr/\nu^2$ and the Prandtl number is the ratio of the kinematic viscosity and the thermal diffusivity of the fluid, $Pr=\nu/a$. Some natural-convection studies introduce the Grashof number (Gr) instead of the Rayleigh number, with $Gr=Ra/Pr$, but in this study we will consequently use the Rayleigh number. The difference between the fluids air and water is expressed by a difference in the Prandtl number; we use $Pr=0.71$ for air and $Pr=7.0$ for water. Because the plate geometry in figure 1.1b does not have a fixed height H, the y-based Rayleigh number will be used for the plate ($Ra_y=g\beta\Delta Ty^3Pr/\nu^2$).

We investigate the natural-convection flow up to $Ra=10^{15}$ for the square cavity and up to $Ra_y=10^{25}$ for the plate. When the Rayleigh number is large (say beyond 10^6) the natural-convection flow takes place in a thin natural-convection boundary layer along the vertical wall. Besides the hydrodynamic boundary layer (defining the velocity field, *i.e.* the flow) there also is a thermal boundary layer (defining the temperature field). For both air and water, the hydrodynamic boundary layer and the thermal boundary layer have the same order of thickness. Because the Prandtl number for water is larger than for air, the thermal boundary layer for water is somewhat thinner than for air. The flow in the square cavity is centro-symmetric with respect to the center of the cavity: the rising boundary layer along the hot left vertical wall corresponds to the falling boundary layer along the cold right vertical wall. Because of the centro-symmetry, it is sufficient to present the results for the boundary layer along the hot wall only.

For the boundary layer along the vertical wall in figure 1.1b, the flow is steady and laminar as long as the Rayleigh number is below a critical value ($Ra_{y,cr}$). At $Ra_{y,cr}$ the steady flow becomes unstable and an unsteady flow with some characteristic frequencies results. When the Rayleigh number is further increased more frequencies enter the flow, which gives a transition until a fully turbulent boundary layer is found. The same occurs in the cavity of figure 1.1a: up to Ra_{cr} the flow is steady and laminar, at Ra_{cr} the flow becomes unsteady oscillating, and for higher Rayleigh numbers the boundary layers along the vertical walls undergo a transition to a fully turbulent state.

1.3. Main questions

The main questions in this study are:
(i) What are the characteristics of the laminar and turbulent flow in the cavity and along the plate, when the Rayleigh number is successively increased.
(ii) What is the asymptotic structure of the laminar and turbulent flow in the limit $Ra \rightarrow \infty$ for the cavity and in the limit $Ra_y \rightarrow \infty$ for the plate.
(iii) How does the flow along the walls of the cavity compare to the flow along the plate.

ad (i). The natural-convection flow is calculated by numerically solving the incompressible Navier-Stokes equations, including the energy equation, for the cavity and by numerically solving the boundary-layer equations for the plate. The Boussinesq approximation is applied to the equations. The boundary-layer equations are a simplified formulation of the Navier-Stokes equations: diffusion in the

y-direction of the vertical boundary is neglected with respect to the diffusion in the x-direction, and also pressure gradients across the boundary-layer thickness are neglected. These simplifications are only justified for a sufficiently large Rayleigh number. The boundary-layer equations have a much simpler mathematical structure than the Navier-Stokes equations, and they require a far less computational effort to solve. In particular the laminar flow along the plate in an isothermal environment is very easy to calculate, because for this case the steady boundary-layer equations (which actually are partial differential equations in the two space coordinates x and y) reduce to ordinary differential equations (which depend on only one transformed coordinate ξ). The laminar flow in the cavity will be calculated by solving the *steady* Navier-Stokes equations. The *unsteady* Navier-Stokes equations in the cavity will be solved to determine at which critical Rayleigh number the steady laminar flow becomes unstable. At Ra_{cr} the Navier-Stokes equations at large time will show a bifurcation, implying that the steady solution branches to an unsteady oscillating solution. We investigate whether the resulting frequencies are related to an instability in the boundary layers along the vertical cavity walls. If the Rayleigh number is gradually increased further beyond Ra_{cr} the flow becomes fully turbulent. The direct simulation of the fully turbulent flow at large Rayleigh numbers, by solving the unsteady three-dimensional Navier-Stokes equations, must await the development of a faster generation computers. Therefore we have time-averaged the Navier-Stokes equations, which yields the Reynolds equations. The correlations between fluctuating quantities in the Reynolds equations are modelled by the $k-\epsilon$ turbulence model. The performance of the standard $k-\epsilon$ model and different existing low-Reynolds-number $k-\epsilon$ models will be compared by solving the turbulent boundary-layer equations along the hot vertical plate in an isothermal environment. The low-Reynolds-number models modify the standard model to account for the low-turbulence levels which occur, for example, very close to the wall. The $k-\epsilon$ models use two partial differential equations for the turbulent quantities k (the kinetic energy of the turbulence) and ϵ (the dissipation rate of turbulent kinetic energy). Next to the $k-\epsilon$ models also the Reynolds-stress model will be used to calculate the turbulent flow along the plate. Besides the equations for k and ϵ, the Reynolds-stress model uses partial differential equations for the turbulent stresses in all directions. The standard $k-\epsilon$ model and two of the best performing low-Reynolds-number $k-\epsilon$ models for the plate (the models of Chien and Jones & Launder) are applied in the Reynolds equations to calculate the turbulent flow in the cavity.

ad (ii). The large-Rayleigh-number laminar and turbulent solutions are used to detect whether the flow shows asymptotic structures in the limit of an infinitely large Rayleigh number. In an asymptotic structure proper scalings for the velocity, the temperature and the space coordinates exist which make the scaled solution independent of the Rayleigh number. Actually the boundary-layer equations are an asymptotic formulation of the Navier-Stokes equations. Also the boundary-layer equations themselves might show an asymptotic behaviour in the limit $Ra_y \to \infty$. An asymptotic solution of the boundary-layer equations is also referred to as a similarity solution. If the environment is isothermal, the laminar boundary-layer equations simplify to ordinary differential equations, defining the well-known

similarity solution of Ostrach. In this study we will analyze all possible temperature distributions $T_\infty(y)$ of the environment that also admit a laminar similarity solution. If a similarity solution of the turbulent boundary-layer equations exists it can be used as a so-called wall function in turbulent computations. For the forced-convection boundary layer these wall functions are well-known. On the contrary, the wall functions for the vertical natural-convection boundary layer are not fully known in the literature; we will investigate here whether we can directly derive them from the numerical results for the turbulent boundary-layer equations. Wall-functions can be valuable in calculations for more complicated configurations, where the computational effort can be reduced by assuming that wall functions correctly describe the flow along the walls, implying that no numerical grid points are needed there. Not only for the plate, but also for the cavity, the proper scalings and asymptotic behaviour of the laminar and turbulent flow will be studied.

ad (iii). The main difference between the plate in an open environment and the cavity is that the plate environment is isothermal whereas the core of the cavity is thermally stratified (the isotherms are horizontal and the temperature increases with the height). By solving the boundary-layer equations for a stratified environment and by comparing this solution with the Navier-Stokes solutions, we will study whether the laminar boundary layer along the vertical cavity wall indeed can be interpreted as a boundary layer along a plate in a stratified environment. The stratification in the cavity for the turbulent case turns out to be much smaller than for the laminar case. Therefore, the turbulent boundary layer along the cavity wall will be compared with the turbulent boundary layer along the plate in an isothermal environment.

2. FLOW EQUATIONS

2.1. Introduction

A mathematical model for fluid flows that includes viscosity was originally published by Navier (1822) and by Stokes (1845). For some special boundary conditions and geometries analytical solutions of the so-called Navier-Stokes equations exist. Apart from a few analytical solutions, for a long time the richness of other solutions remained hidden in the Navier-Stokes equations. Nowadays these solutions can be revealed with the help of a computer. The Computational Fluid Dynamics (CFD) describes how a discrete representation (*discretization*) of the Navier-Stokes equations can be made and how the solution of the discrete system can be determined (*solver*).

In this chapter we introduce the Navier-Stokes equations and the simplifications applied in this study. In particular we will only consider incompressible fluids and the Boussinesq approximation will be applied. In the case the flow is turbulent (instead of laminar), we show how the turbulence can be modelled by a $k-\epsilon$ model. Possible boundary conditions for the equations are given. The principles of the finite-volume method, which is used to discretize the Navier-Stokes equations, are outlined. The line Gauss-Seidel solver is used to iteratively determine the solution of the discrete system. The pressure is iteratively updated by the SIMPLE pressure-correction method. Some relaxation methods to speed up the convergence of the iterative process are summarized.

In the seventies computational packages were developed to numerically solve the Navier-Stokes equations: TEACH, CHAMPION and PHOENICS. Recently FLUENT was added to this list. All these packages use the finite-volume method to discretize the Navier-Stokes equations and handle the pressure iteration by a SIMPLE-like pressure-correction method. The iterative solver uses either a line-coupling method or a field-coupling method. In the present study a code in the same tradition was written to solve the Navier-Stokes equations. Also the code to solve the boundary-layer equations, which are an approximation of the Navier-Stokes equations, was especially developed for this study.

A lot of discretizations and solvers have been proposed in the literature. Which one has to be preferred can be largely problem dependent. We do not claim that the approaches used in our own codes are optimum, giving a desired numerical accuracy of the solution against the lowest computational effort. New methods appearing in the literature, however, have to be interpreted with care: the Navier-Stokes equations are so complex that the superiority of a proposed modification can often only be proved for a selected problem. An extended review of discretizations and solvers for the Navier-Stokes equations is given in the book by Peyret & Taylor (1983). Details about the finite-volume discretization and the SIMPLE solver are given in the book by Patankar (1980).

2.2. Navier-Stokes equations

Considered is the flow of a fluid (with the velocity components u_i) in time (t) and space (with the Cartesian coordinates x_i). The three principal thermodynamic properties of the fluid are: density (ρ), pressure (p) and temperature (T). The classical thermodynamics postulates that the thermodynamic state of a fluid is determined by only two independent thermodynamic properties. A third thermodynamic property is related to the two independent properties by the *equation of state* of the fluid. In differential form it reads

$$\frac{d\rho}{\rho} = \kappa_T dp - \beta dT \tag{2.1}$$

where κ_T is the coefficient of isothermal compressibility and β is the coefficient of thermal expansion. The enthalpy (h) is also frequently used as a thermodynamic property. The equation of state for h is given by

$$dh = \frac{1}{\rho}(1-\beta T)dp + c_p dT \tag{2.2}$$

where c_p is the specific heat at constant pressure. Gradients in the thermodynamic properties can give rise to the flow of the fluid. Conservation laws define the partial differential equations that describe the dependent variables (velocity components and two thermodynamic properties) as a function of the independent variables (time and space coordinates). This system of flow equations is referred to as the Navier-Stokes equations.

Conservation of mass is expressed by the *continuity equation*

$$\frac{\partial}{\partial t}\rho + \frac{\partial}{\partial x_j}\rho u_j = 0. \tag{2.3a}$$

Newton's second law describes the conservation of momentum according to the *momentum equation*

$$\frac{\partial}{\partial t}\rho u_i + \frac{\partial}{\partial x_j}\rho u_j u_i = \rho g_i + \frac{\partial}{\partial x_j}P_{ji}. \tag{2.3b}$$

The first law of thermodynamics conserves energy according to the *energy equation*

$$\frac{\partial}{\partial t}\rho\left(h-\frac{p}{\rho}\right) + \frac{\partial}{\partial x_j}\rho u_j\left(h-\frac{p}{\rho}\right) = P_{ji}\frac{\partial u_i}{\partial x_j} - \frac{\partial q_j}{\partial x_j}. \tag{2.3c}$$

In the energy equation we have excluded transport of energy by radiation. g_i is the gravitational acceleration. The stress tensor P_{ji} is modelled by the Newtonian constitution equation

$$P_{ij} = -p\delta_{ij} - \frac{2}{3}\mu\delta_{ij}\frac{\partial u_k}{\partial x_k} + \mu\left(\frac{\partial u_i}{\partial x_j} + \frac{\partial u_j}{\partial x_i}\right). \tag{2.4a}$$

The conduction vector q_j is modelled by Fourier's law

$$q_j = -\lambda\frac{\partial T}{\partial x_j}. \tag{2.4b}$$

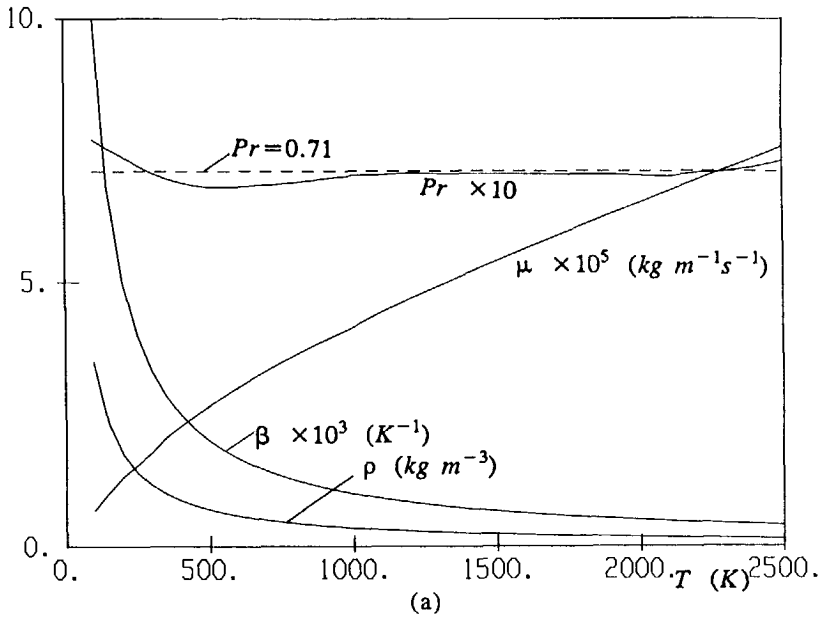

(a)

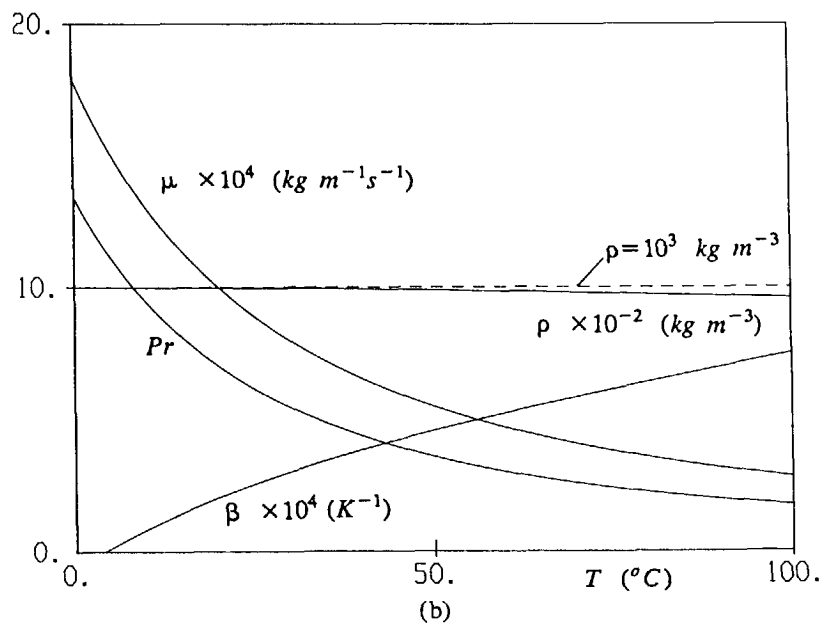

(b)

FIGURE 2.1. Temperature dependence of different properties; (a) for air, (b) for water.

According to the second law of thermodynamics the model parameters μ (dynamic viscosity) and λ (thermal conductivity) have to be positive. The models treat them as thermodynamic properties: they depend on only two independent thermodynamic properties, for example the pressure and the temperature.

The equation of state for gases can be approximated by the gas law

$$\rho = p/RT. \tag{2.5a}$$

Here $R=R_0/M$; $R_0=8.313\ J\ K^{-1}mole^{-1}$ (universal gas constant) and M is the mass of the gas per mole. The gas law is exact for all gases in the limit of vanishingly small pressure. With equation (2.1) this gas law can also be written as

$$\beta = 1/T, \qquad \kappa_T = 1/p. \tag{2.5b}$$

Gases satisfying this gas law for each pressure are referred to as ideal gases. The kinetic gas theory shows that for two-atomic gases the Prandtl number ($Pr=\mu c_p/\lambda$) is constant and equal to one, if vibration and rotation of the atoms are neglected; this implies that for gases with constant c_p the dynamic viscosity and the thermal conductivity similarly depend on the two independent thermodynamic properties. With good accuracy, air can be considered as an ideal gas ($M=0.029\ kg\ mole^{-1}$) with a constant c_p value ($c_p=1006\ J\ kg^{-1}K^{-1}$). The Prandtl number of air equals 0.71 (almost independent of the temperature and pressure). The dynamic viscosity for air is nearly independent of the pressure; it increases with the temperature. For the liquid water as well the pressure dependence of the properties β, c_p, μ and λ (or Pr) is small and they mainly depend on the temperature. Pr and μ strongly decrease with the temperature, whereas c_p and λ are almost constant ($c_p=4200\ J\ kg^{-1}K^{-1}$). Figure 2.1 gives the temperature dependence of ρ, β, μ and Pr for both air and water at a pressure of 1 bar.

2.3. Some simplifications

For air and water c_p can be taken constant and the pressure dependence of the enthalpy can be neglected (this is exact for ideal gases). This reduces equation (2.2) to

$$h = c_p T. \tag{2.6}$$

With this relation the Navier-Stokes equations (2.3) can be rewritten as

$$\frac{\partial \rho}{\partial t} + \frac{\partial}{\partial x_j}\rho u_j = 0 \tag{2.7a}$$

(unsteady term − convection)

$$\frac{\partial}{\partial t}\rho u_i + \frac{\partial}{\partial x_j}\rho u_j u_i = -\frac{\partial p}{\partial x_i} + \rho g_i - \frac{\partial}{\partial x_i}\frac{2}{3}\mu\frac{\partial u_k}{\partial x_k} + \frac{\partial}{\partial x_j}\mu\left(\frac{\partial u_i}{\partial x_j} + \frac{\partial u_j}{\partial x_i}\right)$$

(unsteady term − convection − pressure − buoyancy − dilatation − diffusion) (2.7b)

$$\frac{\partial}{\partial t}\rho T + \frac{\partial}{\partial x_j}\rho u_j T = \frac{\partial}{\partial x_j}\frac{\mu}{Pr}\frac{\partial T}{\partial x_j} + \frac{1}{c_p}\left(\frac{\partial p}{\partial t} + u_j\frac{\partial p}{\partial x_j}\right) + \frac{\mu}{c_p}\Phi \tag{2.7c}$$

(unsteady term − convection − diffusion − compressibility − viscous dissipation)

with

$$\Phi = \frac{\partial u_i}{\partial x_j}\frac{\partial u_i}{\partial x_j} + \frac{\partial u_i}{\partial x_j}\frac{\partial u_j}{\partial x_i} - \frac{2}{3}\frac{\partial u_k}{\partial x_k}\frac{\partial u_l}{\partial x_l}.$$

In this study we consider air and water under conditions for which these fluids can be assumed to be *incompressible*: the density only depends on the temperature (κ_T is set to zero in equation (2.1)) and the compressibility term in the energy balance is neglected. Also the viscous dissipation in the energy balance can be neglected. The density and the coefficients β, μ and Pr are evaluated at a pressure of 1 bar. A detailed analysis of the conditions under which these neglectings hold is given by Gebhart (1962) and by Eshghy & Morrison (1966).

Further simplifications are made in the Boussinesq approximation (for details see Gray & Giorgini, 1976). The Boussinesq approximation treats the coefficients β, μ and Pr as constants, which are evaluated at a characteristic temperature T_0. With exception of the buoyancy term, also the density is assumed to be constant (evaluated at T_0). The density in the buoyancy term is linearized according to

$$\frac{\rho(T)}{\rho(T_0)} = 1 - \beta(T - T_0). \tag{2.8}$$

In two dimensions, the Navier-Stokes equations under the Boussinesq approximation read (taking $g_1 = 0$ and $g_2 = -g$)

$$\begin{aligned}
&\frac{\partial u}{\partial x} + \frac{\partial v}{\partial y} = 0 \\
&\frac{\partial u}{\partial t} + u\frac{\partial u}{\partial x} + v\frac{\partial u}{\partial y} = -\frac{1}{\rho}\frac{\partial p}{\partial x} + \nu\left(\frac{\partial^2 u}{\partial x^2} + \frac{\partial^2 u}{\partial y^2}\right) \\
&\frac{\partial v}{\partial t} + u\frac{\partial v}{\partial x} + v\frac{\partial v}{\partial y} = -\frac{1}{\rho}\frac{\partial p}{\partial y} + g\beta(T - T_0) + \nu\left(\frac{\partial^2 v}{\partial x^2} + \frac{\partial^2 v}{\partial y^2}\right) \\
&\frac{\partial T}{\partial t} + u\frac{\partial T}{\partial x} + v\frac{\partial T}{\partial y} = \frac{\nu}{Pr}\left(\frac{\partial^2 T}{\partial x^2} + \frac{\partial^2 T}{\partial y^2}\right).
\end{aligned} \tag{2.9}$$

Here ν (= μ/ρ) is the kinematic viscosity. In the isothermal, no-flow situation the momentum equation (2.7b) reduces to $-\partial p_s/\partial x_i + \rho(T_0)g_i = 0$, in which p_s is the hydrostatic pressure based on the isothermal temperature T_0. Instead of the full pressure we can also treat the corrected pressure $p^* = p - p_s$ as a variable in the Navier-Stokes formulation. This corrected pressure (with omission of the *-superscript) is used in the Boussinesq formulation (2.9). Gray & Giorgini show that the Boussinesq approximation requires that the characteristic temperature difference (ΔT) is sufficiently small. If the averaged temperature is 15 ^oC, for example, the error in the terms of the Boussinesq formulation (2.9) due to the approximation is smaller than 10% as long as $\Delta T < 28.6\ ^oC$ for air and as long as $\Delta T < 1.25\ ^oC$ for water. This illustrates that the applicability of the Boussinesq approximation is restricted to much smaller temperature differences for water than for air. In particular β for water changes sign at 4 ^oC, implying that the Boussinesq approximation totally fails if the averaged temperature for water comes

close to this value.

2.4. Turbulence modelling

If the characteristic velocity of the flow is u_0 and the characteristic length is x_0, the Reynolds number of the flow can be defined as $Re = u_0 x_0/\nu$. If the Reynolds number is sufficiently small the flow is laminar, but for larger Reynolds numbers the flow becomes turbulent. Part of the turbulent structures are characterized by small, short-living eddies, having the Kolmogorov time scale ($x_0\, Re^{-1/2}/u_0$) and length scale ($x_0\, Re^{-3/4}$). Both memory and speed of present-day computers are insufficient to calculate the details of this turbulent flow: the turbulence has to be modelled. In order to model the turbulence, the turbulent fluctuations in the Navier-Stokes equations are averaged in time. The Reynolds-averaging splits the variable ϕ into a mean part $\bar{\phi}$ and a fluctuating part ϕ'

$$\phi(x_i,t) = \bar{\phi}(x_i) + \phi'(x_i,t); \quad \text{with } \bar{\phi} = \lim_{t^* \to \infty} \int_{-t^*/2}^{t^*/2} \frac{\phi(x_i,t')}{t^*}\, dt'. \tag{2.10}$$

Rewriting the Navier-Stokes equations in terms of equation (2.10) and Reynolds-averaging the result again simplifies the Navier-Stokes equations to the Reynolds equations. If the density fluctuations are neglected, the Reynolds equations read

$$\begin{aligned}
&\frac{\partial \bar{\rho}}{\partial t} + \frac{\partial}{\partial x_j}\bar{\rho}\bar{u_j} = 0 \\
&\frac{\partial}{\partial t}\bar{\rho}\bar{u_i} + \frac{\partial}{\partial x_j}\bar{\rho}\bar{u_j}\bar{u_i} = \\
&-\frac{\partial \bar{p}}{\partial x_i} + \bar{\rho} g_i - \frac{\partial}{\partial x_i}\frac{2}{3}\mu\frac{\partial \bar{u_k}}{\partial x_k} + \frac{\partial}{\partial x_j}\mu\left(\frac{\partial \bar{u_i}}{\partial x_j} + \frac{\partial \bar{u_j}}{\partial x_i}\right) - \frac{\partial}{\partial x_j}\bar{\rho}\overline{u_j' u_i'} \\
&\frac{\partial}{\partial t}\bar{\rho}\bar{T} + \frac{\partial}{\partial x_j}\bar{\rho}\bar{u_j}\bar{T} = \frac{\partial}{\partial x_j}\frac{\mu}{Pr}\frac{\partial \bar{T}}{\partial x_j} - \frac{\partial}{\partial x_j}\bar{\rho}\overline{u_j' T'} + \frac{\mu}{c_p}\Phi + \frac{\bar{\rho}}{c_p}\epsilon
\end{aligned} \tag{2.11}$$

where ϵ is the dissipation rate of turbulent kinetic energy

$$\epsilon = \nu\left(\overline{\frac{\partial u_i'}{\partial x_j}\frac{\partial u_i'}{\partial x_j}} + \overline{\frac{\partial u_i'}{\partial x_j}\frac{\partial u_j'}{\partial x_i}} - \frac{2}{3}\overline{\frac{\partial u_k'}{\partial x_k}\frac{\partial u_l'}{\partial x_l}}\right). \tag{2.12}$$

Because ν is small, both the viscous dissipation and the turbulent dissipation in the energy equation can be neglected. The Reynolds averaging adds the gradients of the so-called *Reynolds stresses* to the momentum equations and it adds the gradients of the turbulent heat fluxes to the energy equation. A different averaging is used in the Large Eddy Simulation of turbulent flows (see *e.g.* Rogallo & Moin, 1984); a filter is applied that only averages the smallest eddies, whereas the representation of the evolution of the larger eddies by the unsteady terms remains unchanged.

The cross-term correlations in the Reynolds equations have to be modelled: this is the *closure problem* of turbulence. Reviews of existing models are given by Reynolds (1976), Rodi (1980) and Lakshminarayana (1985). Two classes of models can be distinguished: eddy-viscosity models and Reynolds-stress models.

The eddy-viscosity models define a model for the turbulent viscosity ν_t in the identities

$$-\overline{u_i' u_j'} = \nu_t \left(\frac{\partial \overline{u_i}}{\partial x_j} + \frac{\partial \overline{u_j}}{\partial x_i} \right) - \frac{2}{3} \delta_{ij} \left(k + \nu_t \frac{\partial \overline{u_k}}{\partial x_k} \right) \tag{2.13a}$$

$$-\overline{u_j' T'} = \frac{\nu_t}{\sigma_T} \frac{\partial \overline{T}}{\partial x_j}. \tag{2.13b}$$

Here σ_T is the turbulent Prandtl number for the temperature and k $(=(u_1'^2+u_2'^2+u_3'^2)/2)$ is the kinetic energy of the turbulent fluctuations. Equations (2.13) have the same structure as equations (2.4). ν_t satisfies the identity

$$\nu_t = c_\mu V L \tag{2.14}$$

where V and L are a characteristic velocity and length for the turbulence. In general c_μ, V and L can still be functions of time and space. ν_t can be approximated in different ways:

(i) ν_t is constant (Boussinesq model). This is a very simplified approach, which does not recognize that turbulence is a property of the flow rather than a property of the fluid.

(ii) zero-equation (or: algebraic) models. These models use an algebraic relation between ν_t and other variables. The most famous algebraic model is Prandtl's mixing-length model. It takes L proportional to the distance to the wall, whereas V is taken as the product of L and the velocity gradient in the direction normal to the wall. An extension of Prandtl's mixing-length model is described by the algebraic model of Cebeci & Smith (see Cebeci & Bradshaw, 1984), which is often used to model turbulent boundary layers. The Cebeci & Smith model is one of the models which we will apply to the turbulent boundary layer along the hot vertical plate in the isothermal environment (see chapter 6).

(iii) one-equation models. These models solve one partial differential equation for a to ν_t related variable. For example, in equation (2.14) the model can use an algebraic expression for V and a differential equation for L.

(iv) two-equation models. These models solve two partial differential equations for two to ν_t related variables. The most famous two-equation model is the $k-\epsilon$ model, giving differential equations for k and ϵ. Concerning equation (2.14), this model uses a constant c_μ and sets $V=k^{1/2}$ and $L=k^{3/2}/\epsilon$. In this study, most of the calculations for the turbulent boundary layer along the hot vertical plate in the isothermal environment (chapter 6) and all turbulent calculations in the cavity (chapter 7) will apply the $k-\epsilon$ model.

Reynolds-stress models derive transport equations, including convection and diffusion, for all the Reynolds stresses $\overline{u_i' u_j'}$ and $\overline{u_j' T'}$. Often some of the resulting partial differential equations are simplified to algebraic equations (giving an algebraic-stress model). We will perform some of the calculations for the turbulent boundary layer along the hot vertical plate in the isothermal environment with the (fully differential) Reynolds-stress model. Details of this model will be given in section 6.11.

In this chapter we only explain the standard $k-\epsilon$ model. Different modifications of the standard $k-\epsilon$ model will be compared for the turbulent flow along the plate and in the cavity. These modifications, giving so-called low-Reynolds-number $k-\epsilon$ models, account for the low turbulence levels in the flow. The precise form of the low-Reynolds-number modifications will be given in the chapters 6 and 7. A form of the (standard) $k-\epsilon$ model was originally proposed by Harlow & Nakayama (1967). The $k-\epsilon$ model is very frequently used in the literature and is usually considered as a good compromise between physical accuracy and computational effort.

The turbulent structures consist of a spectrum of eddies. The size of the largest eddies is often determined by the size of the configuration, whereas the smallest eddies have the Kolmogorov length. The largest eddies extract their kinetic energy from both the gradient-mean-velocity field and the gradient-mean-temperature field. The smaller eddies extract their energy from the nearest larger eddies. Finally, the energy reaches the smallest eddies where it is dissipated by molecular viscosity with a rate ϵ . Therefore k and ϵ are two very characteristic properties of the turbulence, which seem to be a good starting point for modelling the characteristic turbulent velocity ($V=k^{1/2}$) and length ($L=k^{3/2}/\epsilon$). Because the $k-\epsilon$ model treats c_μ, V and L as scalars, also ν_t is a scalar. This absence of a direction dependence implies that the $k-\epsilon$ model cannot be expected to work well in strongly anisotropic turbulence.

We derive the equations for k and ϵ, neglecting the density fluctuations everywhere except in the buoyancy term. c_μ in equation (2.14) is taken constant. The momentum equation in the Reynolds equations (2.11), multiplied with $\overline{u_i}$, and the momentum equation in the Navier-Stokes equations (2.7), multiplied with u_i, are subtracted from each other. After Reynolds-averaging of the result an equation for k is obtained

$$\frac{\partial}{\partial t}\bar{\rho}k + \frac{\partial}{\partial x_j}\bar{\rho}\overline{u_j}k = \tag{2.15}$$

$$\overline{u_i{}'\frac{\partial}{\partial x_j}\mu\left(\frac{\partial u_i{}'}{\partial x_j} + \frac{\partial u_j{}'}{\partial x_i}\right)} - \frac{1}{2}\frac{\partial}{\partial x_j}\bar{\rho}\overline{u_i{}'u_i{}'u_j{}'} + \bar{\rho}P_k + \bar{\rho}G_k - \overline{u_i{}'\frac{\partial p'}{\partial x_i}}$$

I II III IV V

with

$$P_k = -\overline{u_i{}'u_j{}'}\frac{\partial \overline{u_i}}{\partial x_j} \quad , \quad G_k = \overline{\rho' u_i{}'}g_i/\bar{\rho}.$$

The left-hand side consists of an unsteady term and a convection term. The right-hand side consists of viscous dissipation and diffusion (I), turbulent diffusion (II), shearing production (III), buoyancy production (IV) and pressure diffusion (V), Term I is split into a viscous diffusion part and a viscous dissipation part

$$\overline{u_i{}'\frac{\partial}{\partial x_j}\mu\left(\frac{\partial u_i{}'}{\partial x_j} + \frac{\partial u_j{}'}{\partial x_i}\right)} = \frac{\partial}{\partial x_j}\mu\frac{\partial k}{\partial x_j} - \bar{\rho}\epsilon. \tag{2.16a}$$

Term II is modelled according to

$$-\frac{1}{2}\frac{\partial}{\partial x_j}\bar{\rho}\overline{u_i' u_i' u_j'} = \frac{\partial}{\partial x_j}\frac{\bar{\rho}\nu_t}{\sigma_k}\frac{\partial k}{\partial x_j}. \tag{2.16b}$$

Here σ_k is the turbulent Prandtl number for k. The Reynolds stress $-\overline{u_i' u_j'}$ in III is modelled according to equation (2.13a) and $\overline{\rho' u_i'}$ in IV is modelled analogously to equation (2.13b)

$$\overline{\rho' u_i'} = -\frac{\nu_t}{\sigma_T}\frac{\partial \bar{\rho}}{\partial x_i}. \tag{2.16c}$$

Under the Boussinesq approximation density fluctuations are rewritten as temperature fluctuations

$$\overline{\rho' u_i'} = -\bar{\rho}\beta\overline{u_i' T'} = \bar{\rho}\beta\frac{\nu_t}{\sigma_T}\frac{\partial \bar{T}}{\partial x_i}. \tag{2.16d}$$

Term V is neglected. In the $k-\epsilon$ model an approximated expression for ϵ is used; on the right-hand side of equation (2.12) neglected are the second term (which is exact for homogeneous turbulence) and the third term (which indeed vanishes if density fluctuations are neglected). What remains is

$$\epsilon = \nu\overline{\frac{\partial u_i'}{\partial x_j}\frac{\partial u_i'}{\partial x_j}}. \tag{2.17}$$

After some mathematical manipulations with the Navier-Stokes and Reynolds equations an equation for ϵ is found

$$\begin{aligned}
&\frac{\partial}{\partial t}\bar{\rho}\epsilon + \frac{\partial}{\partial x_j}\bar{\rho}\bar{u_j}\epsilon = \\
&\underbrace{-\frac{\partial}{\partial x_k}\left(\mu\overline{u_k'\frac{\partial u_i'}{\partial x_j}\frac{\partial u_i'}{\partial x_j}} + 2\nu\overline{\frac{\partial u_k'}{\partial x_i}\frac{\partial p'}{\partial x_i}} - \mu\frac{\partial \epsilon}{\partial x_k}\right)}_{\text{I}} \underbrace{-2\mu\overline{\frac{\partial u_i'}{\partial x_k}\frac{\partial u_i'}{\partial x_j}\frac{\partial u_k'}{\partial x_j}}}_{\text{II}} \\
&\underbrace{-2\bar{\rho}\nu^2\overline{\frac{\partial^2 u_i'}{\partial x_k \partial x_j}\frac{\partial^2 u_i'}{\partial x_k \partial x_j}}}_{\text{III}} + \underbrace{2\nu\overline{\frac{\partial u_i'}{\partial x_j}\frac{\partial \rho'}{\partial x_j}}g_i}_{\text{IV}} \\
&\underbrace{-2\mu\frac{\partial \bar{u_i}}{\partial x_k}\left(\overline{\frac{\partial u_i'}{\partial x_j}\frac{\partial u_k'}{\partial x_j}} + \overline{\frac{\partial u_j'}{\partial x_i}\frac{\partial u_j'}{\partial x_k}}\right)}_{\text{V}} \underbrace{-2\mu\overline{u_k'\frac{\partial u_i'}{\partial x_j}}\frac{\partial^2 \bar{u_i}}{\partial x_j \partial x_k}}_{\text{VI}}.
\end{aligned} \tag{2.18}$$

Term I consists of three contributions: turbulent diffusion, pressure diffusion and molecular diffusion. The pressure diffusion is neglected and the remaining part is modelled as

$$-\frac{\partial}{\partial x_k}\left(\mu\overline{u_k'\frac{\partial u_i'}{\partial x_j}\frac{\partial u_i'}{\partial x_j}} - \mu\frac{\partial \epsilon}{\partial x_k}\right) = \frac{\partial}{\partial x_j}\left(\mu + \frac{\bar{\rho}\nu_t}{\sigma_\epsilon}\right)\frac{\partial \epsilon}{\partial x_j}. \tag{2.19a}$$

Here σ_ϵ is the turbulent Prandtl number for ϵ. Term II and III both explode for increasing Reynolds number, but their sum remains finite. The sum is modelled as

$$-2\mu\overline{\frac{\partial u_i'}{\partial x_k}\frac{\partial u_i'}{\partial x_j}\frac{\partial u_k'}{\partial x_j}} - 2\bar{\rho}\nu^2\overline{\frac{\partial^2 u_i'}{\partial x_k \partial x_j}\frac{\partial^2 u_i'}{\partial x_k \partial x_j}} = \bar{\rho}(c_{\epsilon 1}P_k - c_{\epsilon 2}\epsilon)\frac{\epsilon}{k}. \qquad (2.19b)$$

$c_{\epsilon 1}$ and $c_{\epsilon 2}$ are model constants. Term IV is modelled as

$$2\nu\overline{\frac{\partial u_i'}{\partial x_j}\frac{\partial \rho'}{\partial x_j}}g_i = c_{\epsilon 1}c_{\epsilon 3}\bar{\rho}G_k\frac{\epsilon}{k}. \qquad (2.19c)$$

$c_{\epsilon 3}$ is a model parameter. Contributions V and VI can be neglected sufficiently far from a wall; close to the wall low-Reynolds-number modifications have to be applied. In the sequel bars to denote the averaged values will be omitted.

2.5. Boundary and initial conditions

According to the classification of Courant (1962) the partial differential equations for u, v, T, k and ϵ are parabolic in time and elliptic in space. Heuristically this implies that initial values for all these variables have to be specified at $t=0$ and a boundary condition for each variable is required at the boundary of the spatial domain.

For the velocity the following types of boundary conditions can be used:
(i) all velocity components are specified (*i.e.* Dirichlet boundary conditions).
(ii) both normal and tangential stress components are specified.
(iii) the normal stress component is specified in combination with the tangential velocity components (*i.e.* Neumann or pressure boundary condition).
(iv) tangential stress components are specified in combination with the normal velocity component.
If the boundary conditions (i) are used for the velocity, it is sufficient to fix only the level of the pressure (for example by prescribing the pressure in one point).

For the temperature two types of boundary conditions can be used:
(i) temperature specified (Dirichlet boundary condition).
(ii) normal component of the conduction vector is specified (Neumann boundary condition).

Boundary conditions for k and ϵ can also be either of the Dirichlet or of the Neumann type; their specification is part of the turbulence model. In turbulence calculations, often k and ϵ (and u, v and T) are not specified at the wall but at the first inner grid point; the solution between this first inner point and the wall is approximated by a universal profile which is known as a *wall function*. The form of the wall function for the vertical natural-convection boundary layer is not clearly known yet. The calculations for the plate in chapter 6 are performed totally up to the wall, applying low-Reynolds-number modifications instead of wall functions. These calculations will be used to derive wall functions for the turbulent natural-convection boundary layer along the vertical plate.

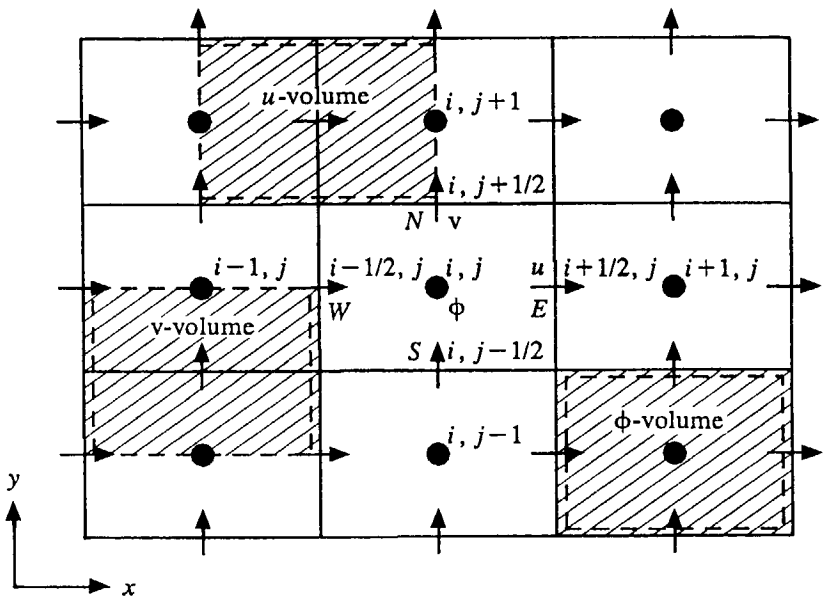

FIGURE 2.2. Finite-volume grid used to discretize the Navier-Stokes equations.

2.6. Discretization of the Navier-Stokes equations

In order to solve the Navier-Stokes (or Reynolds) equations numerically, the equations have to be replaced by a discrete system of algebraic relations between the variables at a finite number of grid points. This *discretization* has to be consistent: the deviation between the discrete equations and the Navier-Stokes equations has to vanish if the number of grid points is increased to infinity. Mostly the differential equations themselves are directly discretized (*e.g.* with finite differences, finite volumes, finite elements or spectral functions). It is also possible to discretize any system that is consistent with the Navier-Stokes equations for an infinite number of grid points (*e.g.* discrete-vortex method, method with cellular automata). Numerical solutions for a problem make only sense if it has been checked that the numerical truncation error, *i.e.* the difference between the finite-grid solution and the zero-grid solution, is sufficiently small. An indication that this error is small can be obtained by repeating the calculation with an increased number of grid points and verifying that this leads to only a small change in the numerical solution.

The present study uses the finite-volume method as introduced by Patankar & Spalding (1972). The finite-volume method divides the computational domain into rectangular volumes, as depicted in figure 2.2. Unknown velocity components are positioned in the middle of the sides of a volume and the scalar unknowns (p, T, k and ϵ) are positioned in the center of the volume. This staggered-grid concept was introduced by Harlow & Welch (1965) and has advantages in discretizing the pressure gradients in combination with the continuity equation.

To explain the finite-volume method we consider a two-dimensional convection-diffusion equation for a scalar transport unknown ϕ (= T, k or ϵ).

$$\frac{\partial \phi}{\partial t} + \operatorname{div} \underline{f} = s^{\phi}. \tag{2.20a}$$

Here, $\underline{f}$ is the flux vector and s^{ϕ} is a source term. $\underline{f}$ is the sum of a convection part $\underline{f}^c = \underline{u}\phi$ and a diffusion part $\underline{f}^d = -\nu^{\phi}\nabla\phi$. Equation (2.20a) is integrated over the finite volume around grid point (i, j), rewriting div $\underline{f}$ as fluxes through the sides of the (i, j)-volume with the help of Gauss' divergence theorem. (The integration is performed over the finite volumes around the staggered grid points for the velocities u and v if the momentum equations are considered, see figure 2.2). We obtain

$$\int_{\text{vol. } (i,j)} \frac{\partial \phi}{\partial t}\, dxdy + \int_{\text{side}} [f^E - f^W]\, dy + \int_{\text{side}} [f^N - f^S]\, dx = \int_{\text{vol. } (i,j)} s^{\phi}\, dxdy. \tag{2.20b}$$

The superscripts E, W, N and S refer to the east, west, north and south side of the volume respectively. The remaining integrals are approximated as

$$\left[\frac{\partial \phi}{\partial t}\right]_{i,j} \Delta x \Delta y + [f_{i+1/2,\,j} - f_{i-1/2,\,j}]\, \Delta y + [f_{i,\,j+1/2} - f_{i,\,j-1/2}]\, \Delta x = s^{\phi}_{i,\,j}\, \Delta x \Delta y + \Delta x \Delta y\, O(\Delta x^2, \Delta y^2) \tag{2.20c}$$

in which the size of the grid is $\Delta x = x_{i+1/2} - x_{i-1/2}$ and $\Delta y = y_{j+1/2} - y_{j-1/2}$. The finite-volume method has the advantage that it gives a conservative discretization: numerical mass, momentum and heat fluxes can be indicated that are conserved over the domain. The integration in time in equation (2.20c) is performed fully implicitly: all spatial derivatives are evaluated at the new time level n. The unsteady term, the fluxes and the source are further discretized with finite differences. The unsteady term at the time level n is optionally discretized with two time levels (B2 scheme) or with three time levels (B3 scheme) giving a first- and second-order truncation error in time respectively

$$\left[\frac{\partial \phi}{\partial t}\right]_{i,j} = \frac{\phi^n_{i,j} - \phi^{n-1}_{i,j}}{\Delta t} + O(\Delta t) \tag{2.21a}$$

$$\left[\frac{\partial \phi}{\partial t}\right]_{i,j} = \frac{3\phi^n_{i,j} - 4\phi^{n-1}_{i,j} + \phi^{n-2}_{i,j}}{2\Delta t} + O(\Delta t^2). \tag{2.21b}$$

Here $\Delta t = t^n - t^{n-1}$. The source term and the diffusion part of the flux are discretized with a second-order truncation error, for example

$$f^d_{i+1/2,\,j} = -\frac{1}{2}(\nu^{\phi}_{i,\,j} + \nu^{\phi}_{i+1,\,j}) \frac{\phi_{i+1,\,j} - \phi_{i,\,j}}{x_{i+1} - x_i} + O(\Delta x^2). \tag{2.21c}$$

In order to discretize the convection flux it is rewritten as

$$f^c_{i+1/2,\,j} = u_{i+1/2,\,j}\phi^E \tag{2.21d}$$

where ϕ^E is an approximation for ϕ at the east side of the volume (i, j). Different approximations for ϕ^E are proposed in the literature, for example:
(i) central scheme

$$\phi^E = (\phi_{i,j}+\phi_{i+1,j})/2$$

(ii) first-order upwind scheme (B2 scheme)

$$\phi^E = \begin{cases}\phi_{i,j} & \text{if } u_{i+1/2,j}\geq 0\\ \phi_{i+1,j} & \text{if } u_{i+1/2,j}<0\end{cases}$$

(iii) second-order upwind scheme (B3 scheme)

$$\phi^E = \begin{cases}(3\phi_{i,j}-\phi_{i-1,j})/2 & \text{if } u_{i+1/2,j}\geq 0\\ (3\phi_{i+1,j}-\phi_{i+2,j})/2 & \text{if } u_{i+1/2,j}<0\end{cases}$$

(iv) QUICK scheme (Quadratic Upstream Interpolation for Convection Kinematics; introduced by Leonard, 1979)

$$\phi^E = \begin{cases}(\phi_{i,j}+\phi_{i+1,j})/2 - (\phi_{i-1,j}-2\phi_{i,j}+\phi_{i+1,j})/8 & \text{if } u_{i+1/2,j}\geq 0\\ (\phi_{i,j}+\phi_{i+1,j})/2 - (\phi_{i,j}-2\phi_{i+1,j}+\phi_{i+2,j})/8 & \text{if } u_{i+1/2,j}<0.\end{cases}$$

Schemes (i), (iii) and (iv) lead to a second-order truncation error in the approximation of div $\mathcal{L}^c$, whereas scheme (ii) gives only first-order accuracy. Shyy (1985) solved the steady one-dimensional convection-diffusion equation with a zero source term, and compared the different approximations for the convection. The central scheme (i) shows wiggles (*i.e.* point-to-point oscillations) if the grid-Reynolds number ($Re_g = |u|\Delta x/\nu^\phi$) becomes larger than two. As a remedy against wiggles an upwind scheme (ii, iii or iv) can be used. The first-order upwind scheme (ii) most effectively damps wiggles, in turn for a smaller order of the truncation error: this scheme is said to show a large artificial (or: numerical) diffusion. De Vahl Davis & Mallinson (1976) show that the artificial diffusion of the first-order upwind scheme in a two-dimensional problem is maximum if the streamlines and grid lines intersect with 45^o. This cross-wind artificial diffusion is removed in the Skew-Upstream-Difference-Scheme of Raithby (1976). This upwind scheme discretizes the convection with first-order accuracy in the local direction of the streamline. Such a scheme makes only sense if the cross-wind artificial diffusion is indeed larger than Shyy's one-dimensional artificial diffusion. Besides accuracy, the choice of the discretization scheme for the convection also influences the stability of the numerical iteration process to solve the discrete system (see next section). Numerical (in)stability indicates whether perturbations are amplified or suppressed during the iteration process. The second-order schemes (and the central-scheme in particular) are less stable than the first-order upwind scheme. In this study we optionally use the central scheme or the hybrid scheme. If the grid-Reynolds number exceeds the value 2, the hybrid scheme locally switches from the central scheme (i) to the first-order upwind scheme (ii) and sets the diffusion contributions to zero.

The pressure plays a peculiar role in the incompressible Navier-Stokes equations, because the pressure does not appear in the continuity equation. Therefore,

the continuity equation acts as a *constraint* on the velocity field: the pressure has to be determined such that the velocity field in the momentum equation satisfies the continuity equation. This implies that the divergence operator in the continuity equation and the gradient operator for the pressure in the momentum equation are closely related. Uncareful discretization of the continuity equation and the pressure gradient can lead to a large numerical inaccuracy (wiggles) in the pressure. Van Kan (1986) shows that the finite-volume method on a staggered grid leads to a proper discretization. For constant ρ it gives

$$\begin{aligned} &\frac{u_{i+1/2,\,j}-u_{i-1/2,\,j}}{\Delta x}+\frac{v_{i,\,j+1/2}-v_{i,\,j-1/2}}{\Delta y}=O(\Delta x^2,\,\Delta y^2)\\ &\left(\frac{\partial p}{\partial x}\right)_{i+1/2,\,j}=\frac{p_{i+1,\,j}-p_{i,\,j}}{\Delta x}+O(\Delta x^2) \qquad (2.21e)\\ &\left(\frac{\partial p}{\partial y}\right)_{i,\,j+1/2}=\frac{p_{i,\,j+1}-p_{i,\,j}}{\Delta y}+O(\Delta y^2). \end{aligned}$$

Here the discretization of the continuity equation is found by integration over the finite volume (i, j).

The grid is constructed by firstly distributing the velocity grid lines such that the boundaries of the physical domain coincide with velocity grid lines. Secondly, the scalar points are placed in the center of the volumes. In order to discretize the boundary conditions, the grid is extended across the boundaries, introducing virtual grid points. The use of virtual points has the advantage that no modification of the discretization of the equations is required in the volumes along the boundaries. A Dirichlet boundary condition for u on the west or east boundary is treated by assigning the value to the unknown at the boundary. Similarly, the value for v is assigned to the unknown at the north or south boundary. Dirichlet boundary conditions for the scalars are discretized with second-order accuracy, using the virtual point. For example

$$\phi_{\mathrm{Dir}}=\frac{\phi_{i\max,\,j}+\phi_{i\max+1,\,j}}{2}+O(\Delta x^2) \qquad (2.21f)$$

where $i\max+1$ denotes the virtual point. The discretization of Neumann boundary conditions with virtual points is straightforward.

2.7. Solving of the discretized system

Many methods exist to solve the discrete system of nonlinear algebraic equations that results after the discretization of the Navier-Stokes equations:

$$\underline{f}(\underline{\phi})=\underline{0}. \qquad (2.22)$$

$\underline{\phi}$ consists of the unknowns for u, v, T, p, k and ϵ at all the grid points. The solving method (*solver*) concerns:
(i) the treatment of the nonlinearities, arising because equation (2.22) cannot be rewritten as $F\underline{\phi}=\underline{b}$, in which F and $\underline{b}$ are independent of $\underline{\phi}$.
(ii) the solving of the linear matrix equation $F\underline{\phi}=\underline{b}$.
Nonlinearities are always treated iteratively, whereas the solution of the matrix

equation $F\underline{\phi}=\underline{b}$ can be either direct or iterative.

The Newton-Raphson method only iterates for the nonlinearities. The method fully linearizes $\underline{f}(\underline{\phi})$ as $J_f(\underline{\phi})\underline{\phi}$, in which J_f is the Jacobian matrix of the vector $\underline{f}$. The Newton-Raphson process iterates according to

$$F^{k-1}\underline{\phi}^k = \underline{r}^{k-1} \tag{2.23}$$

with

$$F^{k-1} = J_f(\underline{\phi}^{k-1}) \quad , \quad \underline{r}^{k-1} = F^{k-1}\underline{\phi}^{k-1} - \underline{f}(\underline{\phi}^{k-1}).$$

k denotes the iteration level. $\underline{\phi}^k$ can directly be solved from this expression by Gauss elimination. The Newton-Raphson iteration process converges with a quadratic speed if the initial guess of $\underline{\phi}$ is chosen sufficiently close to the exact solution. To the author's knowledge no examples exist in which the Reynolds equations, with a $k-\epsilon$ model for turbulence, are solved with the Newton-Raphson method. Vanka (1985) used the Newton-Raphson method, except for the $k-\epsilon$ equations for which a line-iterative method has to be used to prevent the divergence of the iteration process. Disadvantages of the Newton-Raphson method are the large computer memory that is required to store J_f and its small range of convergence (*i.e.* an accurate initial guess is required).

Because of these disadvantages, often the solving of the different transport equations (for u, v, T, k and ϵ) is decoupled. The coupling is achieved by iteration with either a line-coupling or a field-coupling method. The line-coupling or field-coupling method updates the solution of the different discretized transport equations one after the other at a line or one after the other in the whole field respectively. After decoupling the discrete systems belonging to the different transport equations are solved. The uncoupled discretized systems for u, v, k and ϵ still contain nonlinearities. Instead of fully linearizing these nonlinearities by using the Jacobian matrix, often the convecting velocities in the convection terms of the momentum equations, as well as all nonlinearities in the k and ϵ equations, are evaluated at the previous iteration level. A linear equation $F\underline{\phi}=\underline{b}$ for the unknowns of each transport variable remains to be solved. This solving can be either direct or iterative. Examples of iterative methods are point-Jacobi, line Gauss-Seidel or the Strongly-Implicit Procedure (SIP; see Stone, 1968). In the present study the uncoupled transport equations are iteratively solved with a line Gauss-Seidel method. Alternating Gauss-Seidel sweeps are made from the west to the east side and from the east to the west side of the computational domain. To update the solution at line i in a sweep from the west side to the east side, contributions of the lines $i-1$ and i are solved at the new iteration level (*i.e.* they are treated implicitly), whereas contributions of the line $i+1$ are evaluated at the previous iteration level (*i.e.* they are treated explicitly). In a sweep from the east side to the west side the lines $i+1$ and i are treated implicitly, whereas the line $i-1$ is treated explicitly. Also all nonlinearities at the line i are evaluated at the previous iteration level. As a result, during the sweep only a tridiagonal matrix for each variable remains to be solved at line i. The tridiagonal matrix is solved directly. Line coupling is used to iteratively couple the different transport equations: in each Gauss-Seidel sweep the different variables (u, v, T, k and ϵ) are updated one after

the other at a line.

As explained in the previous section, the pressure and the continuity equation are closely related. As a consequence, the iteration for the pressure has to be coupled to the iteration for the continuity equation. All of these so-called pressure-correction methods have in common that the pressure in a finite volume is increased/decreased as long as there is a net inflow/outflow of mass through the sides of the finite volume. A variety of pressure-correction methods exist: SIMPLE, SIMPLEC, SIMPLER, SIMPLEST, PISO *et cetera*. The SIMPLE method (Semi-Implicit Method for Pressure-Linked Equations), which was introduced by Patankar & Spalding (1972), is used in the present study. The working of SIMPLE is illustrated for the simplified system

$$\begin{aligned}
&\frac{\partial u}{\partial x} + \frac{\partial v}{\partial y} = 0 \\
&\frac{\partial u}{\partial t} + U\frac{\partial u}{\partial x} + V\frac{\partial u}{\partial y} = -\frac{1}{\rho}\frac{\partial p}{\partial x} + \nu\left(\frac{\partial^2 u}{\partial x^2} + \frac{\partial^2 u}{\partial y^2}\right) \\
&\frac{\partial v}{\partial t} + U\frac{\partial v}{\partial x} + V\frac{\partial v}{\partial y} = -\frac{1}{\rho}\frac{\partial p}{\partial y} + \nu\left(\frac{\partial^2 v}{\partial x^2} + \frac{\partial^2 v}{\partial y^2}\right).
\end{aligned} \tag{2.24}$$

Here U and V are a fixed convecting velocity field. The finite-volume method, with the central scheme for the convection, gives the following discretization at an equidistant grid

$$\frac{u_{i+1/2,\,j} - u_{i-1/2,\,j}}{\Delta x} + \frac{v_{i,\,j+1/2} - v_{i,\,j-1/2}}{\Delta y} = 0 \tag{2.25a}$$

$$\begin{aligned}
&\frac{1}{\Delta t}(c_1 u_{i+1/2,\,j} - c_2 u^{n-1}_{i+1/2,\,j} + (c_2 - c_1)u^{n-2}_{i+1/2,\,j}) + U\frac{u_{i+3/2,\,j} - u_{i-1/2,\,j}}{2\Delta x} + \\
&V\frac{u_{i+1/2,\,j+1} - u_{i+1/2,\,j-1}}{2\Delta y} = -\frac{p_{i+1,\,j} - p_{i,\,j}}{\rho\Delta x} + \\
&\nu\left(\frac{u_{i+3/2,\,j} - 2u_{i+1/2,\,j} + u_{i-1/2,\,j}}{\Delta x^2} + \frac{u_{i+1/2,\,j+1} - 2u_{i+1/2,\,j} + u_{i+1/2,\,j-1}}{\Delta y^2}\right)
\end{aligned} \tag{2.25b}$$

$$\begin{aligned}
&\frac{1}{\Delta t}(c_1 v_{i,\,j+1/2} - c_2 v^{n-1}_{i,\,j+1/2} + (c_2 - c_1)v^{n-2}_{i,\,j+1/2}) + U\frac{v_{i+1,\,j+1/2} - v_{i-1,\,j+1/2}}{2\Delta x} + \\
&V\frac{v_{i,\,j+3/2} - v_{i,\,j-1/2}}{2\Delta y} = -\frac{p_{i,\,j+1} - p_{i,\,j}}{\rho\Delta y} + \\
&\nu\left(\frac{v_{i+1,\,j+1/2} - 2v_{i,\,j+1/2} + v_{i-1,\,j+1/2}}{\Delta x^2} + \frac{v_{i,\,j+3/2} - 2v_{i,\,j+1/2} + v_{i,\,j-1/2}}{\Delta y^2}\right).
\end{aligned} \tag{2.25c}$$

Here $c_1 = c_2 = 1$ for the B2 scheme in time and $c_1 = 3/2$, $c_2 = 2$ for the B3 scheme in time. The superscript n denotes the time level (the superscript at the new time level is omitted in the equations (2.25)). In this explanation U and V are fixed, whereas in the actual formulation $U = u$ and $V = v$, which have to be iteratively updated as well. This part of the iteration, however, is not essential in the

SIMPLE procedure. SIMPLE is a two-step predictor-corrector method for the solution of the equations (2.25) at the new iteration level k. Firstly, it predicts the velocity at the new iteration level k by solving the momentum equations (2.25b,c), fixing the pressure at the previous iteration level $k-1$. (SIMPLE does not prescribe how the velocity prediction from the momentum equations has to be determined; the velocity prediction can be solved with a direct method, or a new iteration process within SIMPLE can be set up). Secondly, the prediction of the velocities (u^* and v^*) is corrected according to

$$\begin{aligned} u^k_{i+1/2,\,j} &= u^*_{i+1/2,\,j} + \frac{du}{dp}(p'_{i,\,j} - p'_{i+1,\,j}) \\ v^k_{i,\,j+1/2} &= v^*_{i,\,j+1/2} + \frac{dv}{dp}(p'_{i,\,j} - p'_{i,\,j+1}) \end{aligned} \tag{2.26}$$

in which $p'_{i,\,j}$ $(=p^k_{i,\,j}-p^{k-1}_{i,\,j})$ is the pressure correction. The quantities du/dp and dv/dp follow from equations (2.25b,c)

$$\begin{aligned} \frac{du}{dp} &= \frac{\partial u_{i+1/2,\,j}}{\partial p_{i,\,j}} = \left(\frac{c_1\rho\Delta x}{\Delta t} + 2\mu\Delta x\left(\frac{1}{\Delta x^2}+\frac{1}{\Delta y^2}\right)\right)^{-1} \\ \frac{dv}{dp} &= \frac{\partial v_{i,\,j+1/2}}{\partial p_{i,\,j}} = \left(\frac{c_1\rho\Delta y}{\Delta t} + 2\mu\Delta y\left(\frac{1}{\Delta x^2}+\frac{1}{\Delta y^2}\right)\right)^{-1}. \end{aligned} \tag{2.27}$$

Substitution of equation (2.26) into the discretized continuity equation (2.25a) gives an equation for the pressure correction

$$\frac{p'_{i+1,\,j}-2p'_{i,\,j}+p'_{i-1,\,j}}{\Delta x^2} + \frac{p'_{i,\,j+1}-2p'_{i,\,j}+p'_{i,\,j-1}}{\Delta y^2} = \tag{2.28}$$

$$\left(\frac{c_1\rho}{\Delta t}+2\mu\left(\frac{1}{\Delta x^2}+\frac{1}{\Delta y^2}\right)\right)\left(\frac{u^*_{i+1/2,\,j}-u^*_{i-1/2,\,j}}{\Delta x} + \frac{v^*_{i,\,j+1/2}-v^*_{i,\,j-1/2}}{\Delta y}\right).$$

This is nothing but a discretization of a Poisson equation for p'

$$\frac{\partial^2 p'}{\partial x^2} + \frac{\partial^2 p'}{\partial y^2} = \left(\frac{c_1\rho}{\Delta t} + 2\mu\left(\frac{1}{\Delta x^2}+\frac{1}{\Delta y^2}\right)\right)\left(\frac{\partial u^*}{\partial x}+\frac{\partial v^*}{\partial y}\right). \tag{2.29}$$

The equation for the pressure correction can be solved either directly or iteratively. Besides the use of the line Gauss-Seidel method (with line-coupling) for the iterative updating of the transport variables (u, v, T, k and ϵ), it can also be used to update the pressure correction. In the present study both this line Gauss-Seidel iterative solver and the direct solver are optionally used to determine the pressure correction. Even when the velocity prediction and the pressure correction are solved exactly, the corrected velocity field and the corrected pressure at the new iteration level in SIMPLE do not exactly satisfy the momentum equations (2.25b,c). SIMPLEC, SIMPLER, SIMPLEST and PISO modify SIMPLE in order to better solve the momentum equations: SIMPLEC introduces an underrelaxation factor, whereas SIMPLER and PISO extend the two-step predictor-corrector method to a three-step predictor-corrector method. In all these pressure-correction methods, however, repeated k-iterations have to be made to exactly satisfy

equations (2.25).

2.8. Convergence

When a certain iterative strategy has been chosen to solve the discretized system, one hopes that the iteration process fastly converges to the discrete solution. Often relaxation is required to prevent the iteration process from divergence or to speed up convergence. Three forms of relaxation are used here:
(i) relaxation factor. The solution at the new iteration level is found as

$$\phi^k = \alpha\phi^{*k} + (1-\alpha)\phi^{k-1}. \tag{2.30}$$

Here α is the relaxation factor: $\alpha<1$ gives underrelaxation, $\alpha=1$ gives no relaxation and $\alpha>1$ gives overrelaxation. ϕ^{*k} is the solution without relaxation. α can be any function of the dependent or independent variables.
(ii) relaxation with a false time step. The term $(\phi^k_{i,j}-\phi^{k-1}_{i,j})/\Delta t_F$, in which Δt_F is the false time step, is added to the transport equations. This false time step can be any function of the dependent or independent variables.
(iii) source term manipulation. The source term is split as $s=s_1+s_2$ and iterates according to $s_1^{k-1}+(s_2/\phi)^{k-1}\phi^k$.
The values of α, Δt_F or s_1 and s_2 are optimized by trial-and-error.

The speed of convergence of classical iteration processes, like Jacobi and Gauss-Seidel, strongly decreases when the number of unknowns is increased. The use of a multigrid method overcomes this problem (for a review see Stüben & Linden, 1986). The classical iteration methods fastly solve the short-wave components of the solution (*i.e.* waves of only a few times the grid size), but they need many iterations to solve the long-wave components. The multigrid method uses different grids, stepping from one grid to the other by interpolation of the solution. Classical iteration methods are used at each grid. Now the long-wave components no longer delay the convergence because the multigrid method effectively solves them at the coarser grids. The multigrid method has extensively been studied for the Poisson equation, but their development for Navier-Stokes equations is still going on; the multigrid method is not used in the present study.

A criterion has to be formulated to check whether the iteration process can be stopped. When a computer is used, the best solution of the discrete system that can be obtained only has the round-off error of the machine. This round-off-error level is reached after a finite number of iterations. In practice the iteration is stopped earlier, when the convergence error (deviation between the iterated solution and the machine-accurate solution) is sufficiently small. It is reasonable to iterate long enough to get a convergence error that is much smaller than the physical error (error due to modelling of the physics, *e.g.* the turbulence model) and much smaller than the numerical truncation error (error due to the finite grid size in the discretization). Checking that the convergence error is sufficiently small requires the knowledge of the machine-accurate solution, which usually is not available. Therefore one has to rely on checks that *indicate* that the convergence error is small rather than prove it: we will check that the residuals in the discretized equations and the changes in the solution between two iterations are below a small stop criterion.

3. LAMINAR BOUNDARY-LAYER FLOW

3.1. Introduction

If the Rayleigh number is increased to infinity, the solution of the Navier-Stokes equations along a hot vertical plate in an open environment (figure 1.1b) becomes identical to the solution of the boundary-layer equations. When the environment is isothermal and stagnant, a coordinate transformation exists that simplifies the steady, laminar boundary-layer equations from partial differential equations to ordinary differential equations. The solution of this system, which is a similarity solution of the boundary-layer equations, was numerically determined by Ostrach (1953). If the vertical plate is part of a cavity, the environment of the plate (the core of the cavity) will not be isothermal, but stratified.

Semenov (1984) derived the system of ordinary differential equations for all possible distributions of the wall and environment temperature leading to a similarity solution of the steady, laminar boundary-layer equations. Some solutions of Semenov's system are already known in the literature: Ostrach (1953), giving the solution for a constant wall and a constant environment temperature, Sparrow & Gregg (1958), giving part of the class with a variable wall and a constant environment temperature, and Cheesewright (1967) and Yang *et al.* (1972), giving part of the class with a constant wall and a variable environment temperature. Recently Merkin (1985) found that the similarity solution for a variable wall and a constant environment temperature becomes singular if a critical value of the parameter describing the wall temperature is exceeded.

In this chapter the similarity solutions, including the new class which was detected in differential form by Semenov, are numerically calculated for air. In particular it is investigated whether Merkin's singular behaviour is also found for a constant wall and a variable environment temperature. We also determine in which part of the boundary layer the similarity solutions hold. Firstly, the solution must be matchable with the environment solution: the velocity and temperature profiles have to be independent of the position of the far outer edge of the boundary layer. Secondly, a similarity solution holds for small y (coordinate along the plate), if it is matchable to the solution in the small region at the leading edge of the plate, where boundary-layer equations do not apply, but the full Navier-Stokes equations have to be used. If this is not the case, the similarity solution found might be the boundary-layer solution for large y. To check this, also the nonsimilar boundary-layer equations are numerically solved.

When the research described in this chapter was just finished, a related study by Kulkarni *et al.* (1987) was published. They determined a similarity solution for a constant wall temperature and a linear, stably stratified environment. The authors claimed to have found a new class of similarity solutions, but this class was already detected by Semenov (1984). Actually Semenov's new class is more general, because the parameter describing the variation of the environment temperature can be any real number, whereas it has to be an integer in the description of Kulkarni *et al.*. Our study determines the solution of the new class for the

whole range of the parameter describing the variation of the stratification. By comparison with a nonsimilar boundary-layer calculation we will show that the new similarity solution for the stable, linear stratification does not fit in the boundary-layer flow pattern along the hot vertical plate with a sharp leading edge. This is not in line with Kulkarni *et al.*, who suggest agreement between this similarity solution and some numerical and experimental results in the literature.

3.2. Similarity equations

We consider the Navier-Stokes equations under the Boussinesq approximation (2.9) for a steady, laminar flow. When the Rayleigh number of the flow is sufficiently large, boundary layers appear along the fixed walls. The Rayleigh number is defined here as $Ra = g\beta\Delta T H^3 Pr/\nu^2$, in which ΔT and H are a characteristic temperature difference and a characteristic length respectively. In the boundary layer along a vertical wall the Navier-Stokes description can be simplified to boundary-layer equations

$$\begin{aligned} &\frac{\partial u}{\partial x} + \frac{\partial v}{\partial y} = 0 \\ &u\frac{\partial v}{\partial x} + v\frac{\partial v}{\partial y} = -\frac{1}{\rho}\frac{dp}{dy} + g\beta(T-T_\infty) + \nu\frac{\partial^2 v}{\partial x^2} \\ &u\frac{\partial T}{\partial x} + v\frac{\partial T}{\partial y} = \frac{\nu}{Pr}\frac{\partial^2 T}{\partial x^2}. \end{aligned} \tag{3.1}$$

We are searching for solutions that describe the natural-convection boundary-layer flow along a semi-infinite heated vertical plate, with its leading edge at $y=0$, in a stratified environment:

$$\begin{aligned} &y = 0: \quad v \text{ and } T \text{ profile specified} \\ &x = 0: \quad u = 0,\ v = 0,\ T = T_w(y) \\ &x \to \infty: \quad v = 0,\ T = T_\infty(y). \end{aligned} \tag{3.2}$$

Because for $x \to \infty$ the temperature converges to T_∞ and the convection and diffusion terms exponentially decay to zero, it follows from the boundary-layer equations (3.1) that $dp/dy = 0$.

For special distributions $T_w(y)$ and $T_\infty(y)$ a similarity solution of equations (3.1) exists. Such a similarity solution depends on only one scaled coordinate ξ, instead of the two independent $x-y$ coordinates. Recently Semenov (1984) has derived the differential equations for all possible similarity solutions. The temperature is rewritten as

$$T = (m + g(\xi))\ \Delta T\ \ \eta^n + T_0 \tag{3.3}$$

with

$$\begin{aligned} &\xi = 0: \ g(\xi) = 1,\ T_w = (m+1)\ \Delta T\ \eta^n + T_0 \\ &\xi \to \infty: \ g(\xi) = 0,\ T_\infty = m\ \Delta T\ \eta^n + T_0 \end{aligned} \tag{3.4}$$

where n and m are parameters, that can have any real value. T_0 is a fixed temperature. The transformed, dimensionless coordinates in this expression are

$$\xi = \left(\frac{g\beta\Delta T}{\nu^2}|M|\right)^{1/4}(My + N)^{\frac{n-1}{4}}\, x$$
$$\eta = My + N \qquad (\eta \geq 0) \tag{3.5}$$

where N and M are parameters (N is dimensionless and $|M|^{-1}$ has the length dimension). A stream function is introduced as

$$\psi = \left(\frac{g\beta\Delta T\nu^2}{|M|^3}\right)^{1/4}\eta^{\frac{n+3}{4}} f(\xi) \tag{3.6}$$

which defines the u- and v-velocities as

$$u = -\frac{\partial\psi}{\partial y} = \left(\frac{g\beta\Delta T\nu^2}{|M|^3}\right)^{1/4} M\,\eta^{\frac{n-1}{4}}\left(\frac{n-1}{4}\xi f' + \frac{n+3}{4} f\right)$$
$$\mathrm{v} = \frac{\partial\psi}{\partial x} = \left(\frac{g\beta\Delta T}{|M|}\right)^{1/2}\eta^{\frac{n+1}{2}} f'. \tag{3.7}$$

Substitution of these expressions into equations (3.1) yields the following ordinary differential equations for f and g:

$$f''' + \mathrm{sgn}(M)\left[\frac{n+3}{4} ff'' - \frac{n+1}{2} f'^2\right] + g = 0$$
$$g'' + Pr\ \mathrm{sgn}(M)\left[\frac{n+3}{4} fg' - n(g+m)f'\right] = 0 \tag{3.8}$$
$$\xi = 0:\ f = f' = 0,\ g = 1$$
$$\xi \to \infty:\ f' = 0,\ g = 0.$$

Special situations are $m=0$, for the nonstratified environment, and $m=-1$ for the constant wall temperature. The environment is stably stratified if $dT_\infty/dy > 0$ (provided β is positive), hence if $mMn > 0$. The branch with $\mathrm{sgn}(M)=-1$ was discovered by Semenov.

Solutions of equations (3.8) have been determined by Ostrach (1953) ($m=0$, $\mathrm{sgn}(M)=1$, $n=0$), Sparrow & Gregg (1958) ($m=0$, $\mathrm{sgn}(M)=1$, limited n-range), Cheesewright (1967) and Yang *et al.* (1972) ($m=-1$, $\mathrm{sgn}(M)=1$, limited n-range) and Merkin (1985) ($m=0$, $\mathrm{sgn}(M)=1$, whole n-range). No solutions are known for the whole n-range with $m=-1$ and for $\mathrm{sgn}(M)=-1$: these solutions are given here.

3.3. Numerical method

Two methods to solve the ordinary differential equations (3.8) were used: (i) the shooting method with explicit integration, and (ii) the direct method. The outer edge of the boundary layer is numerically taken at the finite distance ξ_{max}. The region $0 \leq \xi \leq \xi_{max}$ is covered with the equidistantly spaced grid points ξ_i ($i = 0, 1, \ldots, imax$).

Method (i) performs an explicit integration from the wall to the outer edge, finding the solution at $i+1$ from a Taylor expansion around i

$$\phi_{i+1} = \phi_i + \sum_{k=1}^{3} \frac{(\Delta\xi)^k}{k!} \phi_i^{(k)} \quad ; \quad \phi = f, g. \tag{3.9}$$

$\Delta\xi$ is the grid size. The derivatives f''', g'' and g''' in this expression follow from equations (3.8). The remaining derivatives are obtained by Taylor expansions similar to equation (3.9). The integration can be started at the wall when the values $f(0)$, $f'(0)$, $f''(0)$, $g(0)$ and $g'(0)$ are known. The values $f(0)$, $f'(0)$ and $g(0)$ are given as boundary conditions, but $f''(0)$ and $g'(0)$ have to be guessed. Repeated integrations (shootings) are required to determine $f''(0)$ and $g'(0)$ such that the boundary conditions for f' and g at the outer edge ξ_{max} are satisfied. The iterative updating of $f'(0)$ and $g'(0)$ is performed with the Newton-Raphson method, requiring the numerical evaluation of

$$\begin{aligned} a_1 &= \frac{\partial f'(\xi_{max})}{\partial g'(0)}, \quad a_2 = \frac{\partial f'(\xi_{max})}{\partial f''(0)}, \\ a_3 &= \frac{\partial g(\xi_{max})}{\partial g'(0)}, \quad a_4 = \frac{\partial g(\xi_{max})}{\partial f''(0)}. \end{aligned} \tag{3.10}$$

$f''(0)$ and $g'(0)$ at the new iterative level k follow from the old level $k-1$ according to

$$\begin{aligned} &f'(\xi_{max}) = \\ &f'^{k-1}(\xi_{max}) + (g'^{k}(0) - g'^{k-1}(0))\, a_1 + (f''^{k}(0) - f''^{k-1}(0))\, a_2 \\ &g(\xi_{max}) = \\ &g^{k-1}(\xi_{max}) + (g'^{k}(0) - g'^{k-1}(0))\, a_3 + (f''^{k}(0) - f''^{k-1}(0))\, a_4. \end{aligned} \tag{3.11}$$

This Newton-Raphson converges with a quadratic speed. The explicit integration (3.9) turned out to be very unstable: small deviations in the solution for $f''^{k}(0)$ and $g'^{k}(0)$ can lead to very large deviations in $f'^{k}(\xi_{max})$ and $g^{k}(\xi_{max})$.

The stability of method (ii) is much better. The equations are discretized according to

$$\begin{aligned} &\frac{f_i - f_{i-1}}{\Delta\xi} - h_i = 0 \quad (i=1, 2,\ldots, imax) \\ &\frac{h_{i+1} - 2h_i + h_{i-1}}{(\Delta\xi)^2} + \\ &\mathrm{sgn}(M) \left[\frac{n+3}{4} f_i \frac{h_{i+1} - h_{i-1}}{2\Delta\xi} - \frac{n+1}{2} h_i^2 \right] + g_i = 0 \quad (i=1, 2,\ldots, imax-1) \\ &\frac{g_{i+1} - 2g_i + g_{i-1}}{(\Delta\xi)^2} + \\ &Pr\ \mathrm{sgn}(M) \left[\frac{n+3}{4} f_i \frac{g_{i+1} - g_{i-1}}{2\Delta\xi} - n(g_i + m)h_i \right] = 0 \quad (i=1, 2,\ldots, imax-1) \end{aligned} \tag{3.12}$$

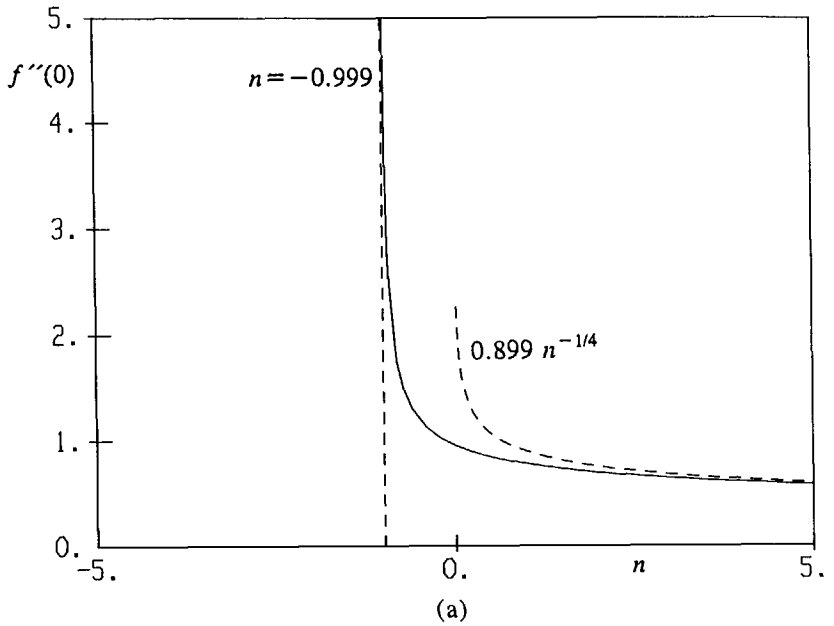

(a)

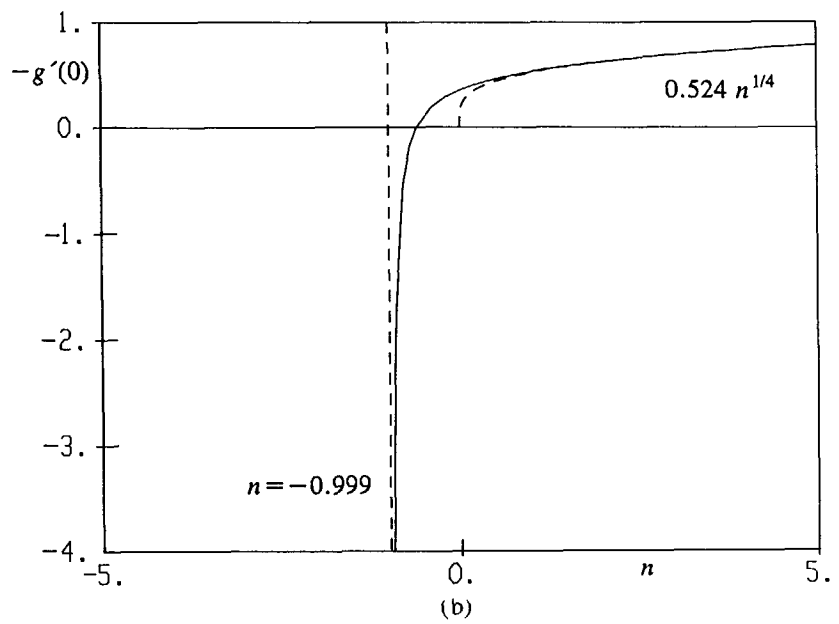

(b)

FIGURE 3.1. Variable wall and constant environment temperature ($m=0$, $\mathrm{sgn}(M)=1$); (a) wall-shear stress, (b) wall-heat transfer.

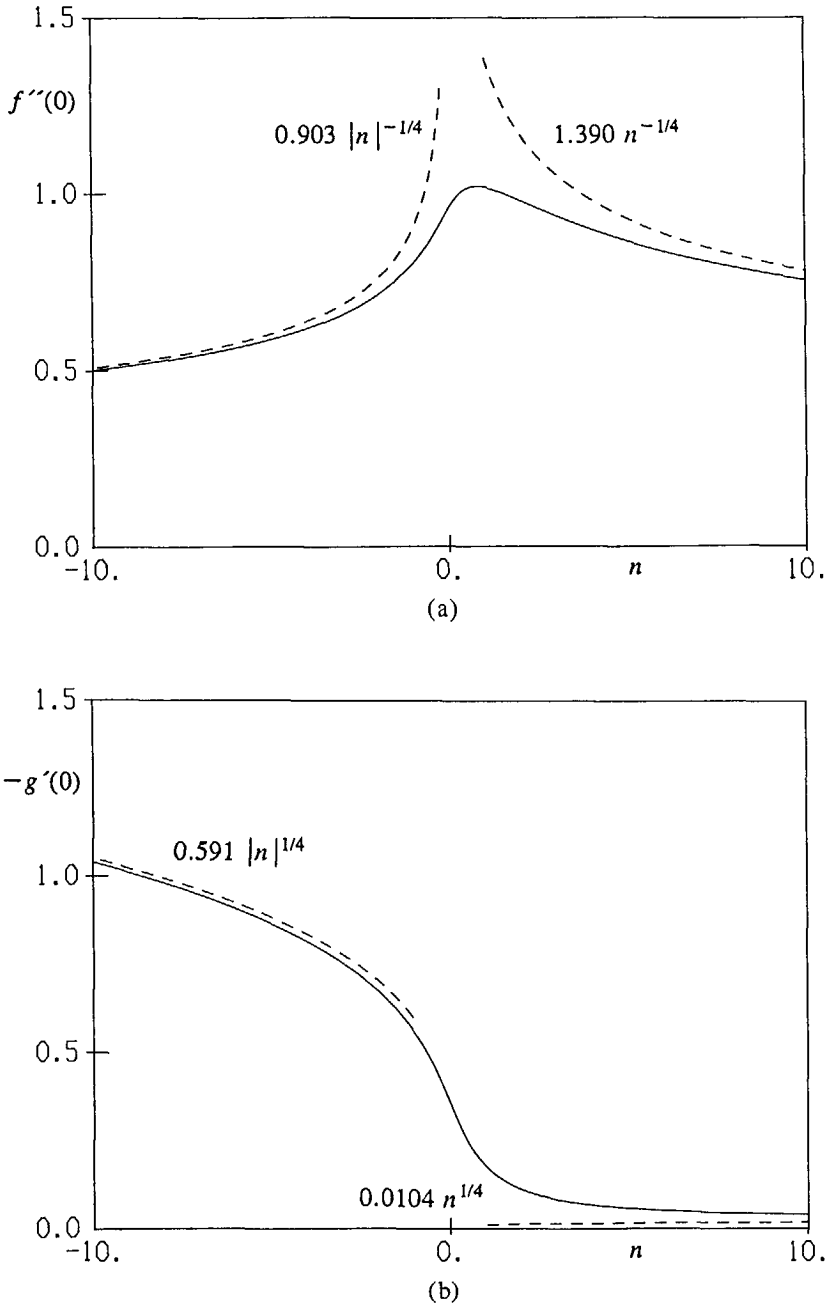

FIGURE 3.2. Constant wall and variable environment temperature ($m=-1$, $\mathrm{sgn}(M)=1$); (a) wall-shear stress, (b) wall-heat transfer.

$$f_0 = 0,\ h_0 = 0,\ g_0 = 0,\ h_{i\max} = 0,\ g_{i\max} = 0.$$

A system of $3(i\max+1)$ nonlinear algebraic equations results, which is solved with the Newton-Raphson method: at each iterative level the system is linearized and the resulting matrix equation is solved directly to update the solution. The discretization (3.12) yields only a sparse Jacobian matrix (having a block-tridiagonal structure) in the matrix equation.

3.4. Calculated similarity solutions

Solutions of equations (3.8) have been determined for air ($Pr=0.71$).

Firstly the similarity solution for the situation with a variable wall temperature and a nonstratified environment ($m=0$, $\mathrm{sgn}(M)=1$) has been determined. Our results in figure 3.1 confirm the results of Merkin (1985): the solution becomes singular if $n \downarrow -0.999$, and no solution seems to exist for smaller values.

Secondly solutions have been determined for a constant wall temperature and a stratified environment ($m=-1$, $\mathrm{sgn}(M)=\pm 1$). Similar to Merkin's analysis for $m=0$ in the limit $n \to \infty$, the behaviour for $m=-1$ in the limit $|n| \to \infty$ can be found with the transformation

$$\begin{aligned} \xi &= |n|^{-1/4}\,\bar{\xi} \\ f(\xi) &= |n|^{-3/4}\,F(\bar{\xi}) \\ g(\xi) &= G(\bar{\xi}). \end{aligned} \tag{3.13}$$

Substitution of these expressions into equations (3.8) leads to

$$\begin{aligned} &F''' + \mathrm{sgn}(M) \times \\ &\left[\frac{1}{4}\left(\mathrm{sgn}(n) + \frac{3}{|n|}\right) FF'' - \frac{1}{2}\left(\mathrm{sgn}(n) + \frac{1}{|n|}\right) f'^2\right] + G = 0 \\ &G'' + Pr\ \mathrm{sgn}(M) \times \\ &\left[\frac{1}{4}\left(\mathrm{sgn}(n) + \frac{3}{|n|}\right) FG' - \mathrm{sgn}(n)\,(G+m)\,F'\right] = 0 \\ &\bar{\xi} = 0\colon\ F = F' = 0,\ G = 1 \\ &\bar{\xi} \to \infty\colon\ F' = 0,\ G = 0. \end{aligned} \tag{3.14}$$

This transformation gives the following relations for the wall-shear stress and the wall-heat transfer

$$\begin{aligned} f''(0) &= |n|^{-1/4}\,F''(0) \\ g'(0) &= |n|^{1/4}\,G'(0). \end{aligned} \tag{3.15}$$

As follows from equations (3.14), F and G become independent of n in the limit $|n| \to \infty$. For $\mathrm{sgn}(M)=1$ the wall-shear stress and the wall-heat transfer are plotted in figure 3.2. Some velocity and temperature profiles are given in figure 3.3. We see that the whole n-range is free from singularities. As shown in detail in figure 3.4, a region with small flow reversal and temperature deficit is found in the outer part of the boundary layer in a stably stratified environment ($n<0$). There is

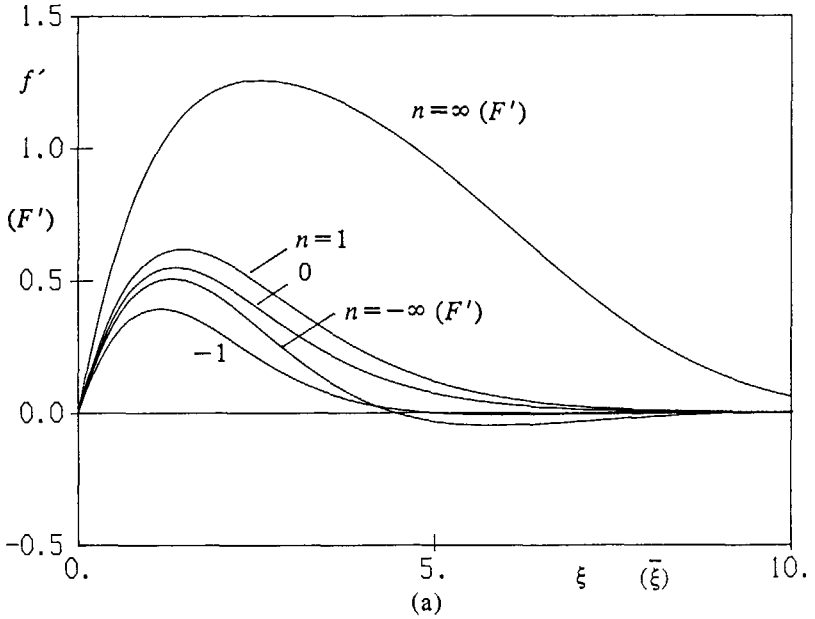

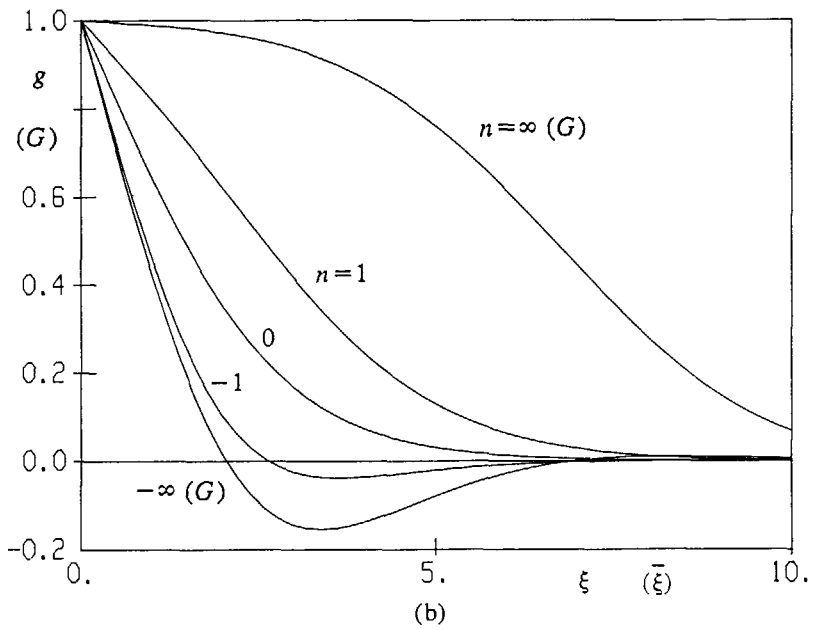

FIGURE 3.3. Constant wall and variable environment temperature ($m=-1$, $\mathrm{sgn}(M)=1$); (a) velocity profiles, (b) temperature profiles.

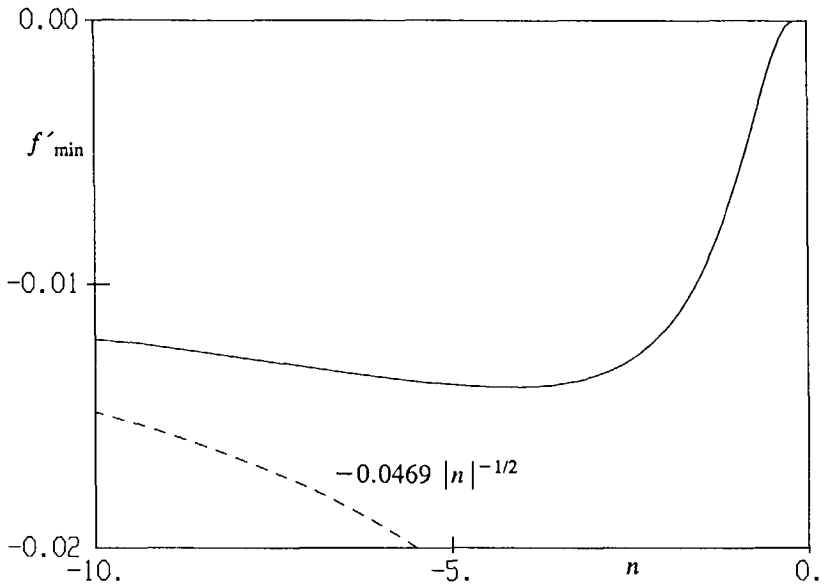

FIGURE 3.4. Flow reversal in the boundary layer for a stably stratified environment ($m=-1$, $\mathrm{sgn}(M)=1$).

no flow reversal or temperature deficit in an unstably stratified environment ($n>0$). The wall-shear stress and the wall-heat transfer for $\mathrm{sgn}(M)=-1$ are given in figure 3.5. We note that in the limit $|n| \to \infty$, the solution for $\mathrm{sgn}(M)=-1$ with $\mathrm{sgn}(n)=\pm 1$ is identical to the solution for $\mathrm{sgn}(M)=1$ with $\mathrm{sgn}(n)=\mp 1$. Increasing n from $-\infty$ to 0 (unstable stratification) gives a zero wall-heat transfer with a temperature identical to 1 everywhere, except in a small region at the outer edge, where the temperature rapidly falls to the zero boundary condition. As illustrated in figure 3.6, the zero boundary condition for the velocity is satisfied in a small region at the outer edge as well. Although the negative n-branch for $\mathrm{sgn}(M)=-1$ describes similarity solutions of the boundary-layer equations, they cannot be part of the flow along the hot plate, because the ξ-dependence of f' and g does not vanish if ξ is increased to infinity. This is required for the matching of the boundary-layer solution (inner solution) with the solution in the environment (outer solution) within the Navier-Stokes description. On the contrary, the velocity and temperature profiles in figure 3.7 show that this matching condition *is* satisfied for the solutions of the positive n-branch (stable stratification). As for the stable stratification with $\mathrm{sgn}(M)=1$, a region with flow reversal is found in the outer part of the boundary layer which is plotted in figure 3.8. Approaching $n \sim 0.6$ shows an enormous growth of $f''(0)$, $g'(0)$ and f'_{min}, which seems to indicate the appearance of a singularity in the $\mathrm{sgn}(M)=-1$ branch.

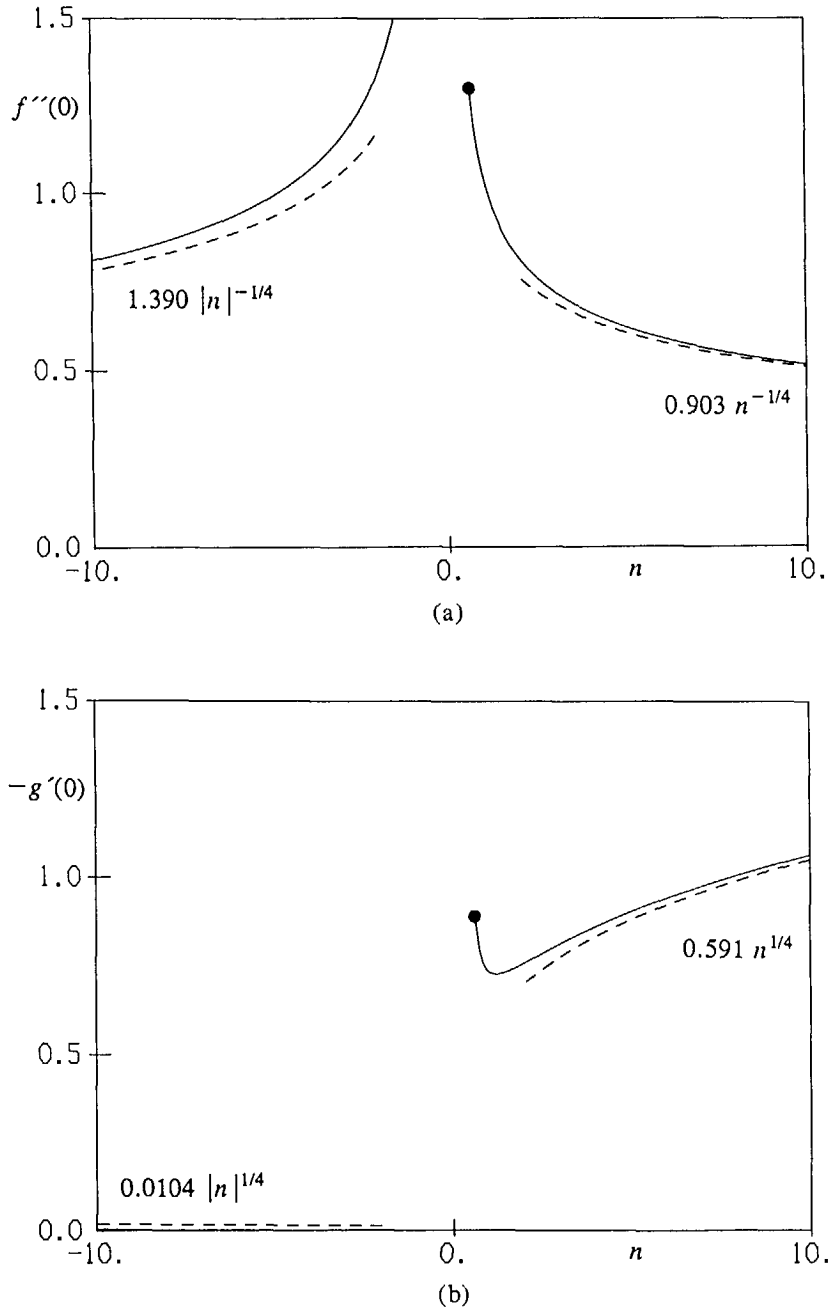

FIGURE 3.5. Constant wall and variable environment temperature ($m=-1$, $\mathrm{sgn}(M)=-1$); (a) wall-shear stress, (b) wall-heat transfer.

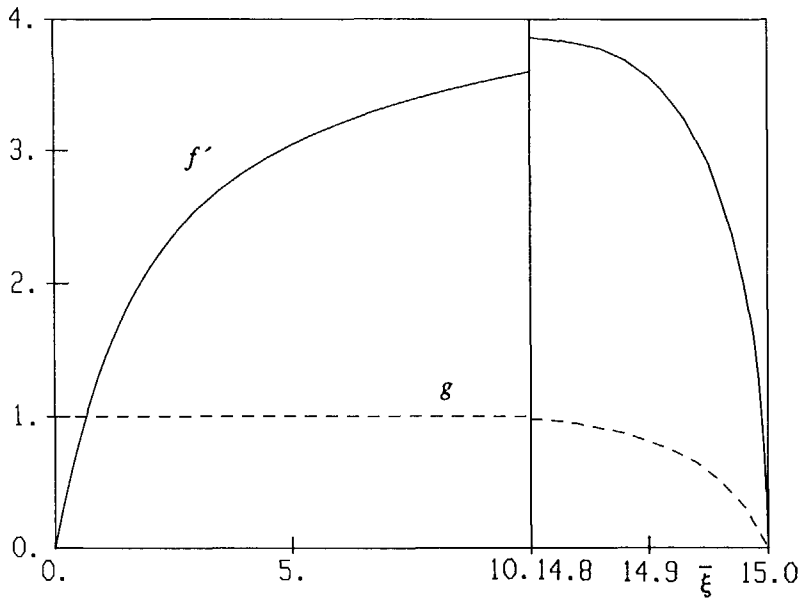

FIGURE 3.6. Velocity and temperature profile for a constant wall temperature and an unstably stratified environment ($m=-1$, $\mathrm{sgn}(M)=-1$, $n=-1$).

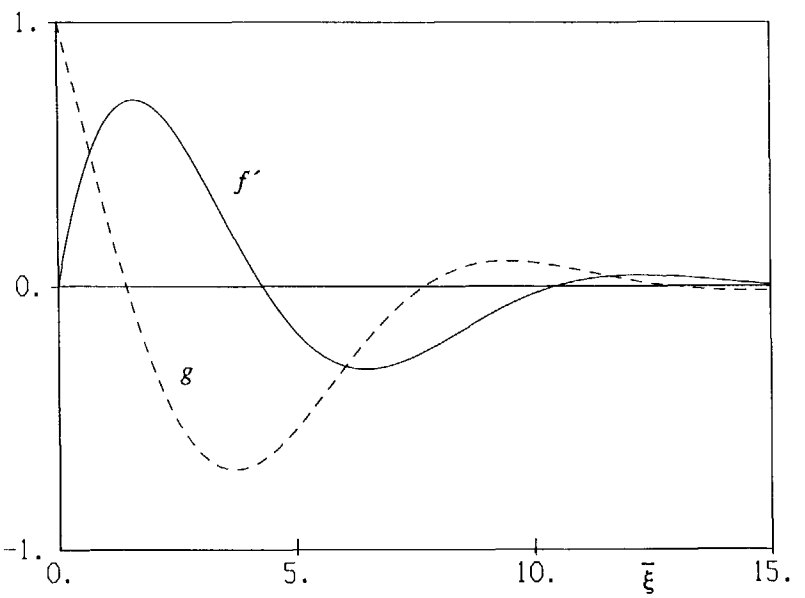

FIGURE 3.7. Velocity and temperature profile for a constant wall temperature and a stably stratified environment ($m=-1$, $\mathrm{sgn}(M)=-1$, $n=1$).

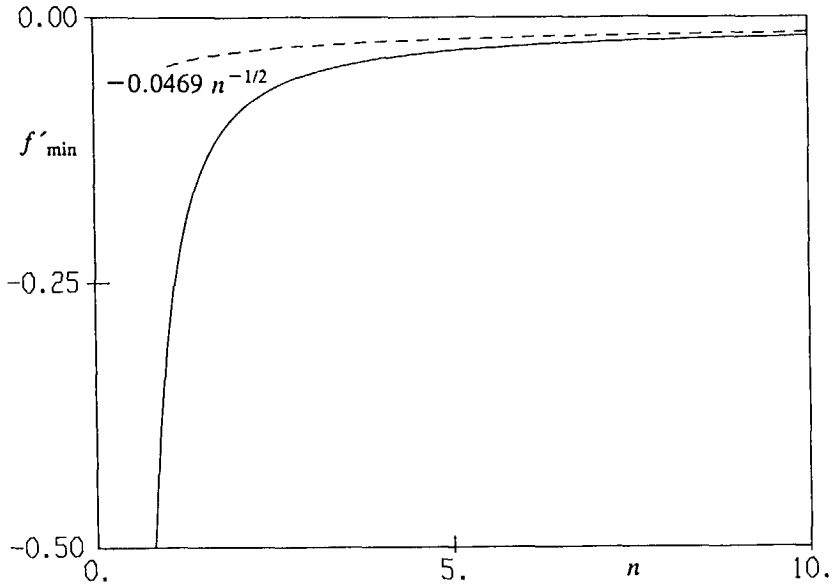

FIGURE 3.8. Flow reversal in the boundary layer for a stably stratified environment ($m=-1$, $\mathrm{sgn}(M)=-1$).

3.5. Meaning of the similarity solutions

For large Rayleigh numbers the Navier-Stokes solution along the vertical plate becomes equal to the solution of the boundary-layer equations. These boundary-layer equations do not hold in a small region, $O(H\ Ra^{-1/3})$, at $y=0$, where the full Navier-Stokes equations have to be used. If the temperature difference at $y=0$ between the wall and the environment is nonzero, it has to be checked by solving the Navier-Stokes equations whether the solution in the $O(H\ Ra^{-1/3})$ layer at $y=0$ matches with Ostrach's similarity solution ($n=0$). We verified this for a problem closely related to the vertical plate in a stratified environment, namely for the hot vertical wall of a square cavity (see next chapter). If, however, the temperature difference between the wall and the environment at $y=0$ is zero, the $n=0$ similarity solution does not apply. Because a rising boundary layer at $y=0$ requires that the wall temperature is not below the environment temperature, the zero temperature difference at $y=0$ can only occur for an unstably stratified environment. Similarity solutions for this case indeed exist and are described by equations (3.8), with $\mathrm{sgn}(M)=1$ and $n>0$.

This implies that the other similarity solutions (the $\mathrm{sgn}(M)=1$ class with $n<0$ and the $\mathrm{sgn}(M)=-1$ class with $n>0$) cannot be the boundary-layer solution for small y. In order to check the meaning of these similarity solutions we have solved the full (nonsimilar) boundary-layer equations (3.1) for a stably stratified environment. The $n=0$ similarity solution was used as a boundary condition at the initial station $y=0$. We tried to solve the discretized boundary-layer equations in a single sweep, going from one y-station to the next larger y-station. The

numerical iteration process, however, failed to converge as soon as flow reversal occurred at an y-station. The reason for this failure seems to be clear: if flow reversal occurs, the boundary-layer equations locally change from a parabolic character to an elliptic character. This means that the single-sweep marching numerical solution technique has to be replaced by a repeated sweep procedure. Due to the elliptic character of the solution of the boundary-layer equations in a stably stratified environment, the solution at the last y-station has to be given as a boundary condition.

Therefore, for a semi-infinite plate in a stable stratification the solution for $y \to \infty$ has to be known. We expect that the similarity class $\mathrm{sgn}(M)=1$ with $n<0$ forms that large y limit. The coefficient n describes how fast the environment temperature approaches the wall temperature for increasing y. The value of N in equations (3.5) is unimportant in the limit $y \to \infty$. The nonsimilar boundary-layer equations (3.1) have been solved for the stable stratification

$$\frac{T_w - T_\infty}{\Delta T} = \frac{1}{y/H + 1} \qquad 0 \leq y/H \leq \infty \tag{3.16}$$

where $\Delta T = T_w - T_\infty(0)$. At the leading edge of the vertical plate ($y=0$) the similarity solution $\mathrm{sgn}(M)=1$ with $n=0$ is prescribed. At a large y-value the similarity solution $\mathrm{sgn}(M)=1$ with $n=-1$ is prescribed. Repeated sweeps are made in the numerical procedure. The calculated dimensionless wall-heat transfer, *i.e.* the Nusselt number, is shown in figure 3.9. The Nusselt number is defined as

$$Nu = -\frac{H}{\Delta T}\left(\frac{\partial T}{\partial x}\right)_w . \tag{3.17}$$

Figure 3.9 shows that the nonsimilar solution smoothly matches both similarity limits

$$\begin{aligned} &\lim\ y/H \downarrow 0 \quad Nu\ Ra^{-1/4} = 0.387 \left(\frac{y}{H}\right)^{-1/4} \\ &\lim\ y/H \to \infty \quad Nu\ Ra^{-1/4} = 0.609 \left(\frac{y}{H} + 1\right)^{-3/2} . \end{aligned} \tag{3.18}$$

The environment temperature can become equal to the wall temperature at a finite distance H. In this case the solving of the (nonsimilar) boundary-layer equations requires a boundary condition at H. We expect that the similarity class $\mathrm{sgn}(M)=-1$ with $n>0$ matches the nonsimilar solution in the limit $y \uparrow H$. To check this, the nonsimilar boundary-layer equations (3.1) have been solved for a linear, stable stratification

$$\frac{T_w - T_\infty}{\Delta T} = 1 - \frac{y}{H} \qquad 0 \leq y/H \leq 1 \tag{3.19}$$

where $\Delta T = T_w - T_\infty(0)$. At $y=0$ the similarity solution $\mathrm{sgn}(M)=1$ with $n=0$ is prescribed. At $y=H$ the similarity solution $\mathrm{sgn}(M)=-1$ with $n=1$ is prescribed (using $M=-1/H$, $N=1$). Actually only the v- and T-profiles have to be specified, and not the u-profile: $v=0$ and $T=T_w$ at $y=H$. The same problem was also

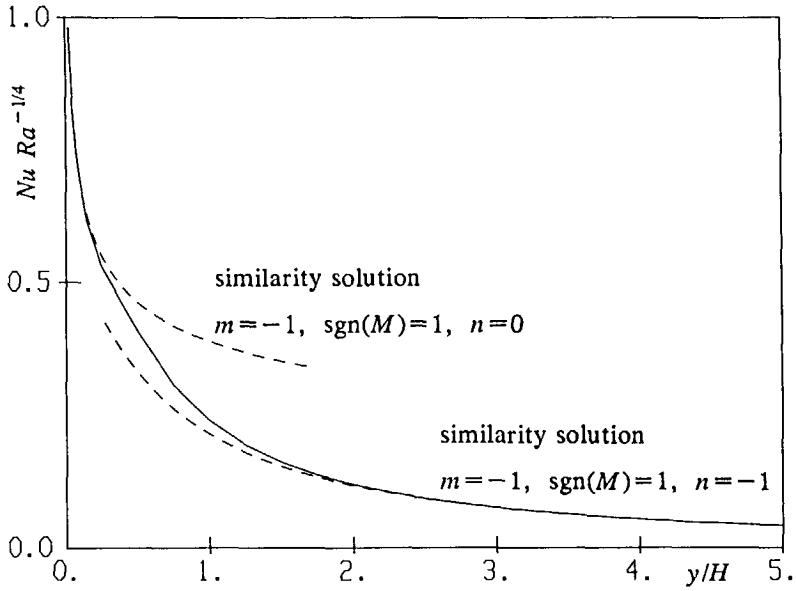

FIGURE 3.9. Wall-heat transfer in the nonsimilar boundary layer along a semi-infinite vertical plate in a stable stratification $(T_w - T_\infty)/\Delta T = (y/H+1)^{-1}$.

solved by Eichhorn (1969) (with series expansions), by Chen & Eichhorn (1976) (with the local nonsimilarity approximation method) and by Venkatachala & Nath (1981) (with a finite-difference numerical method). None of these authors, however, discussed the elliptic character of the boundary-layer equations and the need for a boundary condition at $y=H$. The calculated wall-heat transfer, velocity maximum and velocity minimum are depicted in figure 3.10. Despite the ignorance of the boundary conditions at $y=H$ in the calculation of Venkatachala & Nath (1981), implying an incorrect treatment of the regions with flow reversal, figure 3.10a shows that their wall-heat transfer results agree up to at least a graphical accuracy with our calculation. Very close to $y=H$ we cannot compare the results, because Venkatachala & Nath only presented results up to about $y=0.95\,H$. Figure 3.10 shows that the (nonsimilar) solution smoothly matches the similarity solution for small y. In contrast with our expectation, the solution does *not* match the similarity solution for $y \to H$. In particular, the wall-heat transfer for small y follows Ostrach's similarity solution

$$\lim\ y/H \downarrow 0\ \ Nu\ Ra^{-1/4} = 0.387 \left(\frac{y}{H}\right)^{-1/4} \tag{3.20}$$

whereas close to H the wall-heat transfer does *not* follow the similarity relation

$$\lim\ y/H \uparrow 1\ \ Nu\ Ra^{-1/4} = 0.797 \left(1 - \frac{y}{H}\right). \tag{3.21}$$

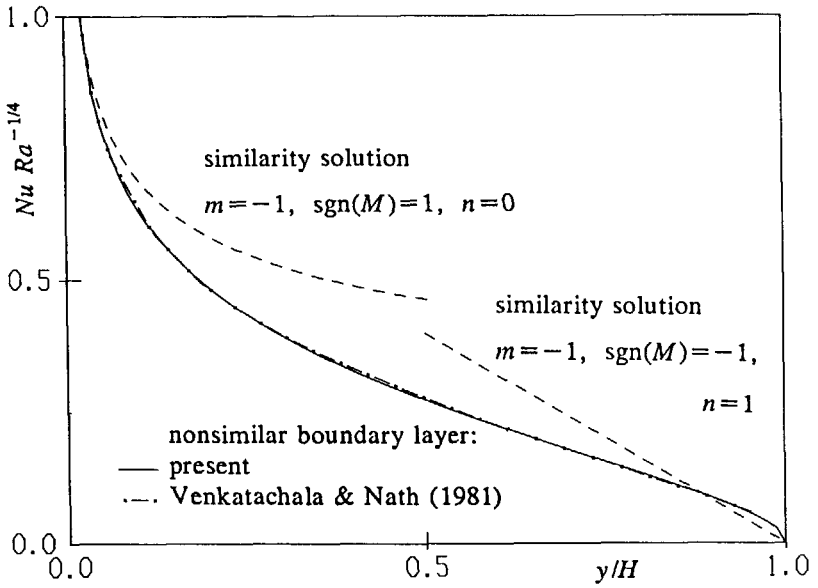

(a)

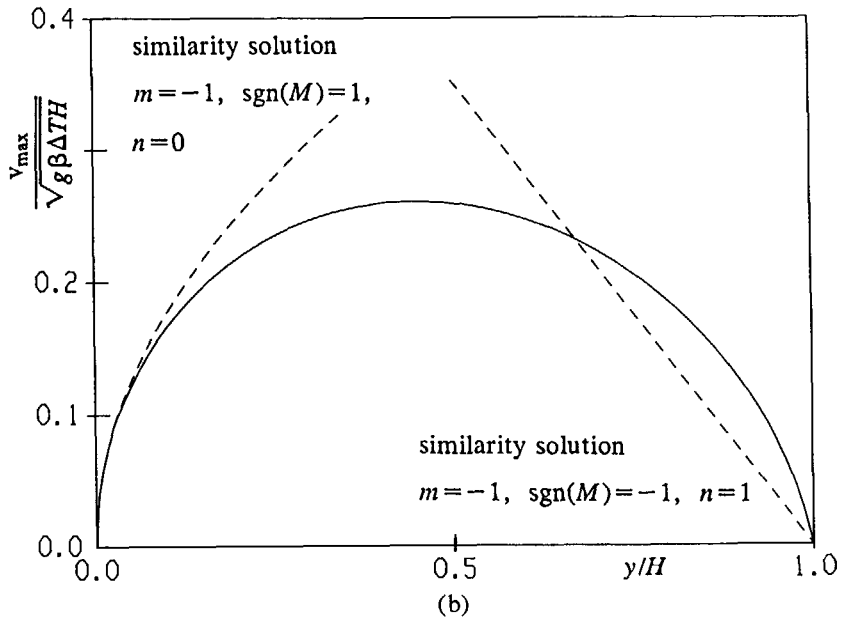

(b)

FIGURE 3.10(a,b). For caption see facing page.

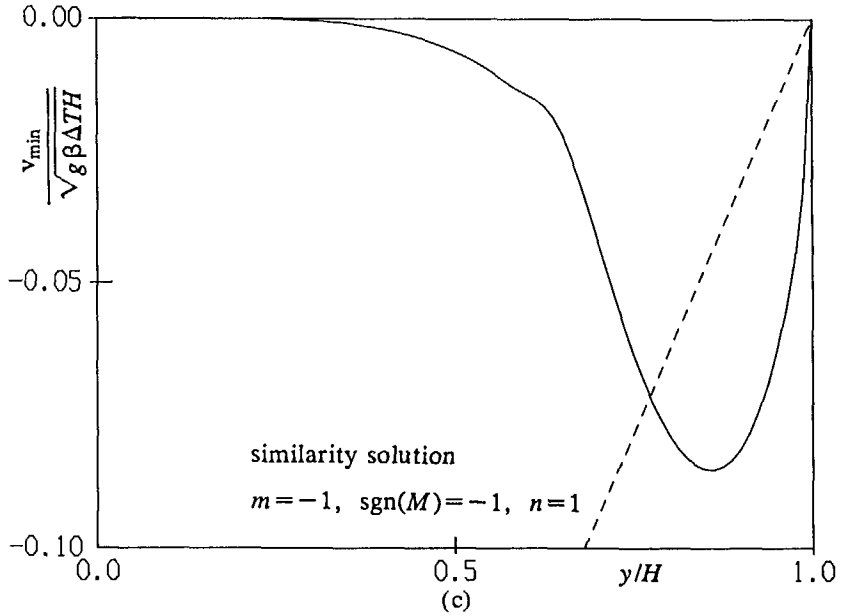

FIGURE 3.10. Nonsimilar boundary layer along a finite vertical plate in a stable, linear stratification ($(T_w-T_\infty)/\Delta T = 1-y/H$); (a) wall-heat transfer, (b) velocity maximum, (c) velocity minimum.

3.6. Conclusion

Solving Semenov's differential equations for air, describing all possible similarity solutions of the steady, laminar natural-convection boundary-layer equations, shows that no singularity occurs in the positive M class for a constant wall and a variable environment temperature. Similarity solutions of the negative M class for an unstable stratification are not usable because the solutions do not smoothly match with the environment velocity and temperature.

Regions with flow reversal and temperature deficit are found in the similarity solution for a stably stratified environment. The boundary-layer equations change from the parabolic type to the elliptic type when regions with flow reversal occur, implying that to determine a nonsimilar solution the single sweep marching numerical technique has to be replaced by a multiple-sweep technique. Besides the solution at the first y-station, also the solution at the last y-station has to be given as a boundary condition.

The similarity solution for a constant wall and environment temperature can be used to initiate the nonsimilar boundary-layer calculation at the leading edge of a hot vertical plate in a stably stratified environment. The similarity class with positive M and $n>0$ gives the initial solution if the stratification is unstable and the wall and environment temperature are equal at the leading edge. The similarity class with positive M and $n<0$ gives the solution in a stable stratification for large y. On the contrary, if the environment temperature in a stable stratification becomes equal to the wall temperature at a finite distance H, the solution close to H does not match the similarity solution of the negative M class with $n>0$.

4. LAMINAR FLOW IN THE CAVITY

4.1. Introduction

The natural-convection problem is characterized by two numbers, the Rayleigh number and the Prandtl number. The proper scalings of the problem are those scalings which make the solution independent of the Rayleigh number if the Rayleigh number is increased to infinity. In the limit of an infinitely large Rayleigh number some terms disappear from the Navier-Stokes formulation, which now simplifies to an asymptotic description. The proper scalings are given by the asymptotic description (for example the boundary-layer equations). In the cavity there are several asymptotic regions, each with its own proper scalings.

There are both physical and computational advantages in the use of a properly scaled Navier-Stokes formulation. The proper scalings split up the Navier-Stokes flow into some elemental asymptotic structures, which help to understand the physics of the flow. In computations the properly scaled (nondimensionalized) formulation diminishes round-off errors, because it prevents that the results fall in a range of extremely small or large values. Another computational advantage is that for large Rayleigh numbers it is sufficiently accurate to solve the asymptotic description. This usually requires less computational effort than the solving of the full Navier-Stokes equations.

Elder (1965) and Gill (1966) have formulated some ideas about the asymptotic equations, and hence the proper scalings, of the steady laminar flow in the cavity with an adiabatic floor and ceiling, that is heated from the vertical side. They distinguish a core and boundary layers along the vertical walls. The core is thermally stratified and has a zero vertical flow. Gill assumes that for large Rayleigh numbers the Navier-Stokes equations reduce to boundary-layer equations. He largely simplified the boundary-layer equations and determined the stratification in such a way that the stream function at the edge of the boundary layer was symmetric with respect to the position of half the cavity height.

In order to verify Gill's asymptotic theory, in this chapter the asymptotic structures, with the proper scalings, are derived by calculating the steady laminar Navier-Stokes flow in the two-dimensional square cavity for air up to a Rayleigh number of 10^9 and for water up to $Ra = 10^{11}$. Further, the thermal stratification as calculated in the large-Rayleigh-number Navier-Stokes solution is used as a boundary condition to solve the boundary-layer equations.

4.2. Steady Navier-Stokes and boundary-layer equations

We consider the steady laminar flow in the square cavity (figure 1.1a) as described by the Navier-Stokes equations under the Boussinesq approximation

$$\frac{\partial u}{\partial x} + \frac{\partial v}{\partial y} = 0$$

$$u\frac{\partial u}{\partial x} + v\frac{\partial u}{\partial y} = -\frac{1}{\rho}\frac{\partial p}{\partial x} + \nu\left(\frac{\partial^2 u}{\partial x^2} + \frac{\partial^2 u}{\partial y^2}\right) \qquad (4.1)$$

$$u\frac{\partial v}{\partial x} + v\frac{\partial v}{\partial y} = -\frac{1}{\rho}\frac{\partial p}{\partial y} + g\beta(T-T_0) + \nu\left(\frac{\partial^2 v}{\partial x^2} + \frac{\partial^2 v}{\partial y^2}\right)$$

$$u\frac{\partial T}{\partial x} + v\frac{\partial T}{\partial y} = \frac{\nu}{Pr}\left(\frac{\partial^2 T}{\partial x^2} + \frac{\partial^2 T}{\partial y^2}\right).$$

These simply are equations (2.9) without the unsteady terms. The cavity has a hot left vertical wall (T_h) and a cold right vertical wall (T_c). The floor and ceiling are both adiabatic ($\partial T/\partial y=0$). The height of the cavity is H.

The variables are nondimensionalized with the length scale x_0, the velocity scale u_0, the characteristic temperature T_0, and the characteristic temperature difference ΔT:

$$\left\{\frac{u}{u_0}, \frac{v}{u_0}, \frac{T-T_0}{\Delta T}, \frac{p}{\rho u_0^2}\right\} = f\left\{\frac{x}{x_0}, \frac{y}{x_0}, \frac{x_0 g\beta\Delta T}{u_0^2}, \frac{\nu}{u_0 x_0}, Pr\right\}. \tag{4.2}$$

The geometry and boundary conditions for the temperature determine length and temperature scales: $x_0 = H$, $T_0 = T_c$, $\Delta T = T_h - T_c$. The zero boundary condition for the velocity does not define a velocity scale. Therefore the velocity scale can be freely constructed with the help of H and the coefficients $g\beta\Delta T$ and ν; a possible choice is $u_0=(g\beta\Delta T\nu)^{1/3}$. Because of the free choice of the velocity scale, the number of independent variables in equation (4.2) reduces with one,

$$\left\{\frac{u}{u_0}, \frac{v}{u_0}, \frac{T-T_c}{\Delta T}, \frac{p}{\rho u_0^2}\right\} = f\left\{\frac{x}{H}, \frac{y}{H}, Ra, Pr\right\}. \tag{4.3}$$

In this relation the Rayleigh number is defined as $Ra=g\beta\Delta TH^3Pr/\nu^2$. Hence, the dimensionless Navier-Stokes solution depends on only two characteristic numbers, namely the Rayleigh number and the Prandtl number.

With the large-Rayleigh-number Navier-Stokes solutions in the square cavity it will be checked whether the hot vertical wall of the cavity can be considered as a part of a semi-infinite hot vertical plate, placed in a stagnant, stratified environment. More precisely, in the asymptotic limit of $Ra \to \infty$, the Navier-Stokes description along the hot wall is expected to simplify to the boundary-layer equations

$$\begin{aligned}
&\frac{\partial u}{\partial x} + \frac{\partial v}{\partial y} = 0 \\
&u\frac{\partial v}{\partial x} + v\frac{\partial v}{\partial y} = -\frac{1}{\rho}\frac{dp}{dy} + g\beta(T-T_c) + \nu\frac{\partial^2 v}{\partial x^2} \\
&u\frac{\partial T}{\partial x} + v\frac{\partial T}{\partial y} = \frac{\nu}{Pr}\frac{\partial^2 T}{\partial x^2} \\
&x = 0: \quad u=v=0, \quad T=T_h \\
&x \to \infty: \quad v=0, \quad T=T_\infty(y).
\end{aligned} \tag{4.4}$$

Because for $x \to \infty$ the temperature converges to $T_\infty(y)$ and the convection and the diffusion terms vanish, the pressure in the boundary-layer equations (4.4) is only

the hydrostatic pressure, which directly follows from the prescribed stratification:

$$\frac{p(x,y)}{\rho g \beta \Delta T H} = \int_0^y \frac{T_\infty(y') - T_c}{\Delta T\, H}\, dy' + \frac{p^*}{\rho g \beta \Delta T H} \tag{4.5}$$

where p^* is a fixed pressure level. The solution of the boundary-layer equations does not explicitly depend on the Rayleigh number if it is scaled according to

$$\left\{ \frac{u}{u_0} Ra^{1/12},\ \frac{v}{u_0} Ra^{-1/6},\ \frac{T-T_c}{\Delta T},\ \frac{p}{\rho u_0^2} Ra^{-1/3} \right\} = f\left\{ \frac{x}{H} Ra^{1/4},\ \frac{y}{H},\ Pr \right\} \tag{4.6}$$

4.3. Numerical method

In order to numerically determine the Navier-Stokes solution, the equations (4.1) are discretized with the finite-volume method on a staggered grid as described in section 2.6. The convection terms are discretized with the central scheme. The equations are solved in the steady formulation, implying that the time step in the B2 scheme for the time integration is set to infinity. The domain is covered with a nonequidistant grid, having a concentration of grid lines along the walls. The u-grid points are positioned in the x-direction according to

$$\frac{x_i}{H} = \frac{i}{imax} - \frac{1}{2\pi} \sin\left(2\pi \frac{i}{imax} \right) \qquad i = 0,1,\ldots,imax. \tag{4.7}$$

The same spacing is used for the v-grid points in the y-direction. The pressure is updated with the SIMPLE pressure-correction method, taking $\Delta t \to \infty$ in equation (2.28). The line Gauss-Seidel iteration is used to solve both the transport variables (u, v and T) and the pressure correction. Convergence of the Navier-Stokes solution becomes more difficult the larger the Rayleigh number is, and relaxation is required to prevent divergence. Part of the convergence problems are expected to be due to the calculation of the pressure in the boundary layers along the vertical walls. In contrast with the Navier-Stokes equations, the boundary-layer equations do not have a transport equation for the normal velocity component u, but the u-component directly follows from the continuity equation. This boundary-layer feature is not reflected by the Navier-Stokes solver, which determines a pressure correction via the continuity equation and which determines the u-component via the u-transport equation.

The boundary-layer equations are parabolic as long as the environment is isothermal or unstably stratified ($dT_\infty/dy \leq 0$). Because of this parabolic character, it is more suitable to modify the position of some of the grid points used to discretize the elliptic Navier-Stokes equations (see figure 2.2), when the boundary-layer equations are solved. To discretize the boundary-layer equations we take the same grid points for v as in the discretization of the Navier-Stokes equations, but the grid points for T are moved to the v-grid points and the grid points for u are only staggered with respect to the v-grid points in the x-direction. Further, a first-order upwind discretization is used for the convection in the y-direction. In this way only one sweep from the beginning to the end of the domain (in which the updating process at a line is repeated until a convergence

criterion is satisfied) is required to solve the parabolic boundary-layer equations. As illustrated in the previous chapter, regions of flow reversal and temperature deficit appear if the temperature stratification is stable ($dT_\infty/dy > 0$), implying that the boundary-layer equations lose their parabolic character and become elliptic. Due to this elliptic character also on the modified grid repeated sweeps have to be made. The flow reversal, however, is small and the equations are still nearby parabolic. Therefore also for the stable stratification the line-updating process in each sweep on the modified grid is repeated until convergence at that line is reached. This contrasts the Navier-Stokes solver, in which only one line-updating is made in each sweep.

4.4. Gill's asymptotic formulation

Since Prandtl (1904) derived the boundary-layer equations, and actually introduced the mathematical technique of asymptotic series (singular perturbation theory) to solve flow problems, a large literature on this subject has been established. The asymptotic theory searches for the proper scalings in the asymptotic limit of an infinitely large Rayleigh number, and it derives the corresponding asymptotic equations. These scalings can be different in different regions, and the asymptotic solutions have to be matched according to a certain matching principle. The asymptotic solution holds exactly in the limit $Ra \to \infty$, and can be used as a good approximation of the Navier-Stokes solution for a large, but finite, Rayleigh number.

The asymptotic theory for the natural-convection flow in cavities is still in development. Ostrach (1972, 1982) has given reviews. Two basic configurations have been considered in literature, the rectangular cavity and the horizontal cylinder, for two basic modes, heating from the vertical side and heating from below. For large Rayleigh numbers there seems to be a core with boundary layers along the heated walls. There has been some doubt on the right structure of the core flow; Batchelor (1954) suggested an isothermal core with constant vorticity for the configuration with heating from the vertical side. At the moment it seems (experiments Elder 1965, theoretical considerations Ostrach & Hantman 1981, and different numerical studies including the present one) that the core becomes isothermal and rotating if the cavity is heated from below, whereas it becomes thermally stratified and almost stagnant with horizontal streamlines if the cavity is heated from the vertical side.

The vertical boundary layers and the core in rectangular cavities have been calculated by Gill (1966) for infinitely large Rayleigh and Prandtl numbers. He assumes that the core is stratified and has horizontal streamlines. Along the vertical walls Gill approximately solves the boundary-layer equations (4.4) by linearizing them. After linearization the boundary-layer equations reduce to an ordinary differential equation in x, in which the y-coordinate appears as a parameter only. The core flow and boundary-layer flow are matched by the condition that the temperature and the normal velocity at the edge of the boundary layer are equal to the temperature and velocity in the core. The solution of equations (4.1), under the given boundary conditions, is centro-symmetric with respect to the centre of the cavity:

$$T(x,y) - T(H/2,H/2) = T(H/2,H/2) - T(H-x,H-y)$$
$$u(x,y) = -u(H-x,H-y). \tag{4.8}$$

Because of the assumption that the streamlines are horizontal in the core, it also follows that the normal velocity at the edge of the boundary layer along both vertical walls is anti-symmetric around $y=H/2$. This symmetry condition dictates how the asymptotic flow in the core and in the boundary layer interact: the stratification in the core has to be such that the normal velocity at the outer edge of the boundary layer is anti-symmetric. Using the symmetry conditions the linearized boundary-layer solution and the core solution can be determined up to a constant. Gill determines this constant by assuming that the vertical entrainment of mass at the ceiling ($y=H$) equals zero. A modified procedure to determine this constant has been proposed by Bejan (1979). He applies the condition that the vertical heat flux through the ceiling is zero. The vertical flux consists of a convection and a diffusion contribution, which are calculated with Gill's approximation of the boundary-layer solution. The constant turns out to be a coefficient that depends on the Rayleigh number; the coefficient converges to Gill's constant in the limit $Ra \to \infty$. From an asymptotic point of view one might doubt the significance of Bejan's correction. The boundary-layer solution is used to calculate the y-diffusion, which actually was neglected when the boundary-layer equations were derived from the Navier-Stokes equations. Therefore Bejan's correction on Gill's constant is a second-order asymptotic effect, which can only be expected to be the right second-order correction if it has been determined in combination with second-order boundary-layer equations and core effects. Graebel (1981) extended Gill's analysis to variable Prandtl numbers. Blythe *et al.* (1983) repeated Gill's analysis (only for the limit $Pr \to \infty$); instead of linearizing the boundary-layer equations, they accurately solved Gill's asymptotic formulation with a numerical method.

Gill's asymptotic structure will be verified by comparison with large-Rayleigh-number Navier-Stokes solutions. In the sequel the mentioned approximation, including Graebel's finite-Prandtl-number correction, will be referred to as the *approximation* of Gill's formulation and the numerical solution of Blythe *et al.* will be referred to as the *exact* solution of Gill's formulation.

4.5. Navier-Stokes solutions

Steady, laminar Navier-Stokes solutions in the cavity are determined for air ($Pr=0.71$) up to $Ra=10^9$ and for water ($Pr=7.0$) up to $Ra=10^{11}$. Benchmark numerical results were obtained by De Vahl Davis (1983) for air up to $Ra=10^6$. Very recently Le Quéré (1990) revisited these benchmark results, and he also added benchmark results for two new cases: air at $Ra=10^7$ and air at $Ra=10^8$. To discretize the equations De Vahl Davis used a finite-difference method and Le Quéré used a spectral method.

Most of the present calculations were made on a 60×60 grid. For Rayleigh numbers up to 10^4 an equidistant grid was used, whereas for larger Rayleigh numbers the nonequidistant grid (4.7) was used. In order to verify the accuracy for larger Rayleigh numbers, we refined the grid up to 120×120 points for air at $Ra=10^6$ and for air at $Ra=10^8$. Table 4.1 summarizes the results at $Ra=10^6$ for

TABLE 4.1. Accuracy of the solution for air at $Ra = 10^6$ (central scheme).

study	grid	S	$\overline{Nu}\ Ra^{-1/4}$	$\frac{v_{max}}{\sqrt{g\beta\Delta TH}}$	$\frac{u_{max}}{(g\beta\Delta T\nu)^{1/3}}$
present	15×15	0.9780	0.2773	0.2977	0.8422
	30×30	0.9367	0.2782	0.2658	0.8174
	60×60	0.9190	0.2789	0.2633	0.8145
	120×120	0.9144	0.2790	0.2621	0.8144
De Vahl Davis	--	--	0.2783	0.2603	0.8121
Le Quéré	--	--	0.2791	0.2618	0.8146

TABLE 4.2. Accuracy of the solution for air at $Ra = 10^8$.

scheme	grid	S	$\overline{Nu}\ Ra^{-1/4}$	$\frac{v_{max}}{\sqrt{g\beta\Delta TH}}$	$\frac{u_{max}}{(g\beta\Delta T\nu)^{1/3}}$
central	15×15	0.9336	0.3134	0.3790	0.6446
	30×30	0.9908	0.2988	0.2827	0.7436
	60×60	0.9942	0.3014	0.2657	0.7421
	120×120	0.9943	0.3020	0.2646	0.8231
hybrid	15×15	0.7732	0.2971	0.3712	0.9209
	30×30	0.9297	0.2937	0.2836	0.7670
	60×60	0.9714	0.2989	0.2667	0.7776
	120×120	0.9808	0.3010	0.2649	0.7937
upwind	15×15	0.5976	0.2995	0.3557	1.111
	30×30	0.8369	0.3014	0.2767	0.9139
	60×60	0.9121	0.3035	0.2633	0.8619
	120×120	0.9502	0.3034	0.2633	0.8321
Le Quéré	--	--	0.3023	0.2637	0.8714

several quantities: the averaged heat transfer through the hot vertical wall ($\overline{Nu}$, in which Nu is the Nusselt number as defined by equation (3.17)), the gradient of the thermal stratification in the centre ($S=(H/\Delta T)\partial T/\partial y$), the vertical velocity maximum at half the cavity height (v_{max}) and the horizontal velocity maximum at half the cavity width (u_{max}). The results, in particular at the finest grids, are in very good agreement with the benchmark results of De Vahl Davis (1983), but the agreement with the revisited benchmark results of Le Quéré (1990) is even better. Table 4.2 refines the grid for $Ra = 10^8$ and also compares different discretizations for the convection (central, hybrid, first-order upwind). By strong grid refinement Le Quéré can convince that his solution at $Ra = 10^8$ is indeed very accurate and that it can be used as a benchmark solution. He does not give a benchmark value for the stratification. Therefore we use our value at the 120×120 grid with the central scheme as a reference value for S; changes in S on the refined grids are smallest with the central scheme, suggesting that this scheme has the highest accuracy. Differences between the schemes are small, with exception of the

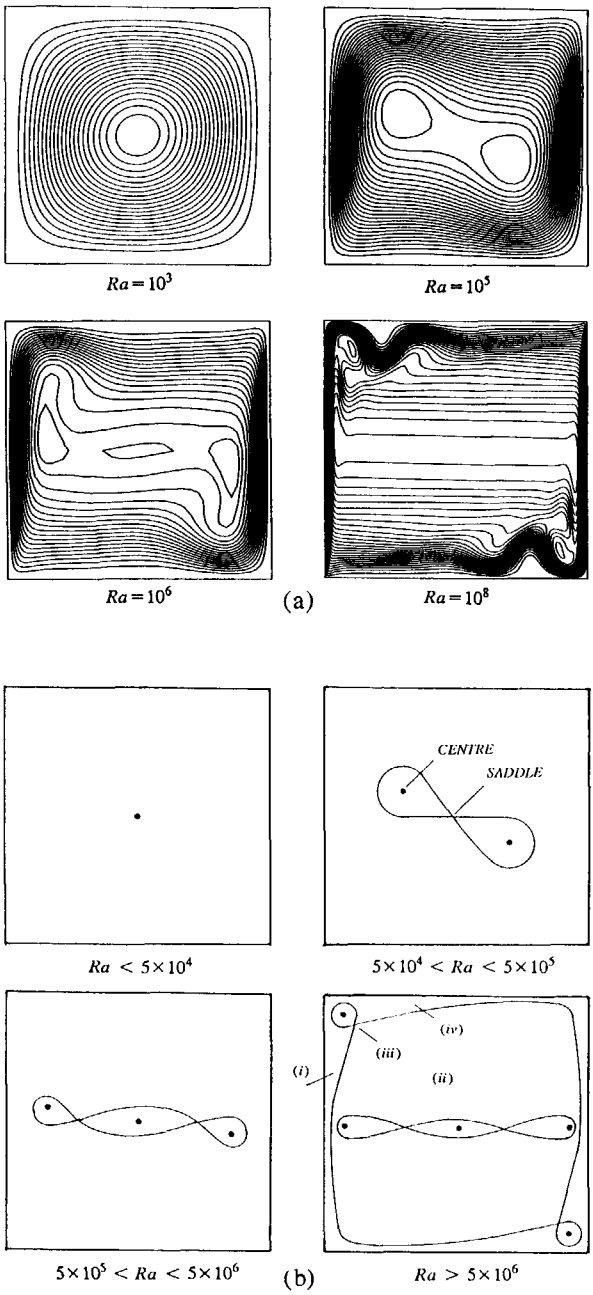

FIGURE 4.1. Structure of the Navier-Stokes solution for increasing Rayleigh number; (a) streamlines for air, (b) topology.

stratification: the hybrid scheme and the upwind scheme considerably underpredict the stratification at the coarser grids. Comparison with the benchmark solution at $Ra=10^8$ shows that our values for the wall-heat transfer and for the vertical velocity maximum at the finest grids are very accurate. The accuracy of our horizontal velocity maximum is somewhat smaller. Relaxation is required to prevent divergence of the numerical iteration process: convergence becomes slower in the sequence upwind scheme, hybrid scheme and central scheme. For air at $Ra=10^9$ a converged solution with the central scheme could no longer be obtained and the hybrid scheme had to be used.

Streamlines of the Navier-Stokes solution for air at increasing Rayleigh number are shown in figure 4.1a. Streamlines are isolines of the stream function ψ, which is defined as $u=-\partial\psi/\partial y$, $v=\partial\psi/\partial x$ and $\psi=0$ at the wall. Special points in the streamline patterns are the stagnant points, *i.e.* the points where $u=v=0$. As indicated in figure 4.1b, a stagnant point can either be a centre or a saddle. The stagnant points define the topological structure of the flow; the streamlines through the saddles give the dividing streamlines of the flow. With the help of the stagnant points, the following ranges can be distinguished (the streamlines are centro-symmetric with respect to $x=y=H/2$):

I. $Ra < 5\times10^4$; one centre at $x=y=H/2$, with unicellular, clockwise rotating flow.
II. $5\times10^4 < Ra < 5\times10^5$; the centre has split up in a saddle, at $x=y=H/2$, and two new centres, forming two clockwise rotating rolls.
III. $5\times10^5 < Ra < 5\times10^6$; the saddle at $x=y=H/2$ has further split up in a centre and two new saddles, giving a total of three clockwise rotating rolls.
IV. $Ra > 5\times10^6$; a centre-saddle combination is formed in the left upper and right below corner, with fast clockwise rotating fluid (vortices). This corner vortex does appear only for air. It does *not* appear for water up to $Ra=10^{11}$, which was the largest Rayleigh number we calculated.

As indicated in figure 4.1b, four asymptotic regions can be distinguished in the last streamline pattern: (i) vertical boundary layer along the heated wall, (ii) core region, (iii) corner region, (iv) horizontal layer.

4.6. Solution of the boundary-layer equations

Figure 4.2 shows the isotherms in the Navier-Stokes solution for air at increasing Rayleigh number. For very small Rayleigh numbers there is only conduction, giving a temperature which only depends on the x-coordinate ($S=0$). For increasing Rayleigh number the temperature in the core of the cavity becomes stratified, *i.e.* the temperature depends only on the vertical coordinate y. The stratification at half the cavity width is shown in figure 4.3a and 4.3b, for air and water respectively. The stratification at the centre (S) is shown in figure 4.3c. Part of the curve in figure 4.3c is broken to indicate that the steady solution for these large Rayleigh numbers is physically unstable (this will be shown in the next chapter). Figure 4.3 shows that for $Ra\to\infty$ the core stratification converges to a limit state; the limit stratification for air is roughly twice the limit stratification for water.

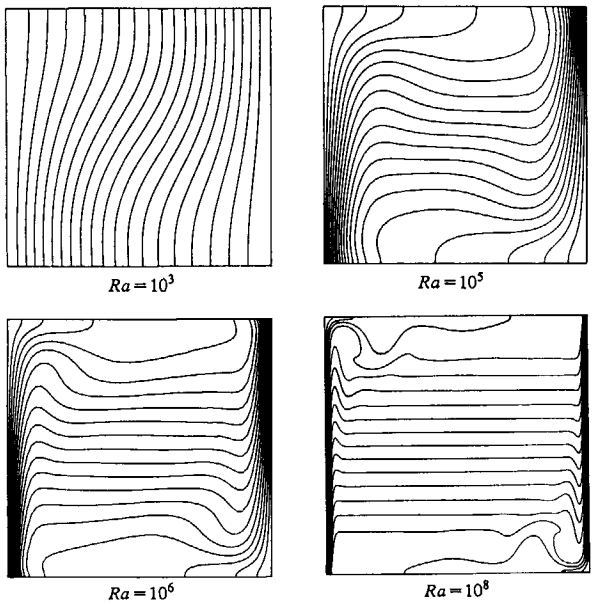

FIGURE 4.2. Isotherms in the Navier-Stokes solution for increasing Rayleigh number (air).

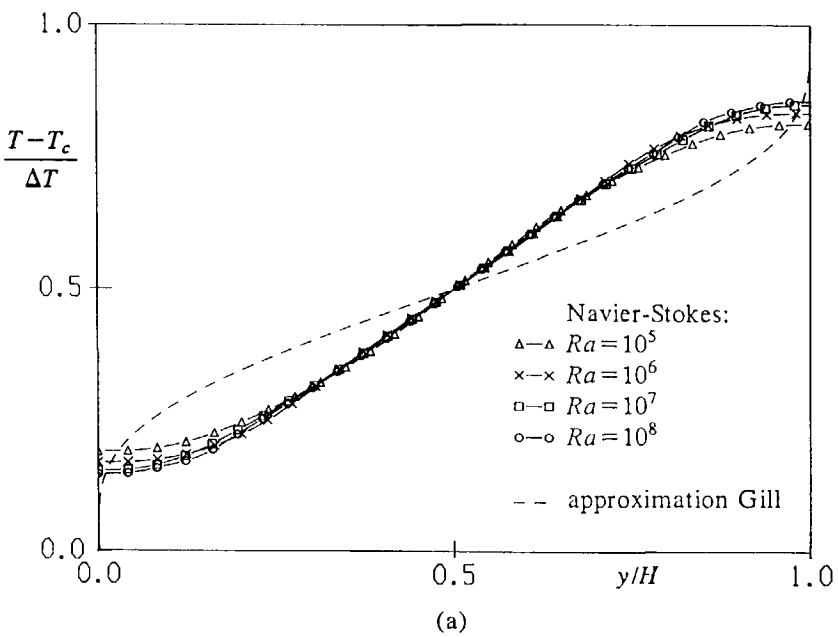

(a)

FIGURE 4.3(a). For caption see facing page.

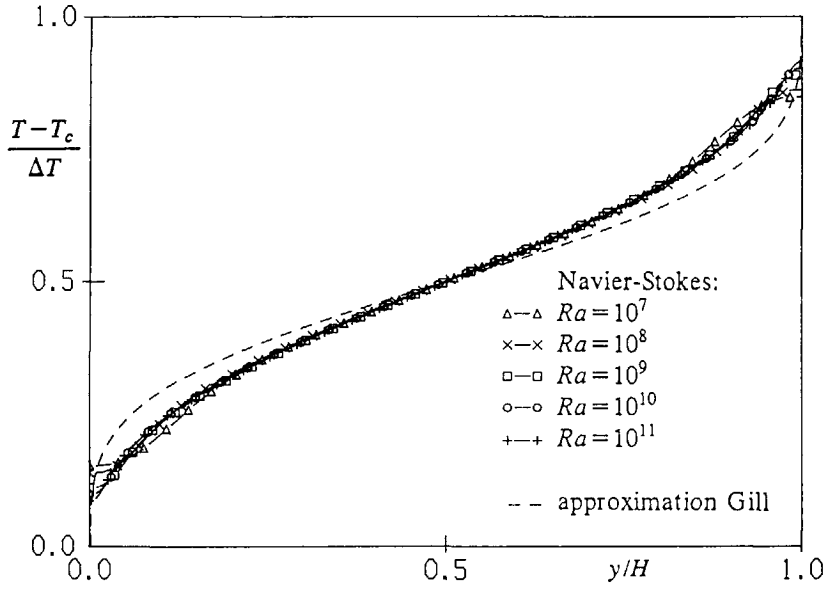

(b)

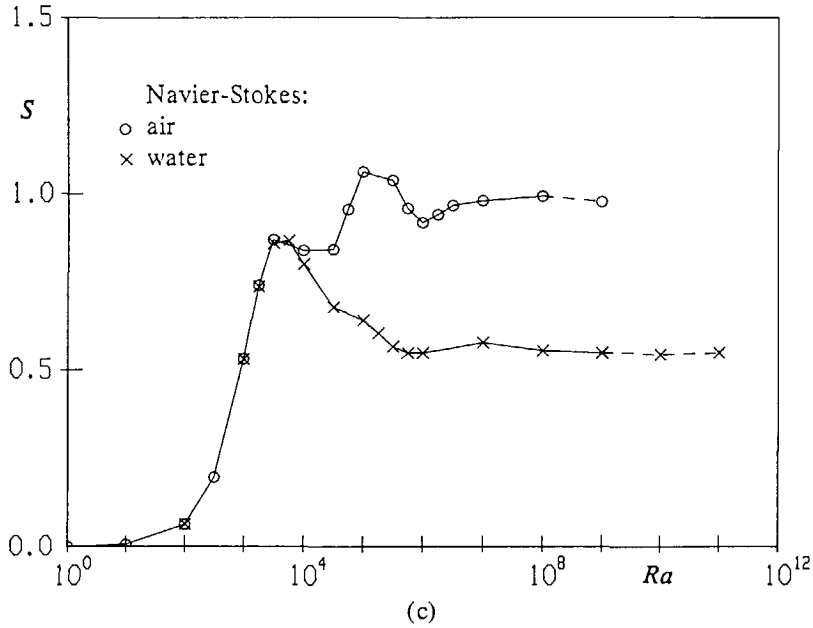

(c)

FIGURE 4.3. Stratification in the core; (a) at $x=H/2$ for air, (b) at $x=H/2$ for water, (c) at the centre.

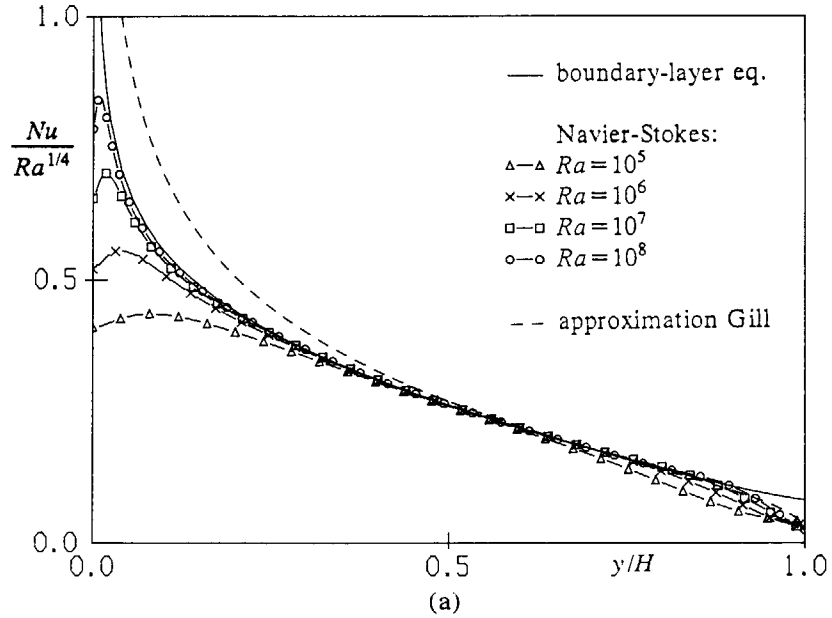

(a)

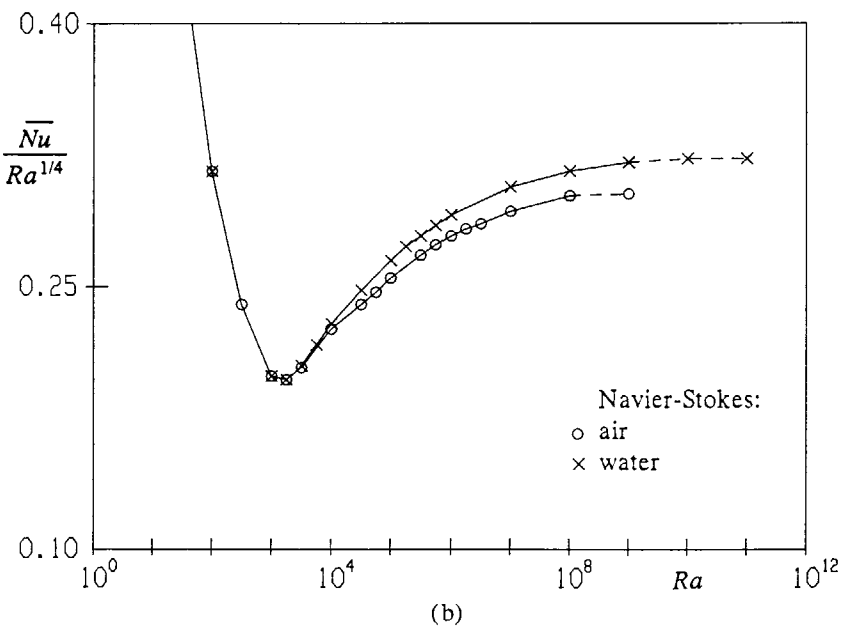

(b)

FIGURE 4.4. Wall-heat transfer; (a) for air, (b) averaged wall-heat transfer.

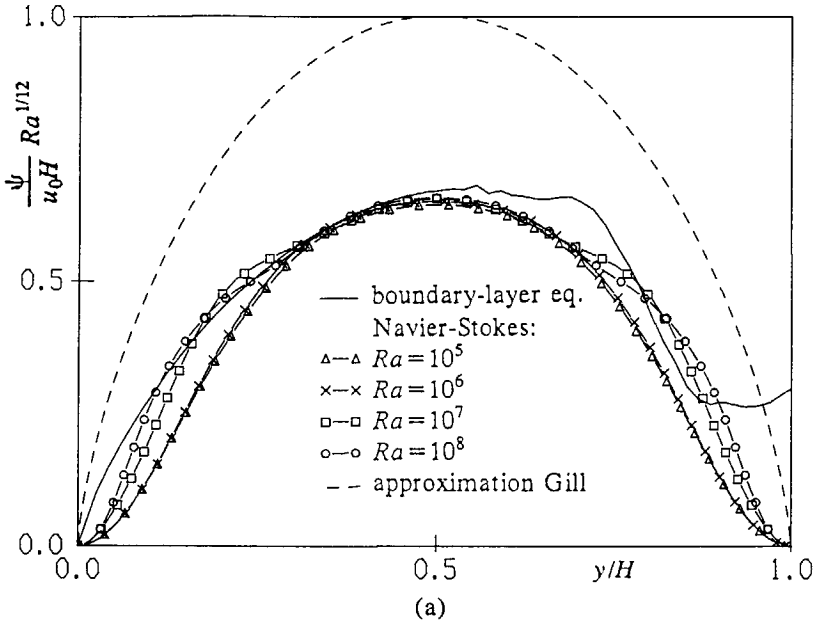

(a)

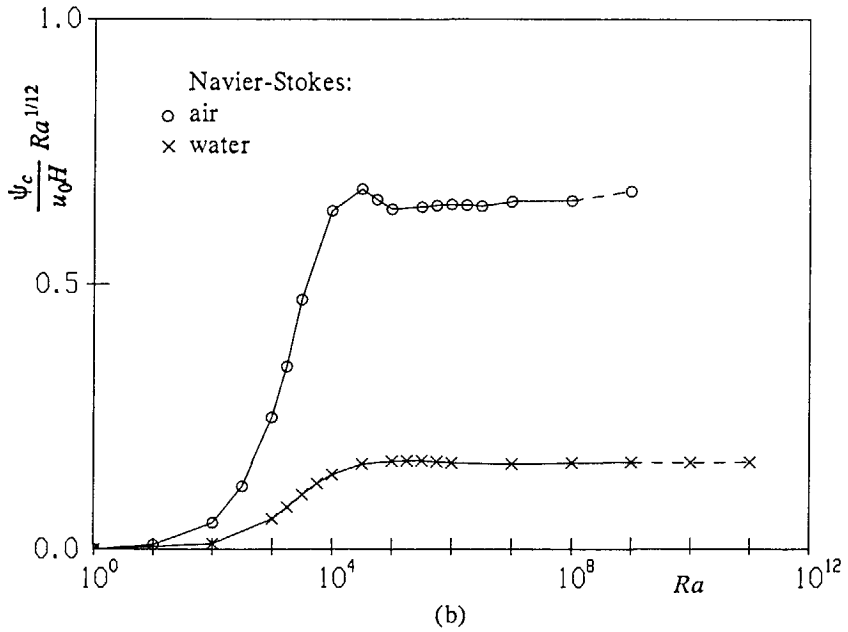

(b)

FIGURE 4.5. Stream function; (a) at $x = H/2$ for air, (b) at the centre.

With the limit stratification of the Navier-Stokes solution prescribed as a boundary condition at the outer edge, the boundary-layer equations (4.4) were solved for air (actually the stratification for $Ra=10^8$ was taken). For $y \downarrow 0$ the solution of the boundary-layer equations simplifies to Ostrach's (1953) similarity solution. This solution was used as a boundary condition at the leading edge. As shown in the previous chapter, regions with flow reversal and temperature deficit are found in the outer part of the boundary layer if the environment is stably stratified. This implies that also a boundary condition is required at the end of the boundary layer at $y=H$. Because the solution at $y=H$ is not known beforehand, the calculation was extended to $y>H$, using the outer-edge temperature $T_\infty(y) = T_\infty(H)$ in this range. For $y \gg H$ the boundary layer returns to Ostrach's similarity solution. The outer edge of the boundary layer in the computational domain was taken far enough to have a negligible effect on the development of the boundary layer (namely at $(x/H)\, Ra^{1/4} = 40$). 40 grid points were used in the y-range $0 < y \leq H$. A same number of grid points was used in the x-direction. Calculations on 80×80 grids gave only very small changes.

The wall-heat transfer in the boundary-layer solution and in the Navier-Stokes solution for increasing Rayleigh number are compared in figure 4.4a for air: the wall-heat transfer in the Navier-Stokes solution converges to the value of the boundary-layer solution in the limit $Ra \to \infty$. In particular in figure 4.4b it is checked that the wall-heat transfer $-(\partial T/\partial x)_w$ in the Navier-Stokes solution for large Rayleigh numbers scales with $(\Delta T/H)\, Ra^{1/4}$, which agrees with the boundary-layer scaling (4.6). Finite-Rayleigh-number effects are restricted to the corners at $y \downarrow 0$ and at $y \uparrow H$. If the Rayleigh number is increased, the position of the maximum in the Navier-Stokes wall-heat transfer moves to $y/H=0$, and for small y values beyond this maximum the wall-heat transfer follows Ostrach's similarity solution,

$$\lim_{Ra \to \infty} Nu\, Ra^{-1/4} = C^*\, (y/H)^{-1/4} \lim_{Ra \to \infty} \left(\frac{T_h - T(H/2,0)}{\Delta T} \right)^{5/4} \tag{4.9}$$

with $C^*=0.387$ for air and 0.459 for water. Here the infinite-Rayleigh-number limit of $(T_h-T(H/2,0))/\Delta T$ is found by extrapolation of the results for the largest calculated Rayleigh numbers to infinity, which gives about 0.86 for air and about 0.91 for water.

In figure 4.5a the stream function at the outer edge of the boundary-layer solution for air is compared with the Navier-Stokes stream function at $x=H/2$ for increasing Rayleigh number. The convergence of the Navier-Stokes stream function to the boundary-layer solution is only clear for y-values up to $H/2$. In particular in figure 4.5b it is checked that the Navier-Stokes stream function at the centre (ψ_c) scales with $u_0 H\, Ra^{-1/12}$, which agrees with the boundary-layer scaling (4.6) (see also next section). For $y>H/2$ the deviation of the boundary-layer solution from the Navier-Stokes solution is large and the stream function in the boundary-layer solution is not symmetric around $y=H/2$. In order to verify the sensitivity of the stream function to the stratification, the boundary-layer equations were solved for different stratifications as sketched in figure 4.6a; both the linearized $Ra=10^8$ Navier-Stokes stratification and the linearized stratification with a sinus

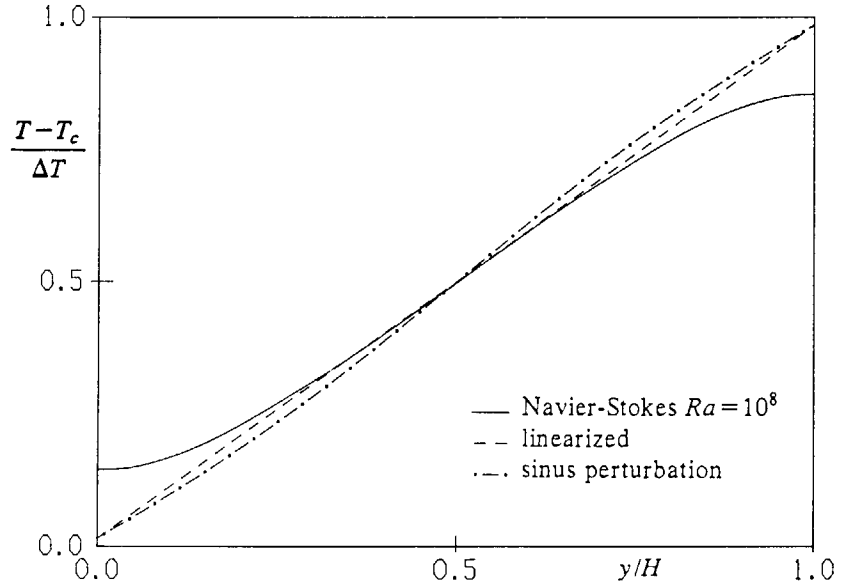

(a)

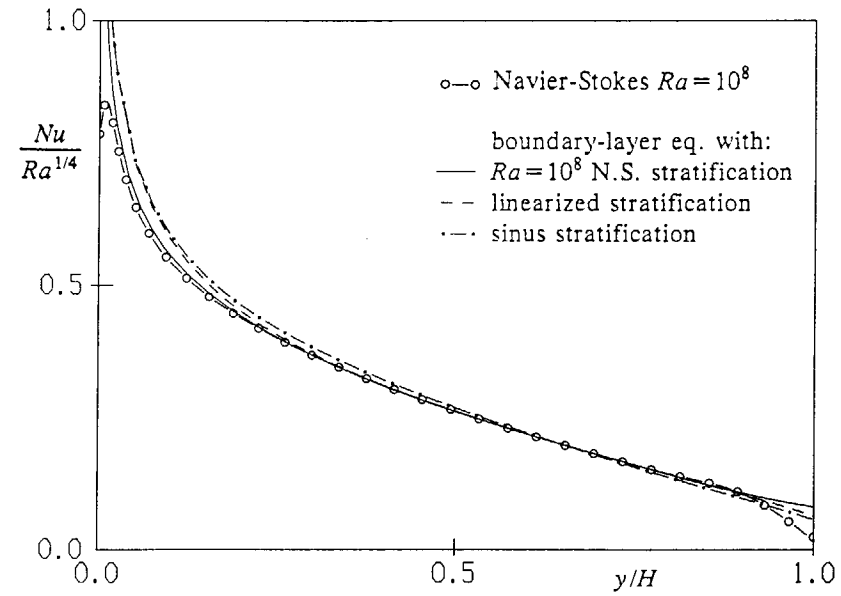

(b)

FIGURE 4.6(a,b). For caption see next page.

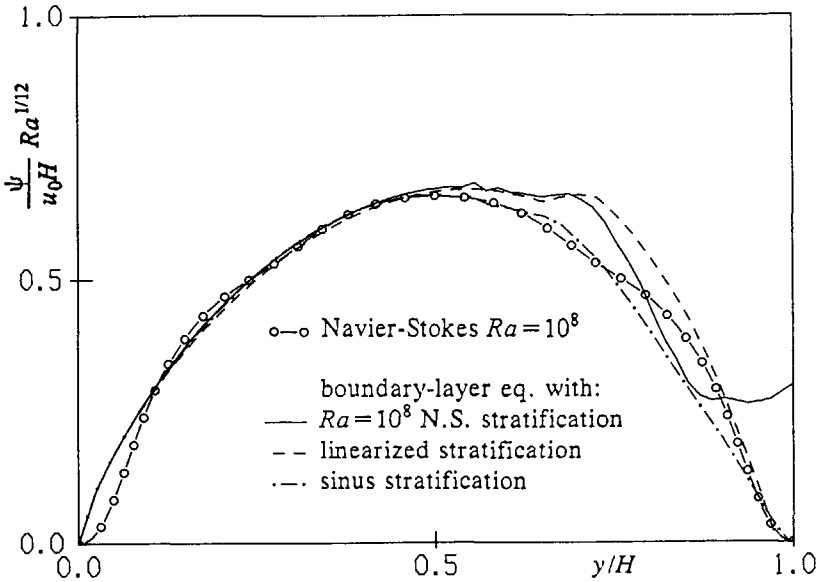

(c)

FIGURE 4.6. Sensitivity of the boundary-layer solution for air to the stratification; (a) core temperatures checked, (b) wall-heat transfer, (c) stream function at the edge.

TABLE 4.3. Comparison of the asymptotic behaviour.
(a) air

formulation	S	$\overline{Nu}\ Ra^{-1/4}$	$\frac{\psi_c}{u_0 H Ra^{-1/12}}$
Navier-Stokes	0.99	0.30	0.66
boundary-layer eq.	0.99	0.31	0.67
Gill-exact	0.52	0.32	0.74
Gill-approximation	0.49	0.36	1.0
similarity solution	0.	0.22	1.17

(b) water

formulation	S	$\overline{Nu}\ Ra^{-1/4}$	$\frac{\psi_c}{u_0 H Ra^{-1/12}}$
Navier-Stokes	0.55	0.32	0.16
boundary-layer eq.	--	--	--
Gill-exact	0.52	0.32	0.16
Gill-approximation	0.42	0.36	0.21
similarity solution	0.	0.26	0.65

perturbation were used. Changing the stratification has a small influence on the wall-heat transfer (figure 4.6b), but it has a large influence on the stream function for $y>H/2$ (figure 4.6c). The linearized stratification removes the deviation in the stream function with the Navier-Stokes solution close to the ceiling, and the sinus perturbation makes the stream function practically symmetric. The large sensitivity of the stream function to the temperature stratification suggests that the interaction between the core solution and the boundary-layer solution has to be taken into account. This is precisely what is done in the asymptotic description of Gill: as described in section 4.4, he uses the interaction principle of symmetry to couple the stratification to the boundary-layer equations. Gill does not prescribe a fixed stratification, but the stratification is part of the calculation. It remains to be checked that applying the symmetry interaction in the present boundary-layer approach (for example by setting up an iteration process that corrects the prescribed stratification until a symmetric stream function at the outer edge of the boundary-layer solution is found) gives a stratification which is close to the calculated large-Rayleigh-number Navier-Stokes limit.

Table 4.3 compares some asymptotic limits in the Navier-Stokes solution with the boundary-layer solution, Gill's formulation and Ostrach's similarity solution. The boundary-layer solution is found by prescription of the Navier-Stokes stratification, Gill's formulation uses interaction to calculate the stratification, and Ostrach's similarity solution applies a zero stratification to the boundary-layer equations. The fixed outer-edge temperature in the similarity solution was chosen as $(T_h+T_c)/2$. The agreement of the wall-heat transfer and the stream function at the centre between the Navier-Stokes solution and the boundary-layer solution is good, as just discussed. The agreement between the exact solution of Gill's formulation and the Navier-Stokes solution is very good for water, but for air a significant deviation is found. The reason is that the Prandtl number for water is larger than for air, and therefore closer to the infinite-Prandtl-number limit for which the exact solution of Gill's formulation is available. As expected, the deviation from the Navier-Stokes solution is larger for the approximation of Gill's formulation than for the exact solution of Gill's formulation. For water the accuracy of Gill's approximation is still reasonable, but for air the deviation is large. This shows that Graebel's finite-Prandtl-number corrections (which are included in the approximation of Gill's formulation in table 4.3) are not very accurate for air. Finally, the averaged wall-heat transfer in Ostrach's similarity solution is much too small due to the negligence of the stratification and the fixing of the outer-edge temperature at $(T_h+T_c)/2$.

4.7. Four asymptotic structures

In the previous section the asymptotic structure of the Navier-Stokes solution in the vertical boundary layer and in the core was shown to satisfy Gill's asymptotic description. In this section some further details for the vertical boundary layer and the core are given and the structure of the two other asymptotic regions, namely the corner and the horizontal boundary layer, is described. The proper scalings as calculated in the large-Rayleigh-number Navier-Stokes solution are summarized in table 4.4.

TABLE 4.4. Navier-Stokes scalings for the steady laminar flow.

region	quantity	scaling	examples		
			quantity	air	water
vertical boundary layer	u	$(g\beta\Delta T\nu)^{1/3}\,Ra^{-1/12}$	$\dfrac{v_{max}}{\sqrt{g\beta\Delta TH}}=$	0.27	0.089
	v	$\sqrt{g\beta\Delta TH}$			
	T	ΔT	$\dfrac{y_{vmax}}{H\,Ra^{-1/4}}=$	1.2	1.4
	x	$H\,Ra^{-1/4}$	$\overline{Nu}\,Ra^{-1/4}=$	0.30	0.32
	y	H			
core	u	$(g\beta\Delta T\nu)^{1/3}\,Ra^{-1/12}$	$\dfrac{\psi_c}{u_0 H\,Ra^{-1/12}}=$	0.66	0.16
	v	$v \ll u$			
	T	ΔT			
	x	H	$S=$	0.99	0.55
	y	H			
corner	T	ΔT	$Nu_{max}\,Ra^{-1/3}=$	0.19	0.24
	y	$H\,Ra^{-1/3}$	$\dfrac{y_{Numax}}{H\,Ra^{-1/3}}=$	3.8	3.9
horizontal layer	u	$(g\beta\Delta T\nu)^{1/3}$	$\dfrac{u_{max}}{(g\beta\Delta T\nu)^{1/3}}=$	0.82	0.24
	v	$v \ll u$			
	T	ΔT			
	x	H	$\dfrac{y_{umax}}{H\,Ra^{-3/16}}=$	2.3	1.6
	y	$H\,Ra^{-3/16}$			

4.7.1. *vertical boundary layer along the heated wall*

The presence of the horizontal walls is felt by the vertical boundary layer via the temperature stratification in the core. Firstly the stable stratification gives small regions with flow reversal and temperature deficit in the outer part of the boundary layer. The flow reversal changes the parabolic character of the boundary-layer solution in an isothermal environment into an elliptic character. Secondly the stable stratification achieves that mass is moved into the hot boundary layer at heights smaller than $H/2$, and is moved out from the boundary layer at larger heights. In figure 4.4 it was shown that the wall-heat transfer in the Navier-Stokes solution for $Ra \to \infty$ satisfies the boundary-layer equations. In analogy, according to the boundary-layer scalings, the x-coordinate, the vertical velocity, and the temperature in the Navier-Stokes solution should scale with $H\,Ra^{-1/4}$, $u_0\,Ra^{1/6}$ and ΔT respectively in the limit $Ra \to \infty$. The velocity scale $u_0(Ra/Pr)^{1/6} = (g\beta\Delta TH)^{1/2}$ is known as the buoyant velocity scale. The correctness of these scalings is verified for the v-profile at $y=H/2$ for air in figure 4.7a. The velocity maximum is shown in figure 4.7b. For small y values the velocity maximum follows Ostrach's similarity solution

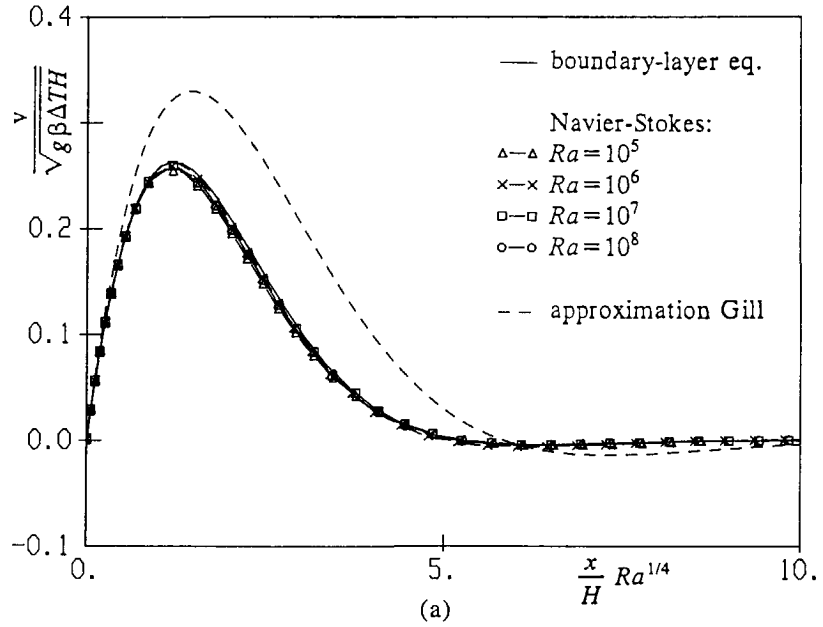

(a)

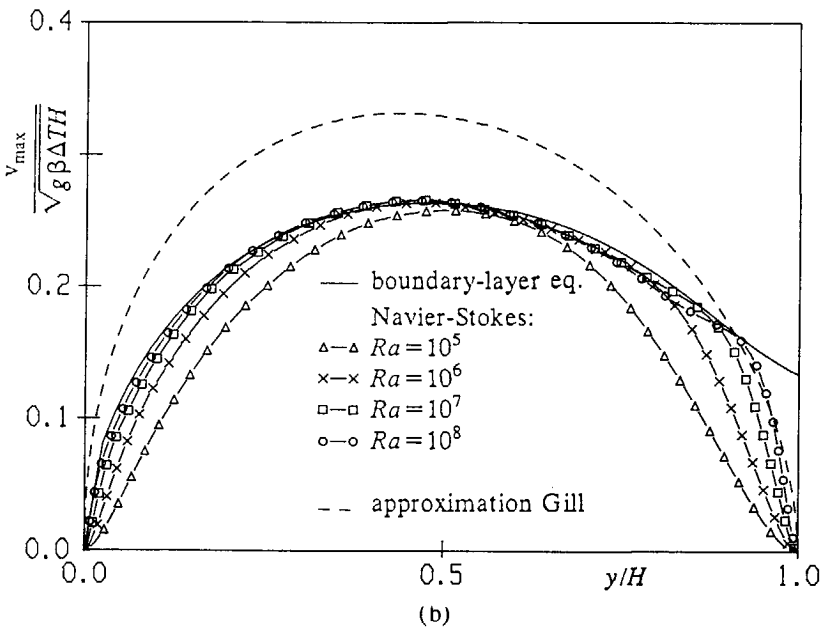

(b)

FIGURE 4.7(a,b). For caption see next page.

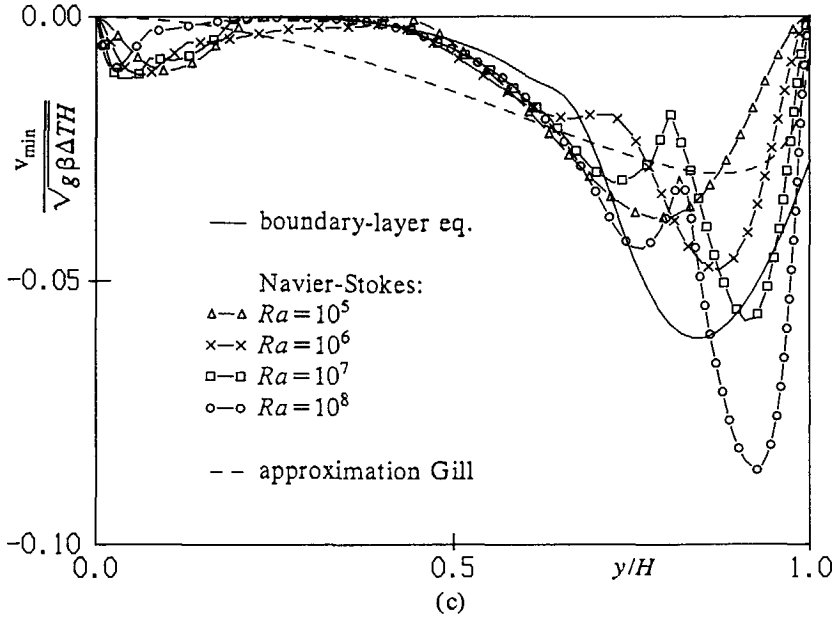

(c)

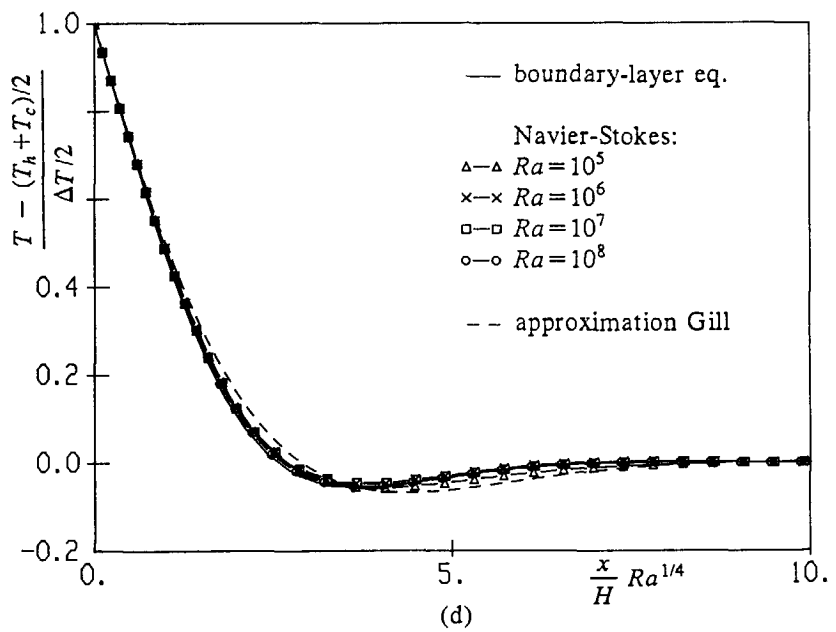

(d)

FIGURE 4.7. Vertical boundary layer for air; (a) vertical velocity at $y=H/2$, (b) maximum in the vertical velocity, (c) minimum in the vertical velocity, (d) temperature at $y=H/2$.

$$\lim_{Ra\to\infty} \frac{v_{max}}{\sqrt{g\beta\Delta TH}} = C^* \sqrt{y/H} \lim_{Ra\to\infty} \left(\frac{T_h - T(H/2,0)}{\Delta T} \right)^{1/2} \tag{4.10}$$

with $C^*=0.555$ for air and 0.263 for water. This similarity solution, which assumes an isothermal environment, only moves mass into the boundary layer and the velocity maximum increases with increasing y. No mass is moved out through the outer edge of the boundary-layer edge as occurs in the case of a the stratified environment for $y>H$. Hence, due to the stratification, the velocity maximum deviates form Ostrach's solution for larger y and the velocity maximum is largest at $y\sim H/2$. Reaching $y/H=1$, the maximum in the boundary-layer solution deviates from the Navier-Stokes solution; the Navier-Stokes solution smoothly falls back to zero, whereas the boundary-layer solution hits the ceiling with a finite velocity maximum. The minimum of the velocity, *i.e.* the maximum of the flow reversal, is shown in figure 4.7c for air. Deviations in the minimum between the boundary-layer solution and the Navier-Stokes solutions will be discussed in section 4.7.3. The scaling of the temperature profile at $y=H/2$ for air is verified in figure 4.7d.

4.7.2. *core region*

The Navier-Stokes solutions show that for increasing Rayleigh number the temperature becomes stratified in the core and the velocities in the core become much smaller compared to the velocities in the vertical boundary layers. Moreover the streamlines become horizontal in the core. Therefore the core velocities can be fitted to

$$\begin{aligned} \lim_{Ra\to\infty} \frac{u}{u_0} &\div Ra^{-a} \qquad a > -1/6 \\ \lim_{Ra\to\infty} \frac{v}{u_0} &\div Ra^{-b} \qquad b > a. \end{aligned} \tag{4.11}$$

The length scale in the core is expected to be H; the horizontal velocity can transport the mass from the hot vertical boundary layer, which is proportional to $u_0\, Ra^{1/6} \times H\, Ra^{-1/4}$, to the cold boundary layer if $a=1/12$. Integration of the horizontal velocities at $x=H/2$ gives the stream function of figure 4.5a. The scaling with $a=1/12$ for the horizontal velocity in the core agrees with the boundary-layer scaling for the normal velocity (4.6) and is checked in figure 4.9a for water. For increasing Rayleigh number the horizontal boundary layers along the horizontal walls becomes thinner and the core becomes larger. Indeed figure 4.9a shows that for increasing Rayleigh number an increasing part of the horizontal velocity falls on a single curve that scales with the velocity $u_0 Ra^{-1/12}$. The figure also shows that the scaled horizontal velocity in the core, $(u/u_0)\, Ra^{1/12}$, becomes infinitely large at $y/H \downarrow 0$ and $y/H \uparrow 1$ for increasing Rayleigh number. Such a growth without bound is also found in the normal velocity at the leading edge of Ostrach's similarity solution. The vertical core velocities are so small that the exponent b in equations (4.11) cannot accurately be determined from the calculated Navier-Stokes solutions. Nevertheless, it is clear that for large Rayleigh numbers we find $v \ll u$ in the core. The core region for air seems to show the same scaling for the

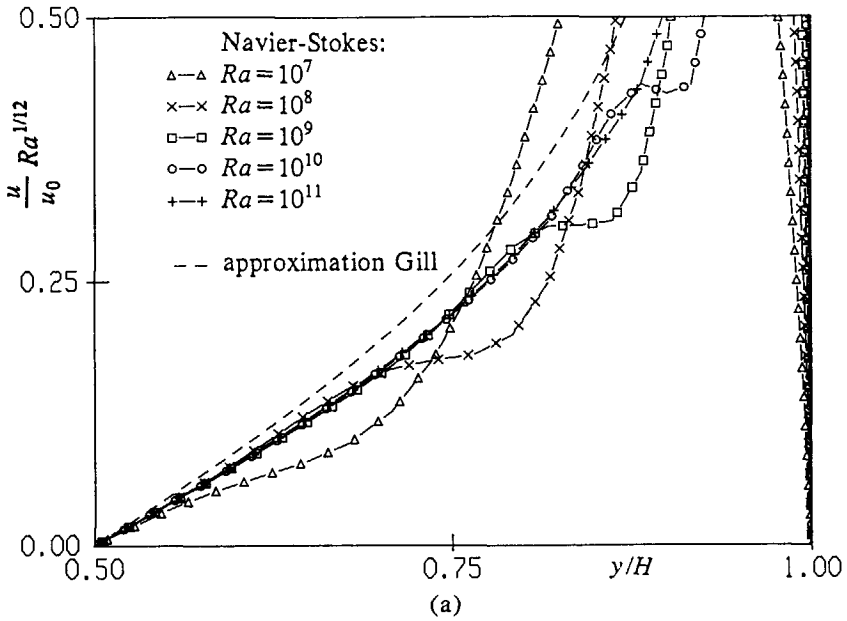

(a)

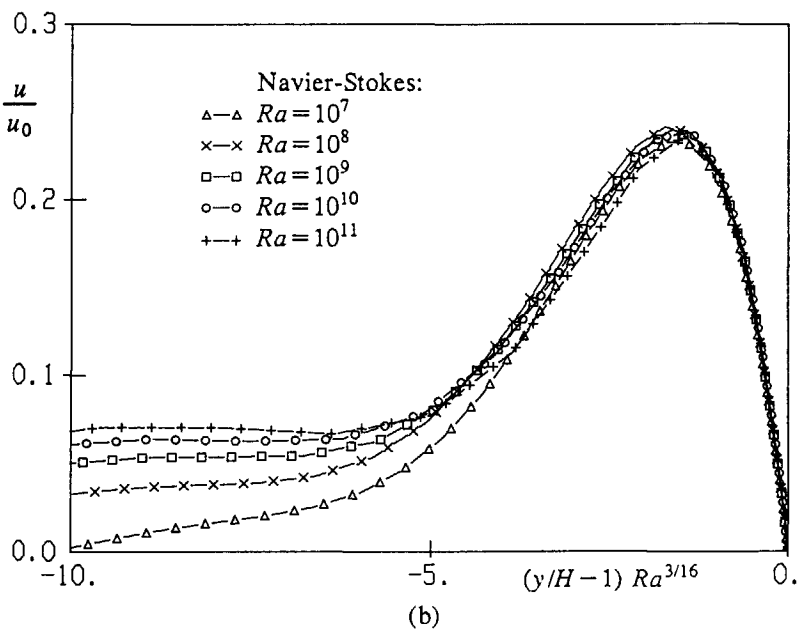

(b)

FIGURE 4.8. Horizontal velocity for water at $x = H/2$;
(a) in the core, (b) in the horizontal layer.

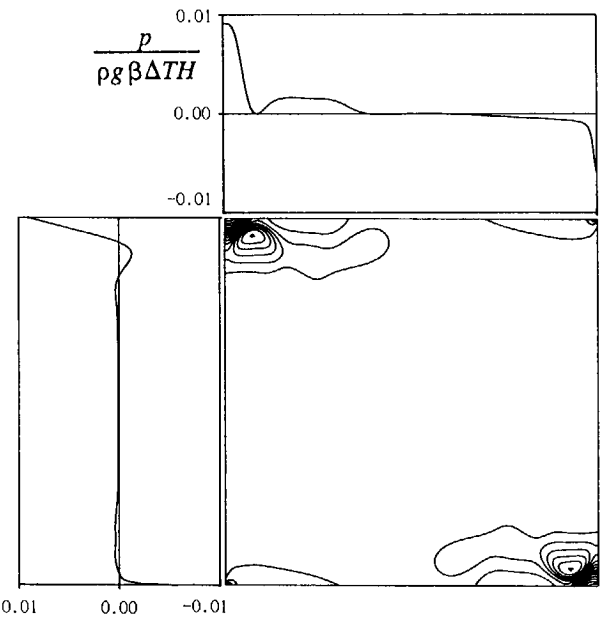

FIGURE 4.9. Pressure, after subtraction of the hydrostatic pressure, for air at $Ra = 10^8$; isobars in the cavity and pressure distribution along the ceiling and along the hot wall.

horizontal velocity as for water; for air, however, even the largest calculated Rayleigh numbers still give a rather thick horizontal boundary layer which makes the verification of the scaling for the horizontal core velocity less clear than for water.

4.7.3. *corner region*

In the left upper corner the vertically rising boundary layer hits the ceiling with a finite velocity maximum. In this region the flow can no longer be described with boundary-layer equations. No clear scalings can be derived from the large-Rayleigh-number Navier-Stokes solution, implying that full Navier-Stokes equations have to be used in this corner region. Pressure forces become important and achieve that the boundary layer changes direction and is continued as a horizontal layer. Because for large Rayleigh numbers the vertical boundary layers and the core are described by the boundary-layer equations (4.4), the pressure plays only a passive role in these regions and reduces to the hydrostatic pressure (4.5) in the limit $Ra \to \infty$, giving horizontal isobars. Figure 4.9 shows that the pressure becomes active in the left upper corner (and the right below corner); for air at $Ra = 10^8$ we have plotted the isobars after subtraction of the hydrostatic pressure with respect to the core stratification ($T_\infty(y)$ is evaluated at half the cavity width in equation (4.5)). For air a vortex in the streamline pattern (figure 4.1a) characterizes the bending of the vertical layer to the horizontal layer in the corner. The

influence of the vortex is also clearly seen in the minimum velocity for air in figure 4.7c. In the Navier-Stokes solution for $Ra=10^5$ and $Ra=10^6$ the vortex is still absent, and the minimum velocity is relatively close to the boundary-layer solution. With the appearance of the vortex at $Ra=10^7$, a new peak arises in the velocity minimum. It is expected that for increasing Rayleigh number the influence of the vortex disappears and that the Navier-Stokes solution comes closer to the boundary-layer solution. The influence of the vortex on the minimum, however, is still large at $Ra=10^8$. Figure 4.4a shows that the influence of the left below corner (the starting corner of the vertical boundary layer) on the wall-heat transfer fastly disappears with increasing Rayleigh number: the position y/H of the maximum in the wall-heat transfer comes closer to the floor. More precisely, its position y turns out to scale with $H\,Ra^{-1/3}$ $(=(g\beta\Delta TPr/\nu^2)^{-1/3})$. This scaling shows that the size of the cavity (H) does not influence the flow structure at the starting corner.

4.7.4. *horizontal layer*

The horizontal boundary layer along the adiabatic horizontal wall is of a different type than the vertical boundary layer: the horizontal boundary layer is not described by the boundary-layer equations (4.4). The horizontal layer forms the connection between the core flow and the no-slip and adiabatic condition at the horizontal wall. Similarly to the structure in the core, the isotherms and streamlines in the Navier-Stokes solution become horizontal for $Ra \to \infty$. Because the horizontal wall is adiabatic, the horizontal layer is even isothermal (with a temperature below T_h in the horizontal ceiling layer). Considering the u-velocity in figure 4.8a, the horizontal layer in the y-direction can be said to extend roughly from the horizontal wall up to the velocity maximum. As checked in figure 4.8b, the y-coordinate and u-velocity scale with $H\,Ra^{-3/16}$ and u_0 respectively. It is remarkable that this velocity scale $(u_0=(g\beta\Delta T\nu)^{1/3})$ is independent of H. The mass that is transported through the horizontal layer is proportional to $u_0HRa^{-3/16}$, whereas the mass through the core is proportional to $u_0HRa^{-1/12}$. This implies that for an infinitely large Rayleigh number all the mass from the hot vertical boundary layer is transported to the cold vertical boundary layer via the core. This agrees with Gill's assumptions about the asymptotic structure.

4.8. Conclusion

The steady laminar Navier-Stokes solution for air and water in the square cavity heated from the vertical side and with an adiabatic floor and ceiling shows four different streamline patterns (topological structures), when the Rayleigh number is increased up to 10^{11}. The last streamline pattern ($Ra > 5\times10^6$) contains four asymptotic structures: a vertical boundary layer along the heated wall, a core region, a corner region and a horizontal layer.

For increasing Rayleigh number the core becomes thermally stratified and has horizontal streamlines. The vertical temperature gradient in the center of the core scales with $\Delta T/H$ and is roughly twice larger for air than for water. The horizontal velocity in the core scales with $(g\beta\Delta T\nu)^{1/3}\,Ra^{-1/12}$. Comparison with the solution of the boundary-layer equations (using the large-Rayleigh-number temperature

stratification in the core as a boundary condition) shows that for $Ra \to \infty$ the Navier-Stokes solution along the vertical wall converges to the boundary-layer solution. This means that the wall-heat transfer scales with $(\Delta T/H)\, Ra^{1/4}$, the vertical velocity with $(g\beta\Delta TH)^{1/2}$ and the boundary-layer thickness with $H\, Ra^{-1/4}$. Finite Rayleigh-number effects in the Navier-Stokes solution for the vertical layers are restricted to influences in the corners. In the left upper corner the vertical boundary-layer solution hits the ceiling with a nonzero maximum speed. For air a vortex characterizes the process of bending the vertical layer to a horizontal layer. No scalings can be derived in the left upper corner, implying that full Navier-Stokes equations have to be used there. The horizontal layers along the horizontal walls are not described by boundary-layer equations. They have horizontal streamlines and are isothermal. The y-distance to the horizontal wall scales with $H\, Ra^{-3/16}$ and the horizontal velocity scales with $(g\beta\Delta T\nu)^{1/3}$.

The large-Rayleigh-number structures along the vertical walls and in the core, as calculated with the Navier-Stokes equations and the boundary-layer equations, agree with the asymptotic description proposed by Gill.

5. LAMINAR-TURBULENT TRANSITION

5.1. Introduction

The natural-convection flow undergoes a gradual transition from a laminar to a turbulent state when the Rayleigh number is increased above a critical value. This transition can be calculated by numerically solving the unsteady, three-dimensional Navier-Stokes equations. Because of the appearance of very fine eddy structures in the final phase of the transition, such a calculation would require an enormous computational effort. Therefore the present study is restricted to the calculation of the initial phase of the transition: we calculate how the steady, two-dimensional laminar flow looses its stability by solving the unsteady, two-dimensional Navier-Stokes equations.

The stability can be examined by following the evolution of disturbances on a steady laminar flow. Beyond a critical value these disturbances no longer die out and a bifurcation to an unsteady flow is found. For very simple geometries some classical results exist, referring to elementary instability mechanisms. For example we know (i) the Rayleigh/Bénard instability in a horizontal fluid layer that is heated from below, (ii) the instability after a hydraulic jump in a horizontal moving fluid layer and (iii) the Tollmien-Schlichting instability in a boundary layer. In the present approach we only consider two-dimensional disturbances. Three-dimensional effects are certainly important in the fully turbulent flow. Whether the three-dimensional disturbances lead to an earlier instability of the steady, two-dimensional natural-convection flow than the two-dimensional disturbances remains to be investigated.

In this chapter the unsteady, two-dimensional Navier-Stokes equations are numerically solved for the square cavity that is heated differentially over the vertical walls. The stability is calculated for both the cases of conducting and adiabatic horizontal walls. Both air and water are considered. We do not know of stability calculations in the literature for water in the square cavity, neither with conducting nor with adiabatic horizontal walls. The stability for air in the square cavity in the case of conducting horizontal walls, however, was already calculated by Winters (1987) and by Le Quéré & Alziary de Roquefort (1986, 1988). Further, the latter authors (1985) also calculated the stability for air in a cavity with adiabatic horizontal walls and a height-width ratio of 4 and larger. When our calculations on the coarser grids had been finished, and the calculations on the fine 120×120 grids were under way, we received a preprint of a paper by Paolucci & Chenoweth (1989). Their paper gives a detailed numerical study of the stability for air in the square cavity with adiabatic horizontal walls. Our calculations are very similar to those of Paolucci & Chenoweth; the results largely agree.

Although the cavity configuration is more complicated than any of the mentioned simple configurations, the present calculations suggest that mechanisms leading to instabilities in the cavity are closely related to the Rayleigh/Bénard instability, the instability after a hydraulic jump and the Tollmien-Schlichting instability. A better knowledge of the instability mechanisms is important, because they

form the roots of turbulence: it can help to better model the turbulence.

5.2. Unsteady Navier-Stokes equations

We consider the unsteady, two-dimensional flow in the square cavity as described by the Navier-Stokes equations under the Boussinesq approximation (2.9). The cavity has a hot left vertical wall (T_h) and a cold right vertical wall (T_c). Two cases are considered: the case with conducting horizontal walls (*i.e.* these walls have a linear temperature profile: $T=T_h-(x/H)(T_h-T_c)$) and the case with adiabatic horizontal walls ($\partial T/\partial y=0$).

The variables are nondimensionalized with the length scale H, the time scale $H/(g\beta\Delta TH)^{1/2}$, the temperature scale $T_0=T_c$ and the temperature difference $\Delta T=T_h-T_c$. For the vertical velocity the buoyant velocity scale $u_b=(g\beta\Delta TH)^{1/2}$ is used, whereas for the horizontal velocity the velocity scale $u_0=(g\beta\Delta T\nu)^{1/3}$ is used. The nondimensionalization leads to

$$\left\{\frac{u}{u_0}, \frac{v}{u_b}, \frac{T-T_c}{\Delta T}, \frac{p}{\rho u_b^2}\right\} = f\left\{\frac{t\sqrt{g\beta\Delta TH}}{H}, \frac{x}{H}, \frac{y}{H}, Ra, Pr\right\}. \tag{5.1}$$

The Prandtl number (Pr) and the Rayleigh number ($Ra = g\beta\Delta TH^3Pr/\nu^2$) are the only two characteristic numbers in this problem.

The evolution of the following quantities will be examined

$$\begin{aligned} u_{max} &= \text{maximum of } |u(y)| \text{ at } x=H/2 \\ v_{max} &= \text{maximum of } |v(x)| \text{ at } y=H/2 \\ \overline{Nu} &= \left|\int_0^H \left(\frac{\partial T/\Delta T}{\partial x}\right)_{x=0} dy\right|. \end{aligned} \tag{5.2}$$

Here $\overline{Nu}$ (Nusselt number) is the dimensionless averaged heat transfer through the hot vertical wall. A single oscillation in a quantity ϕ can be characterized by its maximum ϕ_{max}, its amplitude δ ($=\phi_{max}-\phi_{min}$) and by its frequency f.

5.3. Numerical method

The spatial derivatives in the Navier-Stokes equations are discretized with the finite-volume method on a staggered grid, as described in section 2.6. The use of the central scheme for the convection, instead of the first-order upwind scheme, is essential in the present stability calculations. The numerical diffusion in the upwind scheme (or the hybrid scheme) damps oscillations and was often found to give an evolution to a steady state in cases where the central scheme predicted an oscillating final state. It is known that the central scheme easily gives wiggles on coarse grids (*i.e.* numerical waves with a wave length of only twice the grid size). These wiggles, however, will disappear if the grid is sufficiently refined. In the present calculations, the appearance of thin boundary layers along the vertical walls requires a nonequidistant grid. The u-grid points are positioned in the x-direction according to equation (4.7) and a same spacing is used for the v-grid points in the y-direction. The time dependence is treated implicitly; the spatial

derivatives are all evaluated at the new time level n, and the time derivatives are approximated with three time levels using the B3 scheme (2.21b).

The discrete equations for the transport variables u, v and T are iteratively solved at each new time level with the line Gauss-Seidel method. The pressure is updated with the SIMPLE pressure-correction method. For small time steps the pressure-correction equation (2.29) reduces to

$$\frac{\partial^2 p'}{\partial x^2} + \frac{\partial^2 p'}{\partial y^2} = \frac{3}{2}\frac{\rho}{\Delta t}\left(\frac{\partial u^*}{\partial x} + \frac{\partial v^*}{\partial y}\right). \tag{5.3}$$

At the walls a zero gradient for the pressure correction is prescribed. The *-superscript refers to the iterating velocity field in the Gauss-Seidel process. When the Gauss-Seidel process is fully converged the right-hand-side of equation (5.3) vanishes, giving a zero pressure correction. Originally we updated the pressure correction with the line Gauss-Seidel method in the same way as for the transport variables. Even for a small time step, many sweeps were required to reach a close-to-zero pressure correction; it is known that the speed of convergence for the Gauss-Seidel iteration decreases when the Poisson equation is solved on a grid with strongly stretched finite volumes. Therefore, instead of using an iterative solver, we decided to solve the pressure correction directly. Discretization of equation (5.3) gives a symmetric band matrix for the Laplace operator, having fixed coefficients which only depend on the geometry. The Choleski decomposition of this matrix (which actually is a LU decomposition that takes the symmetry of the matrix into account) has to be determined only once and can be stored. After each Gauss-Seidel sweep for the transport variables the pressure is determined with the direct solver, implying that the discretized continuity equation is exactly satisfied. The sweep process at the new time level is stopped when the pressure correction in each cell and the net heat flux through the boundaries are below a certain criterion. Typically 5 to 10 sweeps at each time level are sufficient.

5.4. Stability and bifurcation

Although the boundary conditions are steady, this does not necessarily mean that the solution of the Navier-Stokes equations converges to a steady solution at large time. Its large-time behaviour is studied in the qualitative theory of partial differential equations. This theory distinguishes the following solutions to which an initial solution can be attracted for large time: (i) steady-state attractor, (ii) periodic attractor, (iii) quasi-periodic attractor, (iv) strange attractor. All these attractors, except the first, show an essentially unsteady behaviour at large time. The attractors (ii) and (iii) give a solution with only discrete frequencies (spikes) in the Fourier spectrum. The periodic attractor (ii) gives a single-frequency oscillation (or so-called limit cycle). The quasi-periodic attractor (iii) consists of several incommensurate frequencies. The strange attractor, which is also referred to as chaos, is nonperiodic, showing a broad-band spectrum. The occurring attractor might depend on the initial solution at $t=0$: multiple steady or unsteady solutions of the unsteady Navier-Stokes equations can exist for $t \to \infty$. Therefore, variation of the Rayleigh number can give different branches of solutions. These branches can be either stable or unstable against very small disturbances. The

stability against very small disturbances is denoted as the *linear* stability of the solution. The phenomenon that a solution remains on its branch as long as disturbances are small, and only jumps to another branch for sufficiently large disturbances, is referred to as hysteresis. Hysteresis is related to the *nonlinear* stability of the solution.

The large-time behaviour of the Navier-Stokes solution can be studied by increasing the Rayleigh number for a fixed Prandtl number. It can be proved that the solution is steady and unique up to a critical Rayleigh number (see Temam, 1977). Above the critical Rayleigh number the steady solution becomes unstable, *i.e.* disturbances no longer decay for increasing time. The linear stability theory predicts an exponential growth of the unstable disturbances. During the growth of the disturbances, however, nonlinear effects become important and the solution ends up in a new solution that has a linear stability. The Rayleigh number Ra_{cr} at which a certain large-time solution branches to another large-time solution is a bifurcation point of the unsteady Navier-Stokes equations. Different types of bifurcation exist; two well-known types are the pitchfork bifurcation (branching from one steady to another steady solution) and the Hopf bifurcation (branching from a steady solution to an unsteady solution with a single-frequency oscillation). The Hopf bifurcation is related to the periodic attractor (ii).

Winters (1987) describes how the bifurcation from a steady solution can numerically be determined. The unsteady Navier-Stokes equations are linearized around a steady discrete solution. After discretization a system of linear algebraic equations results

$$\frac{\partial \phi}{\partial t} + J\,\phi = 0 \tag{5.4}$$

where J is the Jacobian matrix of the steady part. The steady solution ϕ has a linear stability if all eigenvalues σ of J have $\mathrm{Re}(\sigma) > 0$. If $\mathrm{Re}(\sigma)=\mathrm{Im}(\sigma)=0$ (*i.e.* $\det(J)=0$), the steady solution shows the pitchfork bifurcation. If $\mathrm{Re}(\sigma)=0$ and $\mathrm{Im}(\sigma)=\pm i\omega$, the steady solution shows a Hopf bifurcation, giving the single frequency $f=\omega/(2\pi)$. Winters' method has the advantage that it can locate the position of the Hopf bifurcation without the calculation of the unsteady oscillating solution. If, on the other hand, one wants to determine the bifurcation by the calculation of the unsteady solution, the position of the Hopf bifurcation can be extrapolated from the supercritical oscillating solution with the help of the series expansions of Joseph & Sattinger (1972). For the amplitude and the frequency of the unsteady Navier-Stokes solution at a Rayleigh number sufficiently close to the critical Rayleigh number the series expansions give

$$\begin{aligned} \delta &\div (Ra - Ra_{cr})^{1/2} \\ f - f_{cr} &\div Ra - Ra_{cr}. \end{aligned} \tag{5.5}$$

Winters' method of examining the eigenvalues to determine a bifurcation can also be generalized to determine the linear stability of a single-frequency oscillation; in this case the Floquet multipliers of the system have to be determined (see Guckenheimer & Holmes, 1983). Determining the stability by examining the eigenvalues for less simple unsteady solutions is complicated. The calculation of the

unsteady solution, instead of Winters' steady approach, has the advantage that besides the Hopf bifurcation it can also determine the bifurcation and nonlinear stability for any steady or unsteady solution. In the present study the stability is examined by the calculation of the unsteady Navier-Stokes solution.

Recently a workshop was organized to obtain benchmark numerical results for the Hopf bifurcation in the Navier-Stokes solution at low Prandtl numbers in a shallow cavity with conducting horizontal walls and differentially heated vertical walls (Roux, 1990). We participated in this workshop and our computational code turned out to give good results for this benchmark case (see Henkes & Hoogendoorn, 1990).

The Hopf bifurcation introduces an unsteady solution. Because its spectrum is discrete, we cannot denote this as a turbulent solution. The occurrence of a Hopf bifurcation, however, can be seen as the initial phase of the transition to turbulence. The total path to turbulence seems to consist of different transitions between the attractors (ii), (iii) and (iv) (a review is given by Yang, 1988). If the Rayleigh number is increased sufficiently far, chaos is found, which has the broad-band spectrum that is characteristic for turbulence.

5.5. Instability mechanisms

The present study investigates the stability for air ($Pr=0.71$) and water ($Pr=7.0$) in a square cavity that is heated from the vertical side. Both the cases of conducting and adiabatic horizontal walls are considered.

For increasing Rayleigh number the steady solution in the cavity shows boundary layers along the vertical and horizontal walls and an almost stagnant core with horizontal streamlines. Further, the core is thermally stratified. Gill (1966) has suggested that the vertical velocity in the vertical boundary layers scales with $(g\beta\Delta TH)^{1/2}$, whereas the boundary-layer thickness scales with $H\,Ra^{-1/4}$. The horizontal velocity in the core scales with $(g\beta\Delta T\nu)^{1/3}\,Ra^{-1/12}$, and the characteristic length scale in the core is H. In the previous chapter we showed, by comparison with the steady large-Rayleigh-number solutions of the Navier-Stokes equations, that these indeed are the proper scalings. With the help of these spatial scalings Patterson & Imberger (1980) proposed time scales (*i.e.* the ratio of a length and velocity scale) which are expected to be important in an unsteady evolution. The vertical length scale H and the vertical velocity scale $(g\beta\Delta TH)^{1/2}$ in the vertical boundary layer give the time scale $(H^2/\nu)\,Ra^{-1/2}$. The horizontal length scale H and the horizontal velocity scale $(g\beta\Delta T\nu)^{1/3}\,Ra^{-1/12}$ in the core give the time scale $(H^2/\nu)\,Ra^{-1/4}$. For large Rayleigh numbers the time scale in the core is largest. The present calculations confirm that the time scale in the core is indeed characteristic for the time required for the initial solution to reach its final state (see also Yewell *et al.* 1982, Hyun 1985). The molecular time scale $(H^2/\nu)\,Ra^0$ is the dominant time scale at moderate Rayleigh numbers, but it is of minor importance at the large Rayleigh numbers as considered in the present study.

The distinction of the steady solution in a stratified core region, corners, horizontal boundary layers and vertical boundary layers gives at least three possible instability mechanisms: (i) a Rayleigh/Bénard instability in the horizontal boundary layer or core, (ii) an instability in the horizontal boundary layer or core in the flow

directly after the hydraulic jump in the corner and (iii) a Tollmien-Schlichting instability in the vertical boundary layer.

5.5.1. *Rayleigh/Bénard instability*
For large Rayleigh numbers the stratified core can be considered as inviscid. Stability analysis on the inviscid equations for the stagnant core, as was originally performed by Rayleigh (1883), shows that the stratification is stable if the density decreases with the height (or, if β is positive: if the temperature increases with the height). Moreover the analysis shows that if the steady solution in a stable stratification is disturbed, the flow returns to its original state in an oscillatory way, showing damped internal gravity waves with frequencies that scale with the Brunt-Väisälä frequency $(g\beta\Delta TH)^{1/2}/H$. Rayleigh (1916) also showed that viscosity can delay the instability in the unstably stratified environment until a critical Rayleigh number is exceeded. He calculated a pitchfork bifurcation at $Ra_{cr}=1708$ in the classical problem of an infinite horizontal fluid layer that is heated from below. (Both the horizontal walls, confining the horizontal layer, are rigid and the Rayleigh number is based on the thickness of the layer and the temperature difference across the layer.) Below Ra_{cr} there is a linear thermal stratification and zero convection. Above Ra_{cr} there is convection, showing the well-known Bénard cells, as firstly measured by Bénard (1900). More details about the thermal instability in the stratified environment, which will be referred to here as the Rayleigh/Bénard instability, are given in the book by Drazin & Reid (1981).

5.5.2. *instability after a hydraulic jump*
The hydraulic jump is the phenomenon that a thin high-speed horizontal layer (with a free surface) almost discontinuously jumps to a broader low-speed horizontal layer. The hydraulic jump occurs if the local Froude number (Fr) in the horizontal layer exceeds the value one ($Fr=U/(gd)^{1/2}$, where U is the averaged velocity in the layer and d is the thickness of the layer; see for example Turner, 1973). The hydraulic jump can occur in the horizontal layer close to the corner of the cavity, where the vertical boundary layer hits the horizontal wall and bends to a high-speed horizontal layer. If the jump is too strong the flow after the jump becomes unstable and the free-coming jump energy is dissipated via an unsteady oscillating wave pattern. Ivey (1984) has observed such a hydraulic jump during the time evolution to a steady state of water in the heated square cavity at large Rayleigh numbers. The hydraulic jump was also mentioned as a possible instability mechanism in the cavity in the computational study of Paolucci & Chenoweth (1989).

5.5.3. *Tollmien-Schlichting instability*
The Tollmien-Schlichting instability generates so-called traveling waves with the wave length λ in the vertical boundary layer. The waves move upwards with the wave speed λf. The Tollmien-Schlichting instability of the natural-convection boundary layer along a semi-infinite, hot vertical plate in an isothermal environment has been studied theoretically by Nachtsheim (1963). He numerically solved the Orr-Sommerfeld equations. These equations approximately describe the evolution of disturbances on the steady solution of the boundary-layer equations. The

approximations are: linear disturbances, locally parallel flow (*i.e.* zero normal velocity) and certain assumptions about the shape of the disturbances (both in space and time). Some studies have made a similar stability analysis, but without the parallel-flow assumption (Haaland & Sparrow 1973, Tzuoo *et al.* 1985, Lee *et al.* 1987). The critical Rayleigh number ($Ra_{y,cr}$), the frequency (f) and the wave length (λ) are summarized in table 5.1. The Rayleigh number in the table is based on the y-coordinate along the vertical plate and on $\Delta T=2(T_h-T_\infty)$, where T_∞ is the isothermal environment temperature. The factor 2 is introduced to make a senseful comparison with the cavity geometry: replacing T_∞ by the centre temperature in the cavity, $(T_h+T_c)/2$, gives the earlier definition $\Delta T=T_h-T_c$.

Of course, because of the horizontal walls, the boundary layer along the hot wall in the cavity differs from the boundary layer along the hot vertical plate in an open isothermal environment. In the previous chapter we showed that the main influence of these horizontal walls on the development of the vertical boundary layer is via the thermal stratification in the core. The linear stability analysis of Gill & Davey (1969) takes the stratification into account. It determines the stability against small disturbances of the boundary layer in an infinitely tall vertical slot with a stably stratified core, in which the temperature linearly increases with the height. The differences with the present square cavity situation are that the steady basic flow of Gill & Davey is a parallel flow (and therefore it does not describe the development of the boundary-layer flow starting at the bottom) and that the wall temperature is not isothermal, but increases with the height in the same linear way as the core. The core stratification is described by the temperature gradient S. Their results in table 5.1 show that the critical Rayleigh number strongly depends on the stratification.

Jaluria & Gebhart (1974), Gebhart & Mahajan (1975) and Gebhart (1988) have experimentally studied the transition of the natural-convection boundary layer for water along a vertical plate with a constant wall-heat flux placed in an isothermal environment. The first unsteadiness in the experiments shows a single-frequency oscillation. The time oscillation corresponds to traveling waves, which move upward through the vertical boundary layer. Moreover the unsteadiness for larger Ra_y values still shows a single oscillation, in which the frequency is independent of y. This y-independence implies that the dimensionless frequency $f\nu^{1/3}/(g\beta\Delta T)^{2/3}$ is independent of Ra_y. Gebhart & Mahajan (1975) indicate this dimensionless frequency as the 'characteristic frequency' of the boundary layer. The Orr-Sommerfeld stability analyses do not find a single frequency for supercritical Ra_y values, but a continuous spectrum of unstable modes. Of course, one has to realize that the Orr-Sommerfeld equations only describe the linear stability of a simplified boundary-layer flow. Gebhart & Mahajan, however, note that the frequency which is most strongly amplified in the Orr-Sommerfeld solution for supercritical Ra_y values closely follows a curve in which $f\nu^{1/3}/(g\beta\Delta T)^{2/3}$ is independent of Ra_y. In particular this is true for Ra_y values sufficiently far beyond $Ra_{y,cr}$, whereas the deviation for values closer to $Ra_{y,cr}$ is a bit larger. As indicated in table 5.1, the theoretical frequency $f\nu^{1/3}/(g\beta\Delta T)^{2/3}$ for water, as found by Gebhart & Mahajan on the mentioned curve, is close to the experimental result of Jaluria & Gebhart (1974). The agreement for air between this theoretical value and the

TABLE 5.1. Comparison of the Tollmien-Schlichting instability in the vertical boundary layer.

(a) air

study	$Ra_{y,cr}$	$\frac{f\nu^{1/3}}{(g\beta\Delta T)^{2/3}}$	$\frac{\lambda(g\beta\Delta T)^{1/3}}{\nu^{2/3}}$
plate, theoretical:			
Nachtsheim (1963)	3.82×10^5	0.0162	211
Gill & Davey (1969)	$1.13\times10^8\ S^3$ *)	0.0239	161
Gebhart & Mahajan (1975)	--	0.0351	--
Lee *et al.* (1987)	1.73×10^6	0.0263	156
plate, experimental:			
Eckert & Soehnghen (1951)	6×10^8	0.0415	--
Kitamura *et al.* (1985)	--	0.0063	100
adiabatic cavity:			
present	2.25×10^8 *)	0.0226	94
Paolucci & Chenoweth (1989)	2.55×10^8 *)	0.0228	--

(b) water

study	$Ra_{y,cr}$	$\frac{f\nu^{1/3}}{(g\beta\Delta T)^{2/3}}$	$\frac{\lambda(g\beta\Delta T)^{1/3}}{\nu^{2/3}}$
plate, theoretical:			
Nachtsheim (1963)	2.82×10^5	0.0228	57
Gill & Davey (1969)	$2.21\times10^8\ S^3$ *)	0.0234	56
Gebhart & Mahajan (1975)	--	0.0251	--
Lee *et al.* (1987)	1.12×10^6	0.0293	53
plate, experimental:			
Jaluria & Gebhart (1973)	2×10^9	0.0248	--
Kitamura *et al.* (1985)	--	0.0063	100
adiabatic cavity:			
present	$\sim10^{10}$ *)	0.0328	56

*) $y=H$

experimental value of Eckert & Soehnghen (1951) is a bit worse. If Ra_y is further increased the experiments show that more frequencies enter the flow and the transition to the turbulent state is found. The precise transition is a complicated process. Jaluria & Gebhart (1974) emphasize that the whole transition process can *not* be described as a function of Ra_y alone (for a fixed Prandtl number). In mathematical terms, they suggest that several stable solutions exist in the transition regime; whether the experiments give the one or the other solution depends on the

precise experimental situation. This can explain the large difference between the theoretical and experimental critical Rayleigh numbers in table 5.1. Although the fully turbulent natural-convection boundary-layer flow shows a broad-band spectrum of frequencies, Kitamura *et al.* (1985) experimentally observed coherent structures in the turbulence. The main characteristic of this coherent structure is a motion of large eddies, with a dominant frequency that can be fitted to $f\nu^{1/3}/(g\beta\Delta T)^{2/3}=0.0063$ (see table 5.1).

We conclude from table 5.1 that, with exception of the experiments of Kitamura *et al.* in the turbulent regime, both the theoretical stability analyses and the experiments more or less predict the same frequency $f\nu^{1/3}/(g\beta\Delta T)^{2/3}$ and wave length $\lambda(g\beta\Delta T)^{1/3}/\nu^{2/3}$ for the first unsteadiness. This is in particular true for water, whereas the agreement for air is less good. The critical Rayleigh numbers in the different studies largely deviate.

All the theoretical stability analyses mentioned in the last three sections have in common that they are simplified linear stability analyses for simple configurations. It is not beforehand clear how these results relate to the stability of the flow in the square cavity heated from the side. Therefore in the next two sections we give the stability results for the cavity flow, as calculated from the unsteady, two-dimensional Navier-Stokes equations.

5.6. Conducting horizontal walls

The stability for air in the case of conducting horizontal walls has already been investigated in different other studies, but no studies are known for water. Le Quéré & Alziary de Roquefort (1986, 1988) treated the problem by a similar approach as used in the present study, namely by solving the unsteady, two-dimensional Navier-Stokes equations. They used a spectral method to discretize the equations. Increasing the Rayleigh number from 10^6 up to 10^7, they find transitions (showing hysteresis) from the steady solution for air to three unsteady oscillating branches, with the dimensionless frequencies $fH/(g\beta\Delta TH)^{1/2}=$ 0.255, 0.29 and 0.32 respectively. The frequency of the oscillation for supercritical Rayleigh numbers is almost independent of the Rayleigh number if it is nondimensionalized with the Brunt-Väisälä frequency $(g\beta\Delta TH)^{1/2}/H$. The intermediate frequency corresponds to a centro-symmetry breaking solution. These frequencies were experimentally verified by Briggs & Jones (1985). These authors (Jones & Briggs, 1989) also numerically calculated the frequencies by solving the unsteady Navier-Stokes equations. Jones & Briggs used the finite-volume method to discretize the equations. Winters (1987) detected five Hopf bifurcations in the steady solution for air, increasing the Rayleigh number from 2×10^6 up to 3×10^6. He used a finite-element method to discretize the steady equations. His dimensionless frequencies for increasing Rayleigh number are 0.254, 0.215, 0.290, 0.173 and 0.325 respectively. The three highest frequencies seem to correspond to those found in the mentioned unsteady calculations and experiments.

In the present study calculations were made in the Rayleigh number range $10^6 - 3\times10^6$ for air and in the range $10^6 - 6\times10^6$ for water. The large-time solution for a slightly smaller Rayleigh number was used as an initial condition at

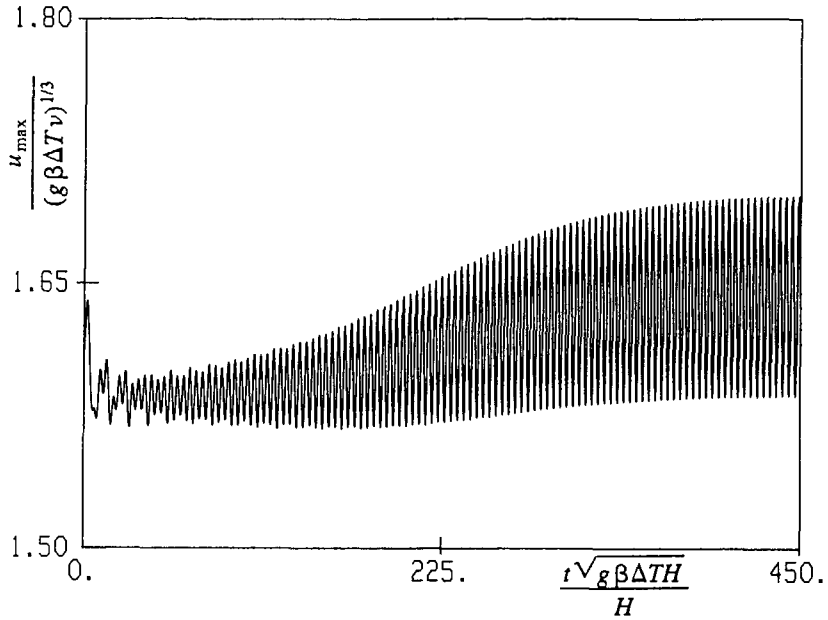

FIGURE 5.1. Time evolution of u_{max} for air at $Ra=2.25\times10^6$ in the case of conducting horizontal walls.

TABLE 5.2 Bifurcation in the case of conducting horizontal walls.

study	air		water	
	Ra_{cr}	$\frac{fH}{\sqrt{g\beta\Delta TH}}$	Ra_{cr}	$\frac{fH}{\sqrt{g\beta\Delta TH}}$
present:				
30×30 grid	1.27×10^6	0.272	1.72×10^6	0.128
60×60 grid	2.07×10^6	0.247	4.65×10^6	0.157
80×80 grid	2.10×10^6	0.248	5.13×10^6	0.158
Le Quéré & AdR (1986)	2.2×10^6	0.255	--	--
Winters (1987)	2.1092×10^6	0.254	--	--
Jones & Briggs (1989)	2.2×10^6	0.249	--	--
experimental, Briggs & Jones (1985)	3×10^6	0.248	--	--

$t=0$. The integration in time was performed until the new large-time behaviour was fully reached. Figure 5.1, for example, shows the time evolution to a periodic state for air at $Ra=2.25\times10^6$, using the steady solution at $Ra=2\times10^6$ as an initial solution.

By time-step refinement, the time step $\Delta t(g\beta\Delta TH)^{1/2}/H=1/8$ was checked to give almost time-step-independent results. In table 5.2 and figure 5.2 the spatial accuracy is verified by refining the grid up to 80×80 grid points. The critical Rayleigh number in table 5.2 was determined by extrapolating the amplitude (δ) to

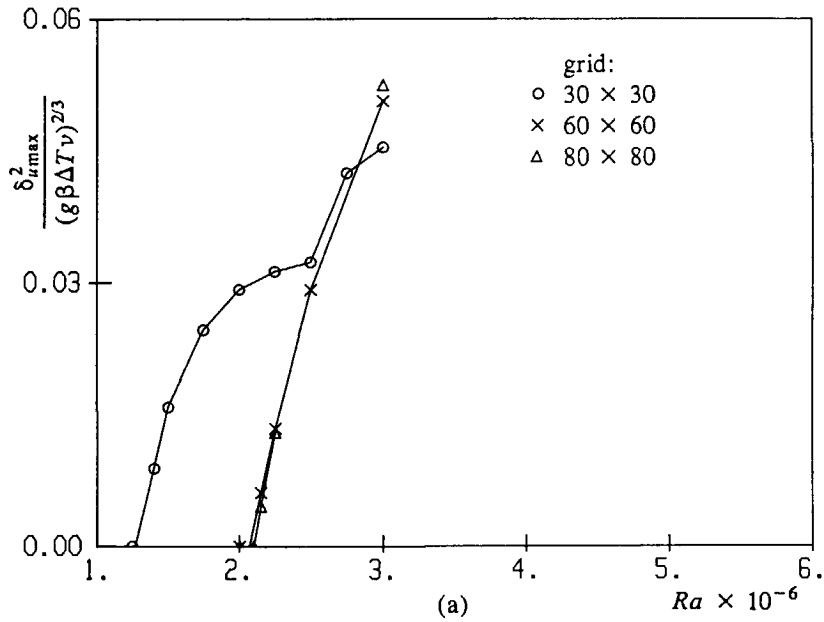

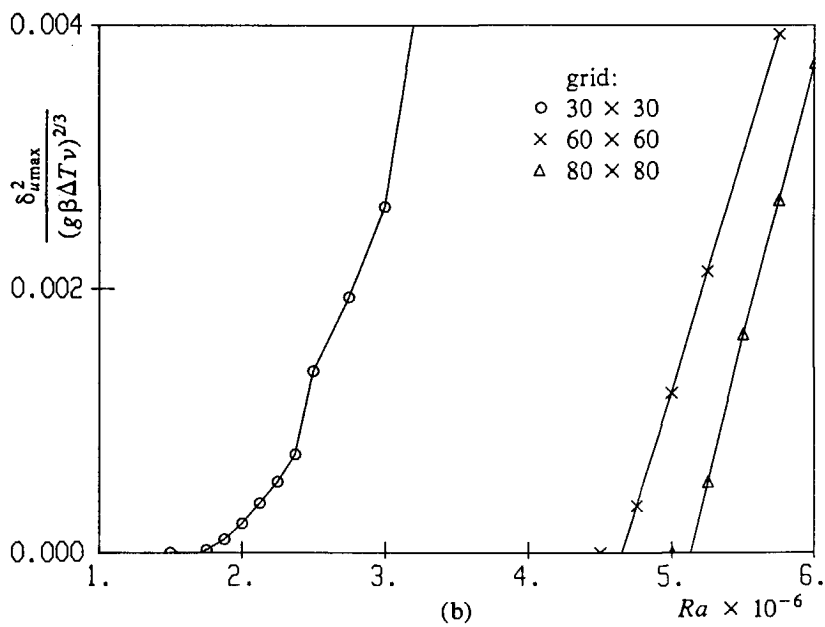

FIGURE 5.2. Bifurcation in the case of conducting horizontal walls; (a) air, (b) water.

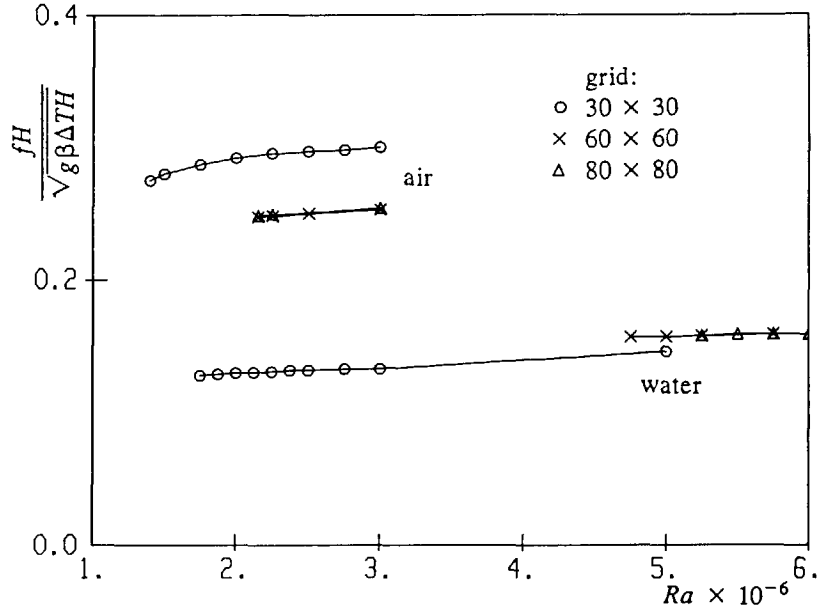

FIGURE 5.3. Frequency in the case of conducting horizontal walls.

zero with the help of equations (5.5). If a Hopf bifurcation in the Navier-Stokes equations occurs, equations (5.5) say that a straight line is found sufficiently close beyond Ra_{cr} when δ^2 is plotted *vs* Ra. Figure 5.2 shows that this is indeed the case at all grids, with exception of the 30×30 grid for water. The latter grid is too coarse to accurately solve the Navier-Stokes equations close to Ra_{cr}. The critical Rayleigh number and frequency at our two finest grids for air are very close. Moreover table 5.2 shows a good accuracy with the existing numerical and experimental studies. In particular Winters (1987) has shown by grid refinement that his results are very accurate; our 80×80 grid for air gives $Ra_{cr}=2.10\times10^6$ with $fH/(g\beta\Delta TH)^{1/2}=0.248$, whereas Winters finds $Ra_{cr}=2.1092\times10^6$ with $fH/(g\beta\Delta TH)^{1/2}=0.254$. The difference between the values for Ra_{cr} at the two finest grids is larger for water than for air, but the difference for the frequency is small for both air and water. Comparison of the critical Rayleigh number on the finest grid for air and water shows that increasing the Prandtl number delays the instability.

In the range of Rayleigh number where the calculations were performed we found either an evolution to a steady state (for $Ra<Ra_{cr}$) or an evolution to a periodic oscillating state (for $Ra>Ra_{cr}$). Beyond Ra_{cr} the same periodicity was found in the quantities u_{max}, v_{max} and Nu. Figure 5.3 verifies that the frequency for supercritical Rayleigh numbers scales with the Brunt-Väisälä frequency $(g\beta\Delta TH)^{1/2}/H$. At a fixed grid the frequency in figure 5.3 remains on a single branch; we did not calculate that the frequency jumped to another branch when the Rayleigh number was changed. This contrasts the calculations of Le Quéré &

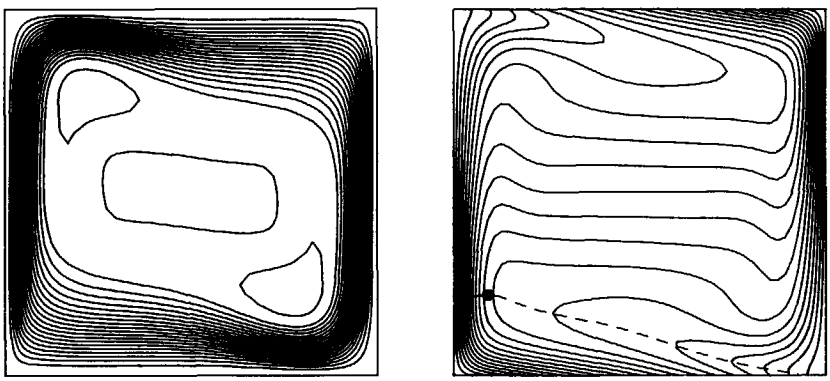

(a) (b)

FIGURE 5.4. Steady flow for air at $Ra=10^6$ in the case of conducting horizontal walls; (a) streamlines, (b) isotherms.
(the broken line indicates up to where the unstable thermal layer extends).

Alziary de Roquefort (1988) and Jones & Briggs (1989), who found different branches of frequencies for air. Hysteresis effects seem to prevent that our periodic solution jumps to another branch and changes frequency. We also calculated the unsteady large-time solution for air at $Ra=5\times10^8$, which is far beyond Ra_{cr}. The solution for this large Rayleigh number is no longer periodic, but chaotic. The dominant frequency, $fH/(g\beta\Delta TH)^{1/2}$, in this unsteady solution is about 0.2−0.25, which is still close to the frequency at Ra_{cr}.

As will be shown in the next section, the instability in the case of adiabatic horizontal walls is delayed until $Ra_{cr}=1.7\times10^8$ for air and until $Ra_{cr}\sim10^{10}$ for water. In order to interpret the nature of the instability in the case of conducting horizontal walls we have compared the steady solution for air at $Ra=10^6$ with the solution for adiabatic horizontal walls at the same Rayleigh number: figure 5.4 shows the streamlines and the isotherms, whereas figure 5.5 compares the velocity at half the cavity height and the temperature at half the cavity width. (The streamlines and isotherms at $Ra=10^6$ for the adiabatic case were already shown in the figures 4.1a and 4.2). $Ra=10^6$ is just below the critical Rayleigh number for air in the conducting case. Both the conducting and the adiabatic solutions show boundary layers along the vertical walls and a stably stratified core. In these regions the solutions only slightly deviate. For example, the velocity maximum at half the cavity height ($v_{max}/(g\beta\Delta TH)^{1/2}$) is 0.304 in the conducting case and 0.263 in the adiabatic case, and the temperature gradient in the cavity centre (S) is 0.71 in the conducting case and 0.92 in the adiabatic case. The main difference is found along the horizontal walls: in the conducting case the temperature decreases with the height in the layer along the horizontal walls. The broken line in figure 5.4b, having $\partial T/\partial y=0$, indicates up to where this unstable layer extends. In the

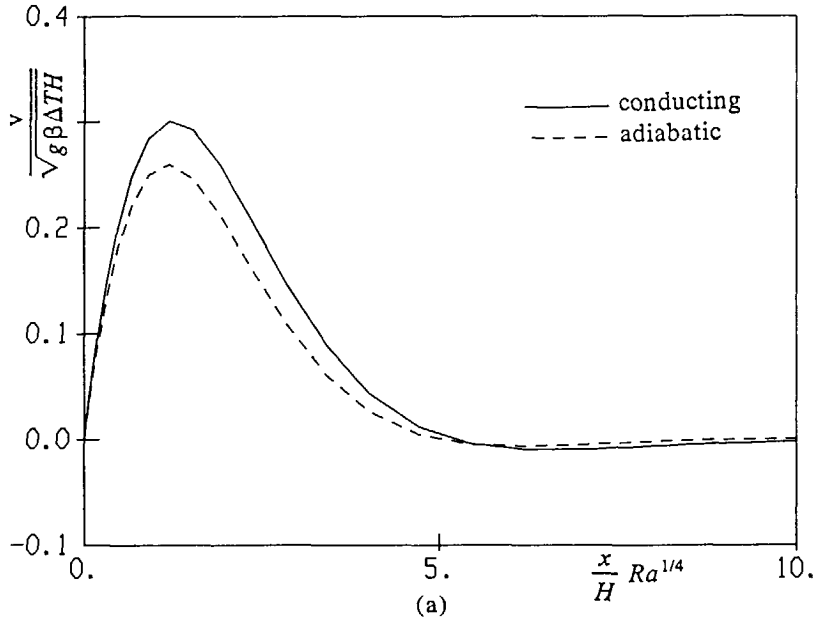

(a)

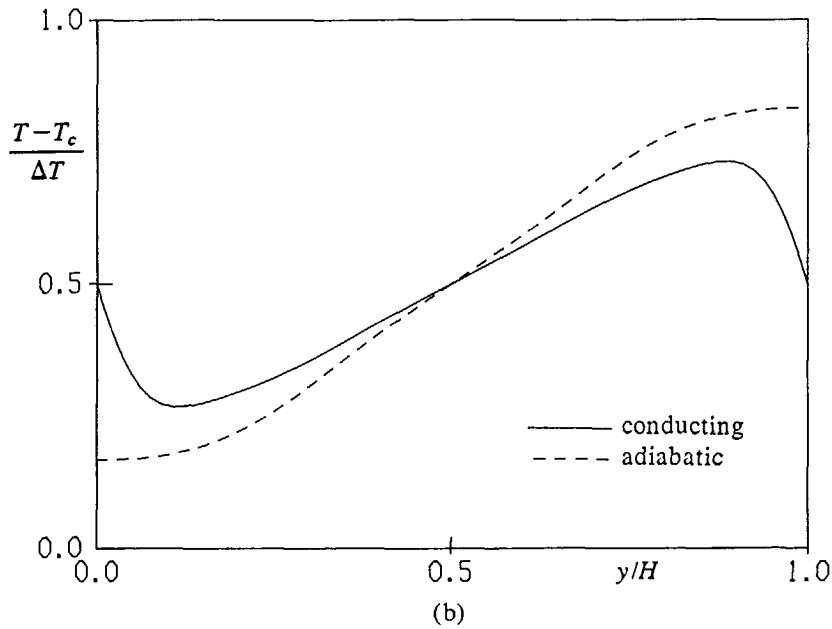

(b)

FIGURE 5.5. Steady flow for air at $Ra=10^6$; (a) vertical velocity at $y=H/2$, (b) temperature at $x=H/2$.

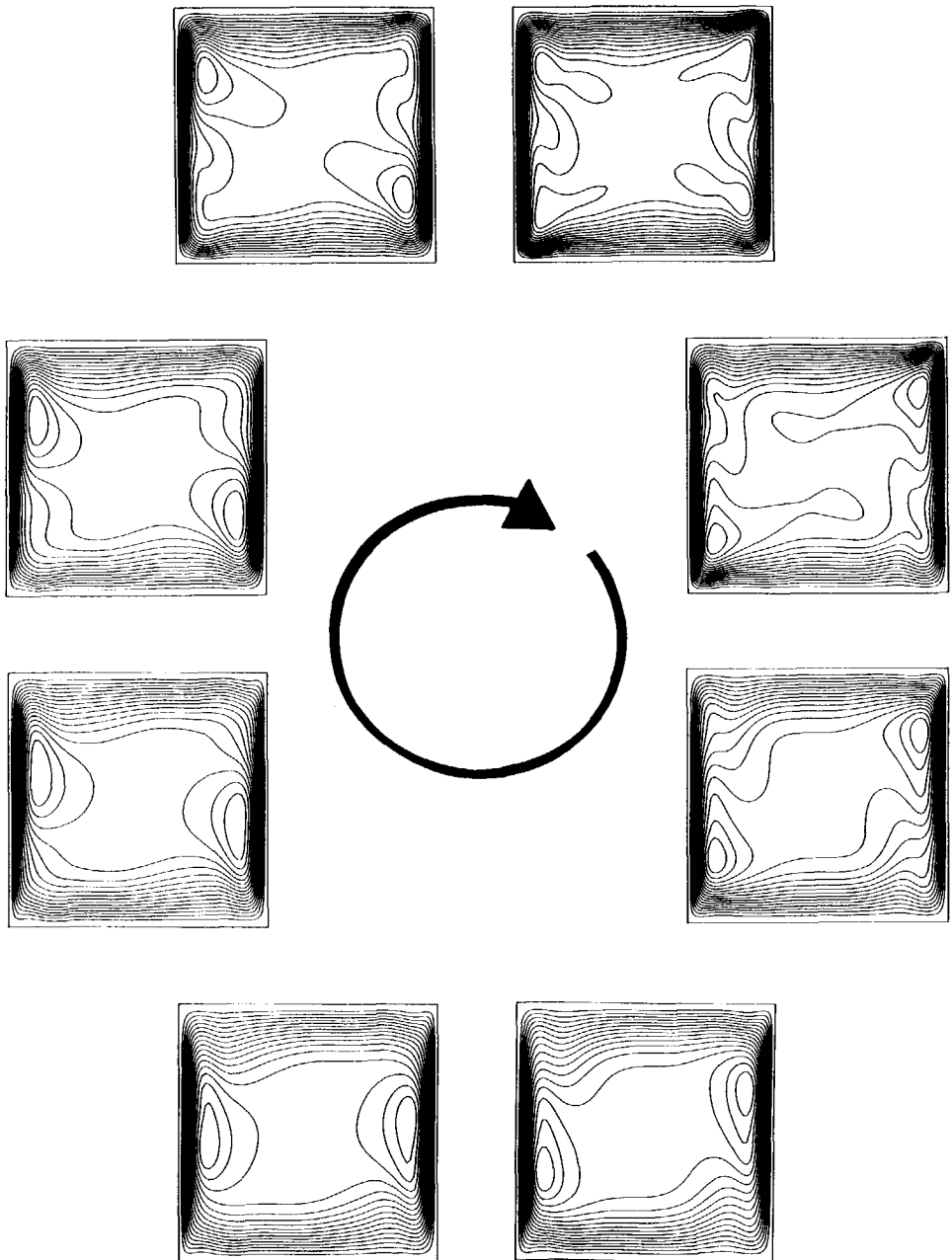

(a)

FIGURE 5.6(a). For caption see facing page.

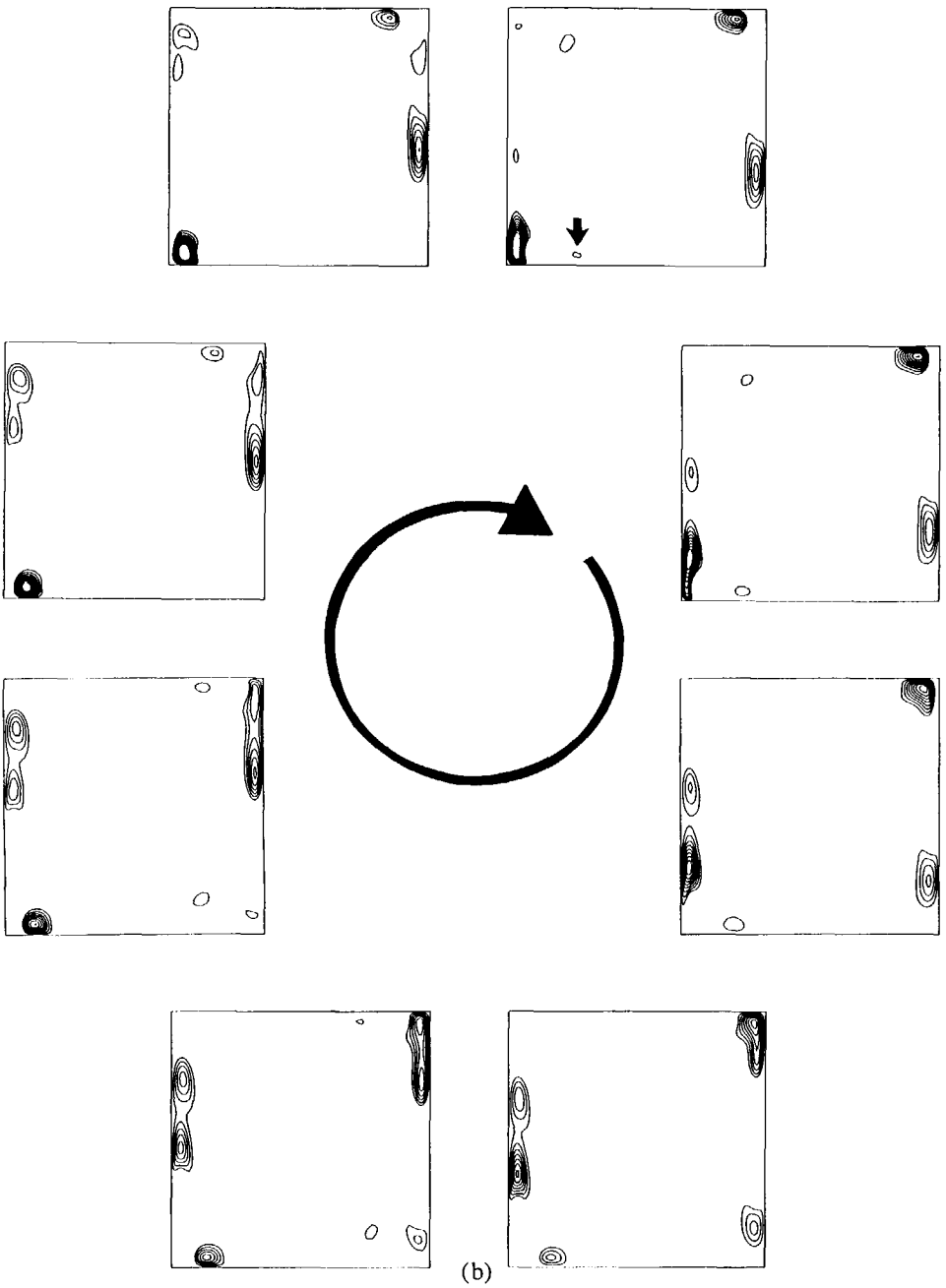

(b)

FIGURE 5.6. Limit cycle for water at $Ra = 6 \times 10^6$ in the case of conducting horizontal walls; (a) streamlines, (b) perturbation in the temperature.

adiabatic case this line coincides with the horizontal wall. As explained in section 5.5, viscosity can stabilize this unstable temperature up to a critical Rayleigh number. The maximum local Rayleigh number at the broken line (based on the local temperature difference with the $T(x)$ temperature at the floor and based on the local height) is 6.1×10^3 for air (and 6.0×10^3 for water at $Ra=4\times10^6$). This maximum is indicated with a dot in figure 5.4b. This value is in order of magnitude comparable to 1708, which is the critical Rayleigh number for the infinite horizontal fluid layer heated from below. If, instead of the maximum in the Rayleigh number, the averaged Rayleigh number on the line is compared, we find $Ra=1334$ for air (and 1148 for water). Hence the averaged Rayleigh number is even closer to 1708 than the maximum Rayleigh number. This agreement suggests that the instability in the cavity with conducting horizontal walls is related to the Rayleigh/Bénard instability in the infinite horizontal fluid layer that is heated from below. For supercritical Rayleigh numbers the frequency in the cavity scales with the Brunt-Väisälä frequency. This indicates that, although the instability seems to be introduced in the viscous horizontal layer, the selected frequency is determined by the wave mode of the inviscid core.

Once the instability has been introduced the unsteady physics can be examined from the evolution of the streamlines and the isotherms in figure 5.6. The figure shows time-lapse pictures after 8 equidistant time intervals. In the first picture, in the right upper corner of figure 5.6a, a vortex is found close to the floor at the outer edge of the vertical boundary layer along the hot wall. During the cycle the vortex rises along the outer edge of the vertical boundary layer. Finally the vortex reaches the ceiling, where it is mixed up with the horizontal layer. Figure 5.6b shows the circulation of small regions (spots) with a locally higher or lower temperature. This figure follows the perturbation in the isotherms, *i.e.* it considers the instantaneous temperature after subtraction of the averaged temperature during the cycle. Only the hot spots are shown; because the flow remains centrosymmetric during the cycle, the cold spots are positioned diagonally opposite to the hot spots. The vertical boundary layer contains both hot *and* cold spots. The position of the instability is indicated with an arrow in the right upper picture: we see the birth of a hot spot. If the reader follows this spot through the sequence of pictures, it can be checked that the spot disappears in the left upper corner after about 2.5 cycles. The instability generates alternating hot and cold spots, which are convected by the vertical boundary layers. A clockwise circulation of hot and cold spots results. The same physics are found for both air and water.

5.7. Adiabatic horizontal walls

The stability for air in cavities with adiabatic horizontal walls and an aspect ratio A (=height-width ratio) in the range 4 to 10 has been calculated by Le Quéré & Alziary de Roquefort (1985). They used a spectral method to discretize the unsteady Navier-Stokes equations. They calculated that the critical Rayleigh number (based on the cavity height) is almost independent of the aspect ratio, namely $Ra_{cr}\sim10^8$. The frequency increases from $fH/(g\beta\Delta TH)^{1/2}=0.478$ at $A=4$ to 0.847 at $A=10$. Further, the frequency for supercritical Rayleigh numbers in a cavity with a given aspect ratio is almost independent of the Rayleigh number if it

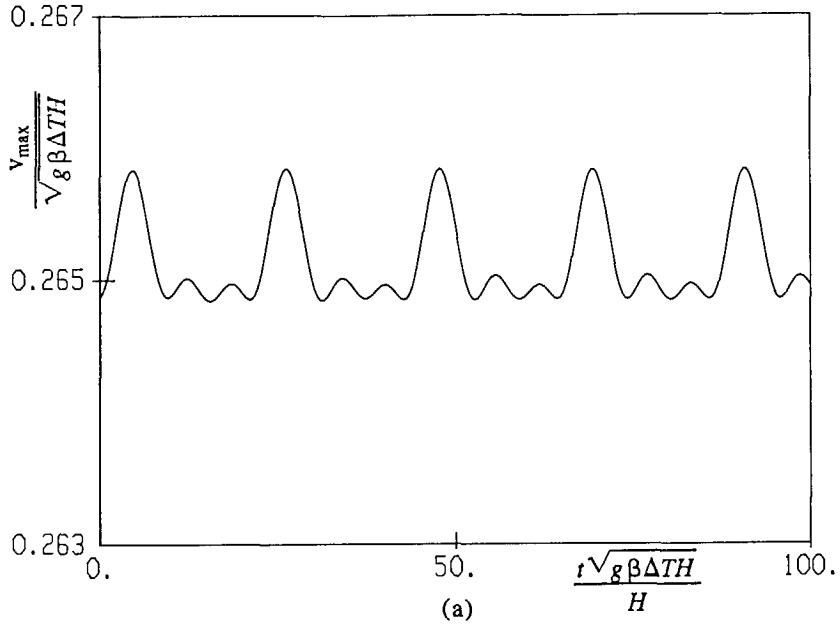

FIGURE 5.7(a). For caption see next page.

is scaled with the Brunt-Väisälä frequency. Le Quéré & Penot (1987) have verified the calculated stability for air in the $A=4$ cavity experimentally. The boundary conditions along the horizontal walls in the experiment were not clearly known, but were expected to be somewhere between the conducting case and the adiabatic case. They measured $Ra_{cr}=1.1\times10^8$ with $fH/(g\beta\Delta TH)^{1/2}=0.522$, which reasonably agrees with their calculations ($Ra_{cr}=4.5\times10^7$ with $fH/(g\beta\Delta TH)^{1/2}=0.578$ for the conducting case, and $Ra_{cr}=1.1\times10^8$ with $fH/(g\beta\Delta TH)^{1/2}=0.478$ for the adiabatic case). When the calculations for air in the square cavity in the present study were under way, Paolucci & Chenoweth (1989) published their stability results for air in the cavity for the aspect ratios $A=0.5$, 1, 2 and 3. They used a finite-difference method on a staggered grid to discretize the unsteady Navier-Stokes equations.

We have calculated the stability for air in the square cavity ($A=1$) with adiabatic horizontal walls by performing unsteady calculations in the Rayleigh-number range 10^8-10^9. The flow at $Ra=10^8$ converges to a steady state. As described in the previous chapter, the steady large-Rayleigh-number flow shows thin boundary layers along the vertical walls, and an almost stagnant, thermally stratified core. In line with the theory of Patterson & Imberger (1980), this large-Rayleigh-number flow reaches its steady state in an oscillatory way. The damped oscillations are internal gravity waves in the core. We calculate that these waves have a frequency $fH/(g\beta\Delta TH)^{1/2}=0.107$, which is almost independent of the Rayleigh number if it is scaled with the Brunt-Väisälä frequency. When the Rayleigh number is increased above 10^8, the flow no longer reaches a steady state at $Ra=1.75\times10^8$.

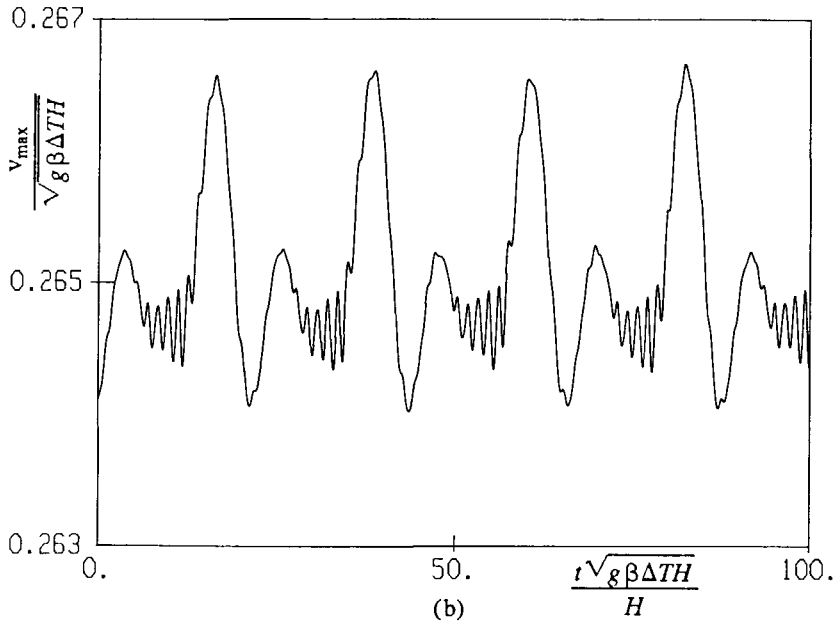

(b)

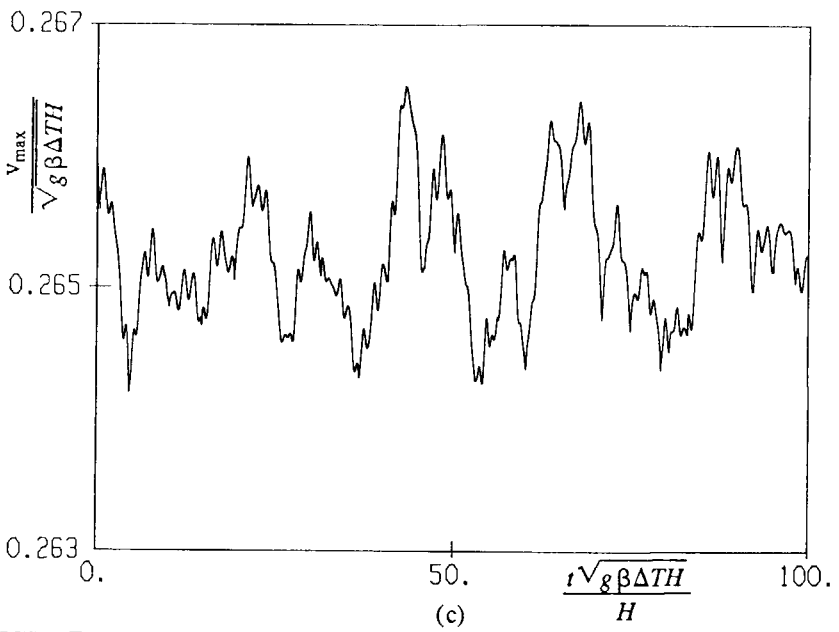

(c)

FIGURE 5.7. Large-time behaviour of the vertical velocity maximum at $y=H/2$ for air in the case of adiabatic horizontal walls; (a) $Ra=2\times10^8$, (b) $Ra=3\times10^8$, (c) $Ra=4\times10^8$.

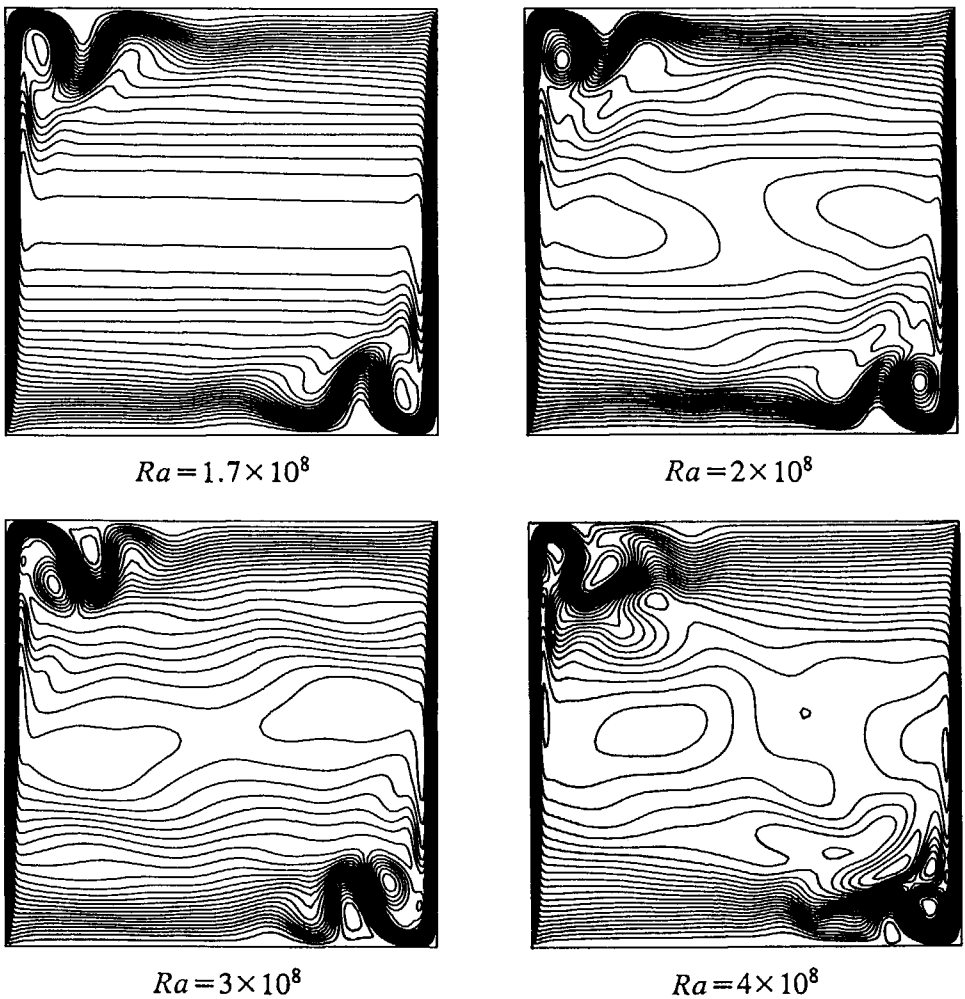

FIGURE 5.8. Streamlines for air in the case of adiabatic horizontal walls.

A Hopf bifurcation occurs at $1.7\times10^8<Ra_{cr,1}<1.75\times10^8$. At $Ra_{cr,1}$ the flow becomes periodic with a frequency $f_1H/(g\beta\Delta TH)^{1/2}=0.0488$. The periodicity in the vertical velocity maximum at half the cavity height at $Ra=2\times10^8$ is shown in figure 5.7a. If the Rayleigh number is further increased a second instability is found at $2\times10^8<Ra_{cr,2}<2.25\times10^8$. The large-time solution for the velocity maximum at $Ra=3\times10^8$ is shown in figure 5.7b. At $Ra_{cr,2}$ the flow becomes quasi-periodic, in which the higher frequency $f_2H/(g\beta\Delta TH)^{1/2}=0.590$ is added to the lower frequency. The values of the two frequencies in this solution were derived directly from the time-dependent solution. The frequencies could have been determined more accurately as the spikes in the Fourier-transformed spectrum of the

TABLE 5.3. Bifurcation for air in the case of adiabatic horizontal walls.

(a) critical Rayleigh number

study	$Ra_{cr,1}$	$Ra_{cr,2}$
present:		
40×40 grid	$2\times10^8-2.25\times10^8$	$2.25\times10^8-2.5\times10^8$
60×60 grid	$1.6\times10^8-1.7\times10^8$	$2.25\times10^8-2.5\times10^8$
80×80 grid	$1.6\times10^8-1.7\times10^8$	$2\times10^8-2.25\times10^8$
120×120 grid	$1.7\times10^8-1.75\times10^8$	$2\times10^8-2.25\times10^8$
Paolucci & Chenoweth (1989)	1.93×10^8	2.55×10^8

(b) frequency and amplitude at $Ra=3\times10^8$

study	$\frac{f_1 H}{\sqrt{g\beta\Delta T H}}$	$\frac{f_2 H}{\sqrt{g\beta\Delta T H}}$	$\frac{\delta_{u\max}}{(g\beta\Delta T\nu)^{1/3}}$
present:			
40×40 grid	0.0223	0.665	0.0398
60×60 grid	0.0385	0.543	0.129
80×80 grid	0.0378	0.594	0.169
120×120 grid	0.0453	0.625	0.264
Paolucci & Chenoweth (1989)	0.0505	0.607	--

solution. As illustrated in figure 5.7c for $Ra=4\times10^8$, increasing the Rayleigh number above $Ra=3\times10^8$ breaks the quasi-periodicity and gives a chaotic solution. Figure 5.8 shows some instantaneous streamline patterns from the large-time solution at different Rayleigh numbers. At $Ra=1.7\times10^8$ the steady core has horizontal streamlines. If the Rayleigh number is increased a wavy pattern is found in the core and in the horizontal layers. In the chaotic solution at $Ra=4\times10^8$ the centro symmetry has been broken.

By time-step refinement the time step $\Delta t(g\beta\Delta TH)^{1/2}/H=1/32$ was checked to give almost time-step-independent results. The spatial accuracy is studied by refining the grid up to 120×120 grid points. In table 5.3 the critical Rayleigh numbers as well as the frequencies and the amplitude at $Ra=3\times10^8$ are summarized for different grids. The critical Rayleigh numbers only slightly depend on the grid used, and the values closely agree with the results of Paolucci & Chenoweth (1989). Also the higher frequency (f_2) only weakly depends on the grid and the value at the finest grids is close to the calculation of Paolucci & Chenoweth. The lower frequency (f_1) shows a larger grid dependence. The lower frequency at our 120×120 grid differs by 10% with the frequency of Paolucci & Chenoweth, who also used a 120×120 grid. The amplitude of the oscillation is even still largely

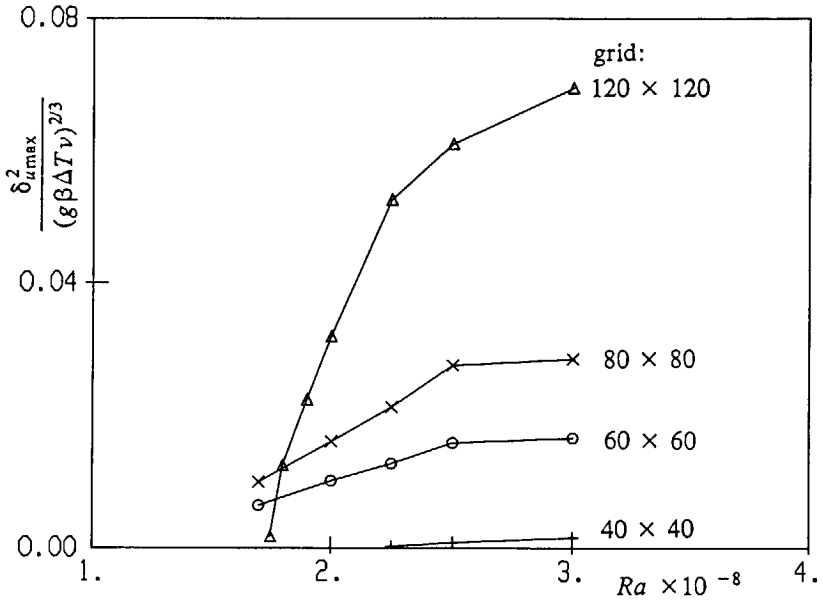

FIGURE 5.9. Grid dependence of the amplitude in the oscillation for air in the case of adiabatic horizontal walls.

grid dependent on our finest grid. Because Paolucci & Chenoweth do not give results for different grids, we cannot say whether their or our 120×120-grid solution is more accurate. From table 5.3 we conclude that further grid refinement is required as far as the amplitude is concerned, whereas the critical Rayleigh numbers and frequencies do not need further grid refinement.

We have plotted δ^2 for $u_{\max}$ *vs* the Rayleigh number at different grids in figure 5.9. Hysteresis was found on the 60×60 and 80×80 grids up to $Ra \sim 2.5\times10^8$: if the Rayleigh number was increased the solution did not give the lower frequency, which was found when the Rayleigh number was decreased. In contrast to the expectation, the amplitude for the 60×60 and 80×80 grids in figure 5.9 does not gradually decrease to zero when the Rayleigh number is decreased below $Ra=1.7\times10^8$: the amplitude abruptly becomes zero and always gives a steady solution. Therefore the 60×60 and 80×80 grids do not describe the Hopf bifurcation very accurately. The 40×40 and 120×120 grids do not show hysteresis, and the amplitude smoothly vanishes for $Ra \downarrow Ra_{cr}$. If the first bifurcation is indeed a Hopf bifurcation a straight line has to be found in the δ^2-Ra curve sufficiently close to Ra_{cr}. With reasonable accuracy this indeed is the case for all grids. From the results on the finest grid we conclude that the first bifurcation is a Hopf bifurcation. Paolucci & Chenoweth draw the same conclusion.

The large-time behaviour of the averaged heat-transfer through the hot vertical wall and of the horizontal velocity maximum at half the cavity height are shown in figure 5.10 for air at $Ra=3\times10^8$. Nu and $v_{\max}$ show both the lower and

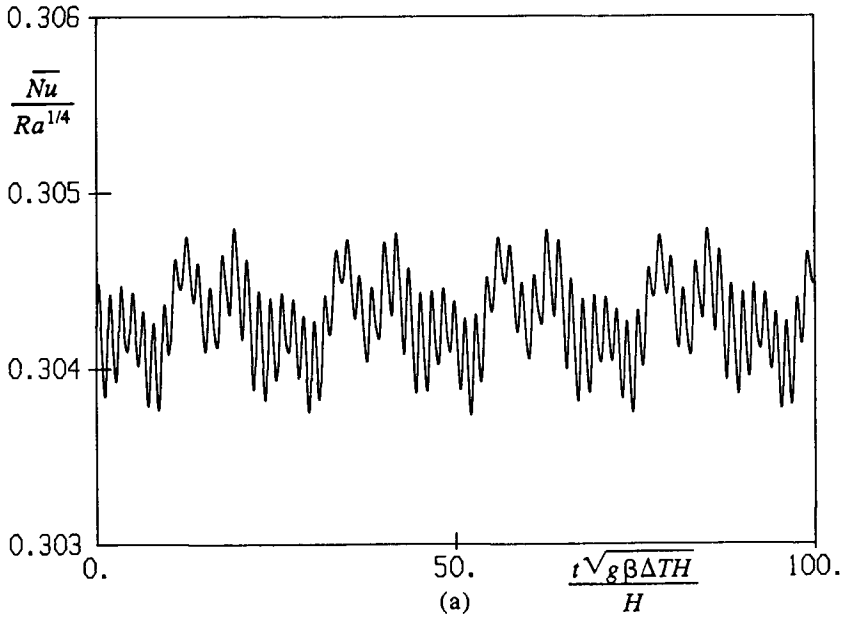

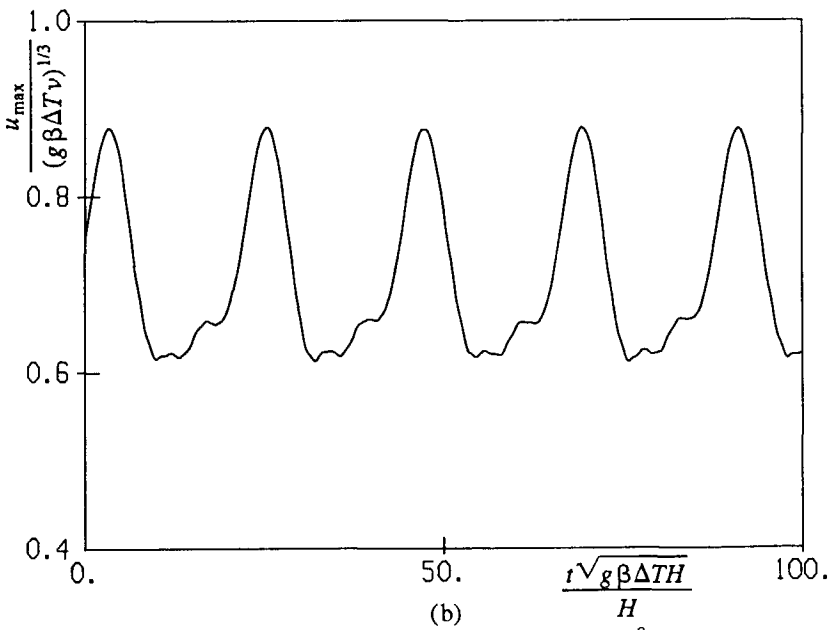

FIGURE 5.10. Large-time behaviour for air at $Ra = 3\times10^8$ in the case of adiabatic horizontal walls; (a) averaged wall-heat transfer, (b) horizontal velocity maximum at $x = H/2$.

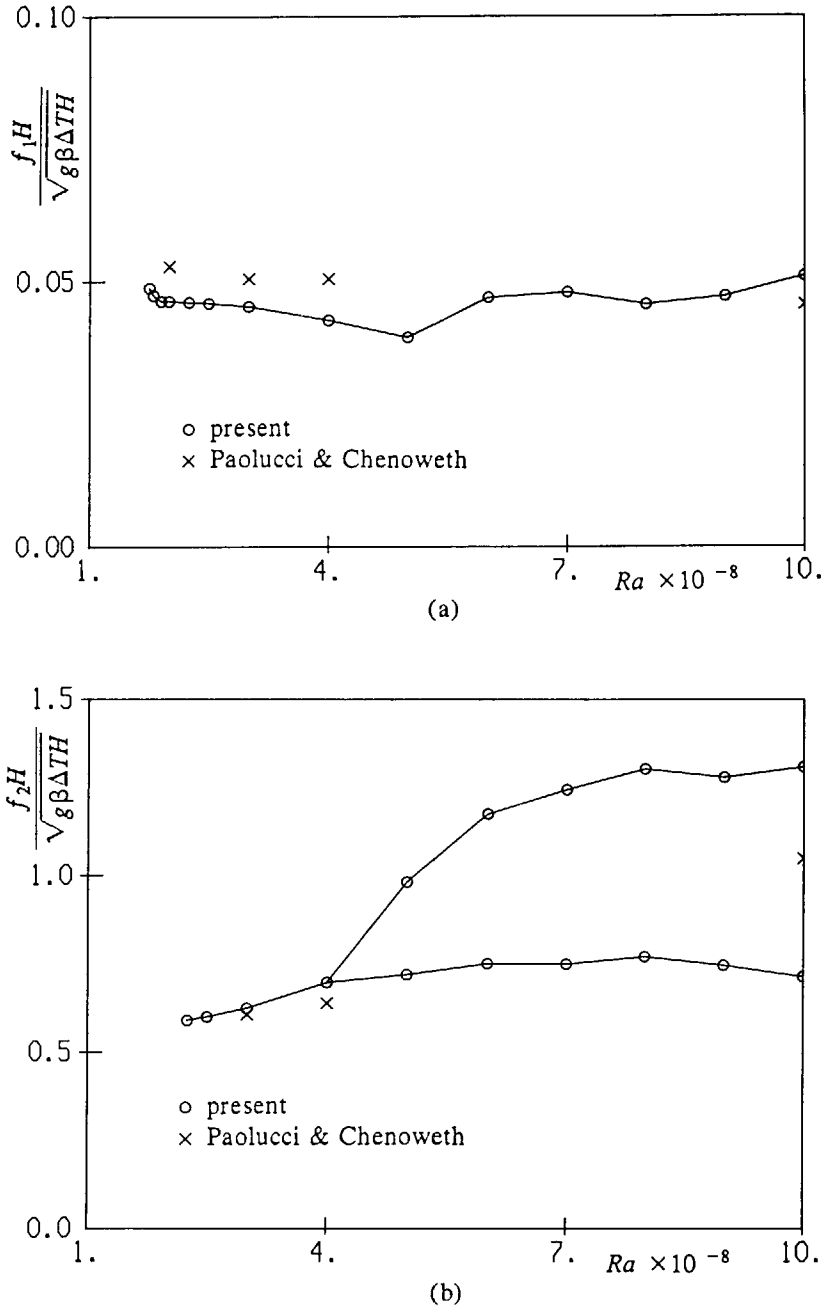

FIGURE 5.11. Frequency for air in the case of adiabatic horizontal walls; (a) lower frequency, (b) higher frequency.

higher frequency, whereas u_{max} only shows the lower frequency. Because $\overline{Nu}$ and v_{max} are quantities of the vertical boundary layer, and u_{max} is not, this suggests that the higher frequency is related to an instability in the vertical boundary layer. The lower frequency can be related to the waves in the streamline pattern in the core and in the horizontal boundary layers of the cavity (figure 5.8). Because the left upper corner shows a hydraulic jump, with a recirculation region, the lower frequency is expected to be related to an instability in the flow directly after the hydraulic jump. The lower (f_1) and higher (f_2) frequency between the critical Rayleigh numbers and $Ra=10^9$ are given in figure 5.11. Both the lower and higher frequency turn out to be almost independent of the Rayleigh number if they are scaled with the Brunt-Väisälä frequency $(g\beta\Delta TH)^{1/2}/H$. Although the solution beyond $Ra=3\times10^8$ is chaotic, it still contains a dominant frequency. The dominant frequency in the chaotic evolution of v_{max} and Nu is not equal. The upper branch in figure 5.11b gives the frequency for v_{max} and the lower branch gives the frequency for Nu; for the largest Rayleigh numbers the dominant frequency for v_{max} is about twice the dominant frequency for Nu. It is remarkable that the dominant frequency, scaled with $(g\beta\Delta TH)^{1/2}/H$, for Nu remains close to the f_2 frequency as calculated directly beyond the second bifurcation. Because Nu represents an averaged quantity, this suggests that the averaged structures in the chaotic solution do not differ very much from the structure in the quasi-periodic solution.

Ivey (1984) performed experiments for the unsteady flow of water in the heated square cavity with adiabatic horizontal walls up to $Ra=1.2\times10^9$. For these Rayleigh numbers he finds an evolution to a steady state. Ivey starts with a flow in rest and suddenly switches on the temperature difference over the vertical walls at $t=0$. The initial phase of the evolution shows oscillations, which finally are damped. The flow visualization shows that these oscillations are initiated in the left upper corner of the cavity, where the hot vertical boundary layer turns to a horizontal layer. During the evolution a hydraulic jump is found in the corner. The released jump energy is dissipated via damped oscillations in the flow beyond the jump. It is emphasized that the hydraulic jump for water at $Ra=1.2\times10^9$ appears only in the initial phase of the evolution, but is absent in the steady final state. Numerical stability studies for the case with water, however, are not reported in the literature.

We have calculated the stability for water by performing unsteady calculations in the Rayleigh number range 10^9-10^{11}. In contrast with Ivey's experiments, the time evolution for a certain Rayleigh number was initiated with the large-time solution for a slightly smaller Rayleigh number. For $Ra=10^9$ we calculate that the flow converges to a steady state in an oscillatory way. The damped oscillations are internal gravity waves in the core which have the frequency $fH/(g\beta\Delta TH)^{1/2}=0.088$. This frequency is almost independent of the Rayleigh number if it is scaled with the Brunt-Väisälä frequency. The steady solution does not show the hydraulic jump, which was found for air. The numerical result that the critical Rayleigh number is larger than 10^9 agrees with Ivey's experiments, who also finds a steady solution up to at least this value. When we further increased the Rayleigh number, a critical Rayleigh number was found beyond which the flow

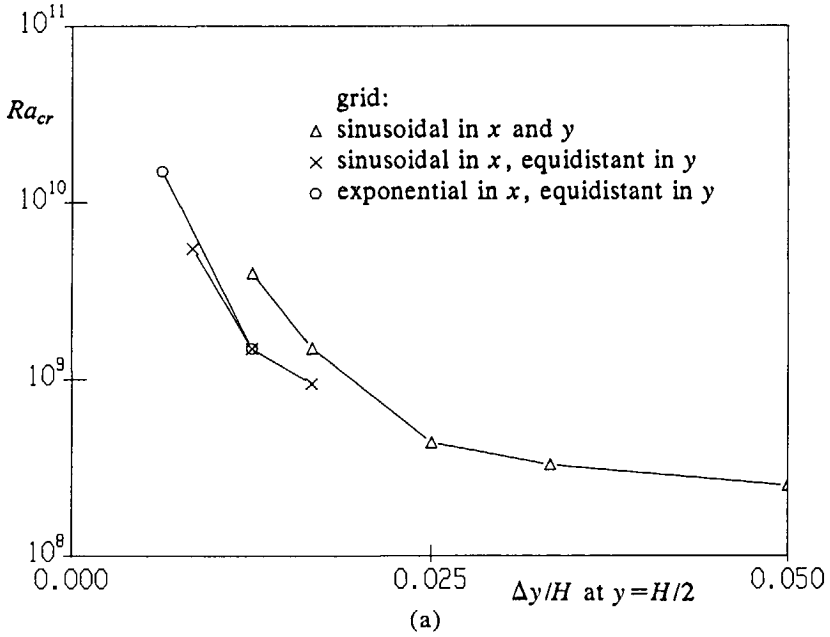

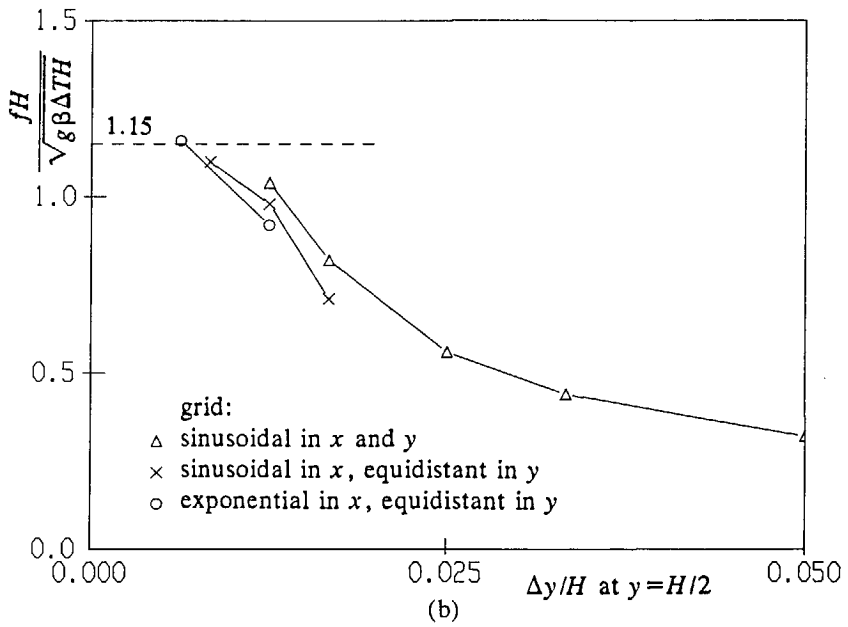

FIGURE 5.12. Grid dependence of the oscillation for water in the case of adiabatic horizontal walls; (a) critical Rayleigh number, (b) frequency.

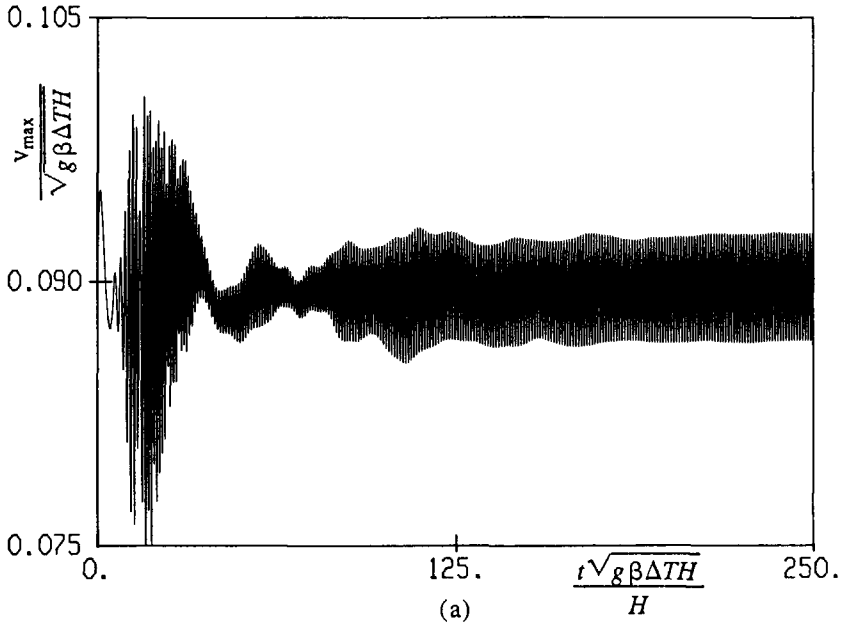

(a)

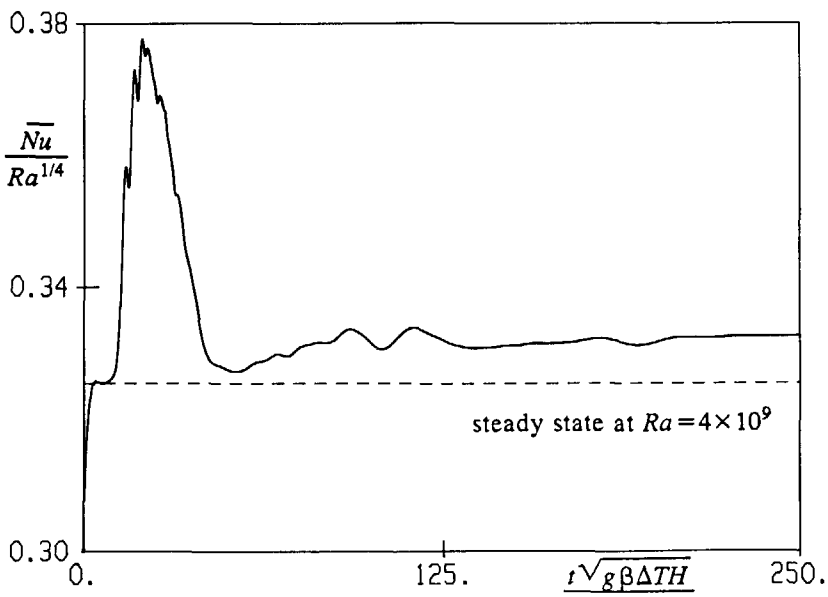

(b)

FIGURE 5.13. Time evolution for water at $Ra=5\times10^9$ in the case of adiabatic horizontal walls at the 160×160 grid, sinusoidal in both the x and y coordinates; (a) vertical velocity maximum at $y=H/2$, (b) averaged wall-heat transfer.

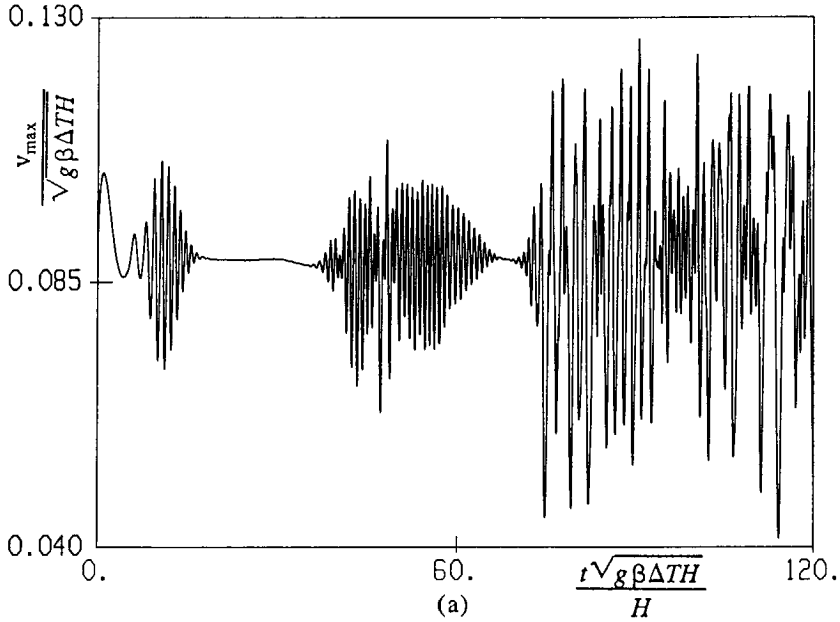

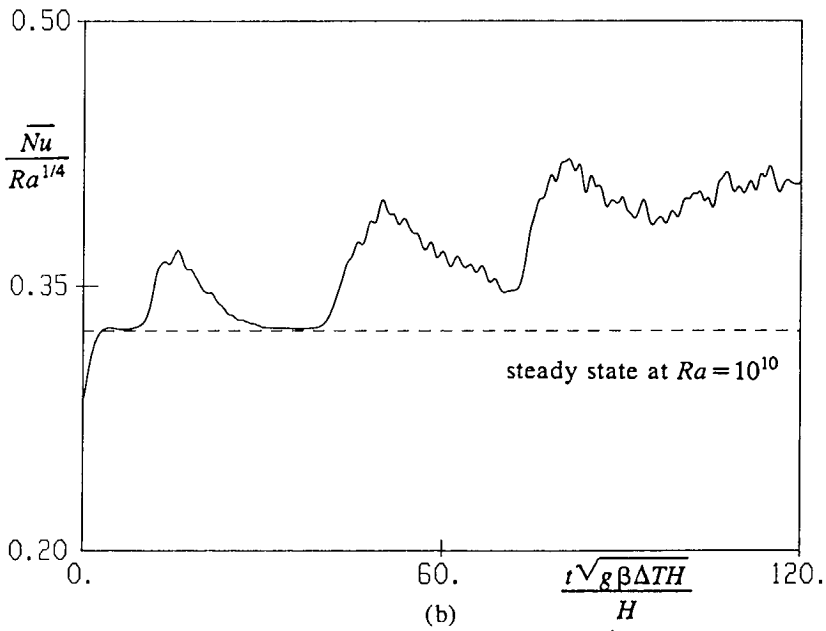

FIGURE 5.14. Time evolution for water at $Ra=2\times10^{10}$ in the case of adiabatic horizontal walls at the 80×160 grid, sinusoidal in the x and equidistant in the y coordinate; (a) vertical velocity maximum at $y=H/2$, (b) averaged wall-heat transfer.

no longer reached a steady final state. The critical Rayleigh number and frequency turns out to be very grid dependent: even the grid dependence of the results on the 160×160 grid is not negligible. Once an oscillation is found for a fixed grid, the frequency is almost independent of the Rayleigh number if it is scaled with the Brunt-Väisälä frequency.

By refining the time step we verified that the time step $\Delta t(g\beta\Delta TH)^{1/2}/H = 1/32$ gives almost time-step-independent results. The spatial accuracy is determined by refining the grid from 40×40 up to 160×160 grid points. Besides the sinusoidal grid (4.7) for the x and y coordinates, we also tried two other grid types: a type that has the sinusoidal grid (4.7) for the x-coordinate and an equidistant grid for the y-coordinate, and a type that also has an equidistant grid for the y-coordinate but uses the following exponential (tangent-hyperbolic) grid for the x-coordinate

$$\frac{x_i}{H} = \frac{1}{2}\left(1 + \frac{\tanh[\alpha_1(i/i\max - 1/2)]}{\tanh(\alpha_1/2)}\right) \qquad i = 0,1,\ldots,i\max. \tag{5.6}$$

Here α_1 follows from the expression $\alpha_2 = \alpha_1/\sinh(\alpha_1)$, in which α_2 is chosen as 0.0015. This grid gives more grid points in the vertical boundary layers than the sinusoidal grid. Figure 5.12 gives the critical Rayleigh number and frequency as calculated at the different grids. As shown in figure 5.13a, the use of the sinusoidal grid for x and y gives a periodic solution beyond Ra_{cr} for large time. The oscillation is only visible in v_{max} (figure 5.13a), but not in Nu (figure 5.13b) and not in u_{max}, which both show a time-independent behaviour for large time. This suggests that the oscillation is due to an instability in the vertical boundary layer. The frequency of the oscillation increases from $fH/(g\beta\Delta TH)^{1/2} = 0.32$ at the 40×40 grid to 1.04 at the 160×160 grid, whereas the critical Rayleigh number increases from 2.5×10^8 to 4×10^9. The $Ra-\delta^2$ curve for the oscillation at this type of grid (not shown here) is a straight line closely beyond Ra_{cr}, which indicates that a Hopf bifurcation is calculated. The averaged wall-heat transfer itself at this grid type remains time-independent at supercritical Rayleigh numbers, but figure 5.13b shows that $Nu\ Ra^{-1/4}$ for supercritical Rayleigh numbers is larger than for the steady solution below Ra_{cr}. Up to the largest Rayleigh number for which the unsteady calculations were performed (10^{11}) the unsteady solution for large time never showed the lower frequency which was found for air. Because the solution for water does not show the hydraulic jump, which occurred for air, the absence of the lower frequency supports the assumption that the lower frequency for air is related to an instability in the flow after the hydraulic jump. The two grid types which use an equidistant grid for the y-coordinate do *not* give a periodic solution for supercritical Rayleigh numbers. Just below Ra_{cr} the solution at the equidistant y-grids reaches the steady state after a long evolution with intermittency: during finite time intervals the solution oscillates with a single frequency. This frequency was used in figure 5.12b. As shown in figure 5.14a, slightly beyond Ra_{cr} the initial phase of the time evolution also shows intermittency until the solution suddenly becomes chaotic. If the time evolution for the averaged wall-heat transfer in figure 5.14b is compared with the evolution for the maximum vertical velocity in figure 5.14a, we see that $Nu\ Ra^{-1/4}$ falls back to a level close to the steady

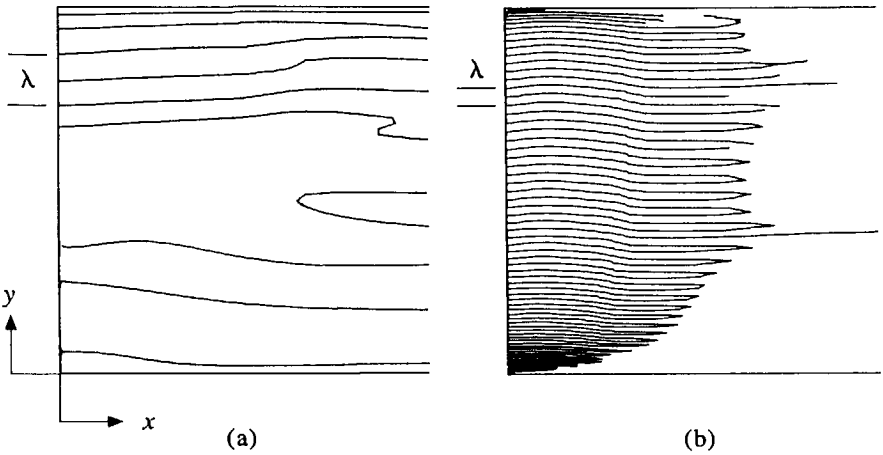

FIGURE 5.15. Traveling temperature waves in the vertical boundary layer along the hot cavity wall (the boundary layer is 20 times enlarged in the x-direction); (a) air at $Ra=3\times10^8$, (b) water at $Ra=5\times10^9$.

solution for subcritical Rayleigh numbers during the time interval that the oscillation in v_{max} is absent. As soon as the solution for v_{max} becomes chaotic, also the averaged wall-heat transfer considerably increases, but it becomes almost time-independent for large time. This clearly illustrates that time fluctuations in the velocity and temperature field lead to an increase of the averaged wall-heat transfer. From figure 5.12 we conclude that further grid refinement (or a better distribution of grid points) is required to calculate the critical Rayleigh number and frequency for water in the case of adiabatic horizontal walls. This can also answer whether the first bifurcation is a Hopf bifurcation or whether it leads to intermittency. Up to now the results at our finest grids approximately give $Ra_{cr}=10^{10}$ with $fH/(g\beta\Delta TH)^{1/2}=1.15$.

It turns out that much more grid points are required for water than for air. The number of grid points required is determined by the wave length of the spatial waves which are introduced by the instability; figure 5.15 shows that the wave length in the vertical boundary layer, which is 20 times enlarged in the x-direction in the figure, is larger for water than for air. This figure gives the lines of zero temperature perturbation for air at $Ra=3\times10^8$ (120×120 grid) and for water at $Ra=5\times10^9$ (160×160 grid, sinusoidal in x and y). The temperature perturbation is defined as the instantaneous temperature minus the averaged temperature during a time oscillation (for air the time averaging was performed over the period of one higher-frequency oscillation, and not over the period of the lower frequency). The zero-perturbation lines give the boundaries of alternating hot and cold spots in the vertical boundary layer. A hot and cold spot together give one wave length. We checked that the zero-perturbation lines at $y>H/2$ are moving upward, which

shows that the instability leads to traveling waves in the vertical boundary layer. The wave speed at $y=0.75H$ is $0.086(g\beta\Delta TH)^{1/2}$ for air and $0.052(g\beta\Delta TH)^{1/2}$ for water. Combining the wave speed (v_{wave}) with the frequency ($(fH/(g\beta\Delta TH)^{1/2}=0.625$ for air and 1.04 for water) gives the wave length ($\lambda=v_{wave}/f$); $\lambda=0.14\,H$ for air and $\lambda=0.05\,H$ for water. These wave lengths are indeed close to the distance between two zero-perturbation lines as indicated in figure 5.15b. One wave length in the figure approximately contains 17 grid points for air, but only 8 for water. At $y<H/2$ the wave length for water in the figure is smaller than for $y>H/2$. Close to $y=0$ the wave length is only twice the grid size, which indicates that the waves close to the leading edge of the vertical boundary layer are not physical waves, but numerical wiggles in the central scheme.

The appearance of traveling waves in the vertical boundary layer of the cavity strongly supports the belief that the instability in the cavity with adiabatic horizontal walls is related to the Tollmien-Schlichting instability in the vertical boundary layer along the hot vertical plate (see section 5.5). The cavity results are added to the summary of existing theoretical and experimental stability results for the plate in table 5.1. The calculated frequencies for air and water in the cavity are reasonably close to the theoretical stability results for the plate. The wave length for water in the cavity is also close to the theoretical wave lengths for the plate, but the wave length for air in the cavity is considerably lower than the plate results. Paolucci & Chenoweth (1989) have compared Ra_{cr} for air in the cavity with the result of Gill & Davey for the plate in a stratified environment. Paolucci & Chenoweth used the stratification gradient $S=1.0$ (which is practically the same as our value $S=0.99$ in table 4.3) in Gill & Davey's expression for Ra_{cr}. This gives $Ra_{cr}=1.13\times10^8$, which is close to the calculated critical Rayleigh number for air in the cavity. We can make the same comparison for water, and substitute $S=0.55$ (see table 4.3) in Gill & Davey's expression for Ra_{cr}. The value $Ra_{cr}=3.7\times10^7$ is found, which is considerably below the calculated critical Rayleigh number for water in the cavity. A remarkable difference between the oscillation in the boundary layer along the heated cavity wall with the stratified core environment and the oscillation in the boundary layer along the heated vertical plate in the isothermal environment (Gebhart & Mahajan, 1975) is that the oscillation for the cavity scales with $(g\beta\Delta TH)^{1/2}/H$, whereas the oscillation for the plate scales with $(g\beta\Delta T)^{2/3}/\nu^{1/3}$. The former is an inviscid scale, but the latter is viscous scale. Hence, although the instability in the cavity seems to be initiated by an unstable viscous Tollmien-Schlichting wave as for the plate configuration, the selected frequency at supercritical Rayleigh numbers is determined by the wave mode of the inviscid core.

5.8. Conclusion

By numerically solving the unsteady, two-dimensional Navier-Stokes equations, we have calculated the stability of the steady laminar natural-convection flow of air ($Pr=0.71$) and water ($Pr=7.0$) in a square cavity that is differentially heated over the vertical walls.

For conducting horizontal walls, the steady flow of air and water looses its stability via a Hopf bifurcation at $Ra_{cr}=2.1\times10^6$ and 5.1×10^6 respectively. At

supercritical Rayleigh numbers the unsteady flow is periodic with a frequency $fH/(g\beta\Delta TH)^{1/2}=0.248$ for air and 0.158 for water. The steady solution at subcritical Rayleigh numbers shows an unstable temperature profile (the temperature decreases with the height) close to the horizontal walls. This indicates that the instability is related to the Rayleigh/Bénard instability. The frequency is almost independent of the Rayleigh number if it is scaled with the Brunt-Väisälä frequency $(g\beta\Delta TH)^{1/2}/H$.

For adiabatic horizontal walls, the steady flow of air looses its stability at $Ra_{cr}=1.7\times10^8$ via a Hopf bifurcation. Below this value the evolution to the steady state shows damped internal gravity waves in the core with a frequency $fH/(g\beta\Delta TH)^{1/2}=0.107$. Beyond Ra_{cr}, the unsteady large-time solution is periodic with the frequency $f_1H/(g\beta\Delta TH)^{1/2}=0.0488$. Slightly above the first critical Rayleigh number a second critical Rayleigh number is found at $Ra_{cr}=2.25\times10^8$. Beyond this second critical Rayleigh number the solution becomes quasi-periodic, in which the higher frequency $f_2H/(g\beta\Delta TH)^{1/2}=0.590$ is added to the lower frequency. The lower frequency which appears most clearly in the core and in the horizontal layers, seems to be related to an instability in the flow after the hydraulic jump in the corner. The higher frequency, which corresponds to traveling waves in the natural-convection boundary layer along the vertical walls, seems to be related to the Tollmien-Schlichting instability as found in the boundary layer along a semi-infinite hot vertical plate.

In the cavity with adiabatic horizontal walls, the solution for water at $Ra_{cr}=10^9$ reaches a steady state after internal gravity waves with a frequency $fH/(g\beta\Delta TH)^{1/2}=0.088$ have been damped. A bifurcation to an unsteady state is found at a larger Rayleigh number, but the calculated values for the critical Rayleigh number and frequency show grid dependence even on our finest 160×160 grid. Moreover the use of a sinusoidal grid in the y-coordinate gives a Hopf bifurcation whereas the use of an equidistant grid in the y-coordinate leads to intermittency. The finest grids give $Ra_{cr}\sim10^{10}$ and $fH/(g\beta\Delta TH)^{1/2}\sim1.15$, but further grid refinement is required to determine these values more accurately. The frequency corresponds to traveling waves in the vertical boundary layer. In contrast to air, water does not show the hydraulic jump and no lower frequency is found. Much more grid points are required for water than for air, because the wave length of the travelling waves is smaller for water ($\lambda\sim0.05\,H$) than for air ($\lambda=0.14\,H$). The frequencies for both air and water are almost independent of the Rayleigh number when they are scaled with the Brunt-Väisälä frequency.

6. TURBULENT BOUNDARY-LAYER FLOW

6.1. Introduction

When the Rayleigh number is increased far enough the flow becomes fully turbulent. The two-equation $k-\epsilon$ model is often used to model the turbulence. The $k-\epsilon$ model is usually applied in combination with analytical wall functions for the velocity and temperature close to a fixed wall to avoid the numerical calculation of the steep gradients in the thin wall region. The wall functions also give boundary conditions for the differential equations for the turbulent kinetic energy k and the dissipation rate of turbulent kinetic energy ϵ. In many flows the use of wall functions actually is not fully justified and Launder (1984) has suggested that it might has become 'time to abandon wall functions'. In the thin wall region the turbulence level is low, and the standard $k-\epsilon$ model has to be corrected for the low-Reynolds-number effects. Different modifications, which lead to so-called low-Reynolds-number $k-\epsilon$ models, have been proposed in the literature.

To compare the performance of the different low-Reynolds-number $k-\epsilon$ models near to a wall, Patel *et al.* (1981, 1985) have solved the turbulent boundary-layer equations for the flow along a flat plate in a uniform oncoming flow, which gives a forced-convection boundary layer. In this chapter a similar comparison will be made for the flow of both air and water along a hot vertical plate placed in an isothermal environment, which gives a natural-convection boundary layer. We determine the accuracy of the models by comparison of the wall-heat transfer and the vertical velocity maximum with existing experimental data. Experimental data for the turbulent natural-convection boundary layer for air were obtained by Cheesewright (1968, 1986), Cheesewright & Ierokipiotis (1981, 1982) and Miyamoto *et al.* (1982, 1983). Furthermore, recently Tsuji & Nagano (1988a,b, 1989) accurately measured the boundary layer for air up to very close to the wall. Besides a comparison of the low-Reynolds-number $k-\epsilon$ models, also comparisons will be given for the standard $k-\epsilon$ model (which applies no low-Reynolds-number modifications) and for the well-known algebraic model of Cebeci & Smith.

When one does not want to extend the calculations up to the wall, the difficulty is that the search for wall functions for the turbulent natural-convection boundary layer along the hot vertical plate has not been completed yet in the literature. Analytically George & Capp (1979) and Cheesewright (1986; Cheesewright & Mirzai, 1988) have given some first proposals for these wall functions. George & Capp divided the boundary layer into an inner and an outer layer. The inner layer starts at the vertical wall and ends at the velocity maximum. This layer was further split into a conductive/thermo-viscous sublayer, directly touching the wall, and into a buoyant sublayer extending to the velocity maximum. They proposed a 1/3-power wall function for the velocity and a $-1/3$-power wall function for the temperature in the buoyant sublayer. A wall function (defect law) was also given in the outer layer, which extends from the velocity maximum up to the outer edge. The analysis of Cheesewright differs from the analysis of George & Capp

on some points. The form of the flow in the conductive/thermo-viscous sublayer remains unchanged. Cheesewright derived wall functions in the lower part of the outer layer (*i.e.* the fully turbulent region between the maxima of the velocity and the turbulent viscosity). These wall functions do not show the 1/3-power dependence, but have logarithmic terms. Cheesewright did not formulate a wall function for the upper part of the outer layer.

Unfortunately experimental data only exist up to an y-based Rayleigh number (Ra_y) of about 5×10^{11}, which might be too low for possible wall functions to appear. In contrast with the experimental approach, the numerical approach can easily follow the boundary-layer flow up to much larger Rayleigh numbers. Once we have determined which low-Reynolds-number models most closely predict the experimental data up to $Ra_y=10^{11}$, it is reasonable to expect these models to work well for larger Rayleigh numbers too. The calculations with the best performing low-Reynolds-number models, namely the models of Chien (1980, 1982) and Jones & Launder (1972), will be extended up to $Ra_y=10^{25}$. These large-Rayleigh-number calculations enable us to study the asymptotic behaviour of the turbulent natural-convection boundary layer. Different quantities are examined and they are fitted with asymptotic curves of the form αRa_y^{γ}. If γ becomes constant for increasing Rayleigh number the proper scaling is found. These proper scalings define the wall functions for the turbulent natural-convection boundary layer. The calculated asymptotic behaviour and the calculated wall functions are compared with the theory of George & Capp and Cheesewright.

It is known that the $k-\epsilon$ model might fail to correctly describe strongly anisotropic turbulent flows, for which it has to be replaced by a Reynolds-stress model. Because the turbulence in the boundary layer along the hot vertical plate shows anisotropy due to the boundary-layer character of the flow and due to the presence of a unidirectional volume force (gravity), this chapter will be closed with a comparison between the $k-\epsilon$ model and the Reynolds-stress model. The low-Reynolds-number modifications of Chien are applied to both models. We do not expect that the Reynolds-stress model can further improve the prediction of the mean-flow quantities in the inner layer, where turbulence is almost absent. We are mainly interested in how it predicts the turbulent quantities in the outer layer. In particular the Reynolds-stress model can answer whether the eddy-viscosity concept in the $k-\epsilon$ model holds.

6.2. Turbulent boundary-layer equations

The time-averaged, two-dimensional, turbulent boundary-layer equations under the Boussinesq approximation read

$$\begin{aligned}
&\frac{\partial u}{\partial x}+\frac{\partial \mathrm{v}}{\partial y}=0\\
&u\frac{\partial \mathrm{v}}{\partial x}+\mathrm{v}\frac{\partial \mathrm{v}}{\partial y}=-\frac{1}{\rho}\frac{dp}{dy}+g\beta(T-T_0)+\nu\frac{\partial^2 \mathrm{v}}{\partial x^2}-\frac{\partial}{\partial x}\overline{u'\mathrm{v}'} \qquad (6.1)\\
&u\frac{\partial T}{\partial x}+\mathrm{v}\frac{\partial T}{\partial y}=\frac{\nu}{Pr}\frac{\partial^2 T}{\partial x^2}-\frac{\partial}{\partial x}\overline{u'T'}.
\end{aligned}$$

The eddy-viscosity model (2.13) is used to model the Reynolds stress and the turbulent heat flux. Application of the boundary-layer simplifications gives

$$\begin{aligned} -\overline{u'v'} &= \nu_t \frac{\partial v}{\partial x} \\ -\overline{u'T'} &= \frac{\nu_t}{\sigma_T}\frac{\partial T}{\partial x}. \end{aligned} \tag{6.2}$$

The following models for the turbulent viscosity are tested:

6.2.1. *algebraic model of Cebeci & Smith*
Cebeci & Smith (1974) formulated an algebraic model to describe the turbulence in a forced-convection boundary layer. This model was slightly modified by Cebeci & Khattab (1975) for a natural-convection boundary layer:

$$\nu_t = \begin{cases} l^2|\partial v/\partial x|\,\gamma_{tr} & \text{if } x<x_c \\ (0.075\delta)^2|\partial v/\partial x|\,\gamma_{tr} & \text{if } x\geq x_c \end{cases} \tag{6.3}$$

with

$$l = \kappa x[1-\exp(-x^+/26)] \quad \text{(Van Driest length)}$$
$$\kappa = 0.41 \quad \text{(Von Karman constant)}$$
$$x^+ = \frac{x v_\tau}{\nu} \;;\; v_\tau = (\nu(\partial v/\partial x)_w)^{1/2}$$

δ is the x-position of v_{95}; $v_{95} = 0.05\, v_{max}$ (boundary-layer thickness).

x_c is chosen such that ν_t is continuous at x_c. γ_{tr} is a function to describe the transition from the laminar ($\gamma_{tr}=0$) to the turbulent ($\gamma_{tr}=1$) state. This model takes the turbulent Prandtl number for the temperature σ_T according to

$$\sigma_T = \frac{0.4\,(1-\exp(-x^+/26))}{0.44\,(1-\exp(-x^+/C^+))}$$

with

$$C^+ = \frac{1}{\sqrt{Pr}}\sum_{i=1}^{5} c_i\,(\log_{10}(Pr))^{i-1}$$

$$c_1 = 34.96,\; c_2 = 28.79,\; c_3 = 33.95,\; c_4 = 6.33,\; c_5 = -1.186.$$

6.2.2. *standard $k-\epsilon$ model*
Two differential equations are introduced to describe the kinetic energy of the turbulent velocity fluctuations k and the dissipation rate of turbulent kinetic energy ϵ (see also section 2.4). Under the boundary-layer simplifications these equations read

$$u\frac{\partial k}{\partial x} + v\frac{\partial k}{\partial y} = \frac{\partial}{\partial x}\left(\nu + \frac{\nu_t}{\sigma_k}\right)\frac{\partial k}{\partial x} + P_k + G_k - \epsilon$$

$$u\frac{\partial \epsilon}{\partial x} + v\frac{\partial \epsilon}{\partial y} = \frac{\partial}{\partial x}\left(\nu + \frac{\nu_t}{\sigma_\epsilon}\right)\frac{\partial \epsilon}{\partial x} + (c_{\epsilon 1} P_k + c_{\epsilon 1} c_{\epsilon 3} G_k - c_{\epsilon 2}\epsilon)\frac{\epsilon}{k} \quad (6.4)$$

with

$$P_k = \nu_t\left(\frac{\partial v}{\partial x}\right)^2, \; G_k = -\frac{\nu_t}{\sigma_T} g\beta\frac{\partial T}{\partial y}, \; \nu_t = c_\mu\frac{k^2}{\epsilon}.$$

As a consequence of the boundary-layer simplifications, the buoyancy-production term G_k can be neglected with respect to the shearing-production term P_k; Lin & Churchill (1978), however, retained the term to model fluids with a Prandtl number larger than 1 (water, oil), but they replaced the temperature's y-gradient by its x-gradient. In the present $k-\epsilon$ calculations for the plate G_k is omitted.

In most existing natural-convection calculations boundary conditions for k and ϵ at the wall are found from the forced-convection wall functions. It is known (see for example Cebeci & Smith, 1974) that close to a fixed wall velocity and temperature profiles in a forced-convection boundary layer, with negligible pressure gradient, can be approximated by logarithmic wall functions,

$$v^+ = \frac{1}{\kappa}\ln(9x^+) \qquad (\kappa=0.41)$$
$$T^+ = 2.195\ln(x^+) + 13.2\,Pr - 5.66 \quad (6.5)$$

with

$$x^+ = \frac{x v_\tau}{\nu}, \; v^+ = \frac{v}{v_\tau}, \; T^+ = \frac{T_w - T}{T_\tau},$$
$$v_\tau = (\nu(\partial v/\partial x)_w)^{1/2}, \; T_\tau = -\frac{\nu}{Pr\, v_\tau}\left(\frac{\partial T}{\partial x}\right)_w.$$

These wall functions can be used in the fully turbulent inertial sublayer at $x^+ > 11.5$. In the viscous sublayer close to the wall, at $x^+ < 11.5$, turbulence can be neglected. Assuming that convection and diffusion of k can be neglected in the inertial sublayer, the differential equation for k in equations (6.4) simplifies to

$$P_k = \epsilon. \quad (6.6)$$

Hence, it is assumed that there is an *equilibrium* of production and dissipation of turbulent energy in the inertial sublayer. Further, Prandtl's mixing-length model is assumed to hold:

$$\nu_t = (\kappa x)^2\frac{\partial v}{\partial x} \qquad (\kappa=0.41). \quad (6.7)$$

With the energy equilibrium (6.6), Prandtl's mixing-length model (6.7) and the expression for ν_t in the $k-\epsilon$ model (6.4), wall functions for k and ϵ are found

$$\frac{k}{v_\tau^2} = \frac{1}{c_\mu^{1/2}}$$
$$\frac{\epsilon\nu}{v_\tau^4} = \frac{1}{\kappa x^+}. \quad (6.8)$$

The wall functions (6.5) and (6.8) do *not* hold for forced-convection boundary layers with large pressure gradients, or if the condition $x^+>11.5$ is not satisfied. They also do not hold for natural-convection boundary layers. Because of lack of natural-convection wall functions for k and ϵ, turbulent natural-convection computational studies still use wall functions like (6.5) and (6.8) in the standard $k-\epsilon$ model. In the present study of the natural-convection boundary layer we do not apply the wall functions (6.5) for the velocity and the temperature. We originally only applied the wall functions (6.8) for k and ϵ. Moreover we took the first inner grid point at $x^+<11.5$; satisfying the condition $x^+>11.5$ gives unrealistic results, because $x^+=11.5$ turns out to be close to the velocity maximum in the natural-convection boundary layer (for example $x^+=41$ at the velocity maximum for $Ra_y=10^{11}$, as calculated for air with the Chien model). This kind of use of the wall functions is in line with some other natural-convection computations like those of Ozoe *et al.* (1985) and Coulter & Guceri (1985). The only difference is that these studies use wall functions for k and ϵ which are slightly different from (6.8), namely

$$\begin{aligned} k &= 0 && \text{at the wall} \\ \epsilon &= \frac{c_\mu^{3/4} k^{3/2}}{\kappa x} && \text{at the first inner gridpoint.} \end{aligned} \tag{6.9}$$

Grid refinement blows up the ϵ value at the first inner grid point in equations (6.8) and (6.9). Despite this unbounded increase of the ϵ value, we checked that grid refinement still gives the convergence to a grid-independent velocity and temperature field. For a given grid, however, the use of the ϵ wall function gives a much larger numerical error for the solution in the inner layer (for example for the wall-heat transfer) as compared to the case in which we directly set ϵ to infinity at the wall. The use of $\epsilon=\infty$ at the wall implies that replacing the wall function for k (6.8) by $k=0$ at the wall leads to identical results. Therefore in order to increase the *numerical* accuracy, we decided to replace the wall functions (6.8) in the standard $k-\epsilon$ model by the Dirichlet boundary conditions $k=0$ and $\epsilon=\infty$ at the wall. The numerical values taken for the constants in the standard $k-\epsilon$ model (6.4) are given in table 6.1, σ_T is taken as 0.9. These values are adopted from the recent literature (see for example Launder, 1988).

6.2.3. *low-Reynolds-number $k-\epsilon$ models*

The standard $k-\epsilon$ model only holds if the turbulence intensity ν_t/ν is large. A measure for the turbulence intensity is given by the turbulence-based Reynolds number, for example $Re_t=k^2/(\nu\epsilon)$. If this Reynolds number is low, for example close to a fixed wall, a modification of the standard $k-\epsilon$ model has to be applied. Low-Reynolds-number effects are modelled by the introduction of the functions f_1, f_2, f_μ, D and E:

$$\begin{aligned} u\frac{\partial k}{\partial x} + v\frac{\partial k}{\partial y} &= \frac{\partial}{\partial x}\left(\nu + \frac{\nu_t}{\sigma_k}\right)\frac{\partial k}{\partial x} + P_k - \epsilon + D \\ u\frac{\partial \epsilon}{\partial x} + v\frac{\partial \epsilon}{\partial y} &= \frac{\partial}{\partial x}\left(\nu + \frac{\nu_t}{\sigma_\epsilon}\right)\frac{\partial \epsilon}{\partial x} + (c_{\epsilon 1} f_1 P_k - c_{\epsilon 2} f_2 \epsilon)\frac{\epsilon}{k} + E \end{aligned} \tag{6.10}$$

TABLE 6.1. Constants and functions in the low-Reynolds-number $k-\epsilon$ models.

model	ϵ_w	c_μ	$c_{\epsilon 1}$	$c_{\epsilon 2}$	σ_k	σ_ϵ	f_μ	f_1	f_2	D	E
standard $k-\epsilon$	∞	0.09	1.44	1.92	1.0	1.3	1.0	1.0	1.0	0.	0.
To & Humphrey	$\epsilon = 2\nu\left(\frac{\partial\sqrt{k}}{\partial x}\right)^2$	0.09	1.44	1.92	1.0	1.3	$\exp\left(\frac{-2.5}{1+Re_t/50}\right)$	1.0	$(1-0.3\exp(-Re_t^2))\, f_3$	0.	0.
									$f_3 = \begin{cases} 1 & \text{if } x^+ \geq 5 \\ 1-\exp(-Re_t^2) & \text{if } x^+ < 5 \end{cases}$		
Lam & Bremhorst (Dirichlet)	$\epsilon = \nu\frac{\partial^2 k}{\partial x^2}$	0.09	1.44	1.92	1.0	1.3	$(1-\exp(-0.0165Re_k))^2(1+20.5/Re_t)$	$1+\left(\frac{0.05}{f_\mu}\right)^3$	$1-\exp(-Re_t^2)$	0.	0.
Lam & Bremhorst (Neumann)	$\frac{\partial\epsilon}{\partial x} = 0$	0.09	1.44	1.92	1.0	1.3	$(1-\exp(-0.0165Re_k))^2(1+20.5/Re_t)$	$1+\left(\frac{0.05}{f_\mu}\right)^3$	$1-\exp(-Re_t^2)$	0.	0.
Chien	$\epsilon = 0$	0.09	1.35	1.8	1.0	1.3	$1-\exp(-0.0115x^+)$	1.0	$1-\frac{2}{9}\exp\left(-\left(\frac{Re_t}{6}\right)^2\right)$	$-2\nu\frac{k}{x^2}$	$-2\frac{\nu\epsilon}{x^2}\exp(-0.5x^+)$
Hassid & Poreh	$\epsilon = 0$	0.09	1.45	2.0	1.0	1.3	$1-\exp(-0.0015Re_t)$	1.0	$1-0.3\exp(-Re_t^2)$	$-2\nu\frac{k}{x^2}$	$-2\nu\left(\frac{\partial\sqrt{\epsilon}}{\partial x}\right)^2$
Reynolds	$\epsilon = \nu\frac{\partial^2 k}{\partial x^2}$	0.084	1.0	1.83	1.69	1.3	$1-\exp(-0.0198Re_k)$	1.0	$\left[1-0.3\exp\left(-\left(\frac{Re_t}{3}\right)^2\right)\right] f_\mu$	0.	0.
Hoffman	$\epsilon = 0$	0.09	1.81	2.0	2.0	3.0	$\exp\left(\frac{-1.75}{1+Re_t/50}\right)$	1.0	$1-0.3\exp(-Re_t^2)$	$-\frac{\nu}{x}\frac{\partial k}{\partial x}$	0.
Jones & Launder	$\epsilon = 0$	0.09	1.44	1.92	1.0	1.3	$\exp\left(\frac{-2.5}{1+Re_t/50}\right)$	1.0	$1-0.3\exp(-Re_t^2)$	$-2\nu\left(\frac{\partial\sqrt{k}}{\partial x}\right)^2$	$2\nu\nu_t\left(\frac{\partial^2 v}{\partial x^2}\right)^2$

$Re_k = \frac{x\sqrt{k}}{\nu}$, $Re_t = \frac{k^2}{\nu\epsilon}$, $x^+ = \frac{x v_\tau}{\nu}$

with

$$P_k = \nu_t \left(\frac{\partial v}{\partial x} \right)^2, \quad \nu_t = c_\mu f_\mu \frac{k^2}{\epsilon}.$$

The low-Reynolds-number models are summarized in table 6.1. All these models are applied with $\sigma_T = 0.9$. Most low-Reynolds-number $k-\epsilon$ models were originally developed for forced-convection boundary layers. Only the To & Humphrey (1986) model, which actually is a modified Jones & Launder model, was developed for natural-convection boundary layers. Lin & Churchill (1978) used the Jones & Launder (1972) model to calculate the natural-convection boundary layer for air.

The choice of the functions f_1, f_2, f_μ, D and E should depend on the following considerations (see also Patel *et al.* 1981, 1985):

(i) *limit for small* x. For small x, the velocity fluctuations can be expanded according to

$$\begin{aligned} u' &= b_1 x^2 + \ldots \\ v' &= a_2 x + b_2 x^2 + \ldots \\ w' &= a_3 x + b_3 x^2 + \ldots . \end{aligned} \tag{6.11}$$

With these series, the quantities k ($= \overline{u_i' u_i'} / 2$), ϵ ($= \nu \overline{\partial u_i'/\partial x_j \; \partial u_i'/\partial x_j}$) and ν_t ($= - \overline{u'v'} / (\partial v/\partial x)$) become (assuming that the turbulence is homogeneous in the y-direction)

$$\begin{aligned} k &= A x^2 + B x^3 + \ldots \\ \epsilon &= \nu (2A + 4B x + \ldots) \\ \nu_t &= \frac{- \overline{a_2 b_1} x^3 + \ldots}{(\partial v/\partial x)_w} \end{aligned} \tag{6.12}$$

with

$$A = (\overline{a_2^2} + \overline{a_3^2}) / 2, \quad B = \overline{a_2 b_2} + \overline{a_3 b_3}.$$

(ii) *D function and boundary conditions for* k *and* ϵ. Using series (6.12), the k-equation close to the wall reduces to

$$\nu \frac{\partial^2 k}{\partial x^2} - \epsilon + D = O(x^3) \tag{6.13}$$

with

$$\frac{\partial^2 k}{\partial x^2} = 2A + 6B x + \ldots .$$

All models apply $k=0$ as a wall condition, which is consistent with series expansion (6.12) for k. Not all models apply the nonzero value $\epsilon = 2\nu A$ as a boundary condition; in order to satisfy equation (6.13) for at least the $O(1)$ terms, models

applying $\epsilon_w=0$ introduce a function D. In this case the effective dissipation becomes $\epsilon-D$.

(iii) f_2 *and E functions*. Close to the wall the ϵ-equation reduces to

$$\nu\frac{\partial^2\epsilon}{\partial x^2} - c_{\epsilon 2} f_2 \frac{\epsilon^2}{k} + E = O(x). \tag{6.14}$$

The choice for f_2 and E should be such that $\partial^2\epsilon/\partial x^2=O(1)$ for small x. For example, if $E=0$ and a nonzero ϵ_w value is prescribed (implying that ϵ is $O(1)$ for small x), consistency is only found with $f_2=O(x^2)$ for small x. Some models introduce a nonzero E term, but its physical meaning is not very clear. Most models choose f_2 such that the decay of isotropic grid turbulence is modelled in agreement with experiments. These experiments show that the turbulent kinetic energy k decays as y^{-n}, with $n=1.25$ for large Re_t (*i.e.* for small y; $Re_t=k^2/(\nu\epsilon)$) and $n=2.5$ for small Re_t (*i.e.* for large y). The decay is described by

$$\begin{aligned}\frac{\partial k}{\partial y} &= -\epsilon \\ \frac{\partial \epsilon}{\partial y} &= -c_{\epsilon 2} f_2 \frac{\epsilon^2}{k}\end{aligned} \tag{6.15}$$

Substitution of $k=c_1 y^{-n}$ and $\epsilon=c_2 y^{-m}$ into equations (6.14) leads to

$$c_{\epsilon 2} f_2 = \frac{n+1}{n}. \tag{6.16}$$

For $Re_t \to \infty$ all models have $f_2=1$, implying (with $n=1.25$) that $c_{\epsilon 2}$ should be 1.8. Indeed all models apply this value, or a value close to it. All models, except the Lam & Bremhorst (1981) model, also approximately reproduce the low-Reynolds-number decay limit, *i.e.* (with $n=2.5$) $f_2=1.4/c_{\epsilon 2}$ in the limit $Re_t \to 0$.

(iv) f_μ *function*. This function should be such that the behaviour $\nu_t=O(x^3)$ in equations (6.10) is reproduced for small x. All models give a power 3 or 4, with the exception of the Reynolds (1976) model which gives a power of 6.

In (i)-(iv) some restrictions for the low-Reynolds-number functions have been formulated. An inconsistency occurs for the Lam & Bremhorst model and for the Reynolds model; the consequences of these inconsistencies and the accuracy of all other models require a comparison with experiments.

6.3. Numerical method

The turbulent boundary-layer equations (6.1) are solved for a semi-infinite hot vertical plate in an isothermal environment. The plate temperature is T_h and the environment temperature is T_∞.

The variables are nondimensionalized with the length scale y_0, the velocity scale v_0, the reference temperature T_0 and the characteristic temperature difference ΔT:

$$\begin{aligned}&\left\{\frac{u}{v_0}, \frac{v}{v_0}, \frac{T-T_0}{\Delta T}, \frac{k}{v_0^2}, \frac{\epsilon y_0}{v_0^3}, \frac{\nu_t}{v_0 y_0}\right\} = \\ &f\left(\frac{x}{y_0}, \frac{y}{y_0}, \frac{g\beta\Delta T y_0}{v_0^2}, \frac{\nu}{v_0 y_0}, Pr\right).\end{aligned} \tag{6.17}$$

The boundary conditions for the temperature determine temperature scales: $T_0=T_\infty$, $\Delta T=T_h-T_\infty$. The semi-infinite plate geometry and the zero boundary conditions for the velocity do not define a length and velocity scale. Therefore these scales are formed with the coordinate y and the coefficients $g\beta\Delta T$ and ν. A possible choice is $y_0=y$ and $v_0=(g\beta\Delta T\nu)^{1/3}$. Because of the free choice of both the length and velocity scale, the number of independent variables in equation (6.17) reduces with two,

$$\left\{\frac{u}{v_0},\ \frac{v}{v_0},\ \frac{T-T_\infty}{\Delta T},\ \frac{k}{v_0^2},\ \frac{\epsilon y}{v_0^3},\ \frac{\nu_t}{v_0 y}\right\} = f\left(\frac{x}{y},\ Ra_y,\ Pr\right). \tag{6.18}$$

The Prandtl number (Pr) is the only characteristic number of the problem. The y-based Rayleigh number ($Ra_y=g\beta\Delta T y^3 Pr/\nu^2$) is nothing but a scaled y-coordinate. The following initial and boundary conditions are applied:

$$\begin{aligned}
&y = y_{start}: \text{ laminar v- and } T\text{-profiles specified}\\
&y = y_{trans}: \text{ nonzero perturbation in } k \text{ and } \epsilon, \text{ typically}\\
&\qquad k=0.5\ v_0^2,\ \epsilon=c_\mu^{1/2}\ k\left|\frac{\partial v}{\partial x}\right|,\ \nu_t=c_\mu\frac{k^2}{\epsilon}\\
&x = 0 \quad : u=v=0,\ T=T_h \qquad\qquad (6.19)\\
&\qquad k \text{ and } \epsilon \text{ specified by the considered } k-\epsilon \text{ model}\\
&x = x_\infty \quad : v=0,\ T=T_\infty\\
&\qquad \text{perturbation in } k \text{ and } \epsilon, \text{ typically}\\
&\qquad k=0.5\ v_0^2,\ \epsilon=c_\mu\frac{k^2}{\nu_t} \text{ with } \nu_t=10.
\end{aligned}$$

The calculations are started at a height corresponding to $Ra_y=10^9$. At y_{start} Ostrach's laminar similarity solution for the hot vertical plate is prescribed. Turbulence is introduced at the height y_{trans} (corresponding to $Ra_y=1.5\times10^9$ for air and to $Ra_y=1.5\times10^{10}$ for water) by switching on the turbulence model and by prescribing an amount of turbulent kinetic energy if a $k-\epsilon$ model is used. The infinitely far outer edge of the boundary layer (x_∞) in formulation (6.19) is moved to the finite distance ($x_{i\max}$) in the computational domain; $x_{i\max}$ is taken far enough to neglect its influence on the development of the boundary layer. Values for k and ϵ close to zero (but such that also k^2/ϵ remains small) are prescribed at this outer edge.

The boundary layer becomes thicker for increasing Ra_y. A disadvantage of the application of our rectangular grid is that the grid line $x_{i\max}$ is not boundary fitted with the thickness of the boundary layer; $x_{i\max}$ is chosen such that it still just covers the boundary-layer thickness at the maximum Ra_y value up to where the calculation is performed. Therefore at the beginning of the boundary-layer calculation at y_{start} many grid points fall outside the boundary-layer thickness, giving there an inefficient use of grid points. Despite this disadvantage, we apply the rectangular grid. A grid similar to distribution (5.6), as was used in the previous chapter for

some of the stability calculations in the cavity, is also applied here to cover the boundary-layer thickness:

$$\frac{x_i}{x_{i\max}} = 1 + \frac{\tanh[\alpha_1(i/i\max - 1)/2]}{\tanh(\alpha_1/2)} \qquad i = 0,1,\ldots,i\max. \tag{6.20}$$

α_1 is derived from the expression $\alpha_2=\alpha_1/\sinh(\alpha_1)$, in which α_2 is chosen close to zero; the smaller α_2, the stronger the grid refinement along the wall. The first inner grid point is approximately positioned at $x_1/x_{i\max}=\alpha_2/i\max$. The suitable choice for α_2 depends on the Ra_y value up to which the calculation is made. For example, $\alpha_2=1.5\times10^{-2}$ is used if the calculation is ended at $Ra_y=10^{12}$, and α_2 is decreased to 1.5×10^{-7} if the calculation is ended at $Ra_y=10^{25}$. The vertical grid spacing is optionally chosen to be equidistant in y or equidistant in $\log(y)$.

The boundary-layer equations are discretized as described in section 4.3. Because the boundary-layer equations are parabolic for an isothermal environment, they can be solved in a single sweep, going from one y-station to the next downstream station. We originally tried to solve the system of nonlinear equations at each y-station with the Newton-Raphson method. This method linearizes the equations at each iterative level, and solves the resulting block tri-diagonal matrix equation with a direct Gauss-elimination. The method converges with a quadratic speed, which was checked for the laminar solution. The turbulence models are so complex that they were only partially linearized; still a fast convergence was found with the Cebeci & Smith model. The $k-\epsilon$ models, however, required a very accurate initial guess to prevent divergence. Therefore we switched over to an uncoupled solution method; during an iteration the different differential equations in the boundary-layer equations are updated one after the other, solving only tri-diagonal matrix equations for each variable. Some relaxation was required to prevent divergence and to obtain a reasonable speed of convergence. We checked that the stop criterion for the iteration process was taken sharp enough to have a negligible influence on the solution. Typically about 50 iterations were sufficient at y-stations in the turbulent region, but much more iterations, up to 500, were required for stations in the transitional region.

6.4. Transition regime

Difficulties can arise to achieve a laminar-turbulent transition with the low-Reynolds-number $k-\epsilon$ models. If the turbulence model is switched on at y_{trans}, without introducing turbulent energy at this station or at the outer edge, the solution remains laminar (with $k=\epsilon=\nu_t=0$ everywhere). If a nonzero k is prescribed at y_{trans} and at the outer edge of the boundary layer, the laminar solution might become turbulent. The solution in the transitional region largely depends on (i) the turbulence model, (ii) the grid and (iii) how much and where energy is introduced. For example, concerning the model used, the standard $k-\epsilon$ most easily becomes turbulent, the transition with the Chien model is a bit more difficult, and the transition with the Jones & Launder model is difficult; it is clear that low-Reynolds-number modifications not only damp turbulence in the inner layer close to the wall, but they also tend to delay the transition. In general, grid refinement as well delays the transition. As illustrated in figure 6.1, a transition can occur if

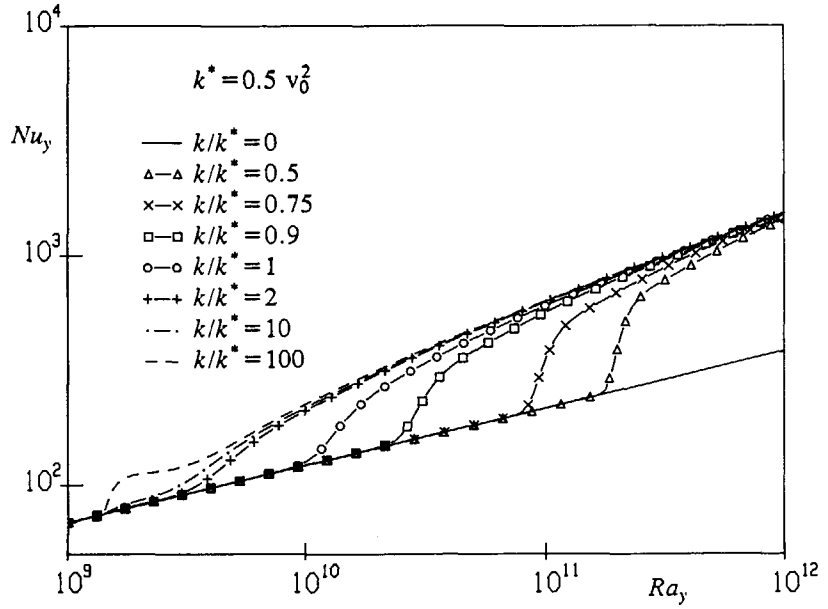

FIGURE 6.1. Transition for air with different amounts of energy at the first station upstream from y_{trans} (Chien model, 100×100 grid, $\alpha_2=1.5\times10^{-2}$ in x-grid, equidistant grid in $\log(y)$, $k=\nu_t=0$ at outer edge).

a sufficient amount of energy is prescribed as a boundary condition at the first y-station upstream of y_{trans}. For the calculations in this figure y_{trans} was fixed at $Ra_y=1.5\times10^9$ and no energy was introduced via the outer edge (*i.e.* $k=\epsilon=\nu_t=0$ at $x_{i\max}$). Increasing the introduced energy at this station gives a faster transition and it helps to prevent a relaminarization of the flow during the transition. We also checked that the introduction of some energy via the outer edge enhances the transition, but it is not required to maintain the turbulent state. If y_{trans} is chosen at a too low Ra_y value (for example at $Ra_y=10^9$ for water) the introduced energy is damped irrespective of its magnitude, which illustrates that below a critical Ra_y value a transition is not possible. Fortunately, once a full transition occurs, the turbulent solution for increasing Ra_y becomes independent of the way the transition is established.

The calculated complicated transition behaviour is due to the existence of two solutions of the turbulent boundary-layer equations (6.1), if a low-Reynolds-number $k-\epsilon$ model (6.10) is used in combination with homogeneous boundary conditions for k and ϵ at the outer edge: in the limit $Ra_y\to\infty$ the equations admit both a laminar solution (with $k=\epsilon=\nu_t=0$ everywhere) and a turbulent solution. That the laminar solution indeed is a solution can be verified by substitution of $k=\epsilon=\nu_t=0$ in equations (6.1) and (6.10). Maybe also the standard $k-\epsilon$ model contains nonuniqueness for $Ra_y\to\infty$, but the laminar solution is not a solution due to the nonzero boundary condition for ϵ at the wall. The turbulent boundary-layer

equations in the isothermal environment are parabolic in the Ra_y coordinate. We assume that the boundary-layer equations give a unique solution for increasing Ra_y once the initial condition at y_{start} (for v and T) and at y_{trans} (for k and ϵ), as well as boundary conditions at the wall and at the outer edge, are specified (this is difficult to prove due to the nonlinearity of the equations). Whether, however, a laminar or a turbulent state is found at $Ra_y \to \infty$ depends on the precise choice of the initial conditions and the boundary conditions. The transition between the laminar and turbulent solution results from the complicated nonlinear stability in Ra_y with respect to the initial and boundary conditions. In particular the laminar solution becomes less stable for increasing Ra_y. Mathematically the boundary-layer equations show a close resemblance with the unsteady Navier-Stokes equations, which are parabolic in time. For example, nonuniqueness as found for the solution at large Ra_y in the turbulent boundary-layer equations, was also found for the large-time Navier-Stokes solution in the previous chapter, where both a steady, although unstable, and an oscillating solution could occur beyond a critical Rayleigh number.

6.5. Existing theory on wall functions

The dimensionless velocity and temperature in the turbulent natural-convection boundary-layer solution (6.18) are

$$\begin{aligned} \frac{v}{(g\beta\Delta T\nu)^{1/3}} &= f_v\left(\frac{x}{y}, Ra_y, Pr\right) \\ \frac{T-T_\infty}{\Delta T} &= f_T\left(\frac{x}{y}, Ra_y, Pr\right). \end{aligned} \tag{6.21}$$

If the Rayleigh number becomes infinitely large, a rescaling might exist, which makes the solution independent of the Rayleigh number. In general, such a similarity solution is described by

$$\begin{aligned} \frac{v}{(g\beta\Delta T\nu)^{1/3}} f_1(Ra_y) &= f_2\left(\frac{x}{y} f_3(Ra_y), Pr\right) \\ \frac{T-T_\infty}{\Delta T} f_4(Ra_y) &= f_5\left(\frac{x}{y} f_6(Ra_y), Pr\right). \end{aligned} \tag{6.22}$$

For a laminar flow the similarity scalings are well known (see also equation (4.6)): $f_1 = Ra_y^{-1/6}$, $f_3 = f_6 = Ra_y^{1/4}$ and $f_4 = 1$. The proper velocity scale for laminar flows, $(g\beta\Delta Ty)^{1/2}$ $(= v_0\, Ra_y^{1/6} Pr^{-1/6}$, with $v_0 = (g\beta\Delta T\nu)^{1/3})$, is here further referred to as the buoyant velocity v_b. The similarity scalings for the turbulent boundary layer are more complicated than for the laminar boundary layer. In particular this is because for large Ra_y the solution across the boundary-layer thickness is split up into several regions, where different scalings hold. For a forced-convection turbulent boundary layer these scalings are well-known: a viscous sublayer close to the wall, an inertial sublayer where the logarithmic wall functions (6.5) hold, and an outer layer at the edge of the boundary layer where defect laws hold. A first analysis to detect the different regions and scalings in the turbulent natural-

convection boundary layer was given by George & Capp (1979) and by Cheesewright (1986). The main steps of their analyses are summarized here.

George & Capp assume that the length scale δ and the velocity scales v_τ and Q_T are important for the proper scaling,

$$\begin{aligned} &\delta = \text{boundary-layer thickness} \\ &v_\tau = (\nu(\partial v/\partial x)_w)^{1/2} \\ &Q_T = -\frac{\nu}{Pr\ \Delta T}\left(\frac{\partial T}{\partial x}\right)_w . \end{aligned} \tag{6.23}$$

In general (with $v_0=(g\beta\Delta T\nu)^{1/3}$),

$$\begin{aligned} \frac{v}{v_0} &= f_v(\zeta, x^+, \lambda, x/\delta, Ra_y^{1/3}, Pr) \\ \frac{T-T_\infty}{\Delta T} &= f_T(\zeta, x^+, \lambda, x/\delta, Ra_y^{1/3}, Pr) \end{aligned} \tag{6.24}$$

with the five dimensionless lengths

$$\zeta = \frac{xNu_y}{y} = \frac{xQ_T}{\nu/Pr}$$

$$x^+ = \frac{x v_\tau}{\nu}$$

$$\lambda = \left(\frac{g\beta\Delta TPr}{\nu^2}\right)^{1/3} x = Ra_x^{1/3}$$

$$x/\delta$$

$$Ra_y^{1/3} = \left(\frac{g\beta\Delta T y^3 Pr}{\nu^2}\right)^{1/3} .$$

In the inner layer the dependence on x/δ is neglected. Moreover a 'local equilibrium state' is assumed in this layer, implying that only v_τ/v_0 and Q_T/v_0 depend on Ra_y. Therefore the explicit dependence on Ra_y can be removed from equations (6.24). If it is further assumed that there is only one length scale in the inner layer (*i.e.* $\zeta \div \lambda$ and $x^+ \div \lambda$) the velocity scales v_τ/v_0 and Q_T/v_0 are even independent of Ra_y. Under these assumptions the wall-shear stress law (with $c_{fy}= 2\nu(\partial v/\partial x)_w/v_b^2$) and the wall-heat transfer law (with $Nu_y= -(y/\Delta T)(\partial T/\partial x)_w$) read

$$c_{fy} = c_1\, Ra_y^{-1/3} \tag{6.25a}$$

$$Nu_y = c_2\, Ra_y^{1/3}. \tag{6.25b}$$

The coefficients c_1 and c_2 only depend on the Prandtl number. In the lower part of the inner layer, the conductive/thermo-viscous sublayer, both convection and turbulence can be neglected. Using Taylor-series expansions in equations (6.1) gives

$$\frac{v}{v_0} = \frac{v_\tau^2}{v_0^2}\, Pr^{-1/3}\,\lambda - \frac{\lambda^2}{2}\left(Pr^{-2/3} - \frac{\lambda}{3}\frac{Q_T}{v_0}\right) + \cdots \tag{6.26a}$$

$$\frac{T-T_\infty}{\Delta T} = 1 - \zeta + \ldots. \tag{6.26b}$$

The assumption of one length scale gives wall functions in the upper part of the inner layer (the buoyant sublayer):

$$\begin{aligned} \frac{v}{v_0} &= f_v^i(\zeta, Pr) \\ \frac{T-T_\infty}{\Delta T} &= f_T^i(\zeta, Pr). \end{aligned} \tag{6.27}$$

In the outer layer George & Capp assume that the proper length, velocity and temperature scales depend on δ, $g\beta$ and $Q_T\Delta T$ only. This gives the following wall functions (defect laws) in the outer layer

$$\begin{aligned} \frac{v_{max}-v}{(g\beta\Delta T\delta Q_T)^{1/3}} &= f_v^o\left(\frac{x}{\delta}\right) \\ \left(\frac{T-T_\infty}{\Delta T}\right)\frac{(g\beta\Delta T\delta Q_T)^{1/3}}{Q_T} &= f_T^o\left(\frac{x}{\delta}\right). \end{aligned} \tag{6.28}$$

These wall functions are independent of the Prandtl number. For a smooth matching of the conductive/thermo-viscous sublayer with the outer layer the equations (6.27) and (6.28) must hold in an intermediate layer, *i.e.* the buoyant sublayer. This gives George & Capp's wall functions for the buoyant sublayer

$$\frac{v}{v_0} = c_1\,\zeta^{1/3} + c_2 \tag{6.29a}$$

$$\frac{T-T_\infty}{\Delta T} = c_3\,\zeta^{-1/3} + c_4. \tag{6.29b}$$

The coefficients c_1, c_2, c_3 and c_4 only depend on the Prandtl number. These 1/3 and $-1/3$ power laws in the buoyant sublayer should be the natural-convection version of the log-law in the inertial sublayer of the forced-convection boundary layer.

Cheesewright has proposed a different wall function. The conductive/thermo-viscous sublayer in his analysis remains, of course, the same as in equations (6.26). He assumes that equations (6.27) still hold in the lower part of the outer layer (*i.e* the region between the positions of the maxima of the velocity and the turbulent viscosity; see section 6.7) and that there is no dependence on ν, which leads to

$$\frac{T-T_\infty}{\Delta T} = c_1 \ln\zeta + c_2. \tag{6.30}$$

Neglecting convection and molecular diffusion in equations (6.1) gives (taking $\sigma_T = 1$)

$$\begin{aligned} \frac{\partial v}{\partial x} &= \frac{v_\tau^2 - g\beta\Delta T\int_0^x \frac{T-T_\infty}{\Delta T}dx}{\nu_t} \\ \frac{\partial}{\partial x}\left(\frac{T-T_\infty}{\Delta T}\right) &= -\frac{Q_T}{\nu_t}. \end{aligned} \tag{6.31}$$

Substitution of equation (6.30) into equations (6.31) gives

$$\frac{v}{v_0} = -c_1 \frac{v_0^2}{Pr\ Q_T^2} \left[Pr \frac{u_\tau^2 Q_T}{v_0^3} \ln\zeta - (c_2 - 2c_1)\zeta - c_1\, \zeta \ln\zeta \right] + c_3. \qquad (6.32)$$

The coefficients c_1, c_2 and c_3 only depend on the Prandtl number. Cheesewright proposed equation (6.30) and equation (6.32) as wall functions in the lower part of the outer layer. He did not formulate a wall function in the upper part of the outer layer.

6.6. Existing experimental and numerical data

It is difficult to accurately measure the natural-convection boundary layer, because of the thinness of the inner layer. Available experimental data are restricted to about $Ra_y = 5\times10^{11}$ for air and to about $Ra_y = 5\times10^{12}$ for water. The measurements are either performed with a hot-wire technique or with laser-Doppler anemometry. Regarding the information provided in the literature, it is usually difficult to judge the accuracy of the measurements. At least it has to be realized that the experimental situation is never the semi-infinite vertical plate in an infinitely large, isothermal environment. The plate is placed in a box with finite dimensions, introducing a temperature stratification along the outer edge of the boundary layer. We have got the 'feeling' that the recent measurements of Tsuji & Nagano (1988a,b, 1989) are the most accurate experimental data at the moment. An argument for this is that Tsuji & Nagano used a much larger box than others, which gives only a slight stratification in the core. Tsuji & Nagano themselves claim that their measurements are accurate because of the use of the hot-wire technique, whereas other recent studies use laser-Doppler anemometry; they argue that laser-Doppler anemometry gives a too large measuring volume close to the wall, which leads to inaccurate results in the inner layer.

Wall-heat transfer measurements for air, as obtained by Cheesewright & Ierokipiotis (1981), Miyamoto *et al.* (1982, 1983) and Tsuji & Nagano (1989) are compared in figure 6.2. The data of Tsuji & Nagano clearly show the laminar-turbulent transition. With reasonably accuracy we can fit all the experiments for the turbulent wall-heat transfer to the curve

$$Nu_y = 0.119\, Ra_y^{1/3}. \qquad (6.33)$$

Experimental data for water are scarcer than for air. Further, the deviations between the different studies are larger for water than for air. Within this experimental uncertainty the wall-heat transfer for water is close to the best fit curve (6.33) for air; for example at $Ra_y = 10^{12}$ Vliet & Liu (1969) and Fujii *et al.* (1970) measure a wall-heat transfer which is respectively 2% below and 9% above this curve. Therefore we assume that equation (6.33) fits the turbulent wall-heat transfer for both air and water.

Miyamoto *et al.* (1983) have measured velocity and temperature profiles for air in the boundary layer along a vertical plate with a constant wall-heat flux. Because Nu_y/y is independent of y according to the best-fit curve (6.33), these measurements are also representative for the vertical plate with a constant wall

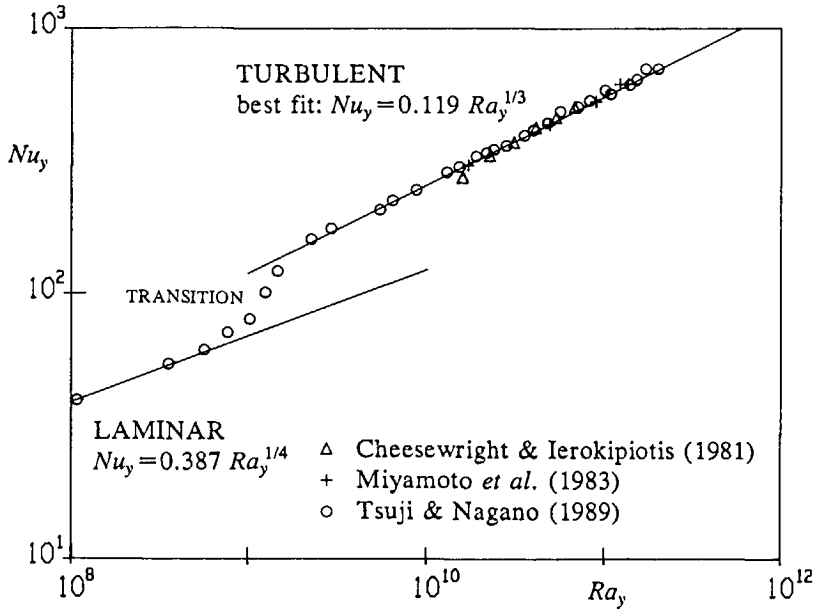

FIGURE 6.2. Comparison of existing experiments for the wall-heat transfer for air.

temperature. Cheesewright (1968, 1986), Cheesewright & Ierokipiotis (1981, 1982) and Tsuji & Nagano (1988a, 1989) have measured velocity and temperature profiles for air along a vertical plate with a constant wall temperature. The measured velocity and temperature profiles are compared in figure 6.3. The profiles were obtained at slightly different Ra_y values, which implies that they can only be expected to coincide if the quantities are nondimensionalized with the proper scalings. In the literature the dimensionless length is usually taken as ζ $(=xNu_y/y)$, whereas the velocity and the temperature are scaled with v_{max} and ΔT respectively. The numerical results in section 6.9 will show that ζ is not the proper dimensionless coordinate in the limit $Ra \to \infty$. Nevertheless, for the Rayleigh-number range where the experiments were obtained, the numerical results predict that ζ is a reasonably suitable dimensionless length for the temperature profiles and, to a less extent, also for the velocity profiles. Also ΔT turns out to be a good temperature scale in the experimental Rayleigh-number range. The numerical results will show that v_{max} is the proper scaling, not only in the experimental Rayleigh-number range, but even up to $Ra_y \to \infty$. Tsuji & Nagano (1989) fit their experimental velocity maxima for air to

$$\frac{v_{max}}{\sqrt{g\beta\Delta Ty}} = 0.407\ Ra_y^{-0.0067}. \tag{6.34}$$

Because the power in the Rayleigh-number dependence is close to zero, which is confirmed by the numerical calculations in section 6.9, the velocity maximum approximately scales with the buoyant velocity $v_b = (g\beta\Delta Ty)^{1/2}$. This implies that,

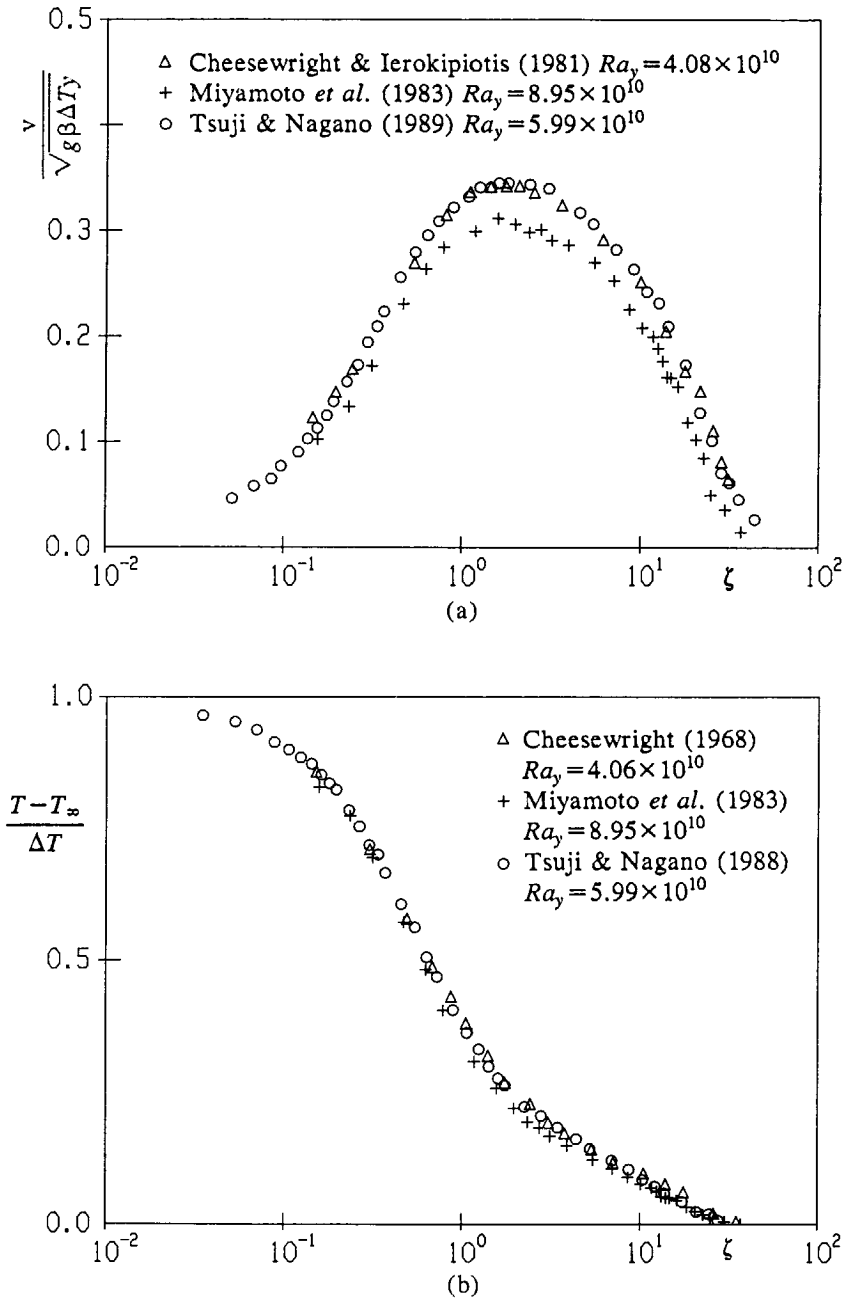

FIGURE 6.3. Comparison of existing experiments for air;
(a) vertical velocity, (b) temperature.

besides v_{max}, also v_b is a proper velocity scale. Regarding these arguments, we expect that the scalings as applied in figure 6.3 are sufficiently accurate to exclude that differences in the experimental results are due to differences in the Rayleigh number. The velocity measurements of Miyamoto *et al.* in figure 6.3a fall somewhat below the experiments of Cheesewright & Ierokipiotis and of Tsuji & Nagano. Because the latter two series of data almost coincide, the velocity data of Miyamoto *et al.* are expected to be the less accurate. The temperature profiles in figure 6.3b, as obtained in the different studies, practically coincide.

Numerical calculations of the turbulent natural-convection boundary layer in the literature are restricted to about $Ra_y = 10^{12}$. A first numerical study of the turbulent natural-convection boundary layer was made by Eckert & Jackson (1951). They approximated the solution of the boundary-layer equations with an integral method, assuming some similarity in the profiles and assuming a strong analogy with the forced-convection boundary-layer. Some of their assumptions do not agree with the more recent studies, including the present one. The results of Eckert & Jackson for the wall-heat transfer are good, but the results for the velocity maximum are not; for example, the wall-heat transfer for air at $Ra_y = 10^{11}$ is 15% above the experimental curve (6.33), the wall-heat transfer for water at $Ra_y = 10^{12}$ is 18% above this curve, and the velocity maximum for air at $Ra_y = 10^{11}$ is 57% above the experimental curve (6.34). More refined calculations, in which differential equations were used to model the turbulence and in which the boundary-layer equations were solved with a finite-difference numerical method, were made by Mason & Seban (1974) and by Plumb & Kennedy (1977). Mason & Seban calculated the boundary layer for air and water, applying an algebraic model for the turbulent mixing length and a differential equation for the turbulent kinetic energy. A reasonably good accuracy is obtained; for example, the wall-heat transfer for air at $Ra_y = 10^{11}$ is 12% below the experimental value (6.33) and the velocity maximum for air at $Ra_y = 3 \times 10^{10}$ is 11% higher than the experiment (6.34). Plumb & Kennedy extended the Jones & Launder low-Reynolds-number $k-\epsilon$ model with a differential equation for the temperature fluctuations T'^2 and calculated the boundary layer for air. Their results are close to the experiments (the wall-heat transfer at $Ra_y = 10^{11}$ is 11% above the experiment and the velocity maximum at $Ra_y = 7 \times 10^{10}$ is 7% below the experiment). Finally a few models, which are also compared in this chapter, were already applied to the natural-convection boundary layer along the hot vertical plate in the following studies: Cebeci & Khattab (1975) using the Cebeci & Smith model, Lin & Churchill (1978) using the Jones & Launder model, and To & Humphrey (1986) using their own model.

6.7. Comparison of the models

Patel *et al.* (1981, 1985) have compared the performance of some of the low-Reynolds-number $k-\epsilon$ models from table 6.1 for the forced-convection boundary layer along a flat plate. In order to check our numerical code, these calculations were repeated, and a very good agreement was found with their tabulated wall-shear stress coefficients. Our natural-convection boundary layer calculations with the Cebeci & Smith model, the Jones & Launder model and the To & Humphrey

TABLE 6.2. Numerical accuracy for air at $Ra_y = 10^{11}$.

model	grid	$\frac{Nu_y}{Ra_y^{1/3}}$	$\frac{v_{max}}{\sqrt{g\beta\Delta Ty}}$	$\frac{\nu_{t,max}}{\nu}$
standard $k-\epsilon$	25×25	0.1750	0.3622	257.3
	50×50	0.1789	0.3570	241.1
	100×100	0.1806	0.3549	233.4
	200×200	0.1814	0.3540	229.7
	400×400	0.1817	0.3537	226.9
Chien	25×25	0.1396	0.3358	291.4
	50×50	0.1381	0.3309	270.7
	100×100	0.1376	0.3290	261.2
	200×200	0.1375	0.3281	256.8
	400×400	0.1373	0.3278	253.5
Jones & Launder	25×25	0.1165	0.3421	191.2
	50×50	0.1145	0.3367	183.3
	100×100	0.1138	0.3345	175.4
	200×200	0.1128	0.3350	154.2
	400×400	0.0689	0.4579	22.7

model were compared with the calculations of Cebeci & Khattab (1975), Lin & Churchill (1978) and To & Humphrey (1986) respectively. Present results agree up to at least graphical accuracy, except for the results with the To & Humphrey model, which considerably deviate.

In order to verify the numerical accuracy of the results, we have refined the grid from 25×25 up to 400×400 points. Table 6.2 shows the results for air at $Ra_y = 10^{11}$ with the standard $k-\epsilon$ model, the Chien model and the Jones & Launder model. To obtain a fast transition, the calculations were started at $Ra_y = 10^9$ with a turbulent velocity and temperature profile that fit the experimental data in figure 6.3. Some kinetic energy was introduced both at the initial station and at the outer edge. The constant $\alpha_2 = 1.5 \times 10^{-2}$ was applied in the x-grid (6.20), and the grid was equidistant in y. The calculation was ended at $Ra_y = 10^{11}$. Table 6.2 shows that the results indeed become grid independent if the number of grid points is increased, and that the 50×50 grid already gives an accurate solution. An exception forms the 400×400 grid in the Jones & Launder model. Grid refinement in the Jones & Launder model delays the transition, as can be seen in the decreasing value of the maximum in the turbulent viscosity at $Ra_y = 10^{11}$. At the 400×400 grid the transition is so late, that the solution at $Ra_y = 10^{11}$ is still close to the laminar state. The results to be presented in the sequel are all checked to be accurate; typically a 100×100 grid is used for the calculations up to $Ra_y = 10^{13}$, and a 200×200 grid is used for calculations up to larger Rayleigh numbers.

TABLE 6.3. Comparison of the models for air at $Ra_y=10^{11}$ and for water at $Ra_y=10^{13}$.

(a) air

model	$\frac{Nu_y}{Ra_y^{1/3}}$	$\frac{v_{max}}{\sqrt{g\beta\Delta Ty}}$	$\frac{\nu_{t,max}}{\nu}$
experiment	0.119	0.344	120
Cebeci & Smith	0.089	0.413	48
standard $k-\epsilon$	0.181	0.355	233
To & Humphrey	0.164	0.346	210
Lam & Bremhorst (Dirichlet)	0.132	0.320	241
Lam & Bremhorst (Neumann)	0.132	0.320	240
Chien	0.138	0.329	261
Hassid & Poreh	0.161	0.323	231
Hoffman	0.083	0.422	26
Jones & Launder	0.114	0.335	175

(b) water

model	$\frac{Nu_y}{Ra_y^{1/3}}$	$\frac{v_{max}}{\sqrt{g\beta\Delta Ty}}$	$\frac{\nu_{t,max}}{\nu}$
experiment	0.119	--	--
Cebeci & Smith	0.127	0.251	85
standard $k-\epsilon$	0.381	0.243	544
To & Humphrey	0.218	0.208	459
Lam & Bremhorst (Dirichlet)	0.088	0.166	436
Lam & Bremhorst (Neumann)	0.088	0.166	435
Chien	0.137	0.184	509
Hassid & Poreh	0.161	0.184	461
Hoffman	0.082	0.218	60
Jones & Launder	0.085	0.175	373

Table 6.3 summarizes the turbulent results with the different models for air at $Ra_y=10^{11}$ and for water at $Ra_y=10^{13}$. The wall-heat transfer for air and water are compared with the experiment (6.33), the velocity maximum for air is compared with the experiment (6.34) and the maximum in the turbulent viscosity for air is compared with the experiments at $Ra_y=6.4\times10^{10}$ of Tsuji & Nagano (1988b). No converged results could be obtained with the Reynolds model. Using the Lam & Bremhorst model, the results with the Dirichlet and Neumann boundary condition for ϵ at the wall are indistinguishable. The wall-heat transfer for air at $Ra_y=10^{11}$

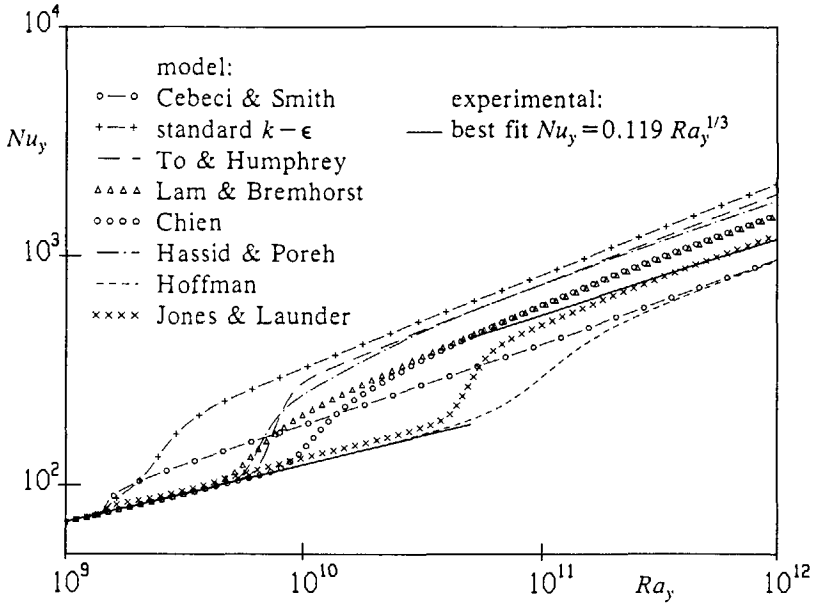

FIGURE 6.4. Wall-heat transfer for air.

is best predicted by the low-Reynolds-number models of Jones & Launder (4% too low), Lam & Bremhorst (11% too high) and Chien (16% too high). In predicting the wall-heat transfer for water at $Ra_y=10^{13}$ the best performing low-Reynolds-number $k-\epsilon$ model is the model of Chien (15% too high), followed by the Lam & Bremhorst model (26% too low) and the Jones & Launder model (29% too low). The standard $k-\epsilon$ model largely overpredicts the wall-heat transfer (by 52% for air at $Ra_y=10^{11}$ and by 220% for water at $Ra_y=10^{13}$). The Cebeci & Smith model is closest to the experimental wall-heat transfer for water; this cannot surprise because Cebeci & Khattab (1975) fitted the constants to the water experiments. All models, with exception of the models of Cebeci & Smith and Hoffman, closely predict the experimental velocity maximum for air. Deviations between the models for this quantity are larger for water than for air. By variation of the energy to trigger the transition it was checked that, in contrast to the wall-heat transfer and the velocity maximum, the maximum of the turbulent viscosity for air at $Ra_y=10^{11}$ and for water at $Ra_y=10^{13}$ is still not fully independent of the introduced energy. Therefore an incomplete transition effect accounts for part of the differences in the turbulent viscosity maximum between the models. All models, with exception of the models of Cebeci & Smith and Hoffman, give for air at $Ra_y=10^{11}$ a turbulent viscosity maximum, which is roughly twice the experimental value. The large difference for the turbulent viscosity between the $k-\epsilon$ models and the experiment will be further investigated in section 6.11, where calculations with the Reynolds-stress model will be compared.

Figure 6.4 shows the wall-heat transfer for air at increasing Rayleigh number.

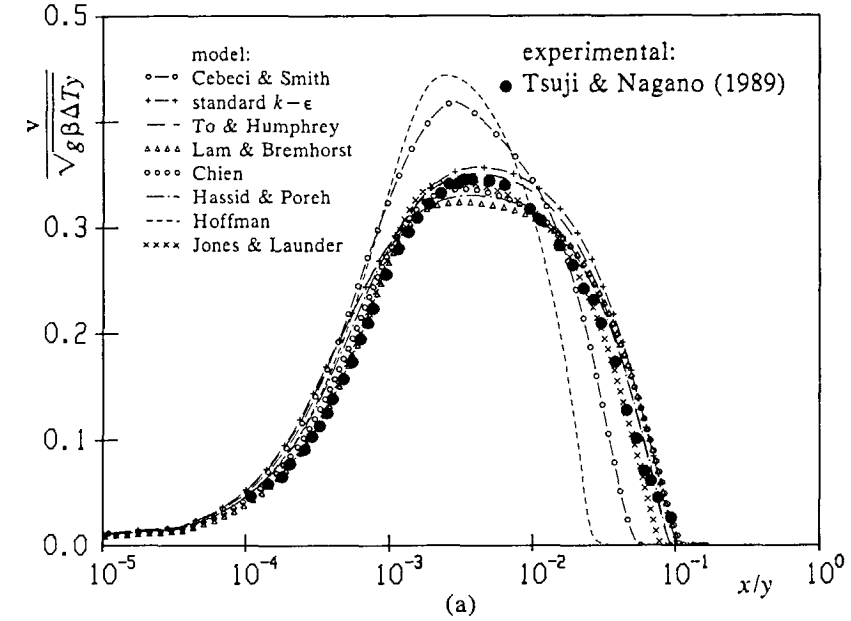

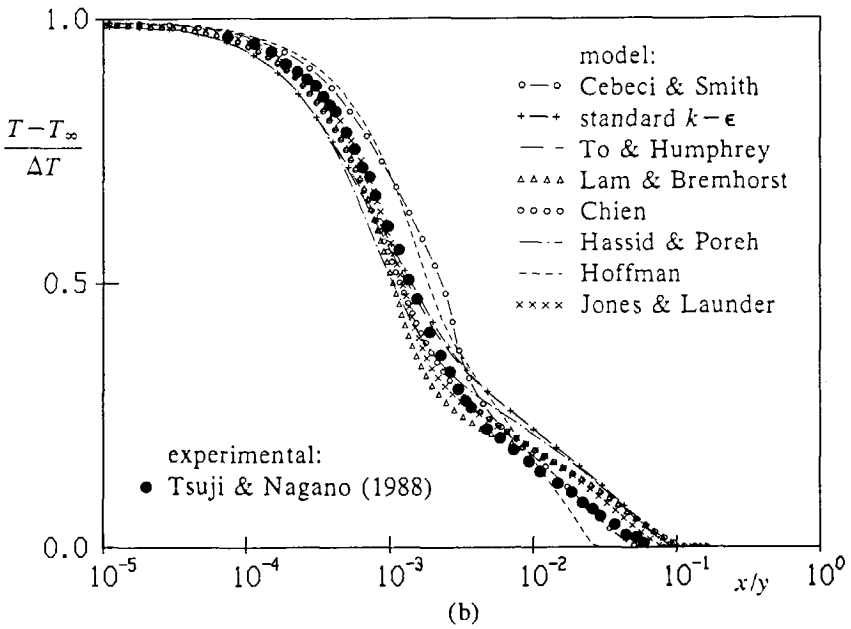

FIGURE 6.5. Air at $Ra_y = 5.99 \times 10^{10}$; (a) vertical velocity, (b) temperature.

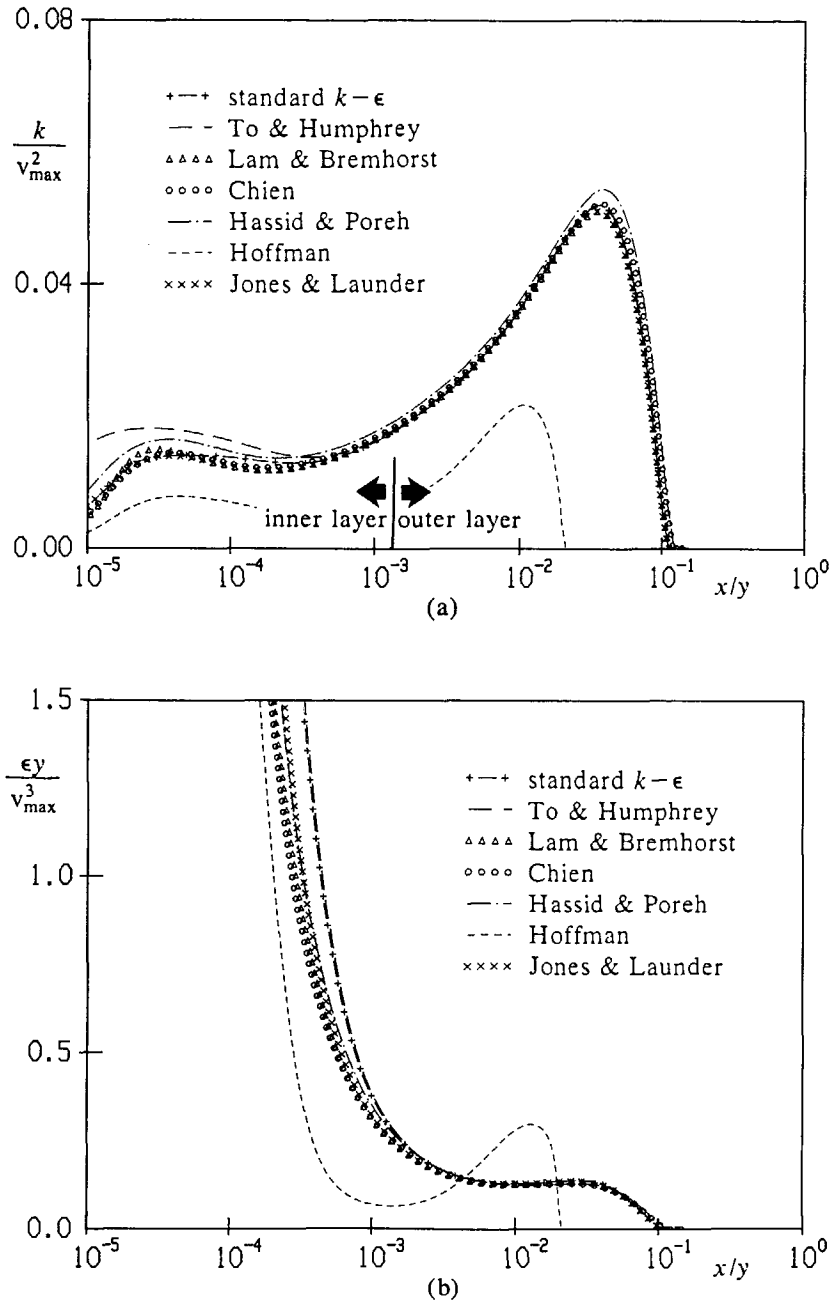

FIGURE 6.6(a,b). For caption see facing page.

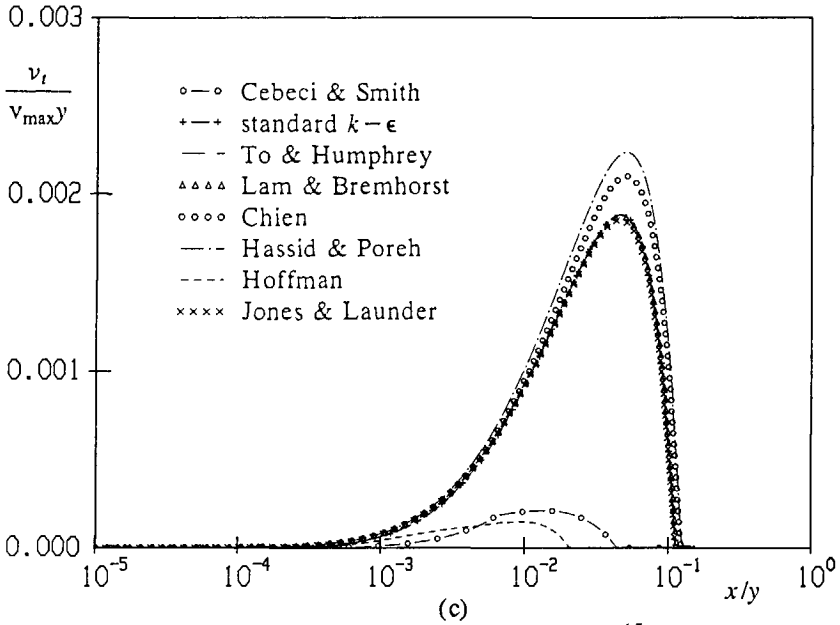

FIGURE 6.6. Turbulent quantities for air at $Ra_y = 10^{15}$; (a) turbulent kinetic energy, (b) dissipation rate of turbulent kinetic energy, (c) turbulent viscosity.

In this figure the calculation is started with a laminar profile to illustrate the different transition behaviour of the models: the stronger the damping of the low-Reynolds-number functions, the lower the turbulent wall-heat transfer, but also, the later the transition. Comparison of the velocity and temperature profiles for air in figure 6.5 shows that all models, with exception of the models of Cebeci & Smith and Hoffman, are close to the experiments of Tsuji & Nagano (1988a, 1989) at $Ra_y = 5.99 \times 10^{10}$. The velocity profiles for the Cebeci & Smith model and the Hoffman model are laminar-like: the velocity maximum is too high and the boundary layer is too thin. The turbulent quantities k, ϵ and ν_t for air are compared in figure 6.6. In order to exclude incomplete transition effects, the turbulent quantities are presented at $Ra_y = 10^{15}$. In the outer layer low-Reynolds-number effects are absent; differences between the profiles (scaled with the velocity scale v_{max} and the length scale y) are totally due to different choices for the high-Reynolds-number constants (c_μ, $c_{\epsilon 1}$, $c_{\epsilon 2}$, σ_k and σ_ϵ; see table 6.1). In particular the strange choice of these constants in the Hoffman model leads to the laminar-like solution (low turbulence, low wall-heat transfer, high velocity). For all models the turbulence becomes fully developed in the outer layer, where k and ν_t reach a maximum, whereas ϵ is almost constant. In the inner layer the turbulent viscosity is almost zero. The low-Reynolds-number functions, however, become active in the inner layer; although they only slightly modify the turbulent quantities there, large changes occur in inner-layer quantities like the wall-heat transfer.

TABLE 6.4. Influence of the different terms in the low-Reynolds-number $k-\epsilon$ models; air at $Ra_y = 10^{11}$.

variation	$\frac{Nu_y}{Ra_y^{1/3}}$	$\frac{v_{max}}{\sqrt{g\beta\Delta Ty}}$
(a) Lam & Bremhorst model		
none	0.132	0.320
$f_\mu = 1$, but f_1 unchanged	+11%	+8%
$f_1 = 1$	+50%	+3%
$f_2 = 1$	0%	0%
$\epsilon_w = 0$, $D = -2\nu(\partial\sqrt{k}/\partial x)^2$	0%	−2%
$\epsilon_w = 0$, $D = -2\nu k/x^2$	−9%	0%
$\epsilon_w = 0$	0%	0%
(b) Chien model		
none	0.138	0.329
$f_\mu = 1$	+13%	+6%
$f_2 = 1$	0%	0%
$E = 0$	0%	0%
$D = D_{Chien}/4$	+21%	+1%
$\epsilon_w = 2\nu(\partial\sqrt{k}/\partial x)_w^2$, $D = 0$	+16%	+1%
$c_{\epsilon 1} = 1.44$, $c_{\epsilon 2} = 1.92$	−3%	+1%
$c_{\epsilon 1} = 1.44$, $c_{\epsilon 2} = 1.92$, $E = 0$, $f_2=1$	−3%	+1%
(c) Jones & Launder model		
none	0.114	0.335
$f_\mu = 1$	+24%	+3%
$f_2 = 1$	0%	0%
$E = 0$	+52%	+3%
$D = 0$	+8%	0%
$\epsilon_w = 2\nu(\partial\sqrt{k}/\partial x)_w^2$, $D = 0$	+5%	0%

6.8. Sensitivity of the model parameters

We have made a sensitivity study for those low-Reynolds-number $k-\epsilon$ models, which turned out to agree best with the experiments in the previous section: the models of Lam & Bremhorst, Chien, and Jones & Launder (these models were also found to perform best for the forced-convection boundary layer by Patel *et al.*, 1981, 1985). The influence on the wall-heat transfer and the velocity maximum of the different terms in these models is given in table 6.4 for air at $Ra_y=10^{11}$. In general, the influence becomes weaker the further a quantity is removed from the wall: the influence is much larger for the wall-heat transfer than for the velocity maximum. In all three models the standard choice $f_2=1$ does not change the wall-heat transfer. Further, the interchange of a nonzero boundary condition for ϵ with a nonzero D term does not drastically change the wall-heat transfer. Setting

$\epsilon_w=0$ (with $D=0$) in the Lam & Bremhorst model or setting $D=0$ (with $\epsilon_w=0$) in the Jones & Launder model also leads to only small changes; decreasing $|D|$ (with $\epsilon_w=0$) in the Chien model, however, enormously increases the wall-heat transfer. Omitting the E term (which has not a clear physical meaning) in the Jones & Launder model drastically increases the wall-heat transfer by 52%. The influence of E in the Chien model, however, can be neglected. Only the Lam & Bremhorst model takes the f_1 function (which also has not a very clear physical meaning) unequal to 1; its influence turns out to be very large. The influence of the f_μ function is large for all models.

The poor performance of the To & Humphrey model, which actually is a modified Jones & Launder model, has also been investigated. Firstly, To & Humphrey exchanged the D term with a nonzero boundary condition for ϵ at the wall, which only leads to small differences. Secondly they added a correction f_3 to the f_2 function, which we also checked to have a negligible effect. Lastly To & Humphrey omitted the E term in the Jones & Launder model; our calculations show that retaining the E term in the To & Humphrey model decreases the wall-heat transfer for air at $Ra_y=10^{11}$ by 28%, giving a value close to the experimental one.

6.9. Numerical determination of wall functions

To find the proper scalings of the turbulent natural-convection boundary layer, the calculations with the standard $k-\epsilon$ model, the Chien model and the Jones & Launder model are extended up to $Ra_y=10^{25}$. The Ra_y dependence of a quantity ϕ is written as $\alpha\, Ra_y^{\gamma}$, with $\gamma=(Ra_y/\phi)[\partial\phi/\partial Ra_y]$. The coefficient γ turns out to be almost independent of the turbulence model used, but α in the inner layer shows a larger model dependence. The infinite-Rayleigh-number limit of γ, in the case it exists, defines the proper scaling for a quantity. Figure 6.7 gives the Ra_y dependence for some characteristic quantities in the inner layer (Nu_y and c_{fy}), between the inner and outer layer (v_{max}) and in the outer layer ($(2k_{max}/3)^{1/2}/v_{max}$, the position x/y of k_{max} and $\psi_\infty/(v_{max}y)$). Here ψ_∞ is the stream function at the outer edge of the boundary layer ($\partial\psi/\partial x=v$, $\partial\psi/\partial y=-u$, $\psi=0$ at $x=0$). The solution in figure 6.7 starts with Ostrach's laminar similarity solution, which is plotted as an unbroken line. Although the calculations were performed up to $Ra_y=10^{25}$, figure 6.7 only shows the solution up to $Ra_y=10^{15}$. Quantitative results for the inner layer are given in table 6.5 up to $Ra_y=10^{25}$.

The wall-heat transfer Nu_y for air in figure 6.7a gives about $\gamma=3/8$ at $Ra_y=10^{12}$ for all models. This value is slightly higher than the experimental value of 1/3. Table 6.5 shows that γ for Nu_y does not seem to become Ra_y independent and γ increases to 0.435 for the Chien model at $Ra_y=10^{25}$. Besides the turbulent solution, the table also gives the laminar solution. Tsuji & Nagano (1988) measured the velocity for air up to very close to the wall, leading to the following best-fit curve for the wall-shear stress ($c_{fy}=2\nu(\partial v/\partial x)_w/v_b^2$):

$$c_{fy} = 1.256\, Ra_y^{-0.249}. \tag{6.35}$$

The wall-shear stress data for air of Cheesewright & Mirzai (1988) are more scattered, but they derived a best-fit curve with a power dependence close to equation

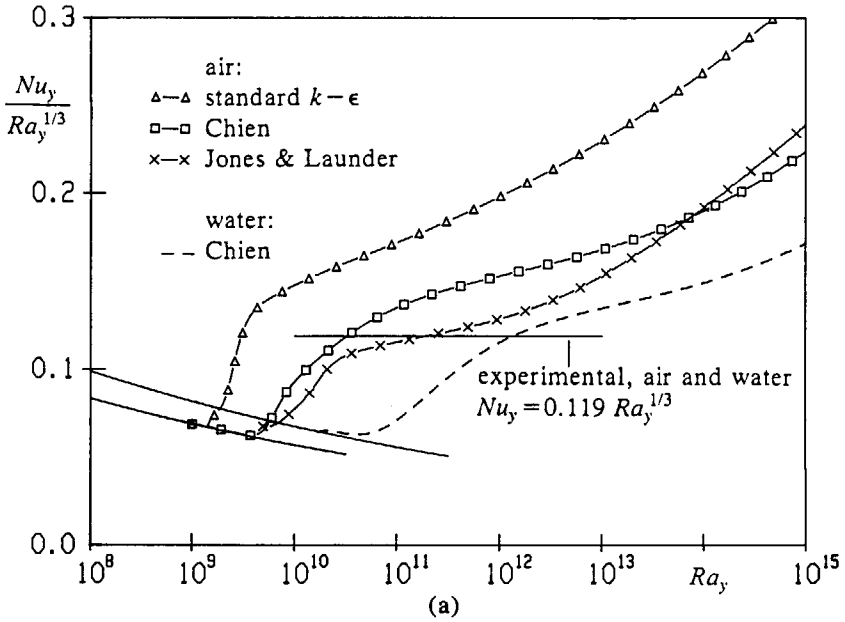

(a)

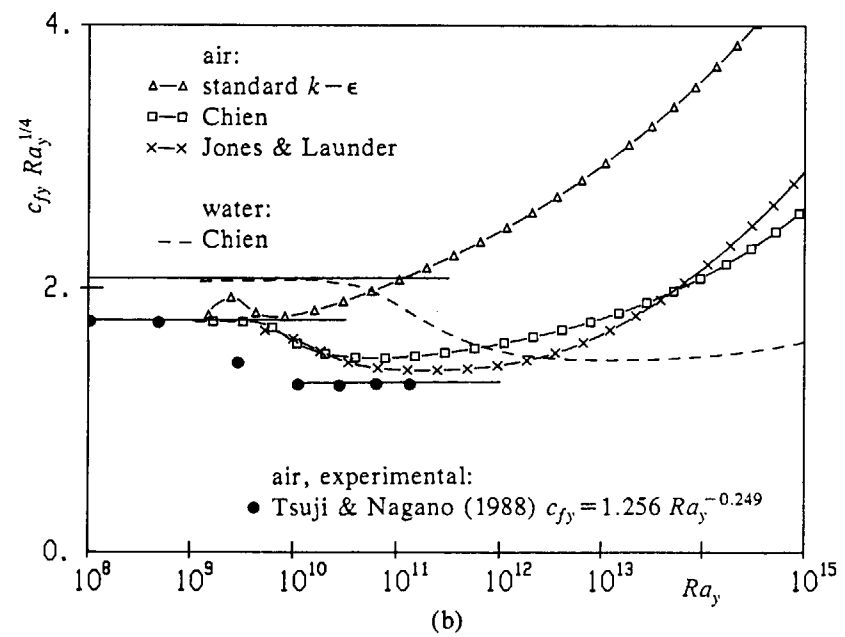

(b)

FIGURE 6.7(a,b). For caption see page 124.

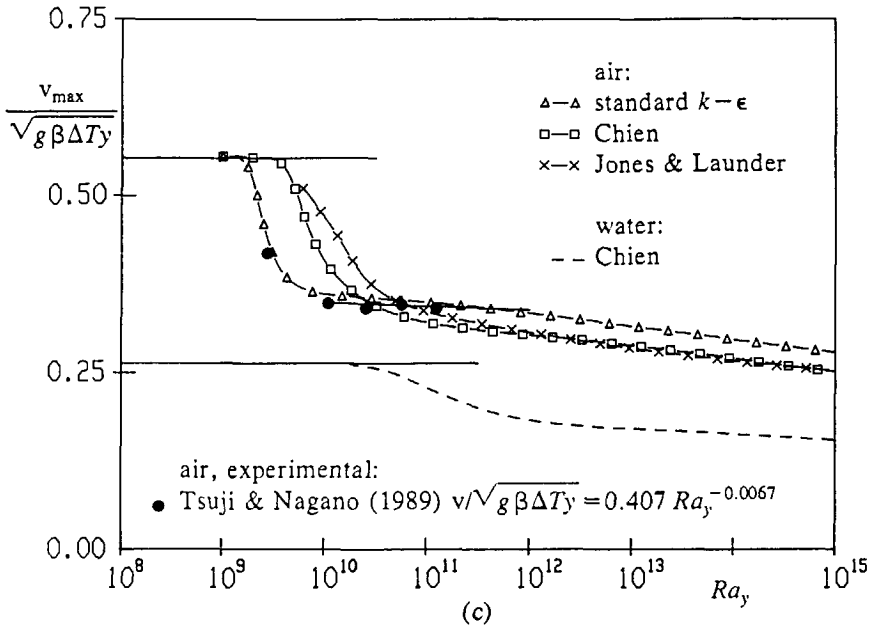

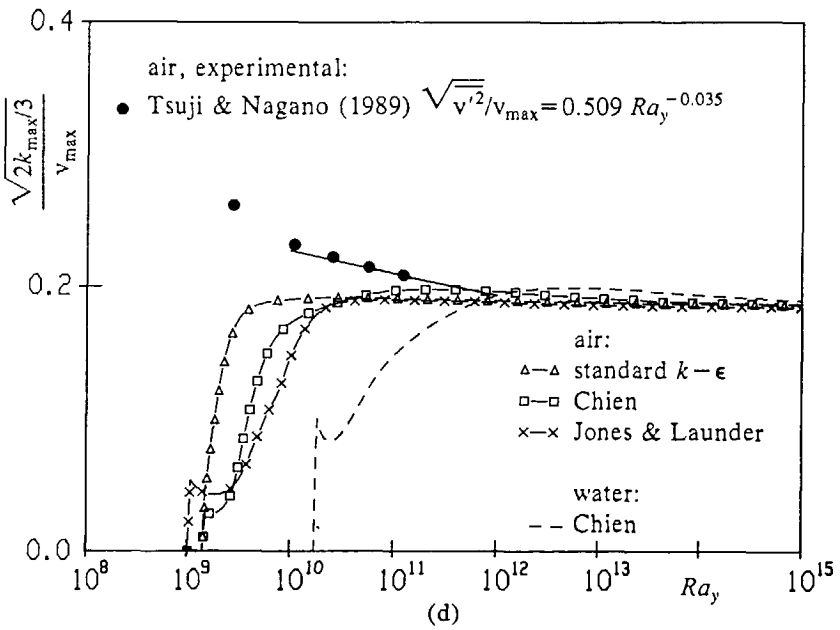

FIGURE 6.7(c,d). For caption see next page.

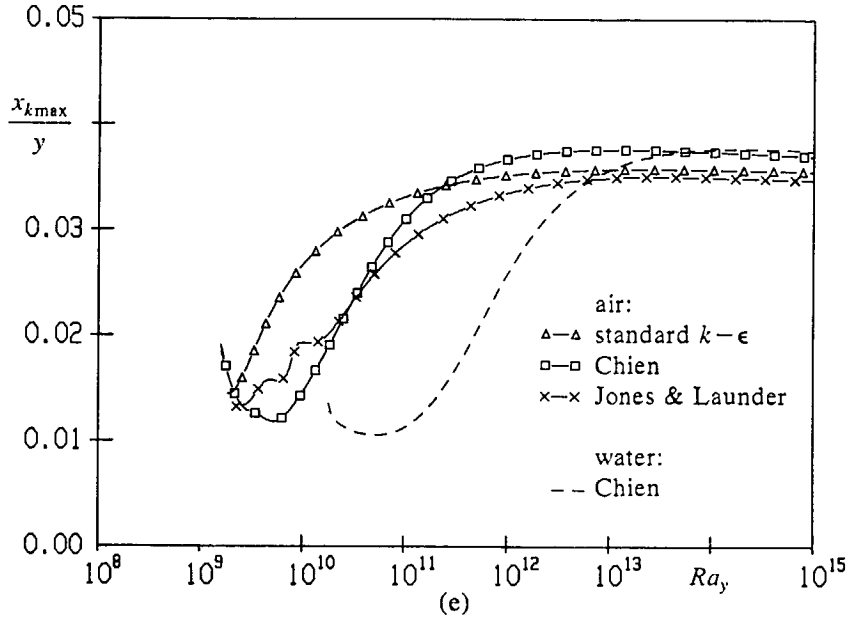

(e)

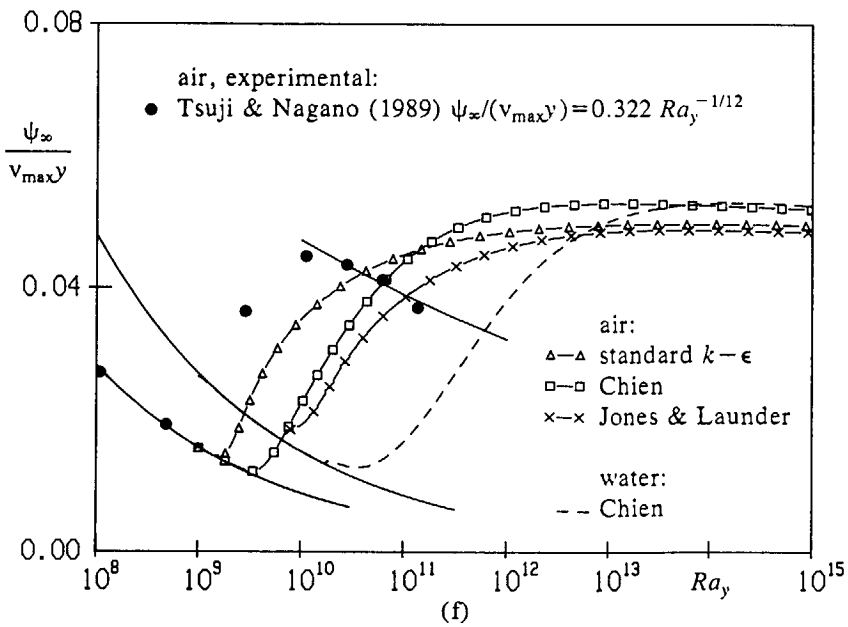

(f)

FIGURE 6.7. Scaling of different quantities in the boundary layer; (a) wall-heat transfer, (b) wall-shear stress, (c) velocity maximum, (d) maximum of the turbulent kinetic energy, (e) position of the maximum of the turbulent kinetic energy, (f) stream function at the outer edge.

TABLE 6.5. Rayleigh-number dependence in the inner layer (Chien model).

(a) air

quantity	laminar	turbulent		
		$Ra_y = 10^{15}$	$Ra_y = 10^{20}$	$Ra_y = 10^{25}$
Nu_y	$0.387\ Ra_y^{1/4}$	$0.0195\ Ra_y^{0.404}$	$0.00819\ Ra_y^{0.426}$	$0.00511\ Ra_y^{0.435}$
c_{fy}	$1.76\ Ra_y^{-1/4}$	$0.0948\ Ra_y^{-0.154}$	$0.0129\ Ra_y^{-0.103}$	$0.00562\ Ra_y^{-0.0871}$
$\frac{v_{max}}{\sqrt{g\beta\Delta Ty}}$	0.555	$0.734\ Ra_y^{-0.0311}$	$0.499\ Ra_y^{-0.0218}$	$0.435\ Ra_y^{-0.0195}$
x_{vmax}/y	$1.25\ Ra_y^{-1/4}$	$0.0237\ Ra_y^{-0.0854}$	$0.00680\ Ra_y^{-0.0535}$	$0.00503\ Ra_y^{-0.0482}$

(b) water

quantity	laminar	turbulent		
		$Ra_y = 10^{15}$	$Ra_y = 10^{20}$	$Ra_y = 10^{25}$
Nu_y	$0.459\ Ra_y^{1/4}$	$0.0211\ Ra_y^{0.394}$	$0.00310\ Ra_y^{0.446}$	$0.00266\ Ra_y^{0.449}$
c_{fy}	$2.08\ Ra_y^{-1/4}$	$0.599\ Ra_y^{-0.222}$	$0.00547\ Ra_y^{-0.0985}$	$0.00251\ Ra_y^{-0.0826}$
$\frac{v_{max}}{\sqrt{g\beta\Delta Ty}}$	0.263	$0.351\ Ra_y^{-0.0239}$	$0.251\ Ra_y^{-0.0160}$	$0.247\ Ra_y^{-0.0157}$
x_{vmax}/y	$1.68\ Ra_y^{-1/4}$	$0.0696\ Ra_y^{-0.109}$	$0.00966\ Ra_y^{-0.0580}$	$0.00774\ Ra_y^{-0.0535}$

(6.35), namely $c_{fy}=1.84\,Ra_y^{-0.26}$. The $-1/4$ power dependence is also calculated by the low-Reynolds-number models in the experimental Rayleigh-number range (see figure 6.7b), but γ remains Ra_y dependent and it decreases to -0.0871 at $Ra_y=10^{25}$ (table 6.5). The scaling with the buoyant velocity $v_b=(g\beta\Delta Ty)^{1/2}$ for the velocity maximum in the experiments of Tsuji & Nagano (1989) is confirmed by the calculations in figure 6.7c. According to table 6.5, only a very small Ra_y dependence in γ persists. The table also shows that a larger Ra_y dependence in γ remains for the position of the velocity maximum. From table 6.5 we conclude that for both air and water none of the inner-layer quantities give fully Ra_y independent γ values in the limit $Ra_y \to \infty$. Also the differences between the models for the inner-layer quantities (mainly differences in α) do not disappear in the limit $Ra_y \to \infty$. For example, the wall-heat transfer with the Jones & Launder model is a bit below the Chien model up to $Ra_y=10^{14}$, but for larger Rayleigh numbers the Jones & Launder model remains a bit above the Chien model up to at least $Ra_y=10^{25}$. The standard $k-\epsilon$ model remains significantly above both the Jones & Launder model and the Chien model up to at least $Ra_y=10^{25}$.

In contrast to the inner-layer quantities, all the outer-layer quantities give a constant γ for increasing Rayleigh number. In particular, the quantities $(2k_{max}/3)^{1/2}/v_{max}$, its position x/y and $\psi_\infty/(v_{max}y)$ in the figures 6.7d,e,f become even constant for increasing Rayleigh number. This implies that y and v_{max} are the proper length and velocity scale in the outer layer. The experiments of Tsuji & Nagano (1989) for $(v'^2)^{1/2}$ are slightly above the calculations of $(2k_{max}/3)^{1/2}$, which is expected to be due to the anisotropy of the turbulence. The experimental values of Tsuji & Nagano (1989) for ψ_∞ in the turbulent regime are somewhat below the calculated turbulent values. The slight stratification in the experiments (about $0.6\,^oC$ per meter) might account for this difference. The asymptotic values for the outer-layer quantities are summarized in table 6.6; there is no Prandtl number dependence, and deviations between the models (figures 6.7d,e,f) are only due to differences in the choice for the high-Reynolds-number coefficients.

Because we calculate that y and v_{max} are the proper length and velocity scale in the outer layer, the buoyant term in the boundary-layer equations (6.1) is of the same order of magnitude as the other terms if the characteristic temperature difference is taken as $v_{max}^2/(g\beta y)$. The calculated outer-layer scalings lead to the following wall functions in the outer layer:

$$\frac{v}{v_{max}} = f_v^o\left(\frac{x}{y}\right)$$
$$\left(\frac{T-T_\infty}{\Delta T}\right)\frac{g\beta\Delta Ty}{v_{max}^2} = f_T^o\left(\frac{x}{y}\right). \qquad (6.36)$$

The existence of these wall functions for increasing Rayleigh number is checked in figure 6.8 for air with the Chien model. The wall functions for the turbulent quantities are verified in figure 6.9. The wall functions in figure 6.8 and 6.9 hold irrespective of the Prandtl number. George & Capp proposed the wall functions (6.28) for the outer layer, which are also irrespective of the Prandtl number. The

TABLE 6.6. Outer-layer scaling of the boundary layer (Chien model).

quantity	laminar		turbulent
	air	water	air and water
$\frac{u_\infty}{v_{max}}$	$-2.11\ Ra_y^{-1/4}$	$-3.61\ Ra_y^{-1/4}$	-0.0702
$\frac{\psi_\infty}{y\,v_{max}}$	$2.82\ Ra_y^{-1/4}$	$4.81\ Ra_y^{-1/4}$	0.0497
$\frac{(2k_{max}/3)^{1/2}}{v_{max}}$	0.	0.	0.183
$\frac{x_{kmax}}{y}$	--	--	0.0354
$\frac{\nu_{t,max}}{y\,v_{max}}$	0.	0.	0.00202
$\frac{x_{\nu t,max}}{y}$	--	--	0.0487

calculated wall functions are consistent with George & Capp's wall functions if $\delta \div y$ and if $(g\beta\Delta T\delta Q_T)^{1/3} \div v_{max}$. The boundary-layer thickness is usually defined as

$$\delta = \int_0^\infty v/v_{max}\, dx = \psi_\infty / v_{max}. \tag{6.37}$$

This indeed is proportional to y according to table 6.6. The proportionality for the velocities holds if

$$Nu_y = C^*\ Pr^{1/2}\ Ra_y^{1/2} \left(\frac{v_{max}}{\sqrt{g\beta\Delta Ty}} \right)^3 \tag{6.38}$$

in which C^* is a constant (also independent of Pr). Comparison of the calculations for Nu_y and v_{max} in table 6.5 shows that this relation indeed holds for increasing Rayleigh number; the large-Rayleigh-number calculations ($Ra_y = 10^{25}$) with the Chien model give a Ra_y independent, and also practically Pr independent, value for C^*, namely 0.0506 for air and 0.0529 for water. Therefore George & Capp's outer-layer length scale, δ, and velocity scale, $(g\beta\Delta T\delta Q_T)^{1/3}$, are similar to the calculated length scale, y, and velocity scale, v_{max}: this gives a full consistency between George & Capp's wall functions and the calculated wall functions. As a consequence the calculations do not agree with Cheesewright's proposal (6.30) and (6.32) for the wall functions in the outer layer. Equation (6.38) is important for the practical use of wall functions (see next section), because it relates a quantity at the wall to a quantity at the outer edge of the inner layer. If Nu_y scales with $Ra_y^{1/3}$, as is found in the experiments up to $Ra_y \sim 5\times10^{11}$, v_{max} scales with $(g\beta\Delta Ty)^{1/2}\ Ra_y^{-1/18}\ Pr^{-1/6}$ according to equation (6.38). Further, if for a fixed

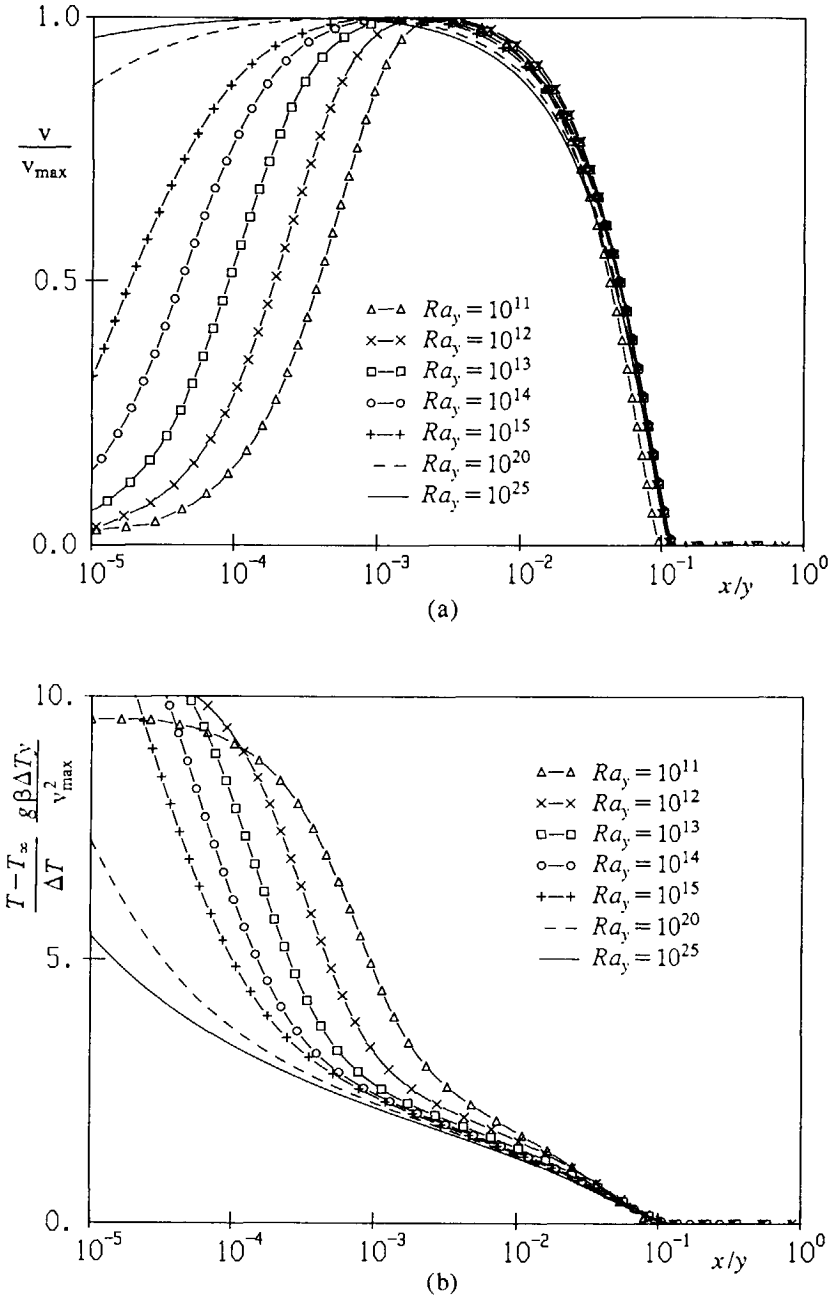

FIGURE 6.8. Wall functions in the outer layer (Chien model); (a) velocity, (b) temperature.

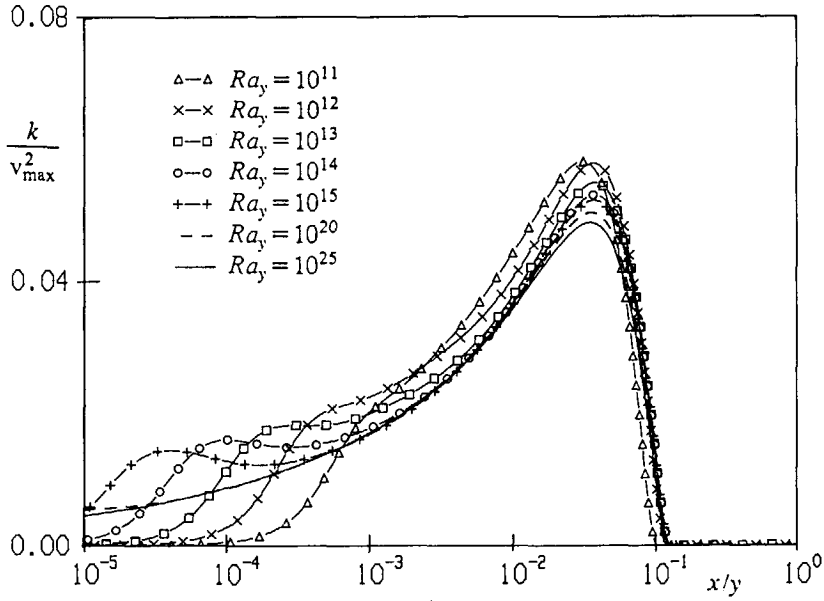

(a)

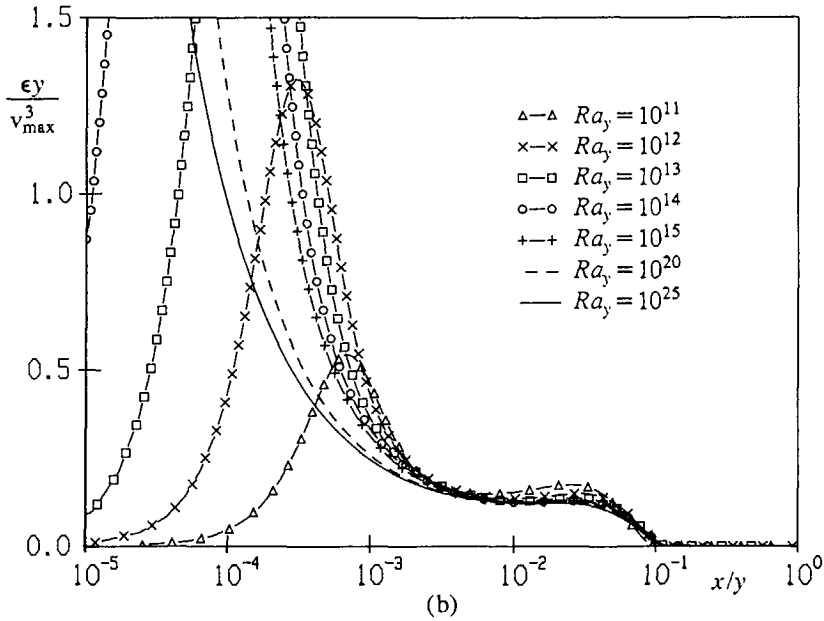

(b)

FIGURE 6.9(a,b). For caption see next page.

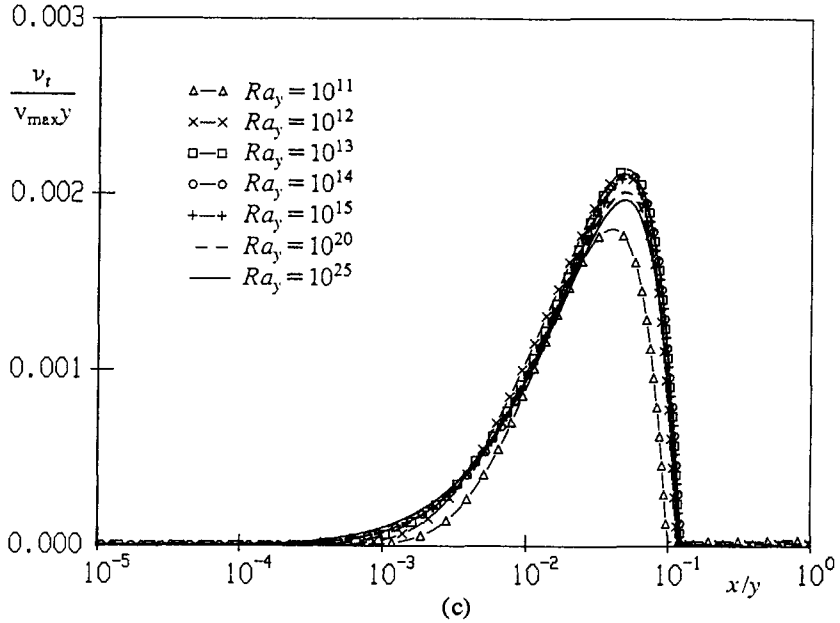

(c)

FIGURE 6.9. Wall functions for the turbulent quantities in the outer layer (Chien model); (a) turbulent kinetic energy, (b) dissipation rate of turbulent kinetic energy, (c) turbulent viscosity.

Prandtl number ν_{max} scales with $(g\beta\Delta T y)^{1/2}$ (which seems to be the limit in the large-Rayleigh-number calculations of table 6.5), Nu_y should scale with $Ra_y^{1/2}$.

The inner layer, which extends from the wall up to the velocity maximum, is much thinner than the outer layer. The velocity and the temperature in the part of the inner layer closest to the wall, the conductive/thermo-viscous sublayer, is given by equations (6.26). Substitution of the experimental relation for the wall-heat transfer (6.33) and the wall-shear stress (6.35) (we take the power 1/4 instead of 0.249) into equations (6.26) gives for air in the conductive/thermo-viscous sublayer:

$$\frac{\nu}{\sqrt{g\beta\Delta T y}} = 0.745\,(\frac{x}{y}\,Ra_y^{1/4}) - 0.593\,(\frac{x}{y}\,Ra_y^{1/4})^2 + 0.0235\,Ra_y^{1/12}\,(\frac{x}{y}\,Ra_y^{1/4})^3 + \cdots \qquad (6.39)$$

$$\frac{T - T_\infty}{\Delta T} = 1 - \zeta + \cdots .$$

The first two terms in the series expansion of the velocity show the laminar velocity and length scale, ν_b and $y\,Ra_y^{-1/4}$ respectively. These laminar scalings are firstly slightly disturbed in the third term, having a $Ra_y^{1/12}$ contribution. The velocity profiles in the inner layer at increasing Rayleigh numbers, as calculated with the Chien model for air, are shown in figure 6.10a. In this figure we have

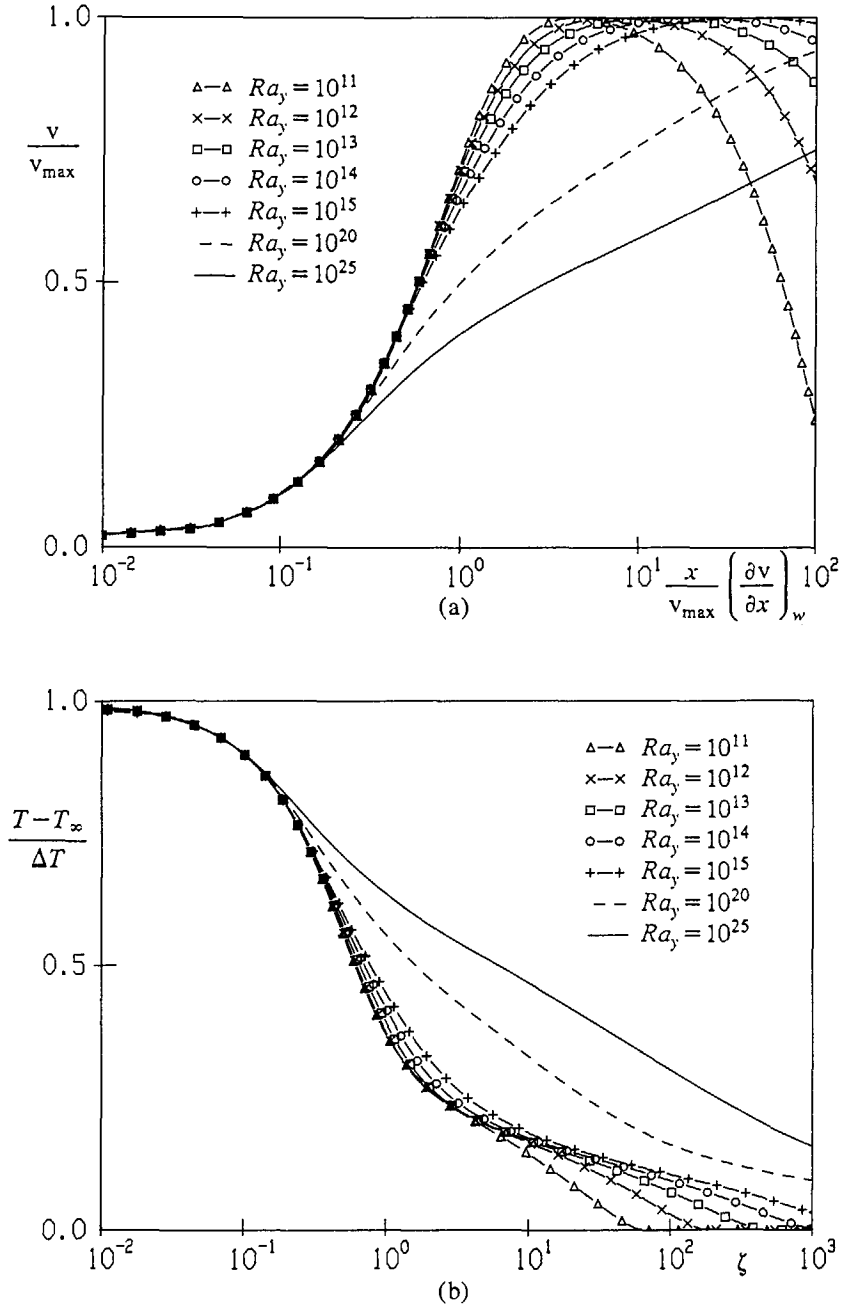

FIGURE 6.10. Profiles in the inner layer (Chien model, air);
(a) velocity, (b) temperature.

modified the laminar scalings a bit: we use v_{max} for the velocity and $v_{max}/(\partial v/\partial x)_w$ for the length. Because v_{max} is close to v_b (figure 6.7c), the modified scalings are consistent with the laminar scalings as long as the wall-shear stress coefficient has a $-1/4$ power dependence on Ra_y. Up to $Ra_y = 10^{15}$ the profiles in figure 6.7b almost coincide in whole the inner layer, *i.e.* up to the velocity maximum. The calculated wall-shear stress for air (figure 6.7b) only approximately shows the $-1/4$ power up to about $Ra_y = 10^{12}$, implying that for larger Rayleigh numbers the laminar scalings no longer hold. Moreover, beyond $Ra = 10^{15}$ the profiles in figure 6.10a do not coincide. Therefore, the scalings v_{max} and $v_{max}/(\partial v/\partial x)_w$ are *not* the proper inner-layer scalings for the velocity profile in the limit $Ra_y \to \infty$. Whatever we tried, the calculations did not give a single velocity and length scale: a wall function for the velocity in the inner layer does not seem to exist. Hence, George & Capp's proposal for the velocity wall function in the buoyant sublayer, (6.27a) or (6.29a), is not confirmed by the calculations. George & Capp's wall function does not even give a reasonable scaling for the lower Rayleigh numbers up to 10^{12}, because $v_0 = (g\beta\Delta T\nu)^{1/3}$ is a bad velocity scale (v_b or v_{max} are much better). Also the $-1/3$ power dependence on Ra_y in George & Capp's wall-shear stress (6.25a) is not confirmed by the experiments, nor by the calculations. On the contrary, the 1/3 power dependence on Ra_y in the wall-heat transfer of George & Capp (6.25b) is confirmed by the experiments, and also by the calculations at moderate Rayleigh numbers. The 1/3 power gives $\zeta \div x/(yRa_y^{-1/3})$ in equation (6.25b), which does not show the laminar length scale. The calculations in figure 6.10b show that the temperature profiles $(T-T_\infty)/\Delta T$ as a function of ζ only approximately coincide up to $Ra_y = 10^{15}$. This temperature profile agrees with the wall function (6.27) as proposed by George & Capp and by Cheesewright for the buoyant sublayer. We could even more or less recognize the $-1/3$ power in the calculations, as appearing in George & Capp's temperature wall function (6.29b) in the buoyant sublayer. For Rayleigh numbers beyond $Ra_y = 10^{15}$, however, the temperature profiles in figure 6.10b deviate from each other, implying that ΔT and $\Delta T/(\partial T/\partial x)_w$ are also *not* the proper inner-layer scalings for the temperature profile in the limit $Ra_y \to \infty$. As for the velocity, we could not derive proper scalings from the calculations. This suggests that a wall function for the temperature in the inner layer does not exist.

6.10. Practical use of wall functions

The existence of wall functions for the vertical natural-convection boundary layer is important for at least two reasons. In the first place it facilitates the verification of (new) high-Reynolds-number turbulence models for the hot vertical plate. Instead of verifying for a large number of Rayleigh numbers that there is agreement between the calculations and the experiments, only the agreement with the measured profile of the wall function has to be verified. In the second place the application of wall functions in calculations of complicated turbulent natural-convection flows can save grid points. This requires the assumption that the wall functions, which could be verified for the hot vertical plate in the isothermal environment, can also be applied to more complicated natural-convection flows, like the boundary-layer flow along a wall with a variable temperature or in a stratified environment (cavities). In this section we give some ideas about how the

wall functions can be implemented in a general natural-convection computation. The actual implementation of the new wall functions in our computational codes has not been performed yet in the present study.

The following formulation is expected to be most suitable for general natural-convection flows (of the heating-from-the-side class);

for the inner layer:

$$\frac{v}{v_{max}} = f_1\left(\frac{x}{v_{max}}\left(\frac{\partial v}{\partial x}\right)_w\right) \tag{6.40a}$$

$$\frac{T-T_\infty}{\Delta T} = f_2(\zeta). \tag{6.40b}$$

for the outer layer:

$$\frac{v_{max}-v}{v_{out}} = f_3\left(\frac{x}{x_{out}}\right) \tag{6.41a}$$

$$\frac{T-T_\infty}{\Delta T}\,\frac{g\beta\Delta T x_{out}}{v_{out}^2} = f_4\left(\frac{x}{x_{out}}\right) \tag{6.41b}$$

$$\frac{k}{v_{out}^2} = f_5\left(\frac{x}{x_{out}}\right) \tag{6.41c}$$

$$\frac{\epsilon x_{out}}{v_{out}^3} = f_6\left(\frac{x}{x_{out}}\right) \tag{6.41d}$$

$$\frac{\nu_t}{v_{out}x_{out}} = f_7\left(\frac{x}{x_{out}}\right) \tag{6.41e}$$

with

$$x_{out} = \delta = \int_0^\infty \frac{v}{v_{max}}\,dx$$

$$v_{out} = v_{max}.$$

In the previous section the profiles (6.40) for the inner layer were only checked to reasonably fit the velocity and temperature in the inner layer of the natural-convection boundary layer along the hot vertical plate in the isothermal environment. These profiles are *not* similarity profiles (wall functions) in the limit $Ra_y \to \infty$, but they only fit the turbulent results up to about $Ra_y = 10^{15}$. Fortunately, only few engineering natural-convection applications have their Rayleigh number beyond 10^{15}. The profiles (6.41) for the outer layer are wall functions for the vertical natural-convection boundary layer in the outer layer. In the previous section they were checked for the hot vertical plate in the isothermal environment up to $Ra_y = 10^{25}$. This value is far beyond the Rayleigh numbers appearing in most practical natural-convection applications. Instead of v_{max}, George & Capp

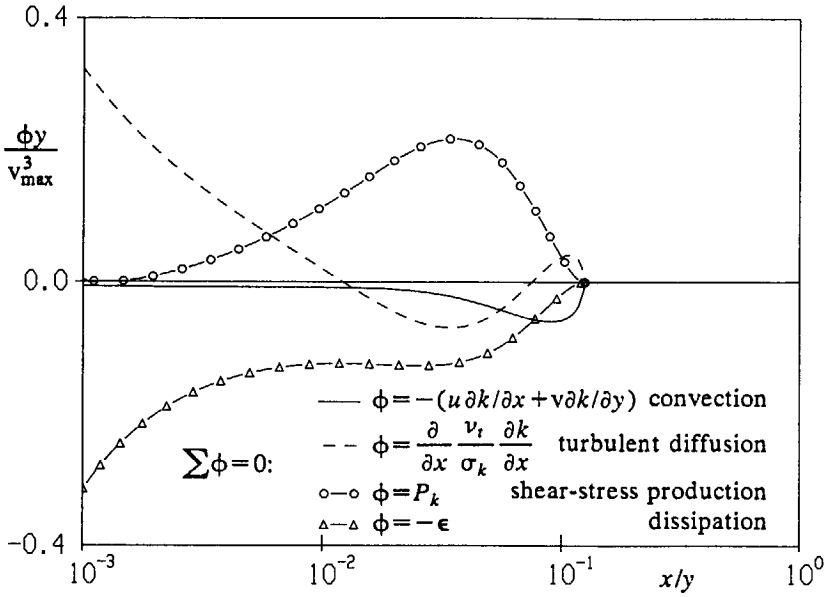

FIGURE 6.11. Different contributions to the k-equation in the outer layer (Chien model, air at $Ra_y=10^{15}$).

proposed $v_{G\&C}=(-g\beta\delta\nu(\partial T/\partial x)_w/Pr)^{1/3}$ for v_{out}. The velocity scale $v_{G\&C}$, however, was checked to be similar to v_{max}. For the plate we found that $\delta \div y$; we do not substitute this in the general formulation of the wall functions (6.41), as this would probably restrict the general applicability.

A remarkable difference between the inertial sublayer of the forced-convection boundary layer and the outer layer of the natural-convection boundary layer is that convection and diffusion for the turbulent kinetic energy can be neglected in the inertial sublayer but not in the outer layer. Neglecting these terms in the forced-convection boundary layer leads to an equilibrium of production and dissipation of turbulent kinetic energy (6.6) in the inertial sublayer. The importance of convection and diffusion in the balance of the kinetic energy in the outer layer of the natural-convection boundary layer is shown in figure 6.11 (the balance is given for air with the Chien model at $Ra_y=10^{15}$; because the proper scalings are used, the balance is actually independent of the Prandtl number and the Rayleigh number). The figure shows that there is no equilibrium of production and dissipation in the natural-convection boundary layer. Therefore the derivation of an analytical representation of the profiles of the wall functions for the natural-convection boundary-layer is more complicated than for the forced-convection boundary layer. For the forced-convection wall functions the equilibrium assumption was used to obtain the analytical forms (6.5) and (6.8). An analytical representation, however, is not essential for the implementation of wall functions in a general computation, because the profiles of the wall functions as calculated

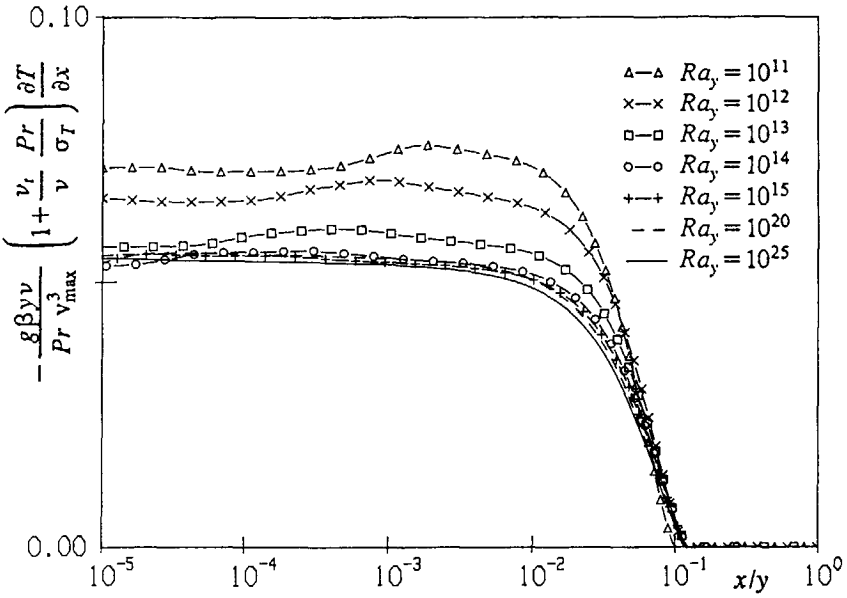

FIGURE 6.12. Total heat flux through the inner and outer layer (Chien model, air).

for the vertical plate can also be used in tabulated form.

When the wall functions (6.41) are used in a general natural-convection computation, the first inner grid point is positioned in the outer layer, *i.e.* beyond the position of the velocity maximum. At the first inner grid point the wall functions (6.41) give Dirichlet boundary conditions for v, T, k and ϵ. At each y grid line in the boundary layer additional equations are required to determine v_{max} and δ. Because δ is related to v_{max} via equation (6.37), actually only an additional equation for v_{max} is required.

The additional equation we are searching for must couple v_{max} to a quantity in the outer layer. Equation (6.38) couples v_{max} to the wall-heat transfer, which is a quantity for the inner layer. The wall-heat transfer in turn can be related to the temperature gradient at the first inner grid point in the outer layer by assuming that convection in the boundary-layer equation for the temperature (6.1) can be neglected. This yields

$$\frac{\partial T}{\partial x} = \left(1+\frac{\nu_t}{\nu}\frac{Pr}{\sigma_T}\right)^{-1}\left(\frac{\partial T}{\partial x}\right)_w . \tag{6.42a}$$

Figure 6.12 verifies that the convection can indeed be neglected for the temperature equation in the inner layer and in part of the outer layer for the plate: in these parts the total heat flux remains constant. Moreover the form of the flux in the figure is chosen such that the constant level converges to the value $C^*=0.0506$ for increasing Rayleigh number, as we also calculated for equations (6.38) in the

previous section. With the help of equation (6.38) for the plate (with $C^*=0.0506$ and $\delta/y=0.0497$, see table 6.6) expression (6.42a) can be rewritten as

$$\frac{v_{max}}{(g\beta\delta\nu)^{1/3}} = \frac{7.35}{Pr^{1/3}} \left[-\left(1+\frac{\nu_t}{\nu}\,\frac{Pr}{\sigma_T}\right)\frac{\partial T}{\partial x} \right]^{1/3}_{\text{first inner grid point.}} \qquad (6.42b)$$

This can be used as the additional equation for v_{max}.

6.11. Reynolds-stress calculations

The $k-\epsilon$ model uses the eddy-viscosity concept in the equations (2.13) to model the Reynolds stresses and the turbulent heat fluxes. The eddy-viscosity based $k-\epsilon$ model has the following characteristics:

(i) The turbulence is modelled by a local *isotropic* effective turbulent viscosity.

(ii) The model gives isotropic turbulent intensities, i.e. $u_i'^2=2k/3$. (Actually the model also adds a contribution $-2\nu_t(\partial u_i/\partial x_i)$, which is negligibly small in boundary-layer flows).

(iii) There is a strict analogy between the Reynolds stresses and the turbulent heat fluxes, as expressed by a constant value for σ_T.

(iv) The turbulent flux vector $-u_i'\phi'$ (i=1,2,3) for a quantity ϕ has the same direction as the mean gradient vector of ϕ.

Tsuji & Nagano (1988b, 1989) have measured the turbulence characteristics in the natural-convection boundary layer. In contrast with (ii), the boundary layer turns out to be anisotropic; for example, the maximum of the turbulent intensity in flow direction ($(v'^2)^{1/2}$) is about 1.5 times the maximum intensity normal to the wall ($(u'^2)^{1/2}$). Also characteristic (iii) does not hold through the whole boundary-layer thickness, and in some parts σ_T is not constant. Further, in contrast to (iv), the turbulent fluxes do not have the direction of the mean gradient field: fluxes in the flow direction have the same order of magnitude as the fluxes normal to the wall. In particular the Reynolds stress $\overline{u'v'}$ does not vanish at the position of the velocity maximum. Characteristic (iv) also leads to a zero G_k source in the natural-convection boundary layer. It does not seem to be very realistic that the turbulence in the $k-\epsilon$ model only extracts its energy from the mean velocity field (via P_k), but not from the mean temperature field (via G_k).

It is clear that some of the characteristics of the $k-\epsilon$ model do not agree with the measured turbulence characteristics. Of course, inaccuracies in the turbulence model do not necessarily lead to an erroneous prediction of the mean velocity and temperature field. Actually, as described in the previous sections, some of the low-Reynolds-number models give a very good prediction for the mean velocity field and the mean temperature field, including the wall-heat transfer and the wall-shear stress. To check the consequences of the use of the eddy-viscosity concept in the $k-\epsilon$ model for the turbulent characteristics, we have also calculated the turbulent natural-convection boundary layer with the Reynolds-stress model, which does not make the restrictions (i)-(iv). Details of the calculations are given in a separate paper by Peeters and the present author (1990); in this section only the main features of the Reynolds-stress results are described. A review of the essentials of Reynolds-stress models is given by Launder (1988). Only To & Humphrey

(1986) have already applied the Reynolds-stress model to the turbulent natural-convection boundary layer along a hot vertical plate. In contrast to our study, in which the fully differential Reynolds-stress model is solved, To & Humphrey used the algebraic Reynolds-stress model, implying that convection and diffusion are neglected in the Reynolds-stress equations. We mentioned in section 6.7 that repeating the $k-\epsilon$ calculations of To & Humphrey with our own computational code led to large deviations; also the results which To & Humphrey presented for the algebraic-stress model could not be reproduced with our code. The use of an algebraic-stress model, however, is not justified in the natural-convection boundary layer, because convection and diffusion processes are important as was illustrated in figure 6.11.

Similar to the derivation of the k-equation in section 2.4, equations for the Reynolds stresses $-\overline{u_i'u_j'}$ and the turbulent heat fluxes $-\overline{u_i'T'}$ can directly be derived from the Navier-Stokes equations (2.7) and the Reynolds equations (2.11):

$$u_k \frac{\partial \overline{u_i'u_j'}}{\partial x_k} = d_{ij} + P_{ij} + G_{ij} + \Phi_{ij} - \epsilon_{ij} \tag{6.43a}$$

$$u_k \frac{\partial \overline{u_i'T'}}{\partial x_k} = d_{i\theta} + P_{i\theta} + G_{i\theta} + \Phi_{i\theta} - \epsilon_{i\theta} \tag{6.43b}$$

with $d=$ diffusion, $P=$ shear-stress production, $G=$ buoyant production, $\Phi=$ correlation with pressure fluctuations including pressure reflections at the wall and $\epsilon=$ dissipation. The expressions for the different terms and the way they are modelled are given in the Appendix. The Appendix also gives the boundary-layer simplifications which are applied to the Reynolds-stress equations along the hot vertical plate. The boundary-layer equations for the Reynolds stresses were solved numerically. The system consists of 12 parabolic partial differential equations: besides the continuity equation, we have an equation for v, T, $\overline{u'v'}$, u'^2, v'^2, w'^2, $\overline{u'T'}$, $\overline{v'T'}$, T'^2, ϵ and ϵ_θ.

If the sum of the equations for the normal stresses (6.43a) is taken, and the result is divided by 2, an equation for k is obtained

$$u\frac{\partial k}{\partial x} + v\frac{\partial k}{\partial y} = \frac{\partial}{\partial x}\left(\nu + c_s \frac{k}{\epsilon}\overline{u'^2}\right)\frac{\partial k}{\partial x} + P_k + G_k - \epsilon + D \tag{6.44}$$

with

$$P_k = \frac{1}{2}P_{ii} = -\overline{u'v'}\frac{\partial v}{\partial x}, \quad G_k = \frac{1}{2}G_{ii} = g\beta\overline{v'T'}.$$

The D term is the low-Reynolds-number modification from the Chien model (see table 6.1). In contrast to the k-equation in the $k-\epsilon$ model (6.10), the G_k term in the turbulent kinetic-energy balance (6.44) for the Reynolds-stress model is nonzero. The term Φ_{ij} in equation (6.43a) contains pressure fluctuations, which redistribute energy over the normal stresses. The total kinetic energy is not directly altered by Φ, as expressed by $\Phi_{ii}=0$, causing that Φ is absent in the k-equation (6.44).

The boundary-layer equations for the Reynolds stresses (6.43) were solved for air up to $Ra_y = 6.38 \times 10^{10}$, which is the Rayleigh number at which Tsuji & Nagano measured the turbulence characteristics. The numerical grid was successively refined up to 200×200 points, showing that the finest grids give almost grid-independent results. A difficulty of using the Reynolds-stress model is that there is no consensus in the literature on the best choice for the numerical values of the model constants. The sensitivity of Nu_y, v_{max} and $\nu_{t,max}$ (the maximum of $-\overline{u'v'}/(\partial v/\partial x)$) to these constants was determined by varying the constants in the range of values reported in the literature. The constants appearing in the model for the pressure fluctuations Φ have the largest influence. For example varying C_1 in Φ (see the Appendix) between 2.0 and 2.4 gives at $Ra_y = 6.38 \times 10^{10}$: $0.116 < Nu_y/Ra_y^{1/3} < 0.128$, $0.364 > v_{max}/(g\beta\Delta Ty)^{1/2} > 0.363$ and $119 > \nu_{t,max}/\nu > 109$. These variations are not very large. The values for the constants applied in the sequel of this section were mainly taken from Hossain & Rodi (1982), who recommended these values for buoyant flows. At $Ra_y = 6.38 \times 10^{10}$ this set of constants gives: $Nu_y/Ra_y^{1/3} = 0.122$, $v_{max}/(g\beta\Delta Ty)^{1/2} = 0.363$ and $\nu_t/\nu = 114$. These values are close to the experiments, which give $Nu_y/Ra_y^{1/3} = 0.119$, $v_{max}/(g\beta\Delta Ty)^{1/2} = 0.345$ and $\nu_t/\nu = 120$. Another difficulty of the use of a Reynolds-stress model close to a fixed wall is that low-Reynolds-number modifications for this model are not well investigated yet in the literature. In the present Reynolds-stress calculations we simply assumed that the low-Reynolds-number modifications of Chien, as originally proposed for the $k-\epsilon$ model, could also be generalized to the Reynolds-stress model (see the Appendix).

Figure 6.13 compares the normal stresses for the Reynolds-stress model with the experimental values. Tsuji & Nagano only measured the normal stresses perpendicular to the wall (u'^2) and in the flow direction (v'^2). The Reynolds-stress model predicts $(u'^2)^{1/2}/v_{max}$ close to the experiment, but the maximum of $(v'^2)^{1/2}/v_{max}$ is overpredicted by 25%. Figure 6.13 also shows that the total turbulent kinetic energy in the Reynolds-stress model is close to the value in the $k-\epsilon$ model (the $k-\epsilon$ model uses the low-Reynolds-number modification of Chien). Therefore, the inclusion of anisotropy in the Reynolds-stress model does not affect the total turbulent kinetic-energy level.

Figure 6.14 compares the measured Reynolds shear stress $\overline{u'v'}$ and the measured turbulent heat flux $u'T'$ with the calculations for both the Reynolds-stress model and the $k-\epsilon$ model. The Reynolds-stress model closely predicts the measurements in the outer layer, but the $k-\epsilon$ model overpredicts the maximum in $\overline{u'v'}/v_{max}^2$ by 38% and the maximum in $u'T'/(v_{max}\Delta T)$ by 32%. Differences between the Reynolds-stress model and the experiments only occur in the inner layer. In contrast to the experiments both the Reynolds-stress model and the $k-\epsilon$ model give a negative stress in the inner layer; the $k-\epsilon$ model changes the sign of the stress precisely at the position of the velocity maximum, whereas the Reynolds-stress model changes the sign at a position very close to the position of the velocity maximum. A possible explanation for the difference between the calculations and the experiments might be an insufficient accuracy of the turbulence measurements in the inner layer. For example, in contrast to the experiments of Tsuji & Nagano, Miyamoto *et al.* (1982, 1983) measured a slightly negative $\overline{u'v'}$

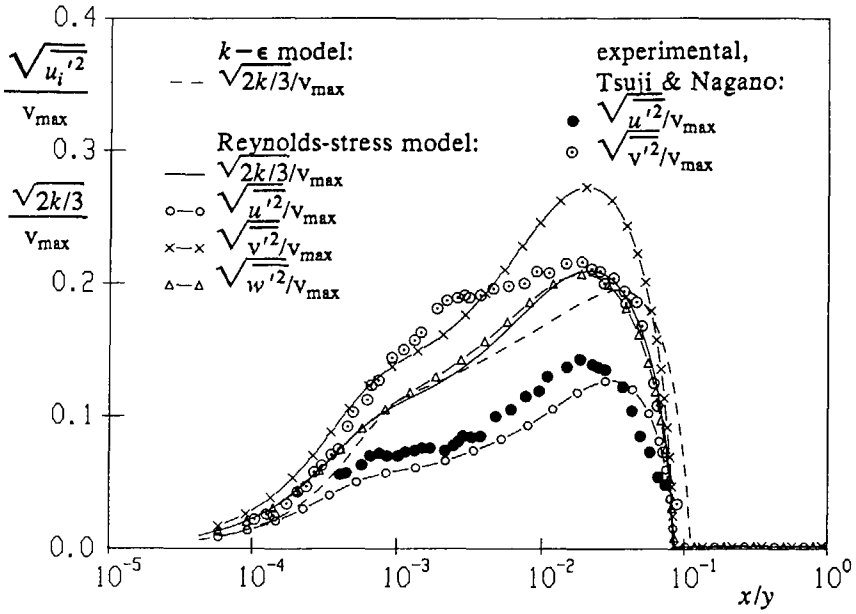

FIGURE 6.13. Anisotropy for air at $Ra_y = 6.38 \times 10^{10}$.

in the inner layer, but less negative than in the calculations. On the other hand, proper near-wall modifications for the Reynolds-stress model have not been fully established yet in the literature, and the modifications applied in the present study might cause an insufficient accuracy in the inner layer.

Closely related to the turbulence quantities $\overline{u'v'}$ and $\overline{u'T'}$ are the turbulent viscosity ν_t $(=-\overline{u'v'}/(\partial v/\partial x))$ and the turbulent Prandtl number for the temperature σ_T $(=\nu_t(\partial T/\partial x)/\overline{u'T'})$. These quantities are compared with the experiments of Tsuji & Nagano in figure 6.15. Because $\overline{u'v'}$ does not vanish precisely at the position of the velocity maximum, the experiments and the Reynolds-stress model give a singularity for ν_t and σ_T at this position. Of course, the $k-\epsilon$ model does not show a singularity because the eddy-viscosity concept prescribes that $\overline{u'v'}=0$ if $\partial v/\partial x=0$, as occurs for the velocity maximum. As we already noted in section 6.7, the maximum of ν_t in the $k-\epsilon$ model is about twice the experimental value. Figure 6.15a shows that this difference is fully corrected by the Reynolds-stress model. Comparison in figure 6.15b of the Reynolds-stress calculation for σ_T with the measured value shows that differences are restricted to the inner layer. In the part of the outer layer close to the position of the velocity maximum the σ_T value as calculated by the Reynolds-stress model is somewhat above the value 0.9, which is the prescribed constant value for σ_T in the $k-\epsilon$ model. In the rest of the outer layer, where the turbulent viscosity has its largest influence, the value of 0.9 is a reasonably accurate choice.

Figure 6.16 shows the production terms P_k and G_k in the equation for the turbulent kinetic energy. The result that G_k becomes nonzero in the Reynolds-stress

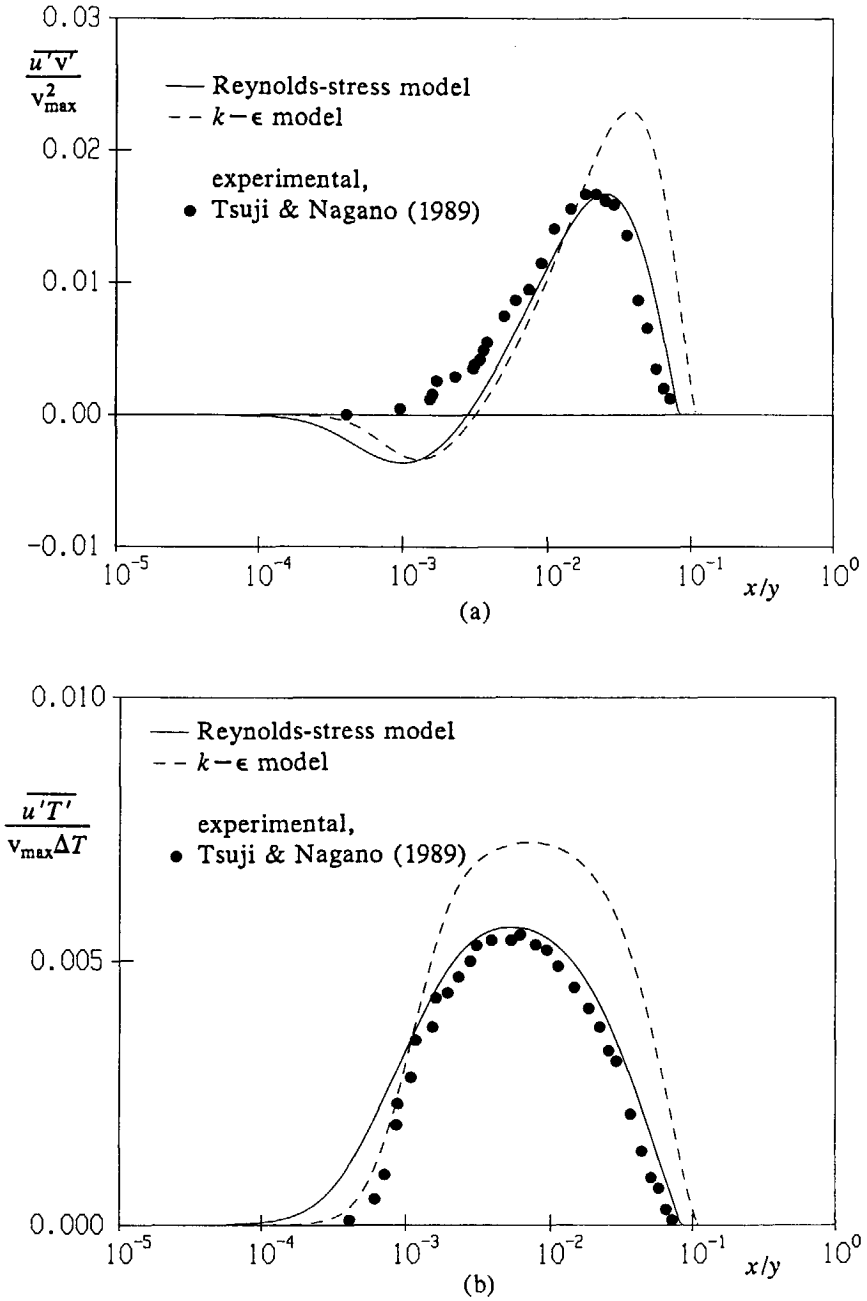

FIGURE 6.14. Turbulence characteristics for air at $Ra_y = 6.38 \times 10^{10}$; (a) Reynolds shear stress, (b) heat flux.

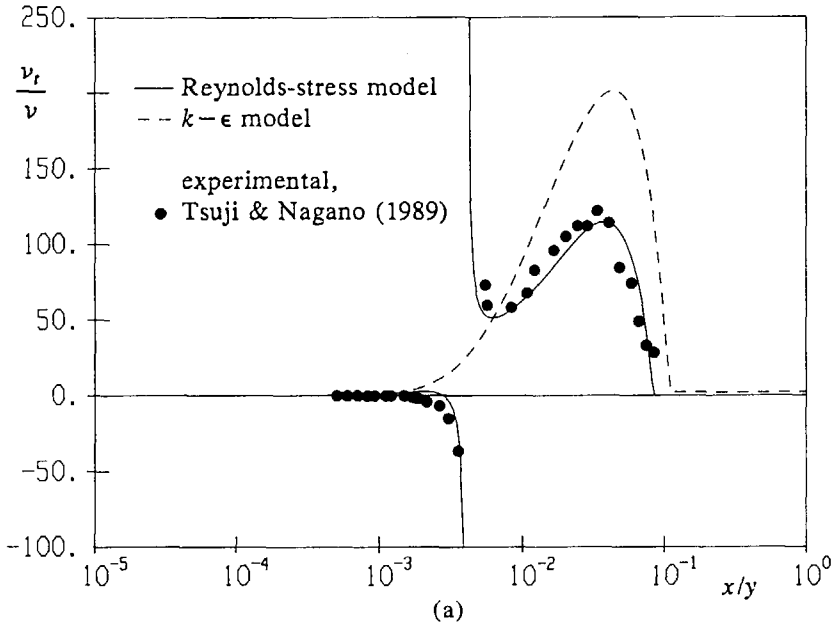

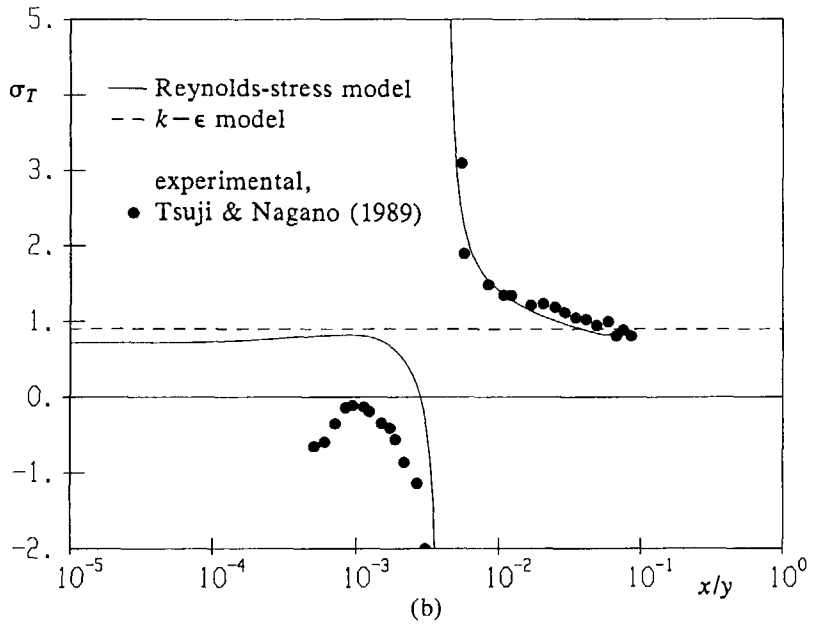

FIGURE 6.15. Additional turbulence characteristics for air at $Ra_y = 6.38 \times 10^{10}$; (a) turbulent viscosity, (b) turbulent Prandtl number for the temperature.

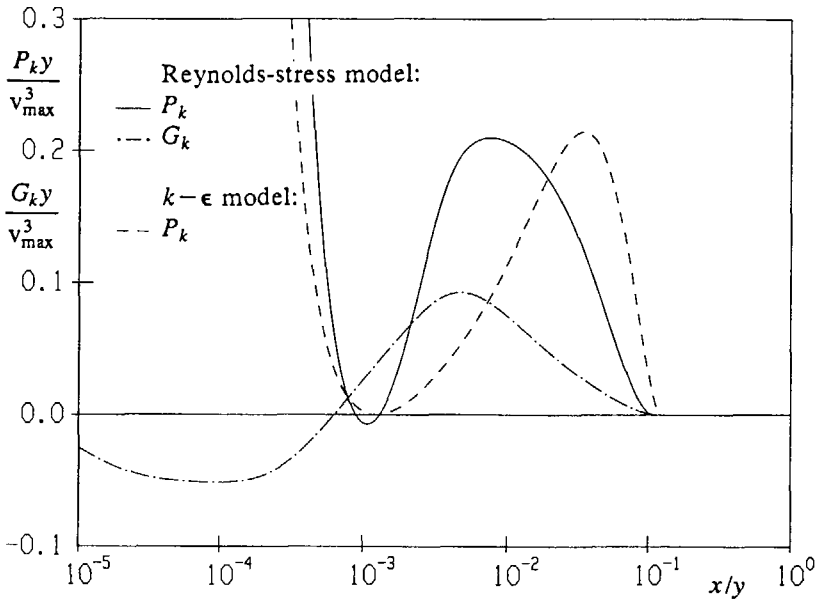

FIGURE 6.16. Balance for the turbulent kinetic energy (air, $Ra_y = 10^{15}$).

model illustrates that this model does not necessarily predict that turbulent heat fluxes have the same direction as the mean temperature gradient. Actually G_k forms about 30% of the total production for k in the Reynolds-stress model. On the contrary, the $k-\epsilon$ model gives a zero G_k term. Furthermore, the position of P_k in the Reynolds-stress model considerably differs from its position in the $k-\epsilon$ model.

6.12. Conclusion

Accurate solutions of the turbulent boundary-layer equations along the hot vertical plate in an isothermal environment were obtained for air and water up to $Ra_y = 10^{25}$. The solution for the low-Reynolds-number $k-\epsilon$ models is nonunique for increasing Rayleigh number: both a laminar and a turbulent solution exist. The solution in the laminar-turbulent transition regime strongly depends on the energy introduced to trigger the transition.

Low-Reynolds-number modifications of the standard $k-\epsilon$ model are needed to predict quantities in the inner layer (like the wall-heat transfer) reasonably close to the experiments. The standard $k-\epsilon$ model (with $k=0$, $\epsilon=\infty$ at the wall) largely overpredicts the wall-heat transfer by 52% for air at $Ra_y = 10^{11}$ and by 220% for water at $Ra_y = 10^{13}$. The low-Reynolds-number models of Lam & Bremhorst, Chien and Jones & Launder perform best: the wall-heat transfer is accurate within about 15% for air at $Ra_y = 10^{11}$ and within about 25% for water at $Ra_y = 10^{13}$. All $k-\epsilon$ models tested (except the Hoffman model) accurately predict the measured velocity maximum. Differences between the models for the outer-layer quantities

(like the maximum turbulent viscosity) are small and only due to differences in the high-Reynolds-number constants. The $k-\epsilon$ models strongly overpredict the maximum of the turbulent viscosity by about 100%. The algebraic model of Cebeci & Smith performs worse than the $k-\epsilon$ models: it gives a laminar-like velocity profile (low turbulence, too high velocity maximum, too thin boundary-layer thickness).

The proper scalings and wall functions can be derived from the $k-\epsilon$ solutions by examining the Ra_y dependence of quantities ϕ in $\phi=\alpha Ra_y^{\gamma}$. Model differences mainly influence the α values in the inner layer, whereas γ is almost independent of the model used.

The value of γ for quantities in the inner layer does not become fully independent of the Rayleigh number up to at least $Ra_y=10^{25}$. For example γ for the wall-heat transfer (Nu_y) for air increases from 3/8 at $Ra_y=10^{12}$ to 0.435 at $Ra_y=10^{25}$, showing that the difference with $\gamma=1/3$, as measured up to about $Ra_y=5\times10^{11}$, becomes larger for increasing Rayleigh number. Because γ remains dependent on Ra_y, wall functions in the inner layer do not seem to exist. A best fit for the results up to about $Ra_y=10^{15}$ is given by the velocity profile v/v_{max} *vs* $(x/v_{max})(\partial v/\partial x)_w$ and the temperature profile $(T-T_\infty)/\Delta T$ *vs* ζ $(=xNu_y/y)$. This velocity profile does not agree with George & Capp's wall function for the velocity in the buoyant sublayer in the inner layer, giving $v/(g\beta\Delta T\nu)^{1/3}$ *vs* ζ. The temperature profile agrees with the wall functions as proposed by George & Capp and Cheesewright.

The γ values in the outer layer become independent of Ra_y for $Ra_y\to\infty$, implying that wall functions in the outer layer exist. The proper length scale is y and the proper velocity scale is v_{max}. The proper temperature scale is $v_{max}^2/(g\beta y)$. George & Capp propose different scalings; our calculations, however, show that their scalings are proportional to v_{max} and y. This implies that the our wall functions are consistent with George & Capp's proposal. On the contrary, they do not agree with Cheesewright's proposal. v_{max} itself approximately scales with the laminar velocity scale $(g\beta\Delta Ty)^{1/2}$.

The differential Reynolds-stress model corrects the shortcomings of the eddy-viscosity concept in the $k-\epsilon$ model. The Reynolds-stress model reasonably predicts the measured anisotropy in the turbulence. The turbulent Prandtl number is only constant in the part of the outer layer not to close to the velocity maximum. Further, the turbulent heat flux does not have the direction of the mean temperature gradient, causing that the buoyant production (G_k) does not vanish, as is found for the $k-\epsilon$ model. The better treatment of the turbulence in the Reynolds-stress model fully corrects the 100%-overprediction for the maximum of the turbulent viscosity in the $k-\epsilon$ model.

7. TURBULENT FLOW IN THE CAVITY

7.1. Introduction

In the previous chapter we have compared a number of turbulence models for the boundary layer along the hot vertical plate in an isothermal environment. In this chapter the standard $k-\epsilon$ model and two of the best performing low-Reynolds-number $k-\epsilon$ models for the plate (the models of Chien and Jones & Launder) are used to calculate the turbulent flow in the square cavity. The turbulent flow of air and water is calculated up to $Ra=10^{15}$. The calculations for air with the Chien model are even extended up to $Ra=10^{17}$.

A difficulty is that accurate experiments for the turbulent flow in the square cavity do not exist. We have used the experimental wall-heat transfer for tall cavities and for the hot vertical plate in an isothermal environment to make a guess of the experimental averaged wall-heat transfer through the vertical wall of the square cavity. The prediction of the different models is compared with this experimental value. The calculated maximum of the vertical velocity in the vertical boundary layer along the wall of the square cavity is compared with the experiments of Cheesewright *et al.* (1986) as obtained in a cavity with a height-width ratio of 5.

As for the laminar case, also for the turbulent case the core of the cavity becomes stratified. Therefore the boundary layer along the hot vertical wall of the cavity is expected to show a close resemblance with the boundary layer along the hot vertical plate in a stratified environment. Here we will only compare the cavity boundary layer with the boundary layer along the plate in an isothermal environment. In particular we compare the scalings for the cavity with the scalings for the plate. The cavity boundary layer for a given fluid is more complicated than the boundary layer along the plate, because characteristic quantities in the cavity, like the wall-heat transfer and the velocity maximum, depend on two variables (Ra and y/H) instead of one (Ra_y). We determine the scalings for the cavity by both examining the quantities at a fixed height for increasing Rayleigh number and by examining the quantities at a fixed Rayleigh number for increasing height. This can answer whether the wall functions as derived for the plate in the previous chapter also apply with a reasonable accuracy to the cavity.

7.2. Reynolds equations

We consider the two-dimensional square cavity that is differentially heated over the vertical walls (figure 1.1a). The left hot wall has a temperature T_h and the right cold wall has a temperature T_c. The height of the cavity is H. The horizontal floor and ceiling are both adiabatic.

The turbulent flow in the cavity is described by the Reynolds equations (2.11), using the eddy-viscosity model (2.13) for the Reynolds stresses and the turbulent heat fluxes. The gradient $-\partial(2k/3)/\partial x_i$ (also referred to as the gradient of the turbulent pressure), which appears in the momentum equations, is neglected. Under the Boussinesq approximation the Reynolds equations read

$$\frac{\partial u}{\partial x} + \frac{\partial v}{\partial y} = 0$$

$$\frac{\partial u}{\partial t} + u\frac{\partial u}{\partial x} + v\frac{\partial u}{\partial y} = -\frac{1}{\rho}\frac{\partial p}{\partial x} + \frac{\partial}{\partial x}(\nu+\nu_t)\left(2\frac{\partial u}{\partial x}\right) + \frac{\partial}{\partial y}(\nu+\nu_t)\left(\frac{\partial u}{\partial y} + \frac{\partial v}{\partial x}\right)$$

$$\frac{\partial v}{\partial t} + u\frac{\partial v}{\partial x} + v\frac{\partial v}{\partial y} = -\frac{1}{\rho}\frac{\partial p}{\partial y} + g\beta(T-T_c) + \frac{\partial}{\partial x}(\nu+\nu_t)\left(\frac{\partial v}{\partial x} + \frac{\partial u}{\partial y}\right) + \frac{\partial}{\partial y}(\nu+\nu_t)\left(2\frac{\partial v}{\partial y}\right)$$

$$\frac{\partial T}{\partial t} + u\frac{\partial T}{\partial x} + v\frac{\partial T}{\partial y} = \frac{\partial}{\partial x}\left(\frac{\nu}{Pr}+\frac{\nu_t}{\sigma_T}\right)\frac{\partial T}{\partial x} + \frac{\partial}{\partial y}\left(\frac{\nu}{Pr}+\frac{\nu_t}{\sigma_T}\right)\frac{\partial T}{\partial y} \qquad (7.1)$$

$$\frac{\partial k}{\partial t} + u\frac{\partial k}{\partial x} + v\frac{\partial k}{\partial y} = \frac{\partial}{\partial x}\left(\nu+\frac{\nu_t}{\sigma_k}\right)\frac{\partial k}{\partial x} + \frac{\partial}{\partial y}\left(\nu+\frac{\nu_t}{\sigma_k}\right)\frac{\partial k}{\partial y} + P_k + G_k - \epsilon + D$$

$$\frac{\partial \epsilon}{\partial t} + u\frac{\partial \epsilon}{\partial x} + v\frac{\partial \epsilon}{\partial y} = \frac{\partial}{\partial x}\left(\nu+\frac{\nu_t}{\sigma_\epsilon}\right)\frac{\partial \epsilon}{\partial x} + \frac{\partial}{\partial y}\left(\nu+\frac{\nu_t}{\sigma_\epsilon}\right)\frac{\partial \epsilon}{\partial y} + (c_{\epsilon 1}f_1(P_k+c_{\epsilon 3}G_k)-c_{\epsilon 2}f_2\epsilon)\frac{\epsilon}{k} + E$$

with

$$P_k = \nu_t\left(2\left(\frac{\partial u}{\partial x}\right)^2 + 2\left(\frac{\partial v}{\partial y}\right)^2 + \left(\frac{\partial u}{\partial y} + \frac{\partial v}{\partial x}\right)^2\right), \quad G_k = -\frac{\nu_t}{\sigma_T}g\beta\frac{\partial T}{\partial y},$$

$$\nu_t = c_\mu f_\mu \frac{k^2}{\epsilon}.$$

Despite the time-averaging, the unsteady terms are kept in the formulation. In fact the time-averaging is restricted to the broad-band spectrum of turbulence, whereas the remaining unsteady terms account for all weak unsteadiness that does not belong to the turbulence. We can also define that the unsteady terms represent all unsteadiness that is not modelled by the turbulence model. In this study we are interested in the large-time behaviour of the Reynolds-averaged flow; we check whether all unsteadiness dies out and a steady final solution is reached.

The Reynolds stresses and the turbulent heat fluxes in the Reynolds equations are modelled with the $k-\epsilon$ model. Three versions of the $k-\epsilon$ model are compared:

(i) *standard* $k-\epsilon$ *model*

$c_\mu=0.09$, $c_{\epsilon 1}=1.44$, $c_{\epsilon 2}=1.92$, $\sigma_T=0.9$, $\sigma_k=1.0$, $\sigma_\epsilon=1.3$,

$f_\mu=f_1=f_2=1.0$, $D=E=0$,

and $k=0$, $\epsilon=\infty$ at the wall.

(ii) *low-Reynolds-number $k-\epsilon$ model of Chien (1980)*

$c_\mu=0.09$, $c_{\epsilon 1}=1.35$, $c_{\epsilon 2}=1.8$, $\sigma_T=0.9$, $\sigma_k=1.0$, $\sigma_\epsilon=1.3$,

$f_\mu=1-\exp(-0.0115x^+)$, $f_1=1.0$, $f_2=1-\frac{2}{9}\exp(-(Re_t/6)^2)$,

$D=-2\nu\frac{k}{x_n^2}$, $E=-\frac{2\nu\epsilon}{x_n^2}\exp(-0.5x^+)$,

and $k=\epsilon=0$ at the wall.

(iii) *low-Reynolds-number $k-\epsilon$ model of Jones & Launder (1972)*

$c_\mu=0.09$, $c_{\epsilon 1}=1.44$, $c_{\epsilon 2}=1.92$, $\sigma_T=0.9$, $\sigma_k=1.0$, $\sigma_\epsilon=1.3$,

$f_\mu=\exp\left(\frac{-2.5}{1+Re_t/50}\right)$, $f_1=1.0$, $f_2=1-0.3\exp(-Re_t^2)$,

$D=-2\nu\left[\left(\frac{\partial\sqrt{k}}{\partial x}\right)^2+\left(\frac{\partial\sqrt{k}}{\partial y}\right)^2\right]$, $E=2\nu\nu_t\left[\left(\frac{\partial^2 u}{\partial y^2}\right)^2+\left(\frac{\partial^2 v}{\partial x^2}\right)^2\right]$,

and $k=\epsilon=0$ at the wall.

In these relations the following dimensionless variables appear: $x^+=x_n v_\tau/\nu$, $v_\tau=(\nu(\partial v_t/\partial x_n)_w)^{1/2}$ and $Re_t=k^2/(\nu\epsilon)$ (x_n is the distance to the closest fixed wall and v_t is the velocity component tangential to that wall).

Rodi (1980) has suggested that the coefficient $c_{\epsilon 3}$ is close to 1 in vertical boundary layers and close to 0 in horizontal boundary layers. An approximation that satisfies both limits is used in the present study

$$c_{\epsilon 3} = \tanh|v/u|. \tag{7.2}$$

In the literature there is still no consensus on the right formulation of $c_{\epsilon 3}$ and G_k. For example Fraikin *et al.* (1982) took $c_{\epsilon 3} = 0.7/c_{\epsilon 1}$ in their turbulent cavity calculations, whereas Ince & Launder (1988) took $c_{\epsilon 3}=1$. The turbulent solution in the cavity consists of natural-convection boundary layers along the vertical walls and an almost stagnant, stably stratified core region. The turbulent solution for air at $Ra=10^{13}$, as calculated with the Chien model, is shown in figure 7.1. The streamlines in the core are practically horizontal. Turbulence is concentrated in the vertical boundary layers and is almost absent in the core. In order to understand the meaning of the G_k term, we remind the stability analyses that were mentioned in section 5.5. The stability analysis for the laminar natural-convection boundary layer along the hot vertical plate in an isothermal environment (see *e.g.* Nachtsheim, 1963) shows that the critical gradients in both the velocity profile and the temperature profile can give an instability (a hydrodynamic and thermal instability respectively), which initiates the transition to turbulence. The hydrodynamic instability mechanism is represented by the P_k term in the k-equation, whereas the

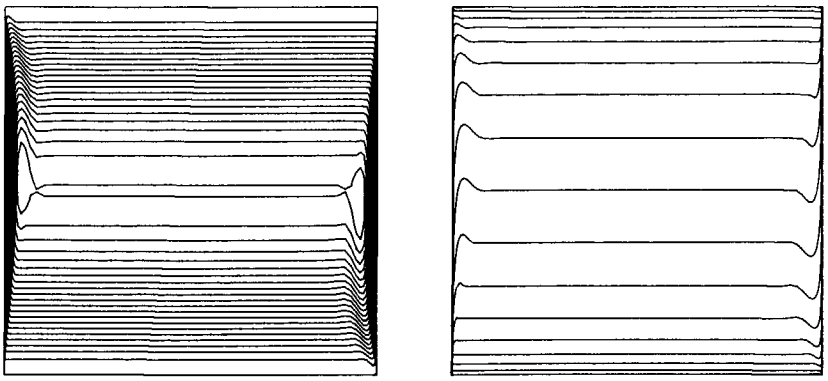

(a) (b)

FIGURE 7.1. Turbulent flow of air at $Ra=10^{13}$ (Chien model); (a) streamlines, (b) isotherms.

thermal instability mechanism is represented by the G_k term. The stability analysis for the core (approximated as an inviscid, stagnant, thermally stratified environment; see *e.g.* Drazin & Reid, 1981) shows that the thermal instability is only damped if the stratification is stable, *i.e.* if the density decreases with the height, or (provided $\beta>0$) if the temperature increases with the height. The present formulation for the thermal source G_k in the k-equation does not seem to be in line with these stability analyses. The source $c_{\epsilon 1}c_{\epsilon 3}G_k$ has the right sign in the stably stratified core, namely ≤ 0, but its value is everywhere close to zero. This is a consequence of the almost horizontal streamlines in the core, giving $c_{\epsilon 3}\sim 0$ according to equation (7.2). Therefore it might be better to use $c_{\epsilon 3}=1$ in the core. Because the y-derivatives in the vertical boundary layers are small compared to the x-derivatives, the present formulation gives $|G_k| << |P_k|$. This implies that the thermal instability mechanism is not accounted for very realistically in the vertical boundary layer. Ince & Launder (1988) have proposed the inclusion of a $\partial T/\partial x$ contribution in the G_k term. Actually the use of the Reynolds-stress model, instead of the $k-\epsilon$ model, automatically leads to such a contribution. In the previous chapter we have used the Reynolds-stress model for the turbulent natural-convection boundary layer along the hot vertical plate in an isothermal environment. In the inner layer (*i.e.* from the wall up to the velocity maximum) G_k is small compared to P_k, but in the outer layer (*i.e.* beyond the velocity maximum) G_k forms about 30% of the total production of turbulent kinetic energy. Although the Reynolds-stress model predicts that G_k cannot be neglected in the turbulent kinetic energy production, in the present cavity calculations we still use the old formulation for G_k, giving a negligible small contribution to the production of k. In analogy with the comparison between the Reynolds-stress model and the $k-\epsilon$ model for the plate (section 6.11), we expect that the negligence of the G_k

production mainly influences the turbulence characteristics, but that it has only a small effect on the mean field quantities.

After nondimensionalization of the dependent and independent variables (with the help of H, $\Delta T=T_h-T_c$, $g\beta$ and ν), the solution in the square cavity depends on only two characteristic numbers: the Prandtl number (Pr) and the Rayleigh number ($Ra=g\beta\Delta T H^3 Pr/\nu^2$). For the given boundary conditions the solution is centro-symmetric with respect to the center of the cavity.

7.3. Numerical method

The spatial derivatives in the equations are discretized with the finite-volume method on a staggered grid as described in section 2.6. The convection terms are discretized with the hybrid scheme. This means that the second-order accurate central scheme for the convection is locally replaced by the first-order accurate upwind scheme as soon as the grid size exceeds a critical value. To be more precisely, the central scheme is replaced by the upwind scheme for the x-convection if $|u|\Delta x/(\nu+\nu_t)>2$ and for the y-convection if $|v|\Delta y/(\nu+\nu_t)>2$. In the calculations as presented here, for the x-convection the hybrid scheme typically turns out to use the central scheme in the vertical boundary layers and the upwind scheme in the core, whereas for the y-convection it uses the upwind scheme in the vertical boundary layers and the central scheme in the core. In the corners and in the horizontal layers the central scheme is used. In comparison with the use of the central scheme for all grid points, the hybrid scheme is more stable (admitting much larger time steps) during the iteration process to solve the discretized system. The appearance of boundary layers requires a nonequidistant grid that gives a strong grid refinement along the walls. The sides of the finite volumes are positioned according to

$$\frac{x_i}{H} = \frac{1}{2}\left(1 + \frac{\tanh[\alpha_1(i/i\max - 1/2)]}{\tanh(\alpha_1/2)}\right) \qquad i = 0,1,\ldots,i\max \tag{7.3a}$$

$$\frac{y_j}{H} = \frac{j}{j\max} - \frac{1}{2\pi}\sin\left(2\pi\,\frac{j}{j\max}\right) \qquad j = 0,1,\ldots,j\max. \tag{7.3b}$$

α_1 is given by $\alpha_2=\alpha_1/\sinh(\alpha_1)$. In most calculations we took $\alpha_2=1.5\times10^{-3}$, but the results for the highest Rayleigh numbers ($Ra>10^{13}$) were obtained with $\alpha_2=1.5\times10^{-4}$. The time dependence is treated implicitly; the spatial derivatives are evaluated at the new time level n, and the time derivatives are approximated with two time levels using the B2 scheme (2.21a). The line Gauss-Seidel method is used to iteratively solve the variables u, v, T, k and ϵ. After each sweep the pressure is updated according to equation (5.3), using the direct solver as described in section 5.3.

The calculation is started with a certain initial field at $t=0$ and we integrate in time until a steady final solution is reached. As already remarked in chapter 5, the time evolution in the cavity is dominated by two time scales: $t_1=(H^2/\nu)Ra^{-1/4}$ and $t_2=(H^2/\nu)Ra^{-1/2}$. The time scale t_1 determines the time to reach the steady state and t_2 determines the required time step. A good initial field for the time evolution can be obtained with the help of the steady formulation: the unsteady

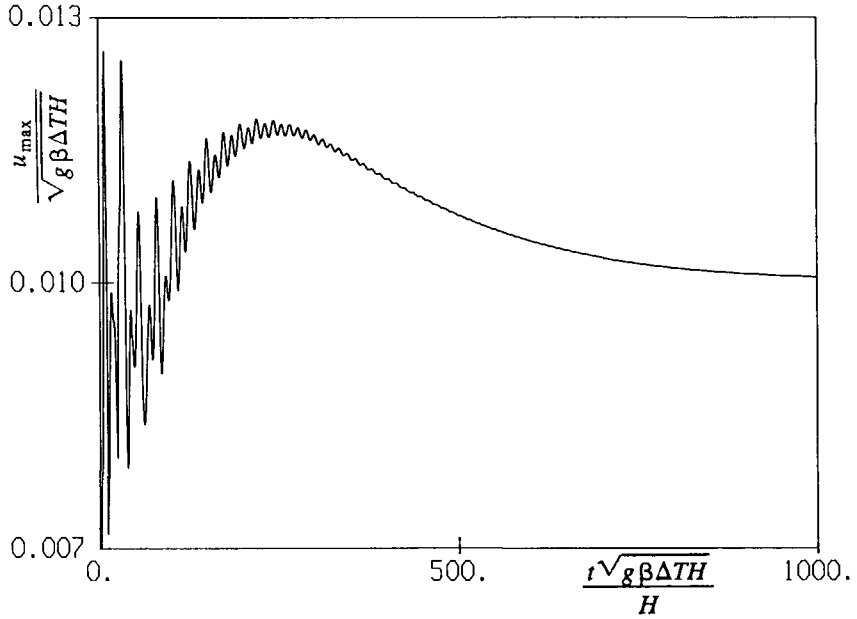

FIGURE 7.2. Typical time evolution to the steady state (Chien model, air at $Ra=10^{11}$).

terms are omitted from the unsteady equations (7.1) and both the transport variables and the pressure correction are iteratively solved with the line Gauss-Seidel method. Some relaxation is required to prevent divergence of the iteration process. After approximately 3000 Gauss-Seidel sweeps the speed of convergence has slowed down, and we switch over to the unsteady, more physical, formulation. At the moment of switching most of the flow details are already solved. The order of $t_1/t_2=Ra^{1/4}$ time steps are still required to reach the fully converged steady state. For example, we find that for $Ra=10^{14}$ about 4000 time steps are sufficient.

As also found by Jones (1985) and Thompson *et al.* (1987), in the present calculations we revealed that the time scale $t_2 \div H/(g\beta\Delta TH)^{1/2}$ (Brunt-Väisälä time scale) determines the maximum time step that still gives a stable numerical time integration. In all cases we used $\Delta t(g\beta\Delta TH)^{1/2}/H=1/4$. A typical time evolution is shown in figure 7.2. The damped oscillations are related to internal gravity waves in the core. The time evolution in figure 7.2 for the turbulent solution of air at $Ra=10^{11}$ as calculated with the Chien model gives a damped oscillation with the frequency $fH/(g\beta\Delta TH)^{1/2}=0.0877$ (this frequency is almost independent of the Prandtl number and it only slightly decreases with increasing Rayleigh number). Ozoe *et al.* (1985) have also calculated the turbulent flow in the same square cavity with the unsteady approach, using the standard $k-\epsilon$ model with wall functions. From one of their figures we derive that the unsteady evolution shows an oscillation with the frequency $fH/(g\beta\Delta TH)^{1/2}=0.083$ ($Ra=6.3\times10^{10}$, $Pr=6.7$; 24×60 grid, $\Delta t(g\beta\Delta TH)^{1/2}/H\sim1/12$). This frequency is close to our result. But in

contrast with our calculations, the oscillation of Ozoe *et al.* does not die out in the core for increasing time. We refined our time step up to $\Delta t(g\beta\Delta TH)^{1/2}/H=1/24$, and we switched over to the central scheme, but we still do not find their periodic behaviour for $t\rightarrow\infty$. In all our calculations the unsteadiness dies out and the turbulent solution reaches a steady final state. Both the use of a slightly different turbulence model or an insufficient numerical accuracy of the results of Ozoe *et al.* may account for the difference.

7.4. Transition regime

For the low-Reynolds-number models of Chien and Jones & Launder, the solution in which k, ϵ and ν_t vanish everywhere satisfies equations (7.1) with its boundary conditions. This solution defines the laminar velocity and temperature field. Hence, all the solutions of the unsteady Navier-Stokes equations (2.9) also satisfy the Reynolds equations (7.1) if a low-Reynolds-number model is applied. This implies that the Reynolds equations with a low-Reynolds-number $k-\epsilon$ model admit at least three types of solutions at large time:

(i) steady laminar solution (zero ν_t)

(ii) unsteady laminar solution (zero ν_t)

(iii) steady turbulent solution (nonzero ν_t).

Solution (i) was studied in chapter 4, and the bifurcation from solution (i) to solution (ii) was studied in chapter 5. In chapter 5 we calculated that the steady laminar solution becomes unstable in time at $Ra_{cr}=1.7\times10^8$ for air and at about $Ra_{cr}=10^{10}$ for water. We also found in chapter 5 that it was necessary to discretize the convection with the central scheme in order to find the bifurcation; the hybrid scheme does not calculate the stability of the steady laminar solution correctly, and often a steady final state was calculated in cases where the central scheme predicted an oscillating state. Because the hybrid scheme was used to solve the Reynolds equations in the present chapter, turbulence died out (*i.e.* ν_t became zero) and a steady laminar solution was found up to Rayleigh numbers considerably above the real stability limit of the steady laminar solution at Ra_{cr}. Of course in principle even for $Ra>Ra_{cr}$ the steady laminar solution is still a good (but unstable) solution of the Navier-Stokes equations and of the Reynolds-equations with a low-Reynolds-number model. The stability of this steady laminar solution is not calculated well by the hybrid scheme, but the accuracy of the calculated steady laminar solution itself seems to be good, because it closely follows the asymptotic branch for the steady laminar solution as derived in chapter 4. The transition to the steady turbulent solution (iii) is studied in this section. Mathematically the transition to solution (iii) can also be interpreted as a bifurcation from solution (i) or from solution (ii). In the present study we only calculate the bifurcation from solution (i) to (iii), because the hybrid scheme fails to reproduce solution (ii). The bifurcation from solution (i) to (iii) is here further referred to as the laminar-turbulent *transition* of the solution (at the Rayleigh number Ra_{trans} and at the height y_{trans}).

The averaged wall-heat transfer in figure 7.3 shows that Ra_{trans} depends on the turbulence model used. The figure also gives the asymptotic branches as calculated for the steady laminar solution in chapter 4 (using no turbulence model):

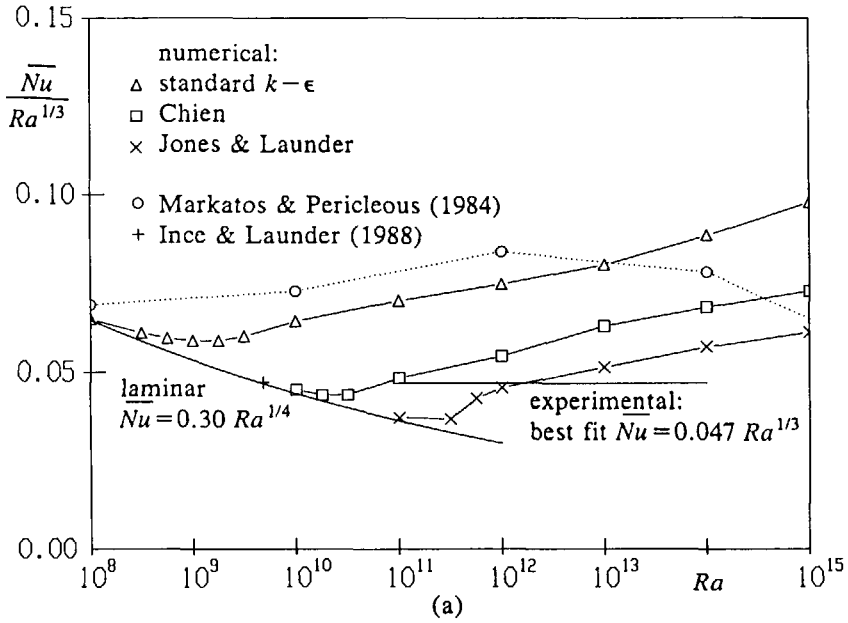

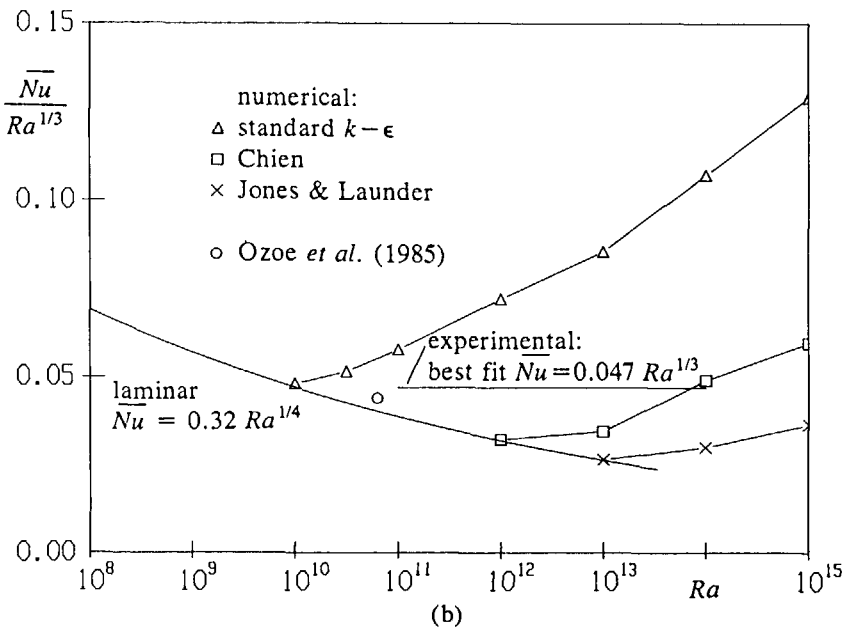

FIGURE 7.3. Averaged wall-heat transfer; (a) air, (b) water.

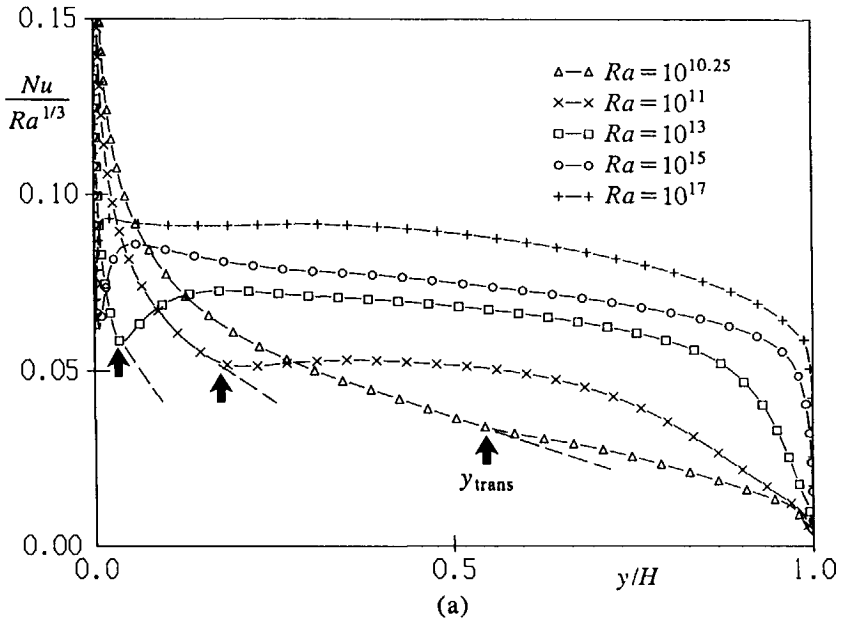

(a)

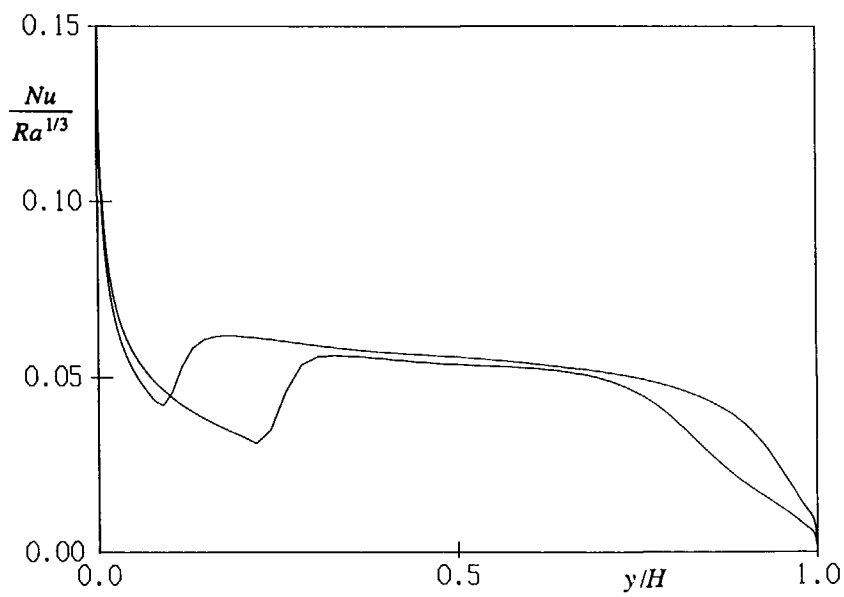

(b)

FIGURE 7.4. Wall-heat transfer for air; (a) with increasing Rayleigh number (Chien model), (b) nonuniqueness of the turbulent solution ($Ra = 10^{13}$, Jones & Launder model).

$\overline{Nu}=0.30\,Ra^{1/4}$ for air or $\overline{Nu}=0.32\,Ra^{1/4}$ for water (see table 4.4). For air, the Chien model goes to turbulence at $Ra_{trans}\sim10^{10}$ and the Jones & Launder model at $Ra_{trans}\sim10^{11}$. Increasing the Prandtl number delays the transition: for water, the Chien model leaves the laminar branch at $Ra_{trans}\sim10^{12}$ and the Jones & Launder model at $Ra_{trans}\sim10^{13}$. The standard $k-\epsilon$ model shows the earliest transition to turbulence, namely at $Ra_{trans}\sim10^{8}$ for air and at $Ra_{trans}\sim10^{10}$ for water. It is remarkable that the values for Ra_{trans} in the standard $k-\epsilon$ model are close to the stability limits of the steady laminar solution as calculated with the unsteady Navier-Stokes equations in chapter 5, whereas the low-Reynolds-number models give considerably larger values.

In contrast to the low-Reynolds-number models, if the standard $k-\epsilon$ model is used the laminar solution (having zero turbulent viscosity) is not a solution of the Reynolds equations (7.1), because it does not satisfy the boundary condition $\epsilon=\infty$ at the wall. We calculate that below a certain Rayleigh number the standard $k-\epsilon$ model gives a turbulent viscosity which is close to zero everywhere. This solution can be interpreted as an approximation of the steady laminar flow. Above a certain Rayleigh number (which we will also indicate as Ra_{trans}) the turbulent viscosity suddenly increases until a fully turbulent solution is found. This sudden increase is also visible in the wall-heat transfer for the standard $k-\epsilon$ model in figure 7.3a.

Examining the development of the wall-heat transfer along the hot vertical wall of the cavity in figure 7.4 shows a sudden increase beyond a certain height (y_{trans}). This increase represents the laminar-turbulent transition within the boundary layer itself. If the Rayleigh number is increased (as illustrated for the Chien model up to $Ra=10^{17}$ in figure 7.4a) y_{trans} moves to $y=0$. Some of the calculations show that the position of the transition (y_{trans}/H) in the steady solution at $t\rightarrow\infty$ is not uniquely given as a function of Pr and Ra. The position depends on the initial solution at $t=0$ with which the evolution to the steady state is started. For example, at the same 80×80 grid we calculate two different steady solutions for air at $Ra=10^{13}$ with the Jones & Launder model (see figure 7.4b): one with an early and the other with a late transition. We have carefully checked the convergence to the steady state for both solutions. The difference between the laminar part of both solutions is related to a difference in the core stratification. The nonuniqueness of the transition region is also found in the experiments of Jaluria & Gebhart (1974) (and private communication with Gebhart) for the heated vertical plate in an isothermal environment. We expect that for a fixed Rayleigh number even more than the two partly turbulent solutions we found can exist: probably y_{trans} can be anywhere between a minimum distance (below which the solution is always laminar) and a maximum distance (beyond which the solution is always turbulent). There is no minimum distance if the Rayleigh number is below Ra_{trans} and the maximum distance decreases to zero if the Rayleigh number is sufficiently far beyond Ra_{trans}. Hence, for very large Rayleigh numbers the boundary layer is fully turbulent and is expected to be unique. A late transition decreases the averaged wall-heat transfer; for each Rayleigh number in figure 7.3 we have selected the averaged wall-heat transfer of the solution with the lowest transition position, in cases where multiple solutions were calculated. Also for the standard

$k-\epsilon$ model nonuniqueness was found; for example two solutions were calculated for air at $Ra=10^{8.75}$ using the 60×60 grid.

The calculated nonuniqueness of the transition of the cavity boundary layer shows a large analogy with the nonuniqueness of the transition in the boundary layer along the plate as calculated in the previous chapter. Mathematically the Reynolds equations (7.1) are parabolic in time whereas the boundary-layer equations (6.1) are parabolic in Ra_y. The solution in time of the Reynolds equations at a fixed Rayleigh number (and in particular the solution at $t\rightarrow\infty$) depends on the amount of turbulent kinetic energy introduced at $t=0$. The solution of the boundary-layer equations for increasing Ra_y depends on the amount of turbulent kinetic energy introduced at the transition station (y_{trans}). The fully turbulent state seems to be independent of the amount of introduced energy in the limit $Ra\rightarrow\infty$ for the Reynolds equations and in the limit $Ra_y\rightarrow\infty$ for the boundary-layer equations.

In this section we have analyzed the transition behaviour within the Reynolds equations that use a $k-\epsilon$ model with the help of some calculated solutions. A more refined mathematical analysis of the nonuniqueness in the transition regime can be obtained by examining the eigenvalues of the Jacobian matrix of the discretized steady part of the Reynolds equations (see also section 5.4). Such an analysis, however, was not performed in the present study.

7.5. Existing experimental and numerical data

Accurate measurements for the turbulent natural-convection flow in the cavity are difficult to obtain. For the comparison of the present numerical results with experiments, we have to rely on experiments performed in cavities with an aspect ratio (A=height/width) larger than 1. Cheesewright *et al.* (1986) and Cheesewright & Ziai (1986) have obtained experimental data for air in the $A=5$ cavity, MacGregor & Emery (1969) have measured a large range of Prandtl numbers in large-aspect-ratio cavities (up to $A=40$), Cowan *et al.* (1982) have measured the flow of water in large-aspect-ratio cavities (up to $A=60$) and Betts & Dafa'Alla (1986) have measured air in the $A=30$ cavity.

At large Rayleigh numbers boundary layers develop along the vertical walls. If for a certain large, but fixed, Rayleigh number the aspect ratio is increased, the rising boundary layer along the hot wall and the falling boundary layer along the cold wall will touch each other and the core region disappears. In the limit of $A\rightarrow\infty$ the flow becomes parallel (*i.e.* one-dimensional). Two-dimensional effects are restricted to a thin region close to the horizontal walls. The turbulence in that case reaches its maximum at the vertical centerline of the cavity. The flow in the large cavities as measured by MacGregor & Emery, Cowan *et al.* and Betts & Dafa'Alla are nearly parallel, giving an averaged wall-heat transfer

$$\overline{Nu}=C\ Ra^{1/3} \tag{7.4}$$

with the constant C is 0.046, 0.043 and 0.053 respectively. The Nusselt number (Nu) is the dimensionless heat transfer through the hot wall: $Nu=-(H/\Delta T)(\partial T/\partial x)_w$. The averaged Nusselt number according to equation (7.4) is independent of the aspect ratio. The boundary layers in the square cavity,

however, are not mixed up; the turbulence is concentrated in the boundary layers and is almost absent at the vertical centerline of the core. Therefore, the averaged wall-heat transfer in the square cavity might differ from equation (7.4). Cheesewright *et al.* (1986) have measured velocity profiles for air as a function of height along both the hot and cold wall in an $A=5$ cavity. In contrast with what follows under the Boussinesq assumption, the deviation from the centro-symmetric state in the experiments is relatively large. Cheesewright *et al.* contribute this deviation to heat losses through the horizontal walls, which were not perfectly adiabatic. Also three-dimensional effects might have influenced the experiment. The heat losses cause the horizontal boundary layer along the ceiling to become turbulent. The boundary layer along the floor is relaminarized, as in our calculations. The aspect ratio 5 is still small enough to give separated vertical boundary layers.

Comparison of different existing wall-heat transfer experiments for the vertical hot plate in an isothermal environment up to about $Ra=10^{12}$ in the previous chapter led to $Nu_y=0.119\,Ra_y^{1/3}$ (equation (6.33); Nu and Ra are based on the coordinate y along the plate and on the temperature difference between the wall and the isothermal environment). Under the approximation that the core in the square cavity is also isothermal, this result can be rewritten as an averaged wall-heat transfer for the cavity:

$$\overline{Nu}=0.047\,Ra^{1/3}. \tag{7.5}$$

We have rescaled Nu_y and Ra_y from equation (6.33) such that $\overline{Nu}$ and Ra in equation (7.5) are based on the cavity height H and twice the temperature difference between the hot wall and the isothermal core. Actually, however, the core of the square cavity is stratified, which might give an averaged wall-heat transfer that differs from equation (7.5). For example, laminar calculations show that the stratification in the core of the square cavity leads to an about 35% higher averaged wall-heat transfer for the cavity compared to the hot plate in an isothermal environment (table 4.3: $Nu=0.30\,Ra^{1/4}$ and $0.22\,Ra^{1/4}$ respectively for air). For the turbulent case, however, we will show in the next section that the stratification in the core of the square cavity is much smaller than for the laminar case. It is remarkable that the averaged wall-heat transfer (7.5), as measured for the plate, is close to relation (7.4), as measured for large-aspect-ratio cavities; equation (7.5) will be used to compare our numerical results in the square cavity with.

Betts & Dafa'Alla have calculated the turbulent flow in the cavity with an infinite aspect ratio, comparing different low-Reynolds-number $k-\epsilon$ models. They find that all these models predict a too high wall-heat transfer and a too low velocity maximum. In order to improve the performance of the Jones & Launder model, Ince & Launder (1988) have modified the E term in the ϵ-equation with the Yap-correction. This correction accounts for the large turbulent diffusion from the centerline of the tall cavity towards the wall. With the Yap-correction, Ince & Launder calculate that $\overline{Nu}=0.051\,Ra^{1/3}$ for $A=\infty$. Further they used this modified model to calculate the cases with $A=10$, 5 and 1. The Yap-correction does not influence the results in the cases with $A=5$ or 1, where the vertical boundary layers are not mixed up at the centerline. They have fitted their numerical results for these finite aspect ratios to $Nu=0.047\,Ra^{1/3}$. As shown in figure 7.3a, their

Rayleigh number in the case of the square cavity turns out to be too small to get a turbulent solution: their wall-heat transfer is practically equal to the laminar result.

Markatos & Pericleous (1984) and Ozoe *et al.* (1985) have calculated the turbulent flow in the square cavity, using the standard $k-\epsilon$ model with wall functions like (6.8) or (6.9). Ozoe *et al.* calculated the flow of water on a 24×60 grid. The distribution of grid points is such that only one grid point falls between the wall and the velocity maximum in the vertical boundary layer. Therefore they do not claim that their results are grid independent. Their averaged wall-heat transfer at $Ra=6.3\times10^{10}$ ($Pr=6.7$) is indicated in figure 7.3b. Markatos & Pericleous calculated the flow of air on a 60×120 grid. The distribution of grid points is such that 10 to 15 points fall in the vertical boundary layer, and care was taken that several of these points fall between the wall and the velocity maximum. They checked that grid refinement up to 100×160 points leads to small changes. Comparison of their wall-heat transfer results with the present results for the standard $k-\epsilon$ model in figure 7.3a shows that our results up to $Ra=10^{12}$ are about 11% lower. For $Ra>10^{13}$ the solution of Markatos & Pericleous is below our solution. The deviations might be due to differences in the boundary conditions for k and ϵ.

7.6. Comparison of the models

Turbulent calculations in the square cavity have been performed for air and water up to $Ra=10^{15}$. For air calculations are also performed at $Ra=10^{16}$ and 10^{17} with the Chien model. For larger Rayleigh numbers the iteration process at a new time step in our implicit numerical time integration could no longer reach a converged solution.

The use of low-Reynolds-number $k-\epsilon$ models requires a sufficient number of grid points in the inner part of the boundary layer. Differences between the models can easily be lost if the number of grid points is too small or if the grid points are not properly distributed. Table 7.1 illustrates the accuracy of the results for air at $Ra=10^{13}$ on different grids (with $\alpha_2=1.5\times10^{-3}$), using 40×40, 60×60 and 80×80 grid points respectively. Here S is the stratification gradient $(H/\Delta T)(\partial T/\partial y)$ at the cavity center, v_{max} is the maximum of the vertical velocity at half the cavity height, and u_{max} is the maximum of the horizontal velocity at half the cavity width. In the horizontal direction at half the cavity height, the 80×80 grid gives about 30 grid points in each vertical boundary layer and about 20 grid points in the core. Within the vertical boundary layer 11 grid points are between the wall and the velocity maximum. The table shows that even the results on the coarsest grid are reasonably accurate. The differences between the grids are smallest for the standard $k-\epsilon$ model. The reason for the high numerical accuracy of the standard $k-\epsilon$ model is that this model sharply fixes the position of the laminar-turbulent transition in the vertical boundary layer. The transition in the other models shows a larger grid dependence, which is related to the nonuniqueness of the steady solution for the low-Reynolds-number models. Table 7.2 illustrates the importance of the proper distribution of grid points. For the 40×40 grid the number of grid points in the inner layer is increased by refining α_2 from 1.5×10^{-1} up to 1.5×10^{-5} (for air at $Ra=10^{13}$ with the Chien model). The solution at the 80×80 grid for the Chien model in table 7.1 is used as an accurate

TABLE 7.1. Numerical accuracy for air at $Ra=10^{13}$.

model	grid	S	$\overline{Nu}\ Ra^{-1/3}$	$\frac{v_{max}}{\sqrt{g\beta\Delta TH}}$	$\frac{u_{max}}{\sqrt{g\beta\Delta TH}}$
standard $k-\epsilon$	40×40	0.3507	0.07845	0.1307	0.007200
	60×60	0.3517	0.07971	0.1279	0.006959
	80×80	0.3515	0.08031	0.1268	0.006953
Chien	40×40	0.3395	0.06648	0.1093	0.006264
	60×60	0.3362	0.06443	0.1052	0.006109
	80×80	0.3408	0.06310	0.1035	0.006001
Jones & Launder	40×40	0.3064	0.05574	0.1152	0.005977
	60×60	0.2923	0.05319	0.1117	0.006242
	80×80	0.3030	0.05150	0.1100	0.006062

TABLE 7.2. Influence of the grid distribution on the numerical accuracy (Chien model, air, $Ra=10^{13}$, 40×40 grid); i_{in} is the number of grid points in the inner layer.

α_2	i_{in}	S	$\overline{Nu}\ Ra^{-1/3}$	$\frac{v_{max}}{\sqrt{g\beta\Delta TH}}$	$\frac{u_{max}}{\sqrt{g\beta\Delta TH}}$
1.5×10^{-1}	0	0.0811	0.01089	0.0664	0.005547
1.5×10^{-2}	2	0.2897	0.05388	0.1172	0.006037
1.5×10^{-3}	5	0.3395	0.06648	0.1093	0.006264
1.5×10^{-4}	8	0.3513	0.06550	0.1104	0.006249
1.5×10^{-5}	11	0.3714	0.06599	0.1141	0.006120
reference solution		0.3408	0.06310	0.1035	0.006001

reference solution. Table 7.2 shows that the solution is inaccurate if the number of grid points in the inner layer is too small ($\alpha_2=1.5\times10^{-1}$ or 1.5×10^{-2}). On the other hand, if a too large percentage of the total number of grid points falls in the inner layer ($\alpha_2=1.5\times10^{-5}$), the accuracy of S and v_{max} decreases as well. The distributions giving the best accuracy use $\alpha_2=1.5\times10^{-3}$ or 1.5×10^{-4}. The results to be presented in the sequel of this chapter (for air and water, at different Rayleigh numbers, for different models) were obtained on either the 60×60 or the 80×80 grid, applying $\alpha_2=1.5\times10^{-3}$ or 1.5×10^{-4}. Many of these calculations were repeated on coarser grids, as just illustrated for one case in table 7.1, to check that the numerical accuracy is sufficient.

Table 7.1 and figure 7.3 show that the differences between the models for the averaged wall-heat transfer are large. Comparison of the calculated averaged wall-heat transfer at $Ra=10^{13}$ for air with the experimental relation (7.5) shows that the Jones & Launder model is best (10% too high), followed by the Chien model (34% too high) and the standard $k-\epsilon$ model (71% too high). For water at

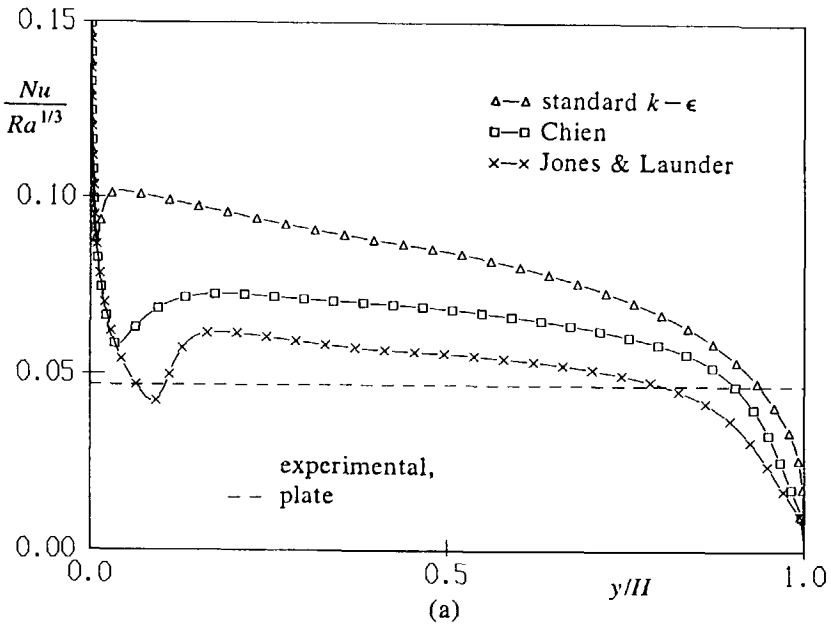

(a)

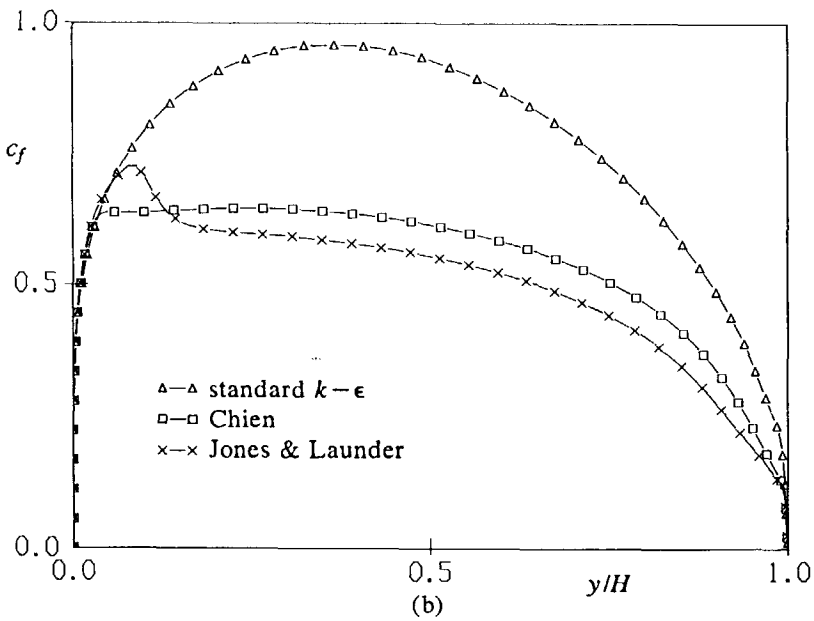

(b)

FIGURE 7.5(a,b). For caption see page 160.

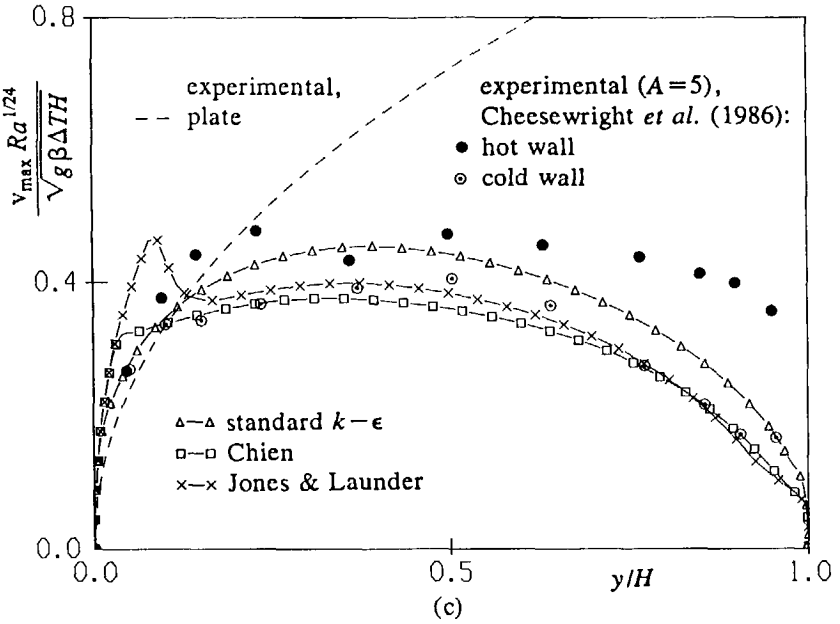

(c)

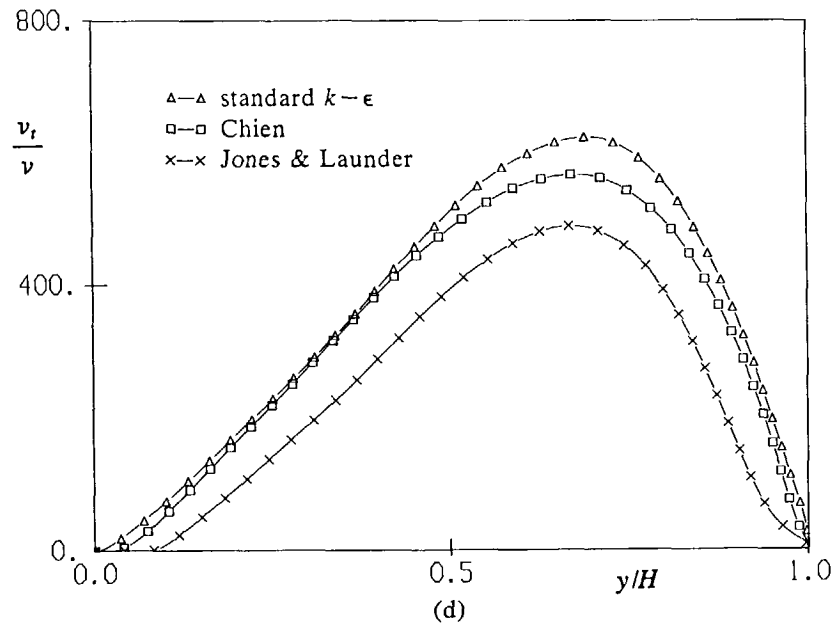

(d)

FIGURE 7.5(c,d). For caption see next page.

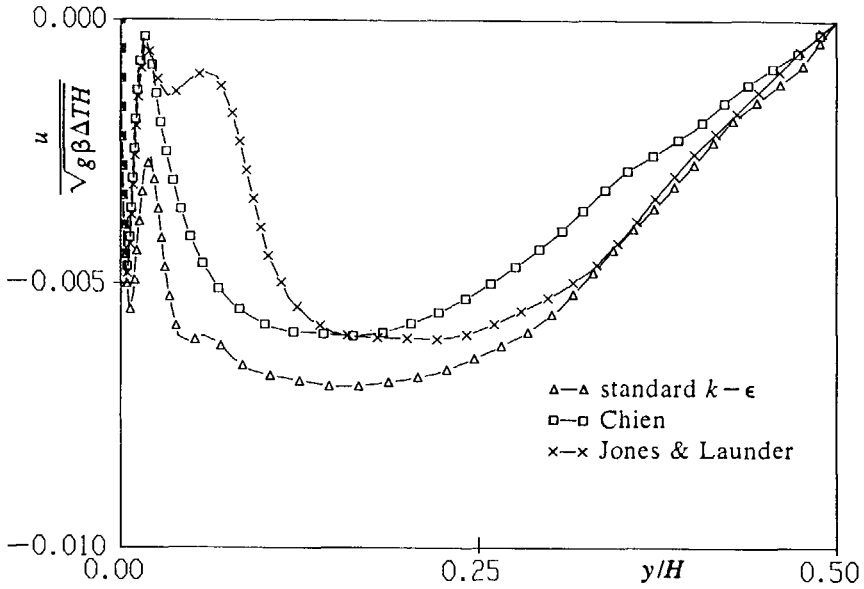

(e)

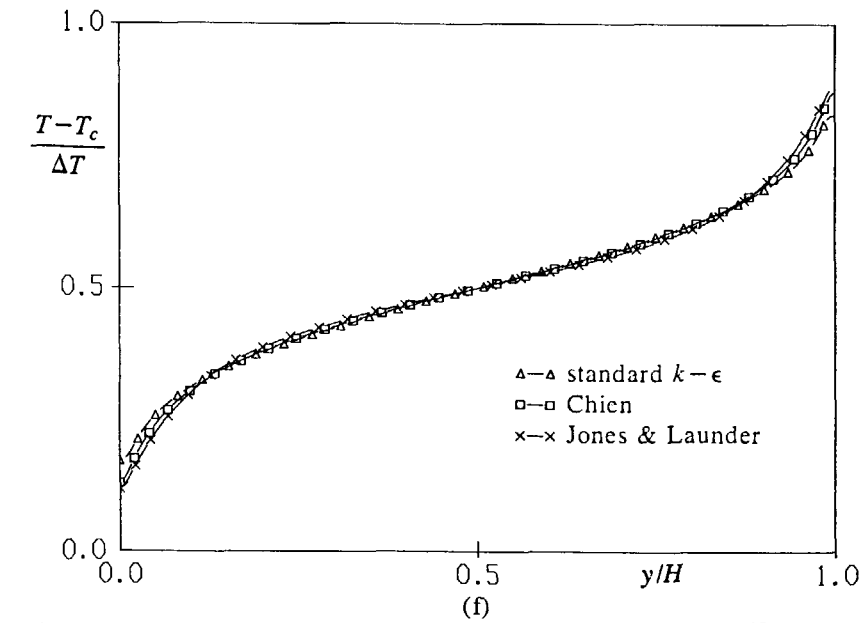

(f)

FIGURE 7.5. Comparison of the models for air at $Ra=10^{13}$; (a) wall-heat transfer, (b) wall-shear stress, (c) vertical velocity maximum, (d) turbulent viscosity maximum, (e) horizontal velocity at $x=H/2$, (f) stratification at $x=H/2$.
(the measure points along the cold wall in figure 7.5c are plotted with $1-y/H$ along the horizontal axis).

$Ra = 10^{14}$ the Chien model is closest to the experiment (5% too high), whereas the Jones & Launder model is 36% too low. The standard $k-\epsilon$ model is much too high (128%). Indeed, the agreement for none of the models is very good over a larger Rayleigh number range. We realize that the sense of this comparison is limited, because the experimental relation (7.5) is based on experiments for the plate (at Rayleigh numbers $Ra_y = 10^{11} - 10^{12}$) and not on experiments for the square cavity (at Rayleigh numbers $Ra = 10^{13} - 10^{14}$) itself. It is clear that there is a strong need for accurate measurements for the large-Rayleigh-number fully turbulent regime in the square cavity.

In figure 7.5 we have compared several quantities, as calculated with the different turbulence models, as a function of height for air at $Ra = 10^{13}$: the wall-heat transfer, the wall-shear stress ($c_f = 2\nu(\partial v/\partial x)_w/(g\beta\Delta TH)$), the maximum of the vertical velocity, the maximum of the turbulent viscosity, the horizontal velocity at half the cavity width and the thermal stratification at half the cavity width. Differences between the turbulence models are largest for quantities in the inner layer, like the wall-heat transfer (figure 7.5a) and the wall-shear stress (figure 7.5b). Differences for the vertical velocity maximum (figure 7.5c) are smaller. The calculated velocity maximum is reasonably close to the experiment of Cheesewright *et al.* (1986) for air at $Ra = 5 \times 10^{10}$ in the $A = 5$ cavity (the velocities are nondimensionalized with the velocity scale $(g\beta\Delta TH)^{1/2}\, Ra^{-1/24}$, see section 7.8). Differences between the models for quantities in the outer layer of the vertical boundary layer are small. For example the small difference in the maximum of the turbulent viscosity (figure 7.5d) as calculated by the Jones & Launder model is due to the slightly later transition of this model. The later transition of the Jones & Launder model is also recognizable in the horizontal velocity at half the cavity width (figure 7.5e). For increasing height figure 7.5e shows that (the modulus value of the horizontal velocity is considered here in the text): (i) a thin high-speed horizontal boundary layer is found close to the floor, (ii) the velocity falls back to an almost zero value directly outside the horizontal boundary layer, and (iii) at the height of the transition the horizontal velocity suddenly increases, it reaches a maximum and falls back to zero at the center. The sudden increase of the horizontal velocity is related to the sudden thickening of the boundary layer at the laminar-turbulent transition position y_{trans}, demanding a larger inflow of fluid from the environment. The thermal stratification in the core (figure 7.5f) is nearly linear, except close to the horizontal walls. Not only for the averaged wall-heat transfer in figure 7.3, but also for all the quantities shown in figure 7.5 the model differences for water were found to be larger than for air.

7.7. Comparison of the cavity with the plate

The vertical gradient of the temperature stratification in the cavity center (S) for air at increasing Rayleigh number is shown in figure 7.6a. S follows the laminar asymptote $S = 0.99$ up to Ra_{trans} (see table 4.4), it increases and reaches a maximum in the first part of the transition regime, and it strongly decreases in the second part of the transition regime until the fully turbulent asymptote is reached. The values of S on the turbulent asymptote are considerably lower than the values on the laminar asymptote. Figure 7.6b gives the stratification at half the cavity

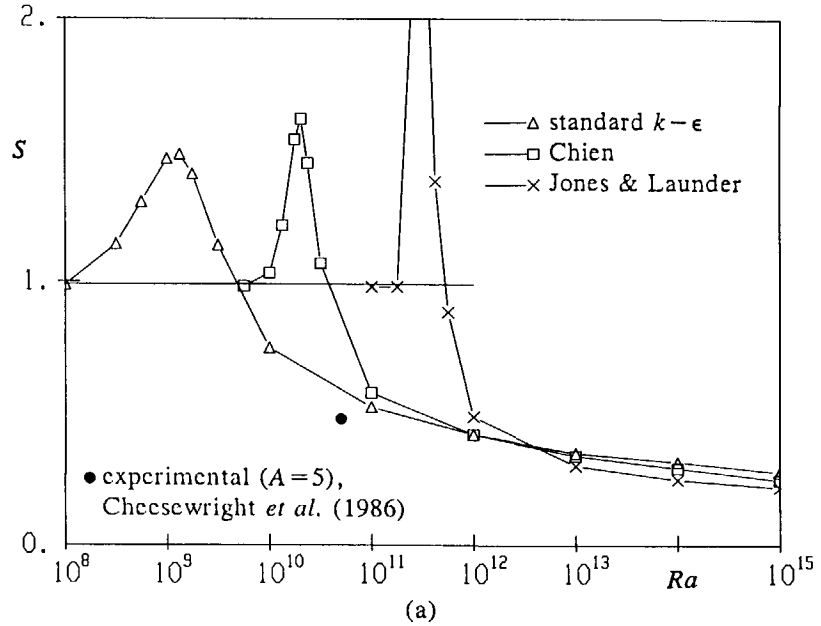

(a)

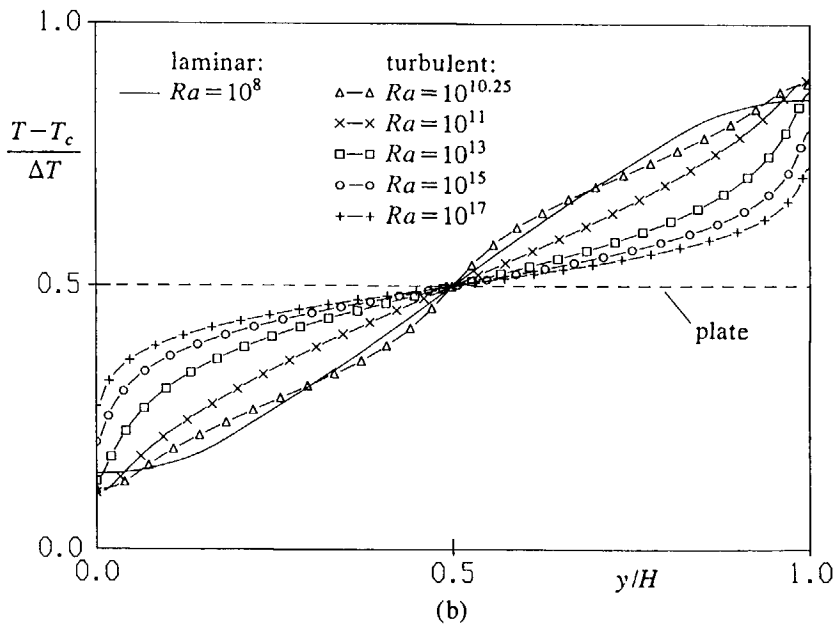

(b)

FIGURE 7.6. Stratification; (a) gradient at the cavity center, (b) at half the cavity width (Chien model).

width up to $Ra=10^{17}$ as obtained for air with the Chien model. This figure shows that the sudden increase of the stratification in the beginning of the transition regime ($Ra=10^{10.25}$) is only a local behaviour at heights around $y=H/2$. As we have shown for the laminar regime in the chapters 3 and 4, also for the transition regime and for the turbulent regime the stratification in the core leads to regions with flow reversal and temperature deficit in the vertical cavity boundary layers (details are not given here). Beyond about $Ra=10^{13}$ all the models in figure 7.6a give values for S in the fully turbulent regime. It is not clear whether the turbulent asymptote reaches a nonzero constant in the limit $Ra \rightarrow \infty$ or whether it totally vanishes. The calculations at the highest Rayleigh numbers ($Ra=10^{15}$ for the standard $k-\epsilon$ model and the Jones & Launder model, $Ra=10^{17}$ for the Chien model) suggest that S vanishes according to $S \div Ra^{-1/16}$. Calculations at even higher Rayleigh numbers are required to draw a definite conclusion about the asymptotic behaviour of S. Figure 7.6a also gives an experimental value for S as measured by Cheesewright *et al.* (1986) for air at $Ra=5\times10^{10}$ in the $A=5$ cavity. This value is close to the prediction of the $k-\epsilon$ model; both the experiment and the $k-\epsilon$ model have already reached the turbulent regime at $Ra=5\times10^{10}$, whereas the low-Reynolds-number models predict a later transition.

Figure 7.6b shows that the core of the cavity becomes nearly isothermal for large Rayleigh numbers, with exception of the parts of the core close to the horizontal walls. In the case of a *total* isothermal core the remaining difference between the cavity boundary layer and the boundary layer along the plate in a isothermal environment would be solely due to the presence of the horizontal boundary layers in the cavity. If we assume that Gill's asymptotic theory for the laminar cavity flow (which was verified to be correct in chapter 4) can also be applied to the turbulent cavity flow, the influence of these horizontal boundary layers on the development of the vertical cavity boundary layers vanishes in the limit $Ra \rightarrow \infty$. Gill's theory also says, however, that the core stratification is such that the normal velocity at the edge of the vertical cavity boundary layer is symmetric with respect to half the cavity height. Therefore the core can never become isothermal over the whole height, because this would give an *in*flow of mass at the boundary-layer edge for all heights. This inflow was calculated for the plate in the previous chapter (see table 6.6). The horizontal flow gives an essential difference between the plate in the isothermal environment and the cavity.

Despite the difference in the horizontal velocity, the smallness of the stratification in the core of the cavity encourages to compare the averaged wall-heat transfer in the cavity with the averaged wall-heat transfer for the plate in the isothermal environment. In figure 7.7a and 7.7b we have compared the averaged wall-heat transfer for air and water respectively. The averaged wall-heat transfer for the plate is obtained by integration of the local wall-heat transfer as given in figure 6.7a. The characteristic temperature for the plate in figure 7.7 is taken as $2(T_h-T_\infty)$, in which T_∞ is the isothermal environment temperature. The unbroken lines in figure 7.7 for the lower Rayleigh numbers represent the laminar solutions for the plate and the cavity respectively (see the tables 4.4 and 6.5). The comparison for air shows that up to $Ra=10^{14}$ the averaged wall-heat transfer for the cavity is above the averaged wall-heat transfer for the plate; as for the laminar

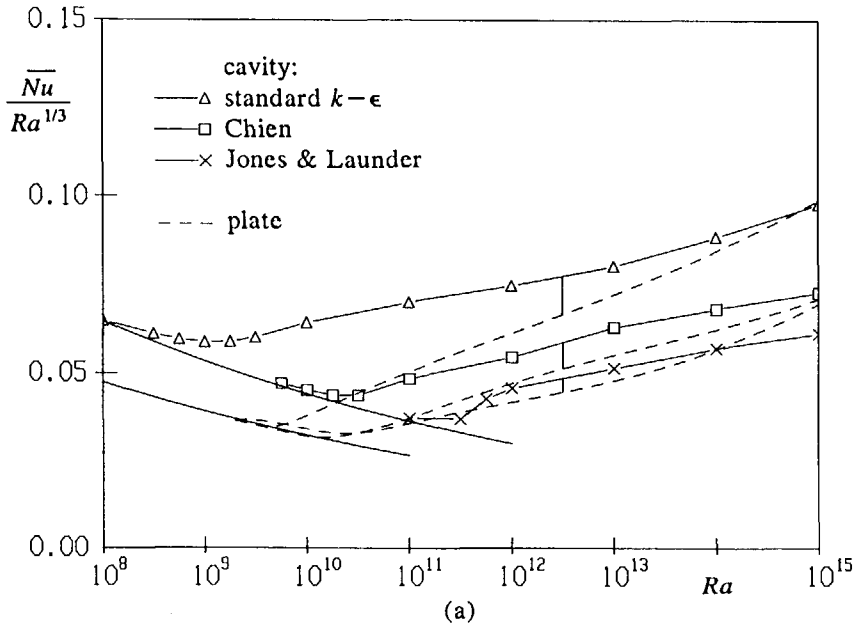

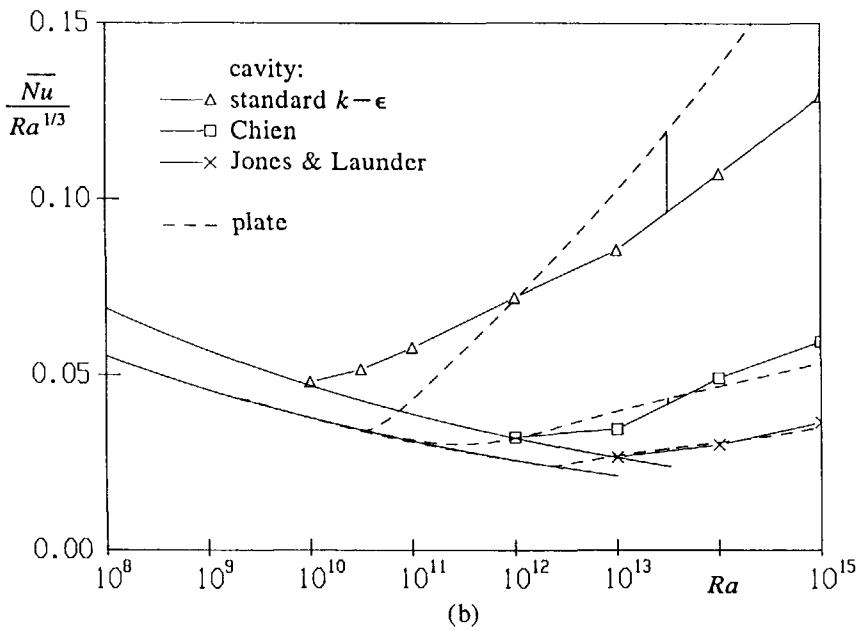

FIGURE 7.7. Comparison between the averaged wall-heat transfer for the cavity and the plate; (a) air, (b) water.

case, the presence of some stratification increases the averaged wall-heat transfer in the turbulent case as well. With exception of the Jones & Launder model at $Ra=10^{15}$, the difference in the averaged wall-heat transfer for air decreases with increasing Rayleigh number, as a consequence of the decreasing core stratification. With exception of the standard $k-\epsilon$ model, the averaged-wall transfer in the cavity for water almost coincides with the plate result. The close agreement is due to the small core stratification for water, which is even smaller than for air (for example, the Chien model at $Ra=10^{15}$ gives $S=0.249$ for air and 0.199 for water). The relatively large difference in the averaged wall-heat transfer with the standard $k-\epsilon$ model for water suggests that the inner-layer quantities in this model are more sensitive to small changes in the core stratification than the inner-layer quantities in the low-Reynolds-number models. On the grounds of the calculations, which practically all show that the presence of a stratification increases the averaged wall-heat transfer, we expect that the experimental relation (7.5), as based on measurements for the plate in an isothermal environment, slightly underpredicts the averaged wall-heat transfer for the cavity up to about 10%.

7.8. Scalings for the turbulent flow in the cavity

In chapter 4 we showed that the proper scalings for the laminar Navier-Stokes flow in the cavity follow from the boundary-layer equations under a fixed stratification $(T-T_c)/\Delta T$; the laminar boundary-layer equations with a fixed stratification have well-defined scalings. In the previous chapter we could derive the proper scalings in the outer layer of the turbulent boundary layer along the plate in an isothermal environment, due to the existence of a similarity solution (wall-function) in the turbulent boundary-layer equations. To derive the scalings for the turbulent flow in the cavity, the Rayleigh-number dependence of different quantities in the calculated solutions of the Reynolds equations (7.1) are examined. These quantities are examined at a fixed position (half the cavity height, half the cavity width *et cetera*) for increasing Rayleigh number. The Ra dependence of a quantity ϕ is written as αRa^{γ}, with $\gamma=(Ra/\phi)[\partial\phi/\partial Ra]$. If γ becomes a constant in the limit $Ra \rightarrow \infty$ the proper scaling is found. Because the stratification in the core of the cavity is small, we expect that the scalings for the turbulent flow in the cavity will show a close analogy with the scalings for the turbulent boundary layer along the plate in the isothermal environment. Such an analogy would imply that the Ra scalings for the cavity approximately follow from the Ra_y scalings for the plate (as summarized in the tables 6.5 and 6.6) by simply replacing y by H in Ra_y.

The Rayleigh-number dependence of the averaged wall-heat transfer has been given in figure 7.3, whereas some other characteristic quantities are followed in figure 7.8. Figure 7.8 shows the Rayleigh-number dependence for some quantities at $y=H/2$, but the resulting γ values in the turbulent regime (as summarized in table 7.3) turn out to hold irrespective of the height y/H. The table also summarizes the scalings for the laminar flow in the cavity. The γ values for the turbulent flow in table 7.3 only *approximately* give the proper scalings, as they were only checked for Rayleigh numbers up to 10^{15} (and up to 10^{17} for air with the Chien model). The values may still show some Rayleigh-number dependence when the Rayleigh number is further increased. In particular the γ values as given for the

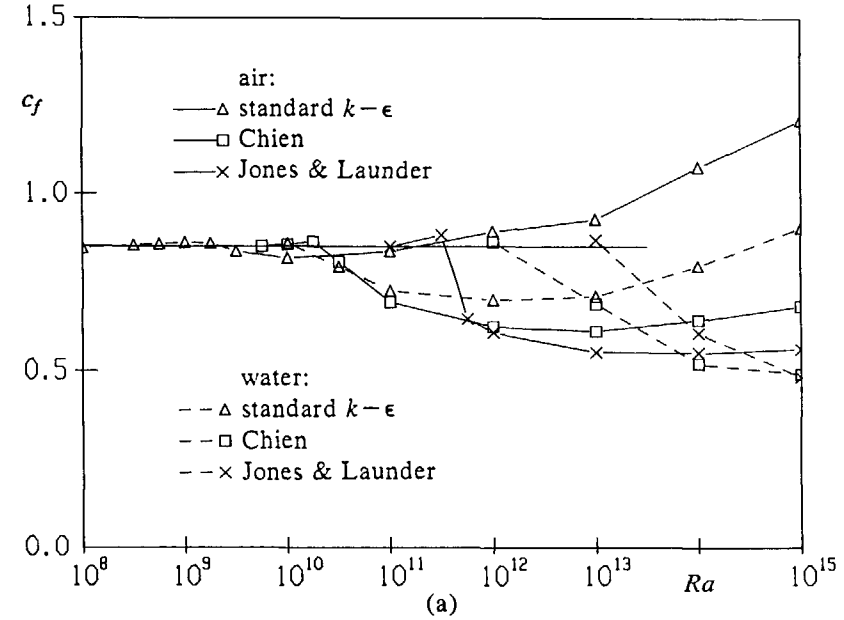

(a)

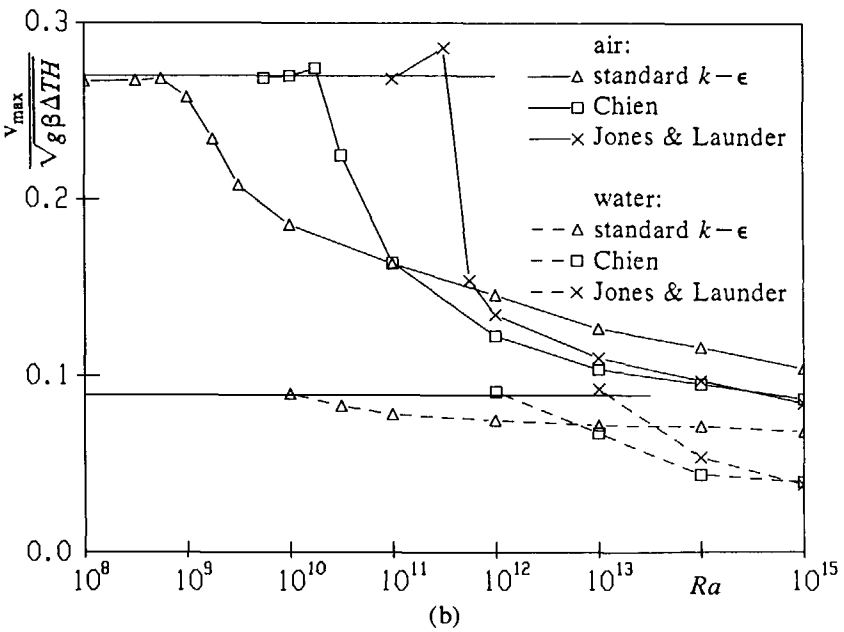

(b)

FIGURE 7.8(a,b). For caption see page 168.

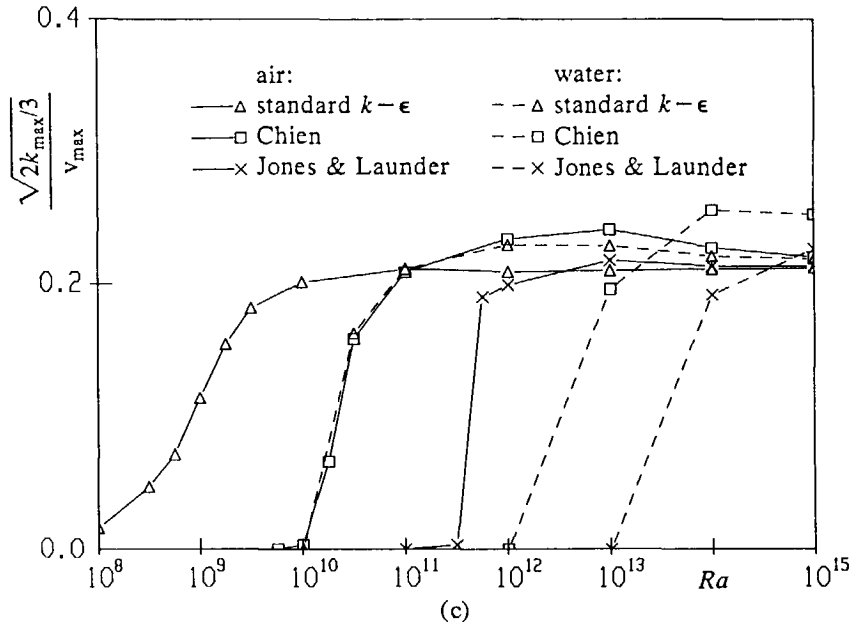

(c)

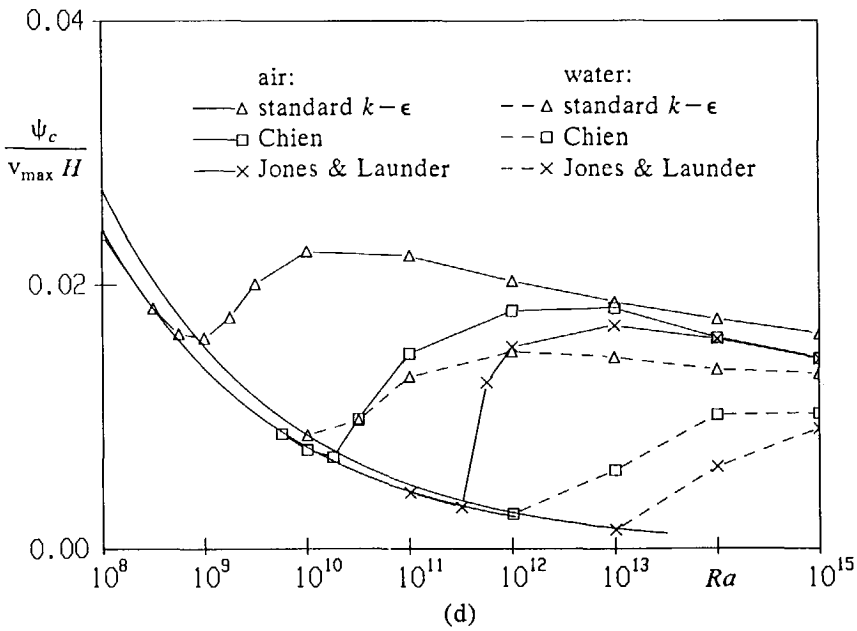

(d)

FIGURE 7.8(c,d). For caption see next page.

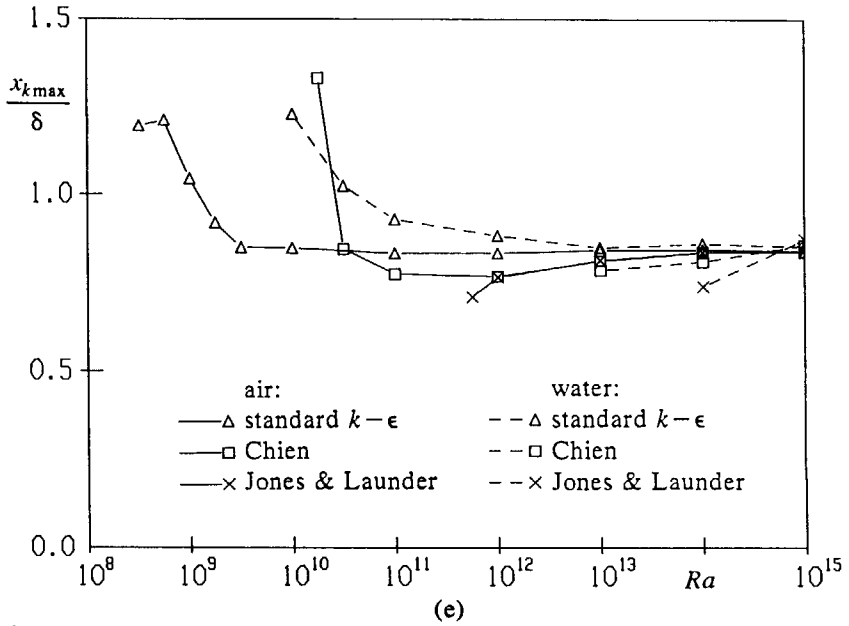

(e)

FIGURE 7.8. Rayleigh-number dependence of different quantities; (a) wall-shear stress at $y=H/2$, (b) vertical velocity maximum at $y=H/2$, (c) maximum of the turbulent kinetic energy at $y=H/2$, (d) stream function at the center, (e) position of the maximum of the turbulent kinetic energy at $y=H/2$ with $\delta=\psi_c/v_{max}$. (the unbroken lines are the laminar branches).

inner-layer quantities are not expected to be the right limits, because in section 6.9 we showed that the inner-layer quantities for the plate even had not reached limiting values at $Ra_y=10^{25}$. The averaged wall-heat transfer (Nu) in figure 7.3 approximately gives $\gamma=3/8$, which is above the experimental value of 1/3. Again, we have to realize that this experimental value was obtained for the plate (at relatively low Rayleigh numbers), and might be insufficiently representative for the cavity. For the plate as well, however, we calculated (figure 6.7a) that γ for Nu_y is about 3/8 at $Ra_y=10^{12}$ (increasing to $\gamma=0.435$ at $Ra_y=10^{25}$). In analogy with the $Ra_y^{-1/4}$ scaling for the wall-shear stress along the plate in part of the turbulent regime (figure 6.7b), the wall-shear stress for the cavity ($c_f=2\nu(\partial v/\partial x)_w/(g\beta\Delta TH)$) in figure 7.8a approximately scales with $Ra^{-1/4}$ in part of the turbulent regime. Also in analogy with the plate (figure 6.7c), the vertical velocity maximum at half the cavity height in figure 7.8b approximately scales with $(g\beta\Delta TH)^{1/2}\,Ra^{-1/24}$, which is close to the buoyant velocity scale $(g\beta\Delta TH)^{1/2}$. As for the plate, also for the turbulent cavity v_{max} turns out to be the proper velocity scale in the outer layer of the boundary layer. This is checked for $(2k_{max}/3)^{1/2}$ at half the cavity height in figure 7.8c (compare figure 6.7d for the plate). The proper length scale in the outer layer becomes clear from the figures 7.8d and 7.8e. Figure 7.8d shows the Ra dependence of δ/H. The boundary-layer thickness

TABLE 7.3. Rayleigh-number dependence for the flow in the cavity.

region	quantity	laminar	turbulent
inner layer	Nu	$Ra^{1/4}$	$\sim Ra^{3/8}$
	c_f	$Ra^{-1/4}$	$\sim Ra^{-1/4}$
	$\frac{v_{max}}{\sqrt{g\beta\Delta TH}}$	Ra^0	$\sim Ra^{-1/24}$
	x_{vmax}/H	$Ra^{-1/4}$	$\sim Ra^{-1/8}$
outer layer	$\frac{\sqrt{2k_{max}/3}}{v_{max}}$	--	Ra^0
	$\frac{\delta}{H} = \frac{\psi_{x=H/2}}{v_{max}H}$	$Ra^{-1/4}$	$\sim Ra^{-1/36}$
	x_{kmax}/δ	--	Ra^0
	$\frac{\nu_{t,max}}{v_{max}\delta}$	--	Ra^0
core	S	Ra^0	$\sim Ra^{-1/16}$
	$\frac{u_{max}}{\sqrt{g\beta\Delta TH}}$	$Ra^{-1/6}$	$\sim Ra^{-5/72}$

δ is defined by equation (6.37), replacing $x=\infty$ by $x=H/2$: $\delta(y)=\psi(H/2,y)/v_{max}(y)$. The Ra dependence for δ/H in the cavity closely resembles the Ra_y dependence for δ/y along the plate, namely $\delta/H \div Ra^{-1/36}$ for the cavity and $\delta/y \div Ra_y^0$ for the plate. Figure 7.8e checks for x_{kmax} (the position of k_{max}) at half the cavity height that δ is the proper length scale in the outer layer. For the plate we found that model differences in the outer-layer quantities, scaled with v_{max} and δ, are small at sufficiently large Rayleigh numbers and only due to differences in the high-Reynolds-number constants. Moreover the scaled outer-layer quantities for the plate are independent of the Prandtl number. The same behaviour as for the plate is found for the outer-layer quantities in the turbulent cavity flow, as shown in the figures 7.8c and 7.8e. Differences between the models for the scaled outer-layer quantities in the cavity almost disappear for increasing Rayleigh number, because the differences in the high-Reynolds-number constants are small. Finally, table 7.3 also gives the Rayleigh-number dependence of the horizontal velocity maximum at half the cavity width. In contrast to the laminar flow, for the turbulent flow in the cavity this maximum does not fall in the horizontal boundary layer, but in the core. The Rayleigh-number dependence of the horizontal core velocity is such that the mass transported through the upper half of the core ($\div H(g\beta\Delta TH)^{1/2}Ra^{-5/72}$) balances the mass transported through the vertical boundary layer at half the cavity height ($\div v_{max}\delta$).

From the comparison between table 7.3 for the cavity and the tables 6.5 and 6.6 for the plate, we conclude that the turbulent scalings with respect to Ra in the cavity indeed closely resemble the turbulent scalings with respect to Ra_y for the plate, if y in Ra_y is replaced by H: differences are restricted to $Ra^{-1/36}$ contributions. On the contrary, for the scalings with respect to y/H this resemblance is restricted to about $y/H=0.3$ at the beginning of the turbulent boundary layer along the hot cavity wall; for larger y/H values the y/H-scalings for the cavity are not simply found from the Ra_y scalings for the plate by splitting Ra_y into $Ra\times(y/H)^3$ and fixing Ra. For example, the vertical velocity maximum along the plate in an isothermal environment monotonously increases with the height, as shown in figure 7.5c for the experimental relation (6.34) (based on the cavity Rayleigh number, $Ra=10^{13}$), whereas the calculated vertical velocity maximum for the cavity in the same figure reaches a maximum at a certain height and decreases until zero at $y=H$. Because this maximum is already reached at a height below $y=H/2$, the difference between the cavity and the plate is not just a local effect close to $y=H$ caused by the cavity corner: the difference must be caused by the small stratification in the core of the cavity. In the previous section we already mentioned that this small stratification is related to a horizontal velocity in the core which is centro-symmetric with respect to half the cavity height. The mass leaving the boundary layer at $y>H/2$ corresponds to the decrease of the vertical velocity maximum. The same kind of difference between the cavity and the plate, as just shown for the vertical velocity maximum, also occurs for most of the other characteristic quantities (c_f, k_{max}, $\nu_{t,max}$). Only the y/H dependence for the wall-heat transfer of the cavity gives a closer resemblance with the plate over almost the whole cavity height: figure 7.5 shows that $Nu/Ra^{1/3}$ only slightly depends on y/H, in analogy with the experiments for the plate (equation (6.33)), which even give a totally height independent wall-heat transfer. Only in the upper corner the wall-heat transfer for the cavity shows a larger y/H dependence.

In section 6.10 we expected the wall functions (6.41) to be applicable to general natural-convection computations. These wall functions use the scalings v_{max} and δ, and have the profiles as calculated for the hot plate in the isothermal environment. To complete the wall-function concept, equation (6.42b) was proposed as the additional equation for v_{max} and δ. The boundary-layer flow in the cavity is an example of a general natural-convection flow, in the sense that the environment of the boundary layer is not isothermal but stratified. Checking whether the wall functions as originally derived for the hot vertical plate in the isothermal environment also apply to a hot vertical wall in a stratified environment is the natural-convection counterpart of checking whether the forced-convection wall functions as originally derived for a plate in an oncoming flow with zero pressure gradient also apply to a plate in a flow with nonzero pressure gradient. To verify whether the natural-convection wall functions apply with a reasonable accuracy to the cavity, first of all requires the finding of a velocity scale and a length scale in the outer layer of the vertical boundary layers in the cavity that not only give Ra independent but also give reasonably y/H independent profiles. The numerical solutions show that these scalings (being functions of Ra and y/H) indeed exist: $v_{out}=(2k_{max}/3)^{1/2}$ is a proper velocity scale and $x_{out}=x_{kmax}$ is a proper

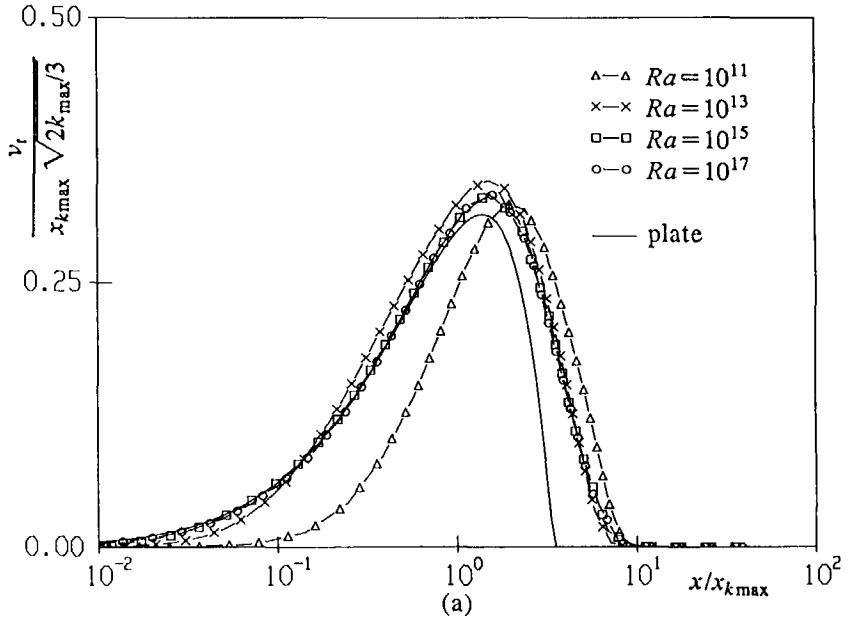

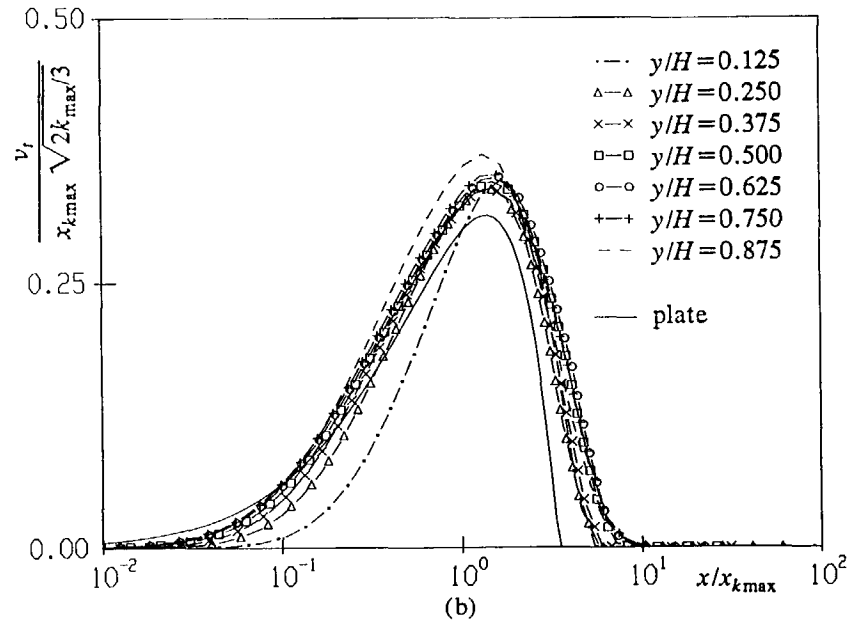

FIGURE 7.9. Outer-layer profiles for the turbulent viscosity (air, Chien model); (a) at $y=H/2$ for increasing Rayleigh number, (b) at $Ra=10^{13}$ for increasing height.

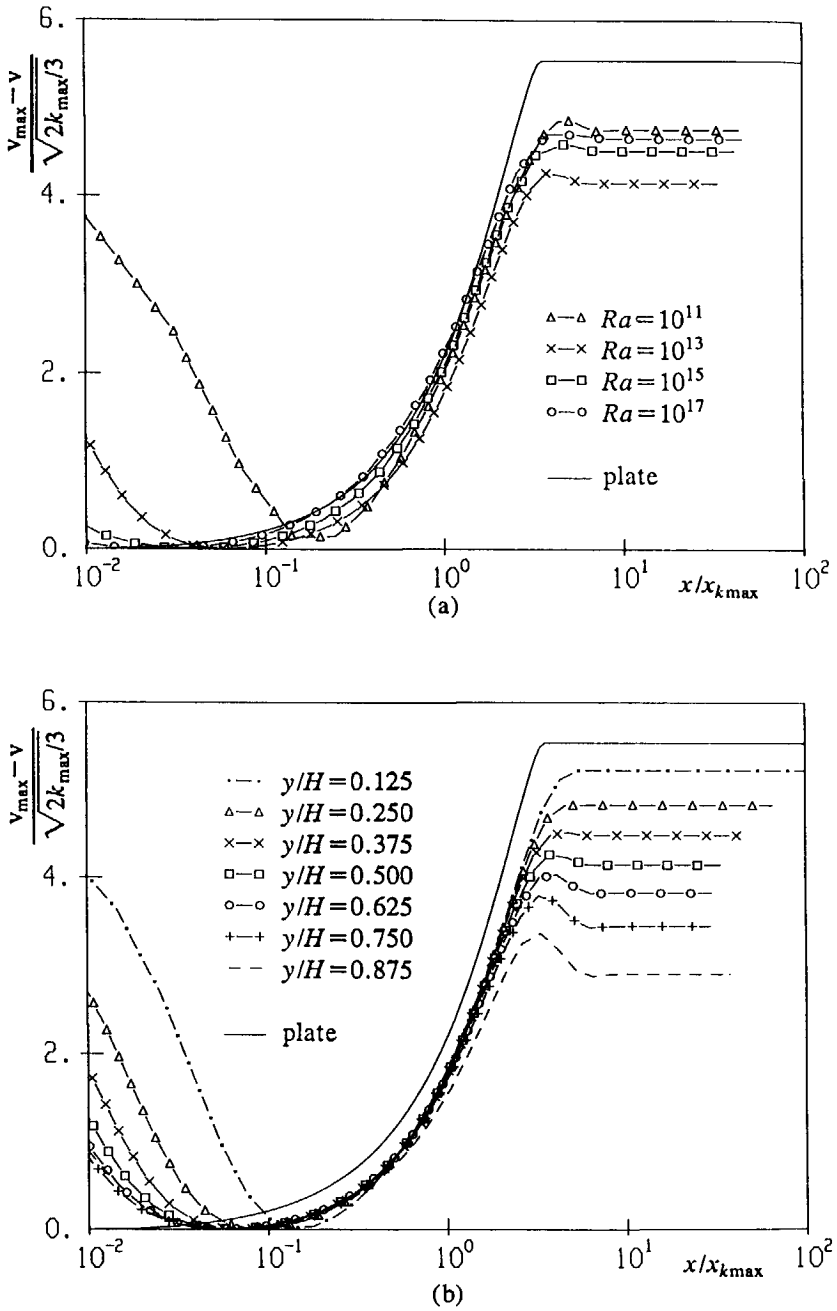

FIGURE 7.10. Outer-layer profiles for the vertical velocity (air, Chien model); (a) at $y=H/2$ for increasing Rayleigh number, (b) at $Ra=10^{13}$ for increasing height.

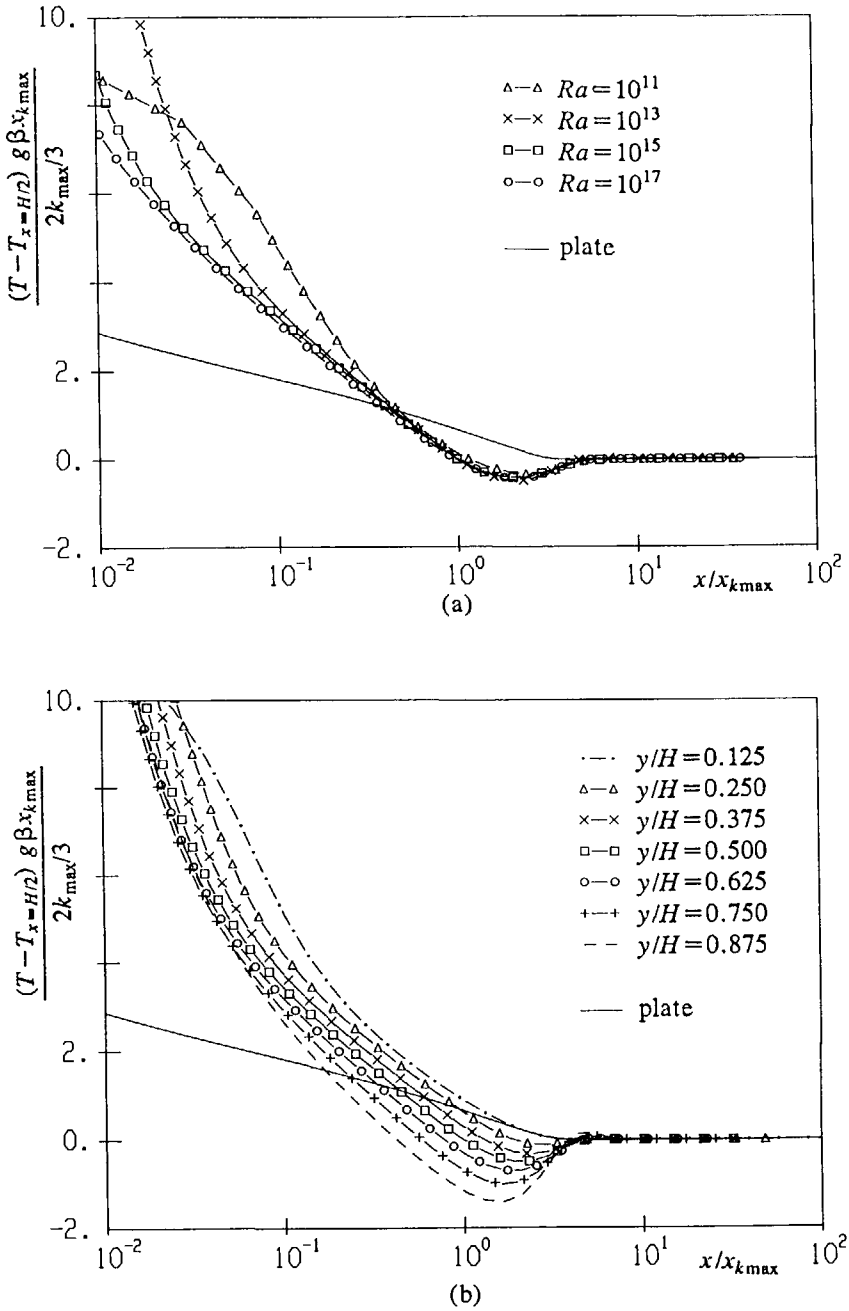

FIGURE 7.11. Outer-layer profiles for the temperature (air, Chien model); (a) at $y=H/2$ for increasing Rayleigh number, (b) at $Ra=10^{13}$ for increasing height.

length scale ($x_{k\max}$ is the position of the maximum of the turbulent kinetic energy). Figure 7.9, for example, shows that the profiles for the turbulent viscosity almost coincide if they are nondimensionalized with these scalings. Moreover the profiles are close to the large-Rayleigh-number solution for the plate. We checked that these also are proper outer-layer scalings for most of the other quantities: $(v_{max}-v)/v_{out}$, k/v_{out}^2 and $\epsilon x_{out}/v_{out}^3$. As shown in figure 7.10 deviations for the scaled velocity only occur at the outer edge. Part of these deviations are due to the regions with flow reversal appearing at the outer edge of the boundary layer in the cavity. Only the scaled temperature profiles, $(T-T_{x=H/2})g\beta x_{out}/v_{out}^2$ *vs* x/x_{out}, do not coincide for increasing height (figure 7.11b). The scaled temperature profiles in the cavity almost coincide for increasing Rayleigh number (figure 7.11a), but these profiles do show a difference with the profile for the plate. This difference with the plate seems to be caused by the regions with temperature deficit which occur at the outer edge of the boundary layer in the cavity. Hence, the cavity calculations show that for all variables (except the temperature) the scalings $(2k_{max}/3)^{1/2}$ and $x_{k\max}$ are more general applicable than the scalings v_{max} and δ as proposed in the wall functions (6.41). Replacing the scalings in the wall functions by $(2k_{max}/3)^{1/2}$ and $x_{k\max}$ causes a difficulty in the practical applicability of the wall functions in computations, because we do not know how to formulate additional equations for the modified scalings. For the scalings v_{max} and δ we could derive the additional equation (6.42b). The application of the wall functions (6.41) (with v_{max} and δ, and the profiles as calculated for the plate) to computations in the cavity will introduce an inaccuracy. The inaccuracy only results with respect to y/H, because with respect to Ra the velocity scale $(2k_{max}/3)^{1/2}$ is similar to v_{max} and the length scale $x_{k\max}$ is similar to δ, as was verified in the figures 7.8c and 7.8e. An indication of the magnitude of the inaccuracy is given in figure 7.12: the figure shows some quantities $\phi_{cavity}/\phi_{plate}$, with $\phi=(2k_{max}/3)^{1/2}/v_{max}$ and with $\phi=x_{k\max}/\delta$. The ϕ profiles are independent of the Rayleigh number for sufficiently large Rayleigh numbers. A perfect applicability of the wall functions (6.41) to the cavity would give $\phi_{cavity}/\phi_{plate}=1$. A value close to 1 is found up to about $y=H/2$, but the deviations become larger at $y>H/2$. The wall functions in section 6.10 also couple v_{max} to the velocity scale of George & Capp $v_{G\&C}=(-g\beta\delta\nu(\partial T/\partial x)_w/Pr)^{1/3}$, as expressed by equation (6.39). We checked that $v_{G\&C}$ for the cavity indeed is similar to v_{max} with respect to Ra in the limit $Ra\rightarrow\infty$. To check their similarity with respect to y/H we have also plotted $\phi_{cavity}/\phi_{plate}$ with $\phi=v_{G\&C}/v_{max}$ in figure 7.12; the agreement between the cavity and the plate is not perfect. Whether, despite the deviations in figure 7.12, the actual implementation of the wall functions (6.41) in the computations for the cavity still gives a reasonable prediction of the boundary-layer flow in the cavity has not been investigated yet in the present study.

In the previous chapter we verified that the profiles (6.40) for the velocity and temperature almost coincide in the inner layer along the plate in the isothermal environment as long as the Rayleigh number is below about $Ra_y=10^{15}$. These profiles practically coincide in the inner layer of the boundary layers for the cavity as well. This is illustrated in figure 7.13 for the temperature profile, $(T-T_{x=H/2})/(T_h-T_{x=H/2})$ *vs* ζ, as calculated with the Chien model for air. Figure 7.13a shows

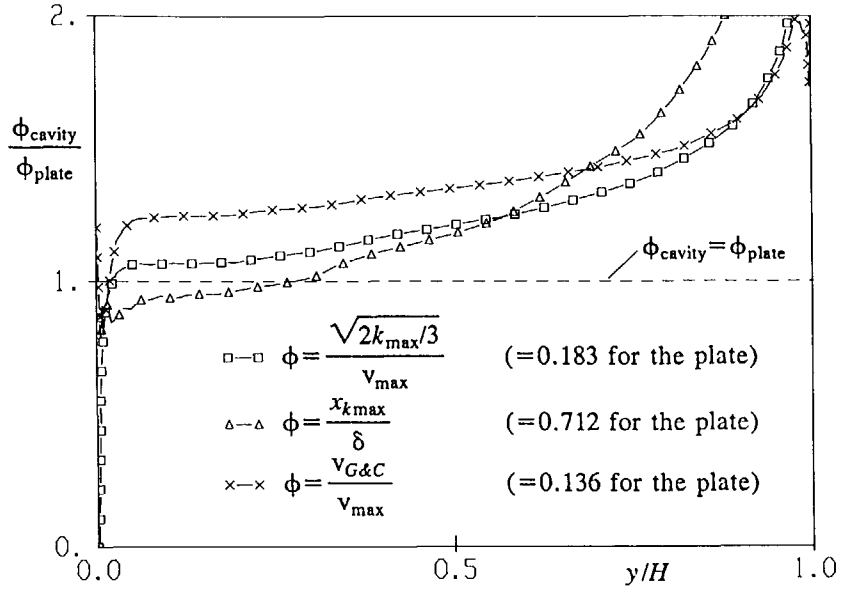

FIGURE 7.12. Comparison of the y-scalings for the cavity with the y-scalings for the plate.

the temperature at half the cavity height for increasing Rayleigh number, whereas figure 7.13b shows the temperature at $Ra=10^{13}$ for increasing height. These profiles for the cavity are also close to the results for the plate (as shown in the figure at the local Ra_y value at half the height of the cavity with $Ra=10^{13}$). In analogy with the plate, the velocity profiles (6.40a) coincide as well (not shown here) and they also have the laminar scalings in part of the turbulent regime, because c_f turned out to scale with $Ra^{-1/4}$ in part of the turbulent regime (figure 7.8a), whereas the vertical velocity maximum closely scales with the laminar velocity scale $(g\beta\Delta TH)^{1/2}$ (figure 7.8b).

7.9. Conclusion

It has been shown that steady turbulent solutions of the Reynolds equations with a $k-\epsilon$ model in the square cavity can be calculated up to large Rayleigh numbers, when in the computational method an unsteady approach to the steady state is used and when the pressure is calculated with a direct solver at each time level. For Rayleigh numbers larger than 10^{17} convergence problems occur. With a good distribution of grid points, in which sufficient grid points fall within the vertical boundary layers, even a coarse 40×40 grid gives reasonably accurate results.

Below a certain Rayleigh number (Ra_{trans}) the solution is laminar everywhere, but beyond Ra_{trans} a transition to the turbulent solution is found. Increasing the Prandtl number increases Ra_{trans}: the standard $k-\epsilon$ model finds $Ra_{trans}\sim10^8$ for air and $Ra_{trans}\sim10^{10}$ for water. The Jones & Launder model remains laminar even to

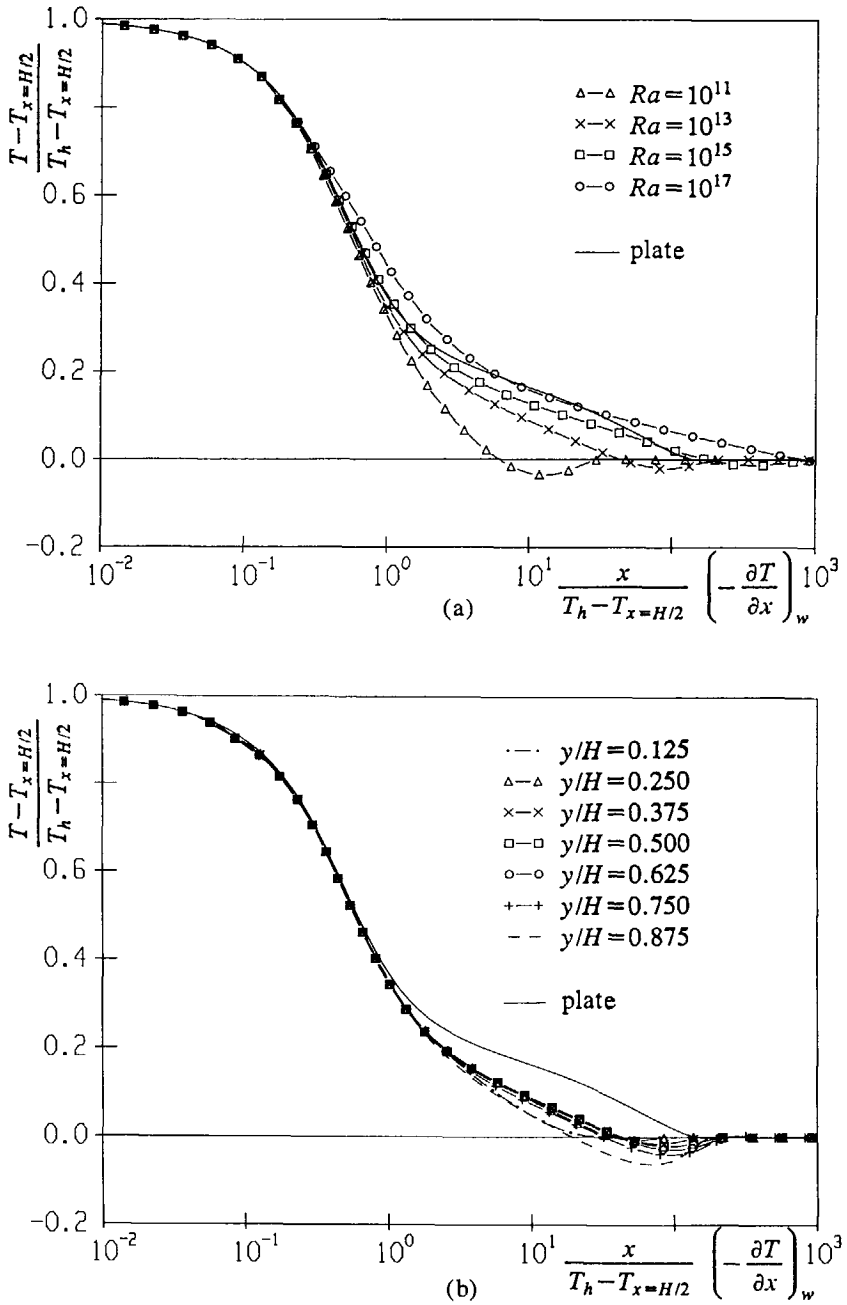

FIGURE 7.13. Inner-layer profiles for the temperature (air, Chien model); (a) at $y=H/2$ for increasing Rayleigh number, (b) at $Ra=10^{13}$ for increasing height.

$Ra_{trans} \sim 10^{11}$ for air and to $Ra_{trans} \sim 10^{13}$ for water. Ra_{trans} in the standard $k-\epsilon$ model is close to the stability limit of the steady laminar solution in the Navier-Stokes equations, as calculated in chapter 5.

For all turbulence models used (standard $k-\epsilon$ model, Chien model and Jones & Launder model) multiple (partly) turbulent solutions exist on the same grid and at a fixed Rayleigh number above Ra_{trans}. This refers to the nonuniqueness of the position y_{trans}/H of the laminar-turbulent transition in the vertical boundary layer. All the models, however, seem to uniquely determine the fully turbulent solution at the largest Rayleigh numbers we considered.

The initial phase of the transition is characterized by a sharp increase of the vertical temperature gradient in the center of the cavity. If the flow becomes fully turbulent this gradient decreases and reaches values considerably below the laminar stratification. Due to the small stratification in the core at large Rayleigh numbers, the calculated averaged wall-heat transfer for the turbulent flow in the cavity is close to the calculated value for the plate in the isothermal environment. Comparison of the averaged wall-heat transfer in the cavity with both the experiments for the plate and the experiments for tall vertical cavities show that the prediction by the standard $k-\epsilon$ model is too high, whereas the low-Reynolds-number models of Chien and Jones & Launder are closer to the experiment. A more definite conclusion about the accuracy of the different turbulence models requires the availability of accurate measurements in the square cavity in the fully turbulent regime.

The scalings with respect to Ra for the turbulent flow in the cavity differ at most with an 1/36 power in Ra from the scalings with respect to Ra_y for the plate in the isothermal environment, when the coordinate y in Ra_y is repaced by H. On the contrary, the scalings in the cavity with respect to y/H follow from the scalings with respect to Ra_y for the plate only up to about $y/H=0.3$. In particular v_{max} and δ, which appear in the wall functions as the proper velocity and length scale, are only proper scalings in the outer layer of the vertical cavity boundary layers with respect to Ra but not with respect to y/H. The proper scalings for the cavity (with respect to both Ra and y/H) are $(2k_{max}/3)^{1/2}$ for the velocity and the position of k_{max} (x_{kmax}) for the length. As a consequence the application of wall functions with v_{max} and δ to computations in the cavity will introduce some inaccuracies.

8. FINAL REMARKS AND CONCLUSIONS

A detailed study has been presented for the large-Rayleigh-number natural-convection flow in the square cavity heated from the side (up to $Ra=10^{15}$) and for the flow along the hot vertical plate (up to $Ra_y=10^{25}$). Different flow phenomena related to the vertical natural-convection boundary-layer flow were studied: laminar flow, stability and bifurcation of the laminar flow, laminar-turbulent transition, fully turbulent flow, wall functions, flow reversal in the boundary layer and thermal stratification. An extensive use was made of numerical methods. Different aspects of the flow as presented here were not earlier described in the literature. Some of the results also verify and extend existing numerical results and theories in the literature. Where possible the results were verified with existing experimental data (*e.g.* for the turbulent flow along the plate). There is a strong need, however, for more experimental natural-convection data in the transition regime and for the fully turbulent flow in the cavity. Experimentalists may be guided in setting up new natural-convection measurements by the results as presented here. This fundamental study can also be a guideline to those engineers who are going to calculate natural-convection heat processes in technical applications.

Having arrived at the end of this thesis we can answer the questions as posed in the introduction (section 1.3):

(i) It has been shown that the steady laminar flow in the cavity reveals four different topological states of its streamline pattern when the Rayleigh number is increased. The streamline pattern for the largest Rayleigh numbers (beyond $Ra=5\times10^6$) shows boundary layers along the vertical walls and it has horizontal streamlines, with low velocities, in the core. The core also becomes thermally stratified. The steady laminar flow in the cavity with adiabatic horizontal walls remains stable up to a critical Rayleigh number of 1.7×10^8 for air and up to about $Ra_{cr}=10^{10}$ for water. At Ra_{cr} the steady laminar flow gives a bifurcation to an unsteady oscillating flow. This unsteady flow shows two frequencies for air and only one for water. One frequency seems to be related to the Tollmien-Schlichting instability in the vertical boundary-layer. The second frequency for air seems to be related to an instability after the hydraulic jump, which occurs in the upper corner of the cavity where the hot vertical boundary layer bends to a horizontal layer. Even on the 160×160 spatial grid, the calculated stability for water still shows some grid dependence and further grid refinement is required to improve the accuracy. Also three-dimensional effects on the stability of air and water remain to be studied. Compared to the adiabatic horizontal walls in the cavity, conducting horizontal walls destabilize the flow and give a Hopf bifurcation at $Ra_{cr}=2.1\times10^6$ for air and at $Ra_{cr}=5.1\times10^6$ for water. This instability seems to be related to the Rayleigh/Bénard instability. For Rayleigh numbers beyond Ra_{cr} the laminar-turbulent transition and the fully turbulent flow in the cavity with adiabatic horizontal walls could be calculated by using $k-\epsilon$ turbulence models. Low-Reynolds-number $k-\epsilon$ models not only damp the turbulence close to the wall

(which decreases the wall-heat transfer) but they also delay the laminar-turbulent transition to higher Rayleigh numbers. The standard $k-\epsilon$ model (with $k=0$ and $\epsilon=\infty$ at the wall and without low-Reynolds-number modifications) gives the fastest transition and the low-Reynolds-number model of Jones & Launder model gives the latest transition. The solution with a low-Reynolds-number model can be nonunique: both a laminar and a turbulent solution exist. In particular also the calculated height position of the transition within the boundary layer in the cavity can be nonunique for Rayleigh numbers in the range 10^{10} up to about 10^{15}. The transition regime requires more attention in future studies, because the low-Reynolds-number calculations show that the transition to the full turbulent state can cover a large part of the Rayleigh-number range that is relevant for many technical applications with natural-convection flows. A definite conclusion about the accuracy of the turbulence models cannot be drawn yet because more experimental data are needed.

The turbulent flow along the plate in the isothermal environment could be calculated with the standard $k-\epsilon$ model, different low-Reynolds-number $k-\epsilon$ models and the fully differential Reynolds-stress model. The standard $k-\epsilon$ model overpredicts the experimental wall-heat transfer for the plate in the isothermal environment up to more than 200% at $Ra_y=10^{13}$ for water. The low-Reynolds-number models of Lam & Bremhorst, Chien and Jones & Launder considerably improve the wall-heat transfer. Application of the differential Reynolds-stress model to the plate does not further improve the mean field quantities, like the wall-heat transfer. The Reynolds-stress model, however, does improve the turbulent quantities: the maximum of the turbulent viscosity is close to the experiment if the Reynolds-stress model is applied, whereas it is overpredicted by about 100% in the $k-\epsilon$ models. The Reynolds-stress model also shows that the eddy-viscosity concept in the $k-\epsilon$ model is not fully justified to describe details of turbulent natural-convection flows. In particular the zero buoyancy production of turbulent kinetic energy in the $k-\epsilon$ model is not correct. It is worthwhile to investigate the modification of the buoyancy production in the $k-\epsilon$ model and the application of the Reynolds-stress model to the turbulent flow in the cavity in a in future study.

(ii) For large Rayleigh numbers different asymptotic structures appear. Some of the similarity solutions of the laminar boundary-layer equations along a hot vertical plate in a stratified environment (namely those belonging to the negative M class with a stably stratified environment), as formulated in differential form by Semenov, were shown to be unmatchable with the environment of the boundary layer. Also the similarity solution with the linear stable stratification does not fit with the nonsimilar boundary-layer solution for the plate with a sharp leading edge in such a stratification. There is flow reversal in part of the outer layer of the boundary layer if the environment has a stable thermal stratification, which changes the parabolic character of the boundary-layer equations into an elliptic character. Some of the similarity solutions can be used as boundary conditions for nonsimilar boundary-layer calculations. For the laminar and turbulent flow in the cavity at large Rayleigh numbers there are four asymptotic flow structures: vertical boundary layers along the vertical walls, a thermally stratified core with horizontal

streamlines, corner regions and horizontal layers along the horizontal walls. The proper scalings of the laminar Navier-Stokes flow in the cavity turn out to be defined by the boundary-layer equations, confirming Gill's asymptotic theory. In particular, the wall-heat transfer $-(\partial T/\partial x)_w$ scales with $(\Delta T/H)Ra^{1/4}$ and the vertical velocity in the boundary layer scales with $(g\beta\Delta TH)^{1/2}$. From the numerical results for the turbulent boundary layer along the hot vertical plate in the isothermal environment up to $Ra_y=10^{25}$ wall functions can be derived in the outer layer (*i.e.* between the vertical velocity maximum and the outer edge). The wall functions in the outer layer, which scale with the velocity v_{max} and the length y, are independent of the Prandtl number and of the low-Reynolds-number terms. These wall functions are consistent with the wall functions as theoretically proposed by George & Capp. In the inner layer of the boundary layer (*i.e.* between the wall and the vertical velocity maximum) the velocity profile v/v_{max} *vs* $(x/v_{max})(\partial v/\partial x)_w$ and the temperature profile $(T-T_\infty)/\Delta T$ *vs* $-(x/\Delta T)(\partial T/\partial x)_w$ closely fit the turbulent results with the $k-\epsilon$ models up to about $Ra_y=10^{15}$. For larger Rayleigh numbers wall functions in the inner layer do not seem to exist. The calculations suggest that the 1/3 power in the wall-heat transfer $(Nu_y \div Ra_y^{1/3}$, with $Nu_y=-(y/\Delta T)(\partial T/\partial x)_w)$, as measured up to $Ra_y=5\times10^{11}$, does not hold for larger Ra_y values: in the numerical results the power increases from 3/8 at $Ra_y=10^{12}$ to 0.435 at $Ra_y=10^{25}$.

(iii) The laminar boundary-layer flow in the cavity for increasing Rayleigh number was shown to become similar to the laminar boundary-layer flow along the hot vertical plate in a stratified environment. The core of the cavity is similar to the environment of the plate, in which the temperature and the velocity only depend on the height (giving thermal stratification and horizontal streamlines). The use of the boundary-layer equations to calculate the cavity flow, instead of the Navier-Stokes equations, is not expected to reduce the computational effort. The reason is that the stratification is not known beforehand (implying that an iteration process is required to account for the interaction between the core and the boundary layer) and because there is flow reversal in the boundary layer (implying that the boundary layer is no longer parabolic and repeated numerical iterations in vertical direction are required to solve the flow). For the turbulent flow the stratification in the core of the cavity is much smaller than for the laminar flow. The core will not become totally isothermal, because some stratification is required to achieve that mass moves from the core into the hot boundary layer in the below half of the cavity and that mass moves out of the boundary layer in the upper half of the cavity. The centro-symmetry of the horizontal velocity in the core of the cavity is essentially different from the horizontal velocity in the isothermal environment of the plate, where mass always moves into the boundary layer. For the turbulent case, the stratification in the core leads to only a small increase of the averaged wall-heat transfer (up to 10%) as compared to the plate in the isothermal environment. Based on the wall functions as derived for the plate, wall functions with the scalings v_{max} and δ (boundary-layer thickness) were assumed to be applicable in general natural-convection calculations. An additional equation was formulated for v_{max} and δ. These indeed are proper scalings in the turbulent boundary layers

for the cavity with respect to Ra, but not with respect to y/H. For the cavity the scalings $(2k_{max}/3)^{1/2}$ (k_{max} is the maximum turbulent kinetic energy) and x_{kmax} (the position of k_{max}) are the proper scalings with respect to both Ra and y/H. The use of $(2k_{max}/3)^{1/2}$ and x_{kmax} in the wall functions requires additional equations for these scalings, which could not be derived here. It remains to be investigated whether the actual implementation of the wall functions (with v_{max} and δ) in turbulent computations of the cavity gives a reasonable prediction of the flow. The results as found here for the wall functions for the plate and the cavity are very promising, and suggest that the practical application of wall functions in general natural-convection computations is indeed realizable.

REFERENCES

Batchelor, G.K. 1954 Heat transfer by free convection across a closed cavity between vertical boundaries at different temperatures. *Q. Appl. Math.* **12**, 209-233.

Bejan, A. 1979 Note on Gill's solution for free convection in a vertical enclosure. *J. Fluid Mech.* **90**, 561-568.

Bénard, H. 1900 Les tourbillons cellulaires dans une nappe liquide. *Revue Gén. Sci. Pur. Appl.* **11**, 1261-1271, 1309-1328.

Betts, P.L. & Dafa'Alla, A.A. 1986 Turbulent buoyant air flow in a tall rectangular cavity. *Proc. ASME Meeting HTD* **60**, 83-91.

Blythe, P.A., Daniels, P.G. & Simkins, P.G. 1983 Thermal convection in a cavity: the core structure near the horizontal boundaries. *Proc. R. Soc. Lond.* A**387**, 367-388.

Briggs, D.G & Jones, D.N. 1985 Two-dimensional periodic natural convection in a rectangular enclosure of aspect ratio one. *J. Heat Transfer* **107**, 850-854.

Cebeci, T. & Bradshaw, P. 1984 *Physical and Computational Aspects of Convective Heat Transfer*. Springer.

Cebeci, T. & Khattab, A. 1975 Prediction of turbulent-free-convective-heat transfer from a vertical flat plate. *J. Heat transfer* **97**, 469-471.

Cebeci, T. & Smith, A.M.O. 1974 *Analysis of Turbulent Boundary Layers*. Academic Press.

Cheesewright, R. 1967 Natural convection from a plane, vertical surface in non-isothermal surroundings. *Int. J. Heat Mass Transfer* **10**, 1847-1859.

Cheesewright, R. 1968 Turbulent natural convection from a vertical plane surface. *J. Heat Transfer* **90**, 1-8.

Cheesewright, R. 1986 The scaling of turbulent natural convection boundary layers in the asymptotic limit of infinite Grashof number. Paper presented at Euromech Colloquium 207, April 7-9, Delft, The Netherlands.

Cheesewright, R. & Ierokipiotis, E. 1981 Velocity measurements in a natural convection boundary layer. Queen Mary College, Faculty of Engineering Research, Report EP 5022.

Cheesewright, R. & Ierokipiotis, E. 1982 Velocity measurements in a turbulent natural convection boundary layer. *Proc. 7th Int. Heat Transfer Conf.*, Munich, vol. 2, pp. 305-309.

Cheesewright, R., King, K.J. & Ziai, S. 1986 Experimental data for the validation of computer codes for the prediction of two-dimensional buoyant cavity flows. *Proc. ASME Meeting HTD* **60**, 75-81.

Cheesewright, R. & Mirzai, M.H. 1988 The correlation of experimental velocity and temperature data for a turbulent natural convection boundary layer. *Proc. 2nd U.K. Nat. Conf. on Heat Transfer*, Glasgow, pp. 79-89.

Cheesewright, R. & Ziai, S. 1986 Distributions of temperature and local heat-transfer rate in turbulent natural convection in a large rectangular cavity. *Proc. 8th Int. Heat Transfer Conf.*, San Francisco, pp. 1465-1470.

Chen, C.C. & Eichhorn, R. 1976 Natural convection from a vertical surface to a thermally stratified fluid. *J. Heat Transfer* **98**, 446-451.

Chien, K.-Y. 1980 Predictions of channel and boundary layer flows with a low-Reynolds-number two-equation model of turbulence. *AIAA*-80-0134.

Chien, K.-Y. 1982 Predictions of channel and boundary-layer flows with a low-Reynolds-number turbulence model. *AIAA J.* **20**, 33-38.

Coulter, J.P. & Guceri, S.I. 1985 Laminar and turbulent natural convection in irregularly shaped enclosures. CAE Report-3/85, Department of Mechanical and Aerospace Engineering, University of Delaware.

Courant, R. 1962 *Methods of Mathematical Physics*, vol. 2. Interscience.

Cowan, G.H., Lovegrove, P.C. & Quarini, G.L. 1982 Turbulent natural convection heat transfer in vertical single water-filled cavities. *Proc. 7th Int. Heat Transfer Conf.*, Munich, vol. 2, pp. 195-204.

De Vahl Davis, G. 1983 Natural convection of air in a square cavity: a benchmark numerical solution. *Int. J. Num. Meth. Fluids* **3**, 249-264.

De Vahl Davis, G. & Mallinson, G.D. 1976 An evaluation of upwind and central difference approximations by a study of recirculating flow. *Comp. Fluids* **4**, 29-43.

Drazin, G. & Reid, W.H. 1981 *Hydrodynamic Stability*. Cambridge University Press.

Eckert, E.R.G. & Jackson, T.W. 1951 Analysis of turbulent free-convection boundary layer on flat plate. *NASA Report* 1015.

Eckert, E.R.G. & Soehnghen, E. 1951 Interferometric studies on the stability and transition to turbulence of a free-convection boundary layer. *Proc. Gen. Discussion Heat Transfer Lond.*, pp. 321-323.

Eichhorn, R. 1969 Natural convection in a thermally stratified fluid. *Prog. Heat Mass Transfer* **2**, 41-53.

Elder, J.W. 1965 Laminar free convection in a vertical slot. *J. Fluid Mech.* **23**, 77-97.

Eshghy, S. & Morrison, F.A. 1966 Compressibility and free convection. *Proc. R. Soc. Lond.* A**293**, 395-407.

Fraikin, M.P., Portier, J.J. & Fraikin, C.J. 1982 Application of a $k-\epsilon$ turbulence model to an enclosed buoyancy driven recirculating flow. *Chem. Engng Commun.* **13**, 289-314.

Fujii, T., Takeuchi, M., Fujii, M., Suzaki, K. & Uehara, H. 1970 Experiments on natural-convection heat transfer from the outer surface of a vertical cylinder to liquids. *Int. J. Heat Mass Transfer* **13**, 753-787.

Gebhart, B. 1962 Effects of viscous dissipation in natural convection. *J. Fluid Mech.* **14**, 225-232.

Gebhart, B. 1988 Transient response and disturbance growth in vertical buoyancy-driven flows. *J. Heat Transfer* **110**, 1166-1174.

Gebhart, B. & Mahajan, R. 1975 Characteristic disturbance frequency in vertical natural convection flow. *Int. J. Heat Mass Transfer* **18**, 1143-1148.

George, W.K. & Capp, S.P. 1979 A theory for natural convection turbulent boundary layers next to heated vertical surfaces. *Int. J. Heat Mass Transfer* **22**, 813-826.

Gill, A.E. 1966 The boundary-layer regime for convection in a rectangular cavity. *J. Fluid Mech.* **26**, 515-536.

Gill, A.E. & Davey, A. 1969 Instabilities of a buoyancy-driven system. *J. Fluid*

Mech. **35**, 775-798.

Graebel, W.P. 1981 The influence of Prandtl number on free convection in a rectangular cavity. *Int. J. Heat Mass Transfer* **24**, 125-131.

Gray, D.D. & Giorgini, A. 1976 The validity of the Boussinesq approximation for liquids and gases. *Int. J. Heat Mass Transfer* **19**, 545-551.

Guckenheimer, J. & Holmes, P. 1983 *Nonlinear Oscillations, Dynamical Systems, and Bifurcations of Vector Fields.* Applied Mathematical Sciences, vol. 42. Springer.

Haaland, S.E, & Sparrow, E.M. 1973 Wave instability of natural convection on inclined surfaces accounting for nonparallelism of the basic flow. *J. Heat Transfer* **96**, 405-407.

Harlow, F.H. & Nakayama, P. 1967 Turbulence transport equations. *Physics Fluids* **11**, 2323-2332.

Harlow, F.H. & Welch, J.E. 1965 Numerical calculation of time-dependent viscous incompressible flow of fluid with free surface. *Physics Fluids* **8**, 2182-2189.

Hassid, S. & Poreh, M. 1978 A turbulent energy dissipation model for flows with drag reduction. *J. Fluids Engng* **100**, 107-112.

Henkes, R.A.W.M. & Hoogendoorn, C.J. 1990 Towards a benchmark solution for oscillating convection: Contribution of the heat-transfer group at Delft University. *Proc. Gamm-Workshop on Numerical Simulation of Oscillatory Convection in Low Pr Fluids*, B. Roux (ed.). To appear in the series Notes on Numerical Fluid Mechanics, pp. 144-152. Vieweg.

Hoffman, G.H. 1975 Improved form of the low Reynolds number $k-\epsilon$ turbulence model. *Physics Fluids* **18**, 309-312.

Hossain, M.S. & Rodi, W. 1982 A turbulence model for buoyant flows and its application to vertical buoyant jets. *Turbulent Buoyant Jets and Plumes*, W. Rodi (ed.), pp. 121-178. Pergamon Press.

Hyun, J.M. 1985 Transient buoyant convection of a contained fluid driven by the changes in the boundary temperatures. *J. Appl. Mech.* **52**, 193-198.

Ince, N.Z. & Launder, B.E. 1988 Computation of turbulent natural convection in closed rectangular cavities. *2nd U.K. Nat. Conf. Heat Transfer*, Glasgow, pp. 1389-1400.

Ivey, G.N. 1984 Experiments on transient natural convection in a cavity. *J. Fluid Mech.* **144**, 389-401.

Jaluria, Y. & Gebhart, B. 1974 On transition mechanisms in vertical natural convection flow. *J. Fluid Mech.* **66**, 309-337.

Jones, D.N. & Briggs, D.G. 1989 Periodic two-dimensional cavity flow: effect of linear horizontal thermal boundary condition. *J. Heat Transfer* **111**, 86-91.

Jones, I.P. 1985 The convergence of a simple iterative strategy for strongly stratified flows. *Num. Meth. on Laminar and Turbulent Flow*, C. Taylor (ed.), pp. 733-740. Pineridge Press.

Jones, W.P. & Launder, B.E. 1972 The prediction of laminarization with a two-equation model of turbulence. *Int. J. Heat Mass Transfer* **15**, 301-314.

Joseph, D.D. & Sattinger, D.H. 1972 Bifurcating time periodic solutions and their stability. *Arch. Rational Mech. Anal.* **45**, 79-109.

Kitamura, K., Koike, M., Fukuoka, I. & Saito, T. 1985 Large eddy structure and heat transfer of turbulent natural convection along a vertical flat plate. *Int. J.*

Heat Mass Transfer **28**, 837-850.

Kulkarni, A.K., Jacobs, H.R. & Hwang, J.J. 1987 Similarity solution for natural convection flow over an isothermal vertical wall immersed in thermally stratified medium. *Int. J. Heat Mass Transfer* **30**, 691-698.

Lakshminarayana, B. 1985 Turbulence modelling for complex flows. *AIAA*-85-1652.

Lam, C.K.G. & Bremhorst, K. 1981 A modified form of the $k-\epsilon$ model for predicting wall turbulence. *J. Fluids Engng* **103**, 456-460.

Launder, B.E. 1984 Numerical computation of convective heat transfer in complex turbulent flows: time to abandon wall functions? *Int. J. Heat Mass Transfer* **27**, 1485-1491.

Launder, B.E. 1988 On the computation of convective heat transfer in complex turbulent flows. *J. Heat Transfer* **110**, 1112-1127.

Lee, S.L., Chen, T.S. & Armaly, B.F. 1987 Wave instability characteristics for the entire regime of mixed convection flow along vertical flat plates. *Int. J. Heat Mass Transfer* **30**, 1743-1751.

Leonard, B.P. 1979 A stable and accurate convective modelling procedure based on quadratic upstream interpolation. *Comp. Meth. Appl. Mech. Engng* **19**, 59-98.

Le Quéré, P. 1990 Accurate solutions to the square thermally driven cavity at high Rayleigh number. Centre National de la Recherche Scientifique LIMSI (Orsay, France), Notes et Documents 90-2.

Le Quéré, P. & Alziary de Roquefort, T. 1985 Transition to unsteady natural convection of air in differentially heated vertical cavities. *4th Int. Conf. Num. Meth. in Laminar and Turbulent Flow*, pp. 841-852. Pineridge Press.

Le Quéré, P. & Alziary de Roquefort, T. 1986 Transition to unsteady natural convection of air in vertical differentially heated cavities: influence of thermal boundary conditions on the horizontal walls. *Proc. 8th Int. Heat Transfer Conf.*, San Francisco, pp. 1533-1538.

Le Quéré, P. & Alziary de Roquefort, T. 1988 On the existence of multiple periodic solutions of the Boussinesq equations. *Mech. Fluids*, C.R. Acad. Sci. Paris, vol. 306 II, 681-687.

Le Quéré, P. & Penot, F. 1987 Numerical and experimental investigation of the transition to unsteady natural convection of air in a vertical differentially heated cavity. *Proc. ASME Meeting HTD* **94**, 75-82.

Lin, S.-J. & Churchill, S.W. 1978 Turbulent free convection from a vertical, isothermal plate. *Num. Heat Transfer* **1**, 129-145.

MacGregor, R.K. & Emery, A.F. 1969 Free convection through vertical plane layers - moderate and high Prandtl number fluids. *J. Heat Transfer* **91**, 391-403.

Markatos, N.C. & Pericleous, K.A. 1984 Laminar and turbulent natural convection in an enclosed cavity. *Int. J. Heat Mass Transfer* **27**, 755-772.

Mason, H.B. & Seban, R.A. 1974 Numerical predictions from vertical surfaces. *J. Heat Transfer* **17**, 1329-1336.

Merkin, J.H. 1985 A note on the similarity solutions for free convection on a vertical plate. *J. Engng Math.* **19**, 189-201.

Miyamoto, M., Kajino, H., Kurima, J. & Takanami, I. 1982 Development of turbulence characteristics in a vertical free convection boundary layer. *Proc. 7th Int. Heat Transfer Conf.*, Munich, vol. 2, pp. 323-328.

Miyamoto, M., Katoh, Y., Kurima, J. & Kajino, H. 1983 An experimental study of turbulent free convection boundary layer along a vertical surface using LDV. *Proc. Osaka Symposium*, July 15, Osaka, Japan.

Nachtsheim, P.R. 1963 Stability of free-convection boundary-layer flows. *NASA TN* D-2089.

Navier, M. 1822 Mémoire sur les lois du mouvement des fluides. *Mém. Acad. Sci.* **6**, 389-416.

Ostrach, S. 1953 An analysis of laminar free-convection flow and heat transfer about a flat plate parallel to the direction of the generating body force. *NACA Report* 1111.

Ostrach, S. 1972 Natural convection in enclosures. *Advances in Heat Transfer*, J.P. Hartnett & I.F. Irvine jr (eds), vol. 8, pp. 161-227. Academic Press.

Ostrach, S. 1982 Natural convection heat transfer in cavities and cells. *Proc. 7th Int. Heat Transfer Conf.*, U. Grigull *et al.* (eds), vol. 1, pp. 365-379.

Ostrach, S. & Hantman, R.G. 1981 Natural convection inside a horizontal cylinder. *Chem. Engng Commun.* **9**, 213-243.

Ozoe, H., Mouri, M., Ohmuro, M., Churchill, S.W. & Lior, N. 1985 Numerical calculations of laminar and turbulent natural convection in water in rectangular channels heated and cooled isothermally on the opposing vertical walls. *Int. J. Heat Mass Transfer* **28**, 125-138.

Paolucci, S. & Chenoweth, D.R. 1989 Transition to chaos in a differentially heated vertical cavity. *J. Fluid Mech.* **201**, 379-410.

Patankar, S.V. 1980 *Numerical Heat Transfer and Fluid Flow*. Hermisphere Publishing Corporation.

Patankar, S.V. & Spalding, D.B. 1972 A calculation procedure for heat, mass and momentum transfer in three-dimensional parabolic flows. *Int. J. Heat Mass Transfer* **15**, 1787-1806.

Patel, V.C., Rodi, W. & Scheuerer, G. 1981 Evaluation of turbulence models for near-wall and low-Reynolds number flows. *Proc. 3rd Symp. on Turbulent Shear Flows*, California, pp. 1-8.

Patel, V.C, Rodi, W. & Scheuerer, G. 1985 Turbulence models for near-wall and low-Reynolds number flows: a review. *AIAA J.* **23**, 1308-1319.

Patterson, J. & Imberger, J. 1980 Unsteady natural convection in a rectangular cavity. *J. Fluid Mech.* **100**, 65-86.

Peeters, T.W.J. & Henkes, R.A.W.M. 1990 The Reynolds-stress model for turbulence applied to the natural-convection boundary layer along a hot vertical plate. Submitted to *Int. J. Heat Mass Transfer*.

Peyret, R. & Taylor, T.D. 1983 *Computational Methods for Fluid Flow*. Springer.

Plumb, O.A. & Kennedy, L.A. 1977 Application of a $k-\epsilon$ model to natural convection from a vertical isothermal surface. *J. Heat Transfer* **99**, 79-85.

Prandtl, L. 1904 Uber Flüssigkeitsbewegung bei sehr kleiner Reibung. *Proc. 3rd Int. Math. Congr.*, Heidelberg, Reprinted in: *Vier Abhandlungen zur Hydro- und Aerodynamik*, Göttingen (1927); *NACA TM* 452 (1928); see also *Coll. Works* II, pp. 575-584 (1961).

Raithby, G.D. 1976 Skew upstream differencing schemes for problems involving fluid flow. *Comp. Meth. Appl. Mech. Engng* **9**, 153-164.

Rayleigh, Lord 1883 Investigation of the character of the equilibrium of an

incompressible heavy fluid of variable density. *Proc. Lond. Math. Soc.* **14**, 170-177.

Rayleigh, Lord 1916 On convection currents in a horizontal layer of fluid, when the higher temperature is on the under side. *Phil. Mag.* **32**, 529-546.

Reynolds, W.C. 1976 Computation of turbulent flows. *Ann. Rev. Fluid Mech.* **8**, 183-208.

Rodi, W. 1980 Turbulence models and their application in hydraulics, a state of the art review. International Association for Hydraulic Research, Delft, The Netherlands.

Rogallo, R.S. & Moin, P. 1984 Numerical simulation of turbulent flows. *Ann. Rev. Fluid Mech.* **16**, 99-137.

Roux, B. (ed.) 1990 *Proc. Gamm-Workshop on Numerical Simulation of Oscillatory Convection in Low Pr Fluids*. To appear in the series Notes on Numerical Fluid Mechanics. Vieweg.

Semenov, V.I. 1984 Similar problems of steady-state laminar free convection on a vertical plate. *Heat Transfer - Sov. Res.* **16**, 69-85.

Shyy, W. 1985 A study of finite difference approximations to steady-state, convection-dominated flow problems. *J. Comp. Phys.* **57**, 415-438.

Sparrow, E.M. & Gregg, J.L. 1958 Similar solutions for free convection from a nonisothermal vertical plate. *Trans. ASME* **80**, 379-386.

Stokes, G.G. 1845 On the theories of internal friction of fluids in motion, and of the equilibrium and motion of elastic solids. *Trans. Camb. Phil. Soc.* **8**, 287-305.

Stone, H.L. 1968 Iterative solution of implicit approximations of multidimensional partial differential equations. *SIAM J. Num. Anal.* **5**, 530-558.

Stüben, K. & Linden, J. 1986 Multigrid methods: an overview with emphasis on grid generation processes. *Numerical Grid Generation in Computational Fluid Dynamics*, J. Häuser & C. Taylor (eds), pp. 483-509. Pineridge Press.

Temam, R. 1977 Navier-Stokes equations. North-Holland Publishing Company.

Thompson, C.P., Wilkes, N.S. & Jones, I.P. 1987 Numerical studies of buoyancy-driven turbulent flow in a rectangular cavity. *Int. J. Num. Meth. Engng* **24**, 89-99.

To, W.M. & Humphrey, J.A.C. 1986 Numerical simulation of buoyant, turbulent flow - 1. Free convection along a heated, vertical, flat plate. *Int. J. Heat Mass Transfer* **29**, 573-592.

Tsuji, T. & Nagano, Y. 1988a Characteristics of a turbulent natural convection boundary layer along a vertical flat plate. *Int. J. Heat Mass Transfer* **31**, 1723-1734.

Tsuji, T. & Nagano, Y. 1988b Turbulence measurements in a natural convection boundary layer along a vertical flat plate. *Int. J. Heat Transfer* **31**, 2101-2111.

Tsuji, T. & Nagano, Y. 1989 Velocity and temperature measurements in a natural convection boundary layer along a vertical flat plate. *Experimental Thermal Fluid Sci.* **2**, 208-215.

Turner, J.S. 1973 Buoyancy Effects in Fluids. Cambridge University Press.

Tzuoo, K.L., Chen, T.S. & Armaly, B.F. 1985 Wave instability of natural convection flow on inclined surfaces. *J. Heat Transfer* **107**, 107-111.

Vanka, S.P. 1985 Block-implicit calculation of steady turbulent recirculating flows. *Int. J. Heat Mass Transfer* **28**, 2093-2103.

Van Kan, J. 1986 A second-order accurate pressure-correction scheme for viscous incompressible flow. *SIAM J. Sci. Statist. Comp.* **7**, 870-891.

Venkatachala, B.J. & Nath, G. 1981 Nonsimilar laminar natural convection in a thermally stratified fluid. *Int. J. Heat Mass Transfer* **24**, 1848-1850.

Vliet, G.C. & Liu, C.K. 1969 An experimental study of turbulent natural convection boundary layers. *J. Heat Transfer* **91**, 517-531.

Winters, K.H. 1987 Hopf bifurcation in the double-glazing problem with conducting boundaries. *J. Heat Transfer* **109**, 894-898.

Yang, K.T. 1988 Transitions and bifurcations in laminar buoyant flows in confined enclosures. *J. Heat Transfer* **110**, 1191-1204.

Yang, K.T., Novotny, J.L. & Cheng, Y.S. 1972 Laminar free convection from a nonisothermal plate immersed in a temperature stratified medium. *Int. J. Heat Mass Transfer* **15**, 1097-1109.

Yewell, R., Poulikakos, D. & Bejan, A. 1982 Transient natural convection experiments in shallow enclosures. *J. Heat Transfer* **104**, 533-538.

APPENDIX

The terms in the Reynolds-stress equations (6.43) have the following form:

$$d_{ij} = \frac{\partial}{\partial x_k}\left(\nu\frac{\partial\overline{u_i'u_j'}}{\partial x_k} - \overline{u_i'u_j'u_k'} - \frac{\overline{p'u_i'}}{\rho}\delta_{jk} - \frac{\overline{p'u_j'}}{\rho}\delta_{ik}\right) \tag{A.1}$$

$$d_{i\theta} = \frac{\partial}{\partial x_k}\left(\nu\overline{u_i'\frac{\partial T'}{\partial x_k}} + \frac{\nu}{Pr}\overline{T'\frac{\partial u_i'}{\partial x_k}} - \overline{u_i'T'u_k'} - \frac{\overline{p'T'}}{\rho}\delta_{ik}\right) \tag{A.2}$$

$$P_{ij} = -\left(\overline{u_i'u_k'}\frac{\partial u_j}{\partial x_k} + \overline{u_j'u_k'}\frac{\partial u_i}{\partial x_k}\right) \tag{A.3}$$

$$P_{i\theta} = -\left(\overline{u_k'T'}\frac{\partial u_i}{\partial x_k} + \overline{u_i'u_k'}\frac{\partial T}{\partial x_k}\right) \tag{A.4}$$

$$G_{ij} = -\beta\,(\overline{u_i'T'}g_j + \overline{u_j'T'}g_i) \tag{A.5}$$

$$G_{i\theta} = -g_i\beta\overline{T'^2} \tag{A.6}$$

$$\Phi_{ij} = \overline{\frac{p'}{\rho}\left(\frac{\partial u_i'}{\partial x_j} + \frac{\partial u_j'}{\partial x_i}\right)} \tag{A.7}$$

$$\Phi_{i\theta} = \overline{\frac{p'}{\rho}\frac{\partial T'}{\partial x_i}} \tag{A.8}$$

$$\epsilon_{ij} = 2\nu\overline{\frac{\partial u_i'}{\partial x_k}\frac{\partial u_j'}{\partial x_k}} \tag{A.9}$$

$$\epsilon_{i\theta} = \nu\,(1+1/Pr)\,\overline{\frac{\partial u_i'}{\partial x_k}\frac{\partial T'}{\partial x_k}}. \tag{A.10}$$

Triple correlations are modeled with the generalized gradient-diffusion hypothesis, which reads for a double correlation ϕ

$$-\overline{\phi'u_k'} = C_\phi\frac{k}{\epsilon}\,\overline{u_k'u_l'}\frac{\partial\overline{\phi}}{\partial x_l}. \tag{A.11}$$

The modeled terms are

$$d_{ij} = \frac{\partial}{\partial x_k}\left(\nu\frac{\partial\overline{u_i'u_j'}}{\partial x_k} + C_s\frac{k}{\epsilon}\,\overline{u_k'u_l'}\frac{\partial\overline{u_i'u_j'}}{\partial x_l}\right) \tag{A.12}$$

$$d_{i\theta} = \frac{\partial}{\partial x_k}\left(\nu\frac{\partial\overline{u_i'T'}}{\partial x_k} + C_\theta\frac{k}{\epsilon}\,\overline{u_k'u_l'}\frac{\partial\overline{u_i'T'}}{\partial x_l}\right) \tag{A.13}$$

$$\Phi_{ij} = \Phi_{ij}^{(1)} + \Phi_{ij}^{(2)} + \Phi_{ij}^{(3)} + \Phi_{ij,w} \tag{A.14}$$

$$\Phi_{ij}^{(1)} = -C_1\frac{\epsilon}{k}\,(\overline{u_i'u_j'} - \frac{2}{3}k\delta_{ij}), \quad \Phi_{ij}^{(2)} = -C_2\,(P_{ij} - \frac{2}{3}P_k\delta_{ij}),$$

$$\Phi_{ij}^{(3)} = -C_3\,(G_{ij} - \frac{2}{3}G_k\delta_{ij}); \quad P_k = \frac{1}{2}P_{ii}, \quad G_k = \frac{1}{2}G_{ii};$$

$$\Phi_{ij,w} = C_{1w}\frac{\epsilon}{k}\left(\overline{u_k'u_l'}n_k n_l\delta_{ij} - \frac{3}{2}\overline{u_i'u_k'}n_k n_j - \frac{3}{2}\overline{u_j'u_k'}n_k n_i\right) f_w(l/x_n) +$$

$$C_{2w}\left(\Phi_{kl}^{(2)} n_k n_l\delta_{ij} - \frac{3}{2}\Phi_{ik}^{(2)} n_k n_j - \frac{3}{2}\Phi_{kj}^{(2)} n_k n_i\right) f_w(l/x_n);$$

$$f_w(l/x_n) = \frac{k^{3/2}}{c_w \epsilon x_n}$$

$$\Phi_{i\theta} = -C_{1\theta}\frac{\epsilon}{k}\overline{u_i'T'} + C_{2\theta}\overline{u_j'T'}\frac{\partial u_i}{\partial x_j} + C_{3\theta} g_i \beta \overline{T'^2} + \Phi_{i\theta,w} \qquad \text{(A.15)}$$

$$\Phi_{i\theta,w} = -C_{1\theta w}\frac{\epsilon}{k}\overline{u_k'T'}n_k n_i f_w(l/x_n)$$

$$\epsilon_{ij} = \frac{2}{3}\epsilon\left((1-f_s)\delta_{ij} + \frac{3}{2}f_s\frac{\overline{u_i'u_j'}}{k}\right); \quad f_s = \frac{1}{1+Re_t/10}, \quad Re_t = \frac{k^2}{\nu\epsilon} \qquad \text{(A.16)}$$

$$\epsilon_{i\theta} = 0 \qquad \text{(A.17)}$$

$$D_{ij} = -2\nu\,(2-\delta_{ij})\,\frac{\overline{u_i'u_j'}}{x_n^2} \qquad \text{(A.18)}$$

$$D_{i\theta} = -2\nu\,\frac{\overline{u_i'u_j'}}{x_n^2}. \qquad \text{(A.19)}$$

n_i $(i=1,2,3)$ is the unit vector normal to the wall. x_n is the distance to the wall. For the hot vertical plate the wall is positioned at $x=0$, implying that $x_n=x$. The Rotta model is used for Φ and the Shir model is used for Φ_w. Φ_w accounts for pressure refections at the wall. To account for low-Reynolds-number effects the terms D_{ij} and $D_{i\theta}$, which are based on the Chien model, have been added to the equations (6.43a) and (6.43b) respectively. ϵ is described by the equation

$$u_k\frac{\partial\epsilon}{\partial x_k} = \frac{\partial}{\partial x_k}\left(\nu\frac{\partial\epsilon}{\partial x_k} + C_\epsilon\frac{k}{\epsilon}\overline{u_k'u_l'}\frac{\partial\epsilon}{\partial x_l}\right) +$$

$$c_{\epsilon 1}\left(P_k + c_{\epsilon 3} G_k\right)\frac{\epsilon}{k} - f_2\, c_{\epsilon 2}\frac{\epsilon^2}{k} + E. \qquad \text{(A.20)}$$

f_2 and E are low-Reynolds-number terms from the Chien model (see table 6.1). T'^2 is described by the equation

$$u_k\frac{\partial\overline{T'^2}}{\partial x_k} = d_\theta + 2P_\theta - 2\epsilon_\theta + D_\theta \qquad \text{(A.21)}$$

with

$$d_\theta = \frac{\partial}{\partial x_k}\left(\frac{\nu}{Pr}\frac{\partial\overline{T'^2}}{\partial x_k} - \overline{u_k'T'^2}\right), \quad P_\theta = -\overline{u_k'T'}\frac{\partial T}{\partial x_k}$$

$$\epsilon_\theta = \frac{\nu}{Pr}\overline{\frac{\partial T'}{\partial x_k}\frac{\partial T'}{\partial x_k}}, \quad D_\theta = -2\frac{\nu}{Pr}\frac{\overline{\theta'^2}}{x_n^2}.$$

TABLE A.1. Model constants in the Reynolds-stress equations.

C_1 2.2	C_2 0.55	C_3 0.55	$C_{1\theta}$ 3.75	$C_{2\theta}$ 0.5	$C_{3\theta}$ 0.5	C_{1w} 0.6
C_{2w} 0.3	$C_{1\theta w}$ 0.75	c_w 2.53	C_s 0.20	C_θ 0.20	C_ϵ 0.15	$C_{\theta\theta}$ 0.22
$C_{\epsilon\theta}$ 0.22	$c_{\epsilon 1}$ 1.44	$c_{\epsilon 2}$ 1.92	C_{P1} 0.9	C_{P2} 0.72	C_{D1} 1.1	C_{D2} 0.8

d_θ is modeled as

$$d_\theta = \frac{\partial}{\partial x_k}\left(\frac{\nu}{Pr}\frac{\partial \overline{T'^2}}{\partial x_k} + C_{\theta\theta}\frac{k}{\epsilon}\,\overline{u_k' u_l'}\frac{\partial \overline{T'^2}}{\partial x_l}\right). \tag{A.22}$$

ϵ_θ is described by an equation which is modeled by the Jones & Musonge model,

TABLE A.2. Reynolds-stress boundary-layer equations.

variable	convection	diffusion		mean field production	buoyant *production*	viscous dissipation	pressure-strain / scrambling			low-*Re* modification
		molecular	turbulent				turbulent	mean-strain	buoyant	
u	$\frac{\partial u}{\partial x}+\frac{\partial v}{\partial y}=0$									
v	$u\frac{\partial v}{\partial x}+v\frac{\partial v}{\partial y}=$	$\nu\frac{\partial^2 v}{\partial x^2}$	$-\frac{\partial \overline{u'v'}}{\partial x}$		$+g\beta\,(T-T_\infty)$					
T	$u\frac{\partial T}{\partial x}+v\frac{\partial T}{\partial y}=$	$\frac{\nu}{Pr}\frac{\partial^2 T}{\partial x^2}$	$-\frac{\partial \overline{u'T'}}{\partial x}$							
ε	$u\frac{\partial \varepsilon}{\partial x}+v\frac{\partial \varepsilon}{\partial y}=$	$\nu\frac{\partial^2 \varepsilon}{\partial x^2}$	$+C_\varepsilon\frac{\partial}{\partial x}\left(\frac{k}{\varepsilon}\overline{u'^2}\frac{\partial \varepsilon}{\partial x}\right)$	$-C_{\varepsilon 1}\frac{\varepsilon}{k}\overline{u'v'}\frac{\partial v}{\partial x}$	$+C_{\varepsilon 1}\frac{\varepsilon}{k}g\beta\overline{v'T'}$	$-C_{\varepsilon 2}F_2\frac{\varepsilon^2}{k}$				$-2\nu\frac{\varepsilon}{x^2}e^{-0.5x^+}$
$\overline{u'v'}$	$u\frac{\partial \overline{u'v'}}{\partial x}+v\frac{\partial \overline{u'v'}}{\partial y}=$	$\nu\frac{\partial^2 \overline{u'v'}}{\partial x^2}$	$+C_s\frac{\partial}{\partial x}\left(\frac{k}{\varepsilon}\overline{u'^2}\frac{\partial \overline{u'v'}}{\partial x}\right)$	$-\overline{u'^2}\frac{\partial v}{\partial x}$	$+g\beta\,\overline{u'T'}$	$-f_s\,\varepsilon\frac{\overline{u'v'}}{k}$	$-(C_1+\frac{3}{2}C_{1w}f_w)\frac{\varepsilon}{k}\overline{u'v'}$	$+(1-\frac{3}{2}C_{2w}f_w)C_2\,\overline{u'^2}\frac{\partial v}{\partial x}$	$-C_3 g\beta\,\overline{u'T'}$	$-4\nu\frac{\overline{u'v'}}{x^2}$
$\overline{u'T'}$	$u\frac{\partial \overline{u'T'}}{\partial x}+v\frac{\partial \overline{u'T'}}{\partial y}=$	$\nu\frac{\partial^2 \overline{u'T'}}{\partial x^2}$	$+C_\theta\frac{\partial}{\partial x}\left(\frac{k}{\varepsilon}\overline{u'^2}\frac{\partial \overline{u'T'}}{\partial x}\right)$	$-\overline{u'^2}\frac{\partial T}{\partial x}$			$-(C_{1\theta}+C_{1\theta w}f_w)\frac{\varepsilon}{k}\overline{u'T'}$			$-4\nu\frac{\overline{u'T'}}{x^2}$
$\overline{v'T'}$	$u\frac{\partial \overline{v'T'}}{\partial x}+v\frac{\partial \overline{v'T'}}{\partial y}=$	$\nu\frac{\partial^2 \overline{v'T'}}{\partial x^2}$	$+C_\theta\frac{\partial}{\partial x}\left(\frac{k}{\varepsilon}\overline{u'^2}\frac{\partial \overline{v'T'}}{\partial x}\right)$	$-\overline{u'T'}\frac{\partial v}{\partial x}-\overline{u'v'}\frac{\partial T}{\partial x}$	$+g\beta\,\overline{T'^2}$		$-C_{1\theta}\frac{\varepsilon}{k}\overline{v'T'}$	$+C_{2\theta}\overline{u'T'}\frac{\partial v}{\partial x}$	$-C_{3\theta}g\beta\,\overline{T'^2}$	$-2\nu\frac{\overline{v'T'}}{x^2}$
$\overline{u'^2}$	$u\frac{\partial \overline{u'^2}}{\partial x}+v\frac{\partial \overline{u'^2}}{\partial y}=$	$\nu\frac{\partial^2 \overline{u'^2}}{\partial x^2}$	$+C_s\frac{\partial}{\partial x}\left(\frac{k}{\varepsilon}\overline{u'^2}\frac{\partial \overline{u'^2}}{\partial x}\right)$			$-\frac{2}{3}\varepsilon\left(1-f_s+\frac{3}{2}f_s\frac{\overline{u'^2}}{k}\right)$	$-C_1\varepsilon(\frac{\overline{u'^2}}{k}-\frac{2}{3})-2C_{1w}f_w\varepsilon\frac{\overline{u'^2}}{k}$	$-\frac{2}{3}C_2(1-2C_{2w}f_w)\overline{u'v'}\frac{\partial v}{\partial x}$	$+\frac{2}{3}C_3 g\beta\,\overline{v'T'}$	$-2\nu\frac{\overline{u'^2}}{x^2}$
$\overline{v'^2}$	$u\frac{\partial \overline{v'^2}}{\partial x}+v\frac{\partial \overline{v'^2}}{\partial y}=$	$\nu\frac{\partial^2 \overline{v'^2}}{\partial x^2}$	$+C_s\frac{\partial}{\partial x}\left(\frac{k}{\varepsilon}\overline{u'^2}\frac{\partial \overline{v'^2}}{\partial x}\right)$	$-2\,\overline{u'v'}\frac{\partial v}{\partial x}$	$+2g\beta\,\overline{v'T'}$	$-\frac{2}{3}\varepsilon\left(1-f_s+\frac{3}{2}f_s\frac{\overline{v'^2}}{k}\right)$	$-C_1\varepsilon(\frac{\overline{v'^2}}{k}-\frac{2}{3})+C_{1w}f_w\varepsilon\frac{\overline{u'^2}}{k}$	$+\frac{2}{3}C_2(2-C_{2w}f_w)\overline{u'v'}\frac{\partial v}{\partial x}$	$-\frac{4}{3}C_3 g\beta\,\overline{v'T'}$	$-2\nu\frac{\overline{v'^2}}{x^2}$
$\overline{w'^2}$	$u\frac{\partial \overline{w'^2}}{\partial x}+v\frac{\partial \overline{w'^2}}{\partial y}=$	$\nu\frac{\partial^2 \overline{w'^2}}{\partial x^2}$	$+C_s\frac{\partial}{\partial x}\left(\frac{k}{\varepsilon}\overline{u'^2}\frac{\partial \overline{w'^2}}{\partial x}\right)$			$-\frac{2}{3}\varepsilon\left(1-f_s+\frac{3}{2}f_s\frac{\overline{w'^2}}{k}\right)$	$-C_1\varepsilon(\frac{\overline{w'^2}}{k}-\frac{2}{3})+C_{1w}f_w\varepsilon\frac{\overline{u'^2}}{k}$	$-\frac{2}{3}C_2(1+C_{2w}f_w)\overline{u'v'}\frac{\partial v}{\partial x}$	$+\frac{2}{3}C_3 g\beta\,\overline{v'T'}$	$-2\nu\frac{\overline{w'^2}}{x^2}$
$\overline{T'^2}$	$u\frac{\partial \overline{T'^2}}{\partial x}+v\frac{\partial \overline{T'^2}}{\partial y}=$	$\frac{\nu}{Pr}\frac{\partial^2 \overline{T'^2}}{\partial x^2}$	$+C_{\theta\theta}\frac{\partial}{\partial x}\left(\frac{k}{\varepsilon}\overline{u'^2}\frac{\partial \overline{T'^2}}{\partial x}\right)$	$-2\,\overline{u'T'}\frac{\partial T}{\partial x}$		$-2\,\varepsilon_\theta$				$-2\frac{\nu}{Pr}\frac{\overline{T'^2}}{x^2}$
ε_θ	$u\frac{\partial \varepsilon_\theta}{\partial x}+v\frac{\partial \varepsilon_\theta}{\partial y}=$	$\frac{\nu}{Pr}\frac{\partial^2 \varepsilon_\theta}{\partial x^2}$	$+C_{\varepsilon\theta}\frac{\partial}{\partial x}\left(\frac{k}{\varepsilon}\overline{u'^2}\frac{\partial \varepsilon_\theta}{\partial x}\right)$	$-C_{P1}\frac{\varepsilon_\theta}{\overline{T'^2}}\overline{u'T'}\frac{\partial T}{\partial x}$ $-C_{P2}\frac{\varepsilon_\theta}{k}\overline{u'v'}\frac{\partial v}{\partial x}$		$-(C_{D1}\frac{\varepsilon_\theta}{\overline{T'^2}}+C_{D2}\frac{\varepsilon}{k})\varepsilon_\theta$				

ACKNOWLEDGEMENTS

The author thanks professor C.J. Hoogendoorn for his supervision during the past four years of research.

Thanks are also due to ir J.P.M. Dijkman and ir T.W.J. Peeters, who contributed to the research described in this thesis in partial fulfillment of the requirements for their engineering degree.

SUMMARY

This thesis considers the natural-convection flow for two geometries positioned in the gravitational field: a square cavity differentially heated over the vertical walls and a semi-infinite hot vertical plate in an isothermal environment. The temperature difference results into the natural-convection flow of the fluid inside the cavity and along the plate. When the temperature difference is large (or dimensionless: when the Rayleigh number is large) the flow mainly occurs in a thin layer along the vertical walls, which is the so-called natural-convection boundary layer. The flow for both air and water is calculated by numerically solving the two-dimensional, incompressible Navier-Stokes equations, including the energy equation. The Boussinesq approximation is applied. The spatial derivatives in the equations are discretized with the finite-volume method, whereas the time derivatives are discretized with an implicit scheme using three time levels. Besides the Navier-Stokes equations also the boundary-layer equations are numerically solved. The accuracy of the numerical results is checked by grid and time step refinement, and the results are compared with existing experimental data. Different *flow phenomena*, related to the natural-convection boundary-layer flow, are investigated, giving a complete picture of the flow.

All possible *laminar* similarity solutions of the boundary-layer equations, with a constant wall temperature and a variable thermal *stratification* of the environment, are numerically determined. A similarity solution depends on only one transformed coordinate. Some of the similarity solutions have no practical meaning because they cannot be matched with the rest of the flow. If the stratification is stable (*i.e.* the temperature increases with the height) there is *flow reversal* in part of the boundary layer.

The proper *scalings* of the steady laminar flow in the cavity are derived from the steady Navier-Stokes solutions. Proper scalings give a scaled solution that is independent of the Rayleigh number if the Rayleigh number is increased to infinity. The Navier-Stokes equations for large Rayleigh numbers are shown to converge to the boundary-layer equations. Therefore the boundary-layer equations actually describe the scalings of the cavity flow.

When the Rayleigh number exceeds a critical value (Ra_{cr}), the steady laminar solution in the cavity becomes unstable and a *bifurcation* to an unsteady laminar solution is found. The instability is determined by solving the unsteady Navier-Stokes equations. In the case of adiabatic horizontal walls $Ra_{cr}=1.7\times10^8$ is found for air and $Ra_{cr}\sim10^{10}$ for water. The flow for conducting horizontal walls is less stable. Directly beyond Ra_{cr} the unsteady flow shows a single frequency; only air in the case of adiabatic horizontal walls gives two frequencies. Arguments are given that support that the instability for conducting horizontal walls is related to the Rayleigh/Bénard instability, whereas the instability for adiabatic horizontal walls is related to a Tollmien-Schlichting instability in the vertical boundary layer. The second frequency for air in the case of adiabatic horizontal walls seems to be related to an instability after the hydraulic jump, which occurs in the upper corner of the cavity where the hot vertical boundary layer bends to a horizontal layer.

The instabilities initiate the laminar-turbulent *transition*.

When the Rayleigh number is further increased, the flow becomes fully *turbulent*. The turbulent boundary-layer equations, with a $k-\epsilon$ model for the turbulence, are solved for the plate in an isothermal environment. A much better prediction of the wall-heat transfer for the plate is found with the low-Reynolds-number $k-\epsilon$ models of Lam & Bremhorst, Chien and Jones & Launder than with the standard $k-\epsilon$ model. The low-Reynolds-number models delay the transition and their solution can be nonunique. The differential Reynolds-stress model for the turbulent flow along the plate shows that the use of the eddy-viscosity concept in the $k-\epsilon$ models is not fully justified for natural-convection flows. The proper scalings and *wall functions* are derived from the numerical results for the turbulent vertical natural-convection boundary layer along the plate. These wall functions are shown to be consistent with the theoretical proposal of George & Capp for wall functions in the outer part of the boundary layer.

The turbulent flow in the cavity is calculated with the Reynolds equations (*i.e.* the time-averaged Navier-Stokes equations) using the standard $k-\epsilon$ model and the low-Reynolds-number models of Chien and Jones & Launder. A definite conclusion about the accuracy of the turbulence models in the cavity requires the availability of more experimental data. As was also found for the plate, the low-Reynolds-number models delay the transition and their solution can be nonunique. The stratification in the core of the cavity is much smaller for the turbulent flow than for the laminar flow. Due to the small stratification the averaged wall-heat transfer for the turbulent flow in the cavity is only slightly larger than the averaged wall-heat transfer for the plate in the isothermal environment. The scalings of the turbulent flow in the cavity are close to the scalings for the plate with respect to the Rayleigh-number dependence, but not with respect to the height dependence.

SAMENVATTING (summary in Dutch)

Dit proefschrift beschouwt de natuurlijke convectie stroming voor twee geometrieën die zich in het zwaartekrachtsveld bevinden: een vierkante gesloten ruimte met een temperatuurverschil over de vertikale wanden en een half oneindige hete vertikale plaat in een isotherme omgeving. Het temperatuurverschil leidt tot de natuurlijke convectie stroming van het fluidum in de ruimte en langs de plaat. Als het temperatuurverschil groot is (of dimensieloos: als het Rayleigh getal groot is) vindt de stroming voornamelijk plaats in een dunne laag langs de vertikale wanden, hetgeen de zogenaamde natuurlijke convectie grenslaag vormt. De stroming voor zowel lucht als water wordt uitgerekend door de tweedimensionale, incompressibele Navier-Stokes vergelijkingen, inclusief de energie vergelijking, numeriek op te lossen. De Boussinesq benadering wordt toegepast. De ruimtelijke afgeleiden in de vergelijkingen worden gediscretiseerd met de eindige volume methode, terwijl de tijdsafgeleiden worden gediscretiseerd met een impliciet schema dat drie tijdsniveau's gebruikt. Naast de Navier-Stokes vergelijkingen worden ook de grenslaagvergelijkingen numeriek opgelost. De nauwkeurigheid van de numerieke resultaten wordt nagegaan door verfijning van het rekenrooster en de tijdstap, en de resultaten worden vergeleken met bestaande meetresultaten. Verschillende *stromingsverschijnselen*, die verband houden met de natuurlijke convectie grenslaag, worden onderzocht, hetgeen een compleet beeld van de stroming oplevert.

Alle mogelijke laminaire *gelijkvormige* oplossingen van de grenslaagvergelijkingen, met een vaste wandtemperatuur en met een variabele thermische *stratificatie* van de omgeving, worden numeriek bepaald. Een gelijkvormigheidsoplossing hangt slechts van één getransformeerde coördinaat af. Een aantal van die gelijkvormigheidsoplossingen hebben geen praktische betekenis, omdat ze niet bij de rest van de stroming blijken aan te sluiten. Als de stratificatie stabiel is (d.w.z. als de temperatuur toeneemt met de hoogte) treedt er *terugstroming* op in een gedeelte van de grenslaag.

De juiste *schalingen* van de stationaire laminaire stroming in de ruimte worden afgeleid uit de stationaire Navier-Stokes oplossingen. Juiste schalingen geven een geschaalde oplossing die niet meer van het Rayleigh getal afhangt in de limiet van oneindig grote Rayleigh getallen. Er wordt aangetoond dat de Navier-Stokes vergelijkingen in de ruimte bij grote Rayleigh getallen convergeren naar de grenslaagvergelijkingen. Zodoende beschrijven de grenslaagvergelijkingen feitelijk de schalingen van de stroming in de ruimte.

Als het Rayleigh getal een critische waarde overschrijdt (Ra_{cr}), wordt de stationaire laminaire oplossing voor de ruimte instabiel en treedt er een *bifurcatie* naar een instationaire laminaire oplossing op. De instabiliteit wordt bepaald door de instationaire Navier-Stokes vergelijkingen op te lossen. Bij adiabatische horizontale wanden wordt $Ra_{cr} = 1.7 \times 10^8$ gevonden voor lucht, en $Ra_{cr} \sim 10^{10}$ voor water. De stroming bij geleidende horizontale wanden is minder stabiel. Direkt boven Ra_{cr} vertoont de instationaire stroming één enkele frequentie; alleen lucht bij adiabatische horizontale wanden vertoont twee frequenties. Er worden

argumenten gegeven die er op wijzen dat de instabiliteit bij geleidende horizontale wanden gerelateerd is aan de Rayleigh/Bénard instabiliteit, terwijl de instabiliteit bij adiabatische horizontale wanden gerelateerd is aan de Tollmien-Schlichting instabiliteit in de vertikale grenslaag. De tweede frequentie bij lucht voor adiabatische horizontale wanden lijkt te maken te hebben met een instabiliteit na de hydraulische sprong, die optreedt in de bovenhoek van de ruimte waar de vertikale grenslaag zich ombuigt tot een horizontale laag. De instabiliteiten initiëren de laminaire-turbulente *omslag*.

Als het Rayleigh getal verder stijgt, wordt de stroming volledig *turbulent*. De turbulente grenslaagvergelijkingen, met een $k-\epsilon$ model voor de turbulentie, worden opgelost voor de plaat in een isotherme omgeving. Er wordt een veel betere voorspelling van de warmteoverdracht langs de wand van de plaat gevonden met de lage Reynolds $k-\epsilon$ modellen van Lam & Bremhorst, Chien en Jones & Launder dan met het standaard $k-\epsilon$ model. De lage Reynolds modellen stellen de omslag uit en hun oplossing kan niet-eenduidig zijn. Het differentiaal Reynolds-stress model voor de turbulente stroming langs de plaat laat zien dat het gebruik van het turbulente viscositeitsconcept in $k-\epsilon$ modellen niet geheel gerechtvaardigd is bij natuurlijke convectie stromingen. De juiste schalingen en *wandfuncties* worden afgeleid uit de numerieke resultaten voor de turbulente natuurlijke convectie grenslaag langs de plaat. Deze wandfuncties blijken consistent te zijn met het theoretische voorstel van George & Capp omtrent wandfuncties in het buitenste gedeelte van de grenslaag.

De turbulente stroming in de ruimte wordt uitgerekend met de Reynolds vergelijkingen (dit zijn de tijdsgemiddelde Navier-Stokes vergelijkingen) waarbij het standaard $k-\epsilon$ model en de lage Reynolds modellen van Chien en Jones & Launder worden gebruikt. Om een duidelijke conclusie omtrent de nauwkeurigheid van de turbulentie modellen voor de ruimte te kunnen trekken zijn meer meetresultaten nodig. Zoals ook gevonden werd voor de plaat, vertragen de lage Reynolds modellen de omslag en kan hun oplossing niet-eenduidig zijn. De stratificatie in de kern van de ruimte is veel kleiner bij de turbulente stroming dan bij de laminaire stroming. Door de geringe stratificatie is de gemiddelde warmteoverdracht door de wand voor de turbulente stroming in de ruimte slechts weinig groter dan de gemiddelde warmteoverdracht door de wand van de plaat in de isotherme omgeving. De schalingen van de turbulente stroming in de ruimte wijken maar weinig af van de schalingen voor de plaat, althans wat de Rayleigh afhankelijkheid aangaat, maar niet wat de hoogte aangaat.

ABOUT THE AUTHOR

November 12, 1960: born in Delft, The Netherlands.

1973-1979: passing through the Gymnasium β of the Lodewijk Makeblijde College in Rijswijk, The Netherlands. Diploma obtained with honours.

1980-1985: studying at the Faculty of Aerospace Engineering of the Delft University of Technology, The Netherlands. Graduated with honours.
During the final phase of the study there was a stay of three months at the Von Karman Institute in Belgium. The final engineering research took place in the low-speed aerodynamics group of the faculty under the supervision of the professors J.L. van Ingen and A.E.P. Veldman. This research consisted of the numerical calculation of the steady and unsteady forced-convection boundary-layer flow along an indented plate and along a cylinder.

1986-1990: Ph.D. research in the heat-transfer group of the Faculty of Applied Physics at the Delft University of Technology, The Netherlands, under the supervision of professor C.J. Hoogendoorn. The results of that research are described in this thesis.

In July 1990 the author will become an Academy-Fellow of the Royal Dutch Academy of Sciences, for a period of three years.

ISBN 90-9003467-6

printing and binding Huisdrukkerij Delft University, Delft.
printing cover Econoom bv, Beek (L.).
design cover Piet Gerards gvn, Heerlen.
painting on cover Fons Lemmens, Eijsden, © 1990 c/o Beeldrecht Amsterdam.